Departamento de Matemáticas
Facultad de Ciencias
Universidad Autónoma de Madrid

Instituto de Ciencias Matemáticas
(CSIC - UAM - UC3M - UCM)

Instabilities in geophysical fluid dynamics: the influence of symmetry and temperature dependent viscosity in convection

Jezabel Curbelo Hernández

Tesis doctoral dirigida por Ana M. Mancho

This work was supported in part by the JAE-Predoc fellowship program, by the Spanish Ministry of Science under grant MTM2011-26696 and MINECO: ICMAT Severo Ochoa project SEV-2011-0087. We are grateful to CESGA and to CCC of Universidad Autónoma de Madrid for computing facilities.

A mis padres y mi hermano

Abstract

Spectral numerical methods are proposed to solve the time evolution of a convection problem in a 2D domain with viscosity strongly dependent on temperature. We have considered periodic boundary conditions along the horizontal coordinate which introduce the O(2) symmetry into the setting. This motivates the use of spectral methods as an approach to the problem. The analysis is assisted by bifurcation techniques such as branch continuation, which has proven to be a useful, and systematic method for gaining insight into the possible stationary solutions satisfied by the basic equations. Several viscosity laws which correspond to different dependences of the viscosity with the temperature are investigated. Numerous examples are found along the branching diagrams, in which stable stationary solutions become unstable through a Hopf bifurcation. In the neighborhood of these bifurcation points, the scope of our techniques is examined by exploring transitions from stationary regimes towards time dependent regimes.

Our study is mainly focused on viscosity laws that model an abrupt transition of viscosity with temperature. In particular, both a smooth and a sharp transition are explored. Regarding the stationary solutions, the way in which different parameters in the viscosity laws affect the formation and morphology of thermal plumes is discussed. A variety of shapes ranging from spout to mushroom shaped are found. Some stationary stable patterns that break the plume symmetry along their vertical axis are detected, as well as others that correspond to non-uniformly distributed plumes. The main difference between the solutions observed for the smooth and sharp transition laws is the presence in the latter case of a stagnant lid, which is absent in the first law. In both cases, we report time-dependent solutions that are greatly influenced by the presence of the symmetry and which have not previously been described in the context of temperature-dependent viscosities, such as travelling waves, heteroclinic connections and chaotic regimes. Notable solutions are found for the sharp transition viscosity law in which time-dependent solutions alternate an upper stagnant lid with plate-like behaviors that move either towards the right or towards the left. This introduces temporary asymmetries on the convecting styles. This kind of solutions are also related to the presence of the O(2) symmetry and constitute an example of a plate-like convective style which is not linked to a subduction process. These findings provide an innovative approach to the understanding of convection styles in planetary interiors and suggest that symmetry may play a role in describing how planets work.

Finally, the centrifugal and viscosity effects in a rotating cylinder with large Prandtl number are numerically studied in a regime where the Coriolis force is relatively large. Our focus is on aqueous mixtures of glycerine with mass concentration in the range of 60%-90%, and Rayleigh number values that extend from the onset, where thermal convection is in the so-called wall modes regime, in which pairs of hot and cold thermal plumes ascend and descend in the sidewall boundary layer, to values in which the bulk fluid region is also convecting. The mean viscosity, which varies faster than exponentially with variations in the percentage of glycerine, leads to a faster than exponential increase in the Froude number for a fixed Coriolis force, and hence an enhancement of the centrifugal buoyancy effects with significant dynamical consequences are described.

Resumen

En esta tesis proponemos métodos numéricos espectrales, para resolver la evolución temporal de un problema de convección en un dominio 2D con viscosidad fuertemente dependiente de la temperatura. Las condiciones de contorno periódicas a lo largo de la coordenada horizontal introducen la simetría O(2) en el problema lo que motiva el uso de métodos espectrales en este contexto. Realizamos un análisis de las soluciones mediante técnicas propias de la teoría de bifurcaciones, y constatamos que son un método útil y sistemático para describir el panorama de las soluciones estacionarias que satisfacen las ecuaciones básicas. Investigamos varias leyes de viscosidad que corresponden a diferentes dependencias de ésta con la temperatura. A lo largo de los diagramas de bifurcación se encuentran numerosos ejemplos en los que la solución estacionaria estable se vuelve inestable a través de una bifurcación Hopf. En las proximidades de esos puntos examinamos el alcance de nuestras técnicas, explorando la transición desde regímenes estacionarios a regímenes dependientes del tiempo.

Nuestro estudio se centra principalmente en las leyes de la viscosidad que modelan una transición abrupta de la viscosidad con la temperatura. En particular, se exploran tanto una transición suave como una brusca. En cuanto a las soluciones estacionarias, se discute cómo los diferentes parámetros en las leyes de viscosidad afectan a la formación y la morfología de las plumas térmicas. Se encuentran una variedad de la formas que van desde forma de protuberancia ("spout") a la forma de seta. Se detectan algunos patrones de soluciones estacionarias estables que rompen la simetría de la pluma a lo largo de su eje vertical y otros que se corresponden con plumas distribuidas de manera no uniforme. La principal diferencia entre las soluciones observadas para las leyes de transición suave y brusca es la presencia, con esta última ley, de una capa estancada que no está presente con la primera. En ambos casos mostramos soluciones dependientes del tiempo que están muy influenciadas por la presencia de la simetría y que no se han descrito previamente en el contexto de convección con viscosidad dependiente de la temperatura. Estas soluciones son por ejemplo ondas viajeras, conexiones heteroclínicas y regímenes caóticos. Para transiciones bruscas de la ley de viscosidad destacan soluciones dependientes del tiempo, en las que se alternan una capa superior estancada, con una capa o placa que se mueve rígidamente hacia la derecha o la izquierda. Esto introduce estilos de convección que son asimétricos en el tiempo. Este tipo de soluciones también están relacionadas con la presencia de la simetría O(2) y constituyen un ejemplo de convección en forma de placa que no está vinculada a un proceso de subducción. Estos resultados aportan un enfoque innovador para la comprensión de estilos de convección en el interior de planetas y sugieren que la simetría puede desempeñar un papel importante en la descripción de cómo funcionan.

Por último, se estudian numéricamente los efectos centrífugos en un cilindro que rota, en un régimen en el que la fuerza de Coriolis es relativamente grande y en el que el fluido tiene un número de Prandtl alto. Nuestra atención se centra en mezclas acuosas de glicerina con concentraciones de masa en el intervalo de 60 %-90 % y valores de número de Rayleigh que se extienden desde el inicio de la convección térmica; que son el denominado régimen de modos de pared, donde pares de plumas calientes y frías ascienden y descienden en la capa límite de la pared lateral; hasta valores en los que la convección está completamente desarrollada en toda la celda. El aumento de la viscosidad media, que varía con el porcentaje de glicerina considerado, conduce, para una fuerza de Coriolis fija, a un aumento en el número de Froude y por lo tanto, a un incremento de los efectos centrífugos para los que describimos su impacto en la dinámica.

Agradecimientos

Me gustaría que estas líneas sirvieran para expresar mi más profundo y sincero agradecimiento a todas aquellas personas, que de una u otra manera, han hecho que esta tesis fuera posible. En especial a mi directora, Ana María Mancho, por la orientación, el seguimiento y la supervisión continúa de la misma, pero sobre todo por la dedicación, paciencia y tiempo invertido, por la motivación constante, por todo lo que me ha enseñado, y todo lo que he aprendido gracias a ella y por las conversaciones, no sólo académicas, que me mostraban el lado bueno de las cosas y cómo seguir adelante. Agradezco el apoyo recibido a lo largo de estos años, y le doy las gracias por todas las oportunidades que me ha brindado.

En Arizona, Juan M. López me acogió, sin conocerme, abriéndome no sólo las puertas de su despacho sino también las de su casa. Muchas gracias por las discusiones, comidas y paseos, siempre tan provechosos; y por su inestimable ayuda y colaboración. Quisiera agradecer también a Francisco Marques todos sus comentarios y consejos.

I have been fortunate to work with Steve Wiggins: his work philosophy, his enthusiasm and his vision of mathematics have been very enriching for me. Thanks for your help in my search for postdoc. Me gustaría agradecer también al resto de miembros del tribunal, Michael Bestehorn, Angel Castro, Amadeu Delshams, María Higuera, Sergio Hoyas, Santiago Madruga, el interés mostrado en mi trabajo y sus comentarios. Y a mi tutor de tesis, Rafael Orive, no sólo por autorizar y firmar toda la burocracia relacionada con la misma, sino también por su ayuda en temas docentes y departamentales.

He tenido la suerte de conocer y trabajar con diferentes personas, con distintas visiones de las matemáticas e intereses muy variados, no sólo estos últimos cuatro años, Antonio M. Álvarez-Valero, Kayo Ide, Carolina Mendoza, sino desde mis inicios en la Universidad de La Laguna, cuando ni siquiera había terminado la carrera, Víctor Almeida, Juan Carlos Fariña, Lourdes Rodríguez-Mesa. Quisiera agradecer a todas estas personas que han contribuido a mi formación (matemática, geofísica y personal), especialmente a Pepe Méndez; que siempre fue guía, apoyo e impulso, Jorge J. Betancor; que me enseño lo que era una artículo científico y todo el trabajo que hay detrás de él desde la idea inicial hasta su publicación, y Alejandro J. Castro, con el que se inició mi andadura en esto que llaman investigación.

Si intentó recordar los mejores momentos de estos últimos años, muchos han ocurrido en el Instituto de Ciencias Matemáticas o con gente que trabaja o ha trabajado en él. Será difícil olvidar los descansos, los cafés, las meriendas y las interesantes conversaciones de media tarde, a todos; tanto los que siguen, los que acaban de llegar o los que están desperdigados por el mundo; muchas gracias por el buen ambiente, los buenos momentos, y las salidas "siempre exitosas" de

los fines de semana. Una mención aparte merecen todos aquellos con los que en algún momento, he compartido despacho y me han tenido que aguantar muchas horas al día, tanto en la UAM; Beatriz, Iason, Roger, como en el ICMAT, Dani, Viviana y especialmente, a dos grandes amigos: Rafa, compañero de despacho y vecino en la residencia, siempre con una historia que contar, una curiosidad o una anécdota, gracias por hacer cortas las largas tardes en el despacho y enseñarme que se puede aprender divirtiéndose; y Javi, que siempre ha tenido tiempo para escuchar mis problemas académicos (ordenador, cuentas, papeleo, inglés, y un largo etcétera), y también los no académicos. Gracias por decir siempre las palabras apropiadas en el momento adecuado.

Gracias a compañeros y amigos, con quienes he exprimido Madrid, y sus alrededores. Gracias por los largos almuerzos de sábado, por los planes de último momento, las mañanas de compras, las tardes de teatro, las noches de baile y los días de mudanza. Gracias Yasmina por tu ayuda en los no tan buenos momentos, gracias Diana por esas conversaciones sobre futuro tomando café. Gracias también a "los salseros", matemáticos o no, que han hecho que los lunes sean el mejor día de la semana. Especialmente a Tania, con la que he compartido muchos momentos tanto dentro como fuera del instituto. Y gracias también a los que me han tenido que aguantar al llegar a casa, mis compañeros de residencia (especialmente a Dani) y de piso (Adrián, Dani).

Gracias Paloma por ser mi guía y mi transporte en Arizona. Gracias por esas mañanas de trabajo y las tardes/noches de ocio. *I would also like to thank other friends I made in Arizona, in both the first and second stay, for their hospitality. The doors of their house were always open for me. Especially Jenny.*

Por último, quisiera agradecer a mi familia, por su cariño comprensión y apoyo incondicional, que en determinados momentos he necesitado en dosis elevadas y sin el cuál no podría haber llegado a este punto. Gracias papá, por tus consejos, confianza y cariño. Gracias David, por siempre sacarme una sonrisa. Gracias mamá, por volver a llamar cuando no quería responder, por estar siempre al otro lado del teléfono y por el ánimo, apoyo y compresión que me has dado en todo momento. Gracias a los tres, porque aunque nos separen muchos kilómetros siempre han estado cerca.

Gracias.

Contents

List of Notations

a	Inverse of the maximum viscosity contrast	15
a_{lm}^{Y}	Complex coefficients of the expansion	79
α	Thermal expansion coefficient	14
b	Temperature at which the transition occurs	15
β	Parameter that controls how abrupt the viscosity transition with temperature is	15
b_{lm}^{Y}	Real coefficients of the expansion	79
c	Exponential rate in the Torrance and Turcotte viscosity law	15
c_{lm}^{Y}	Real coefficients of the expansion	79
d	Depth between the plates	13
ΔT	Vertical temperature difference	13
$\vec{e}_3$	Unitary vector in the vertical direction	14
F	Gravitational and centrifugal force	93
Fr	Froude number	17
g	Gravity acceleration	14
Γ	Aspect ratio	14
γ	Linear rate in the viscosity law	18
κ	Thermal diffusivity	14
L	Length of plates	13
	Number of nodes in the horizontal direction	78
L_{ij}	Linear operators with non constant coefficients	80
m	Wavenumber	20
M	Number of nodes in the vertical direction	79
	Singular Matrix of a differential algebraic equation (DAE)	84

CHAPTER 1

Introduction

This Ph.D Thesis is based on a compendium of articles and is structured as follows: in this chapter we present an overview of the contents from the geophysical and mathematical points of view; the importance of the issues discussed and the state of the art so far. We also describe the physical setup of the problems under study. In Chapter 2, the specific objectives of the study are described. Chapter 3 presents the results as a series of articles written in collaboration with other authors while preparing this Ph.D. A discussion of the results is provided in Chapter 4. Finally, Chapter 5 presents the conclusions.

1.1. Motivation

Thermal convection of the upper mantle is the driving force of plate tectonics, which causes the continental drift [36, 76, 86, 107]. In recent years, the study of mantle convection has focused on understanding the generation and evolution of plate tectonics [5], although there are still many questions that remain unanswered. As regards the dynamics of the mantle, studies exist about how convection is affected by variations in the basic equations, particularly those that look for a better physical and geochemical approximation to mantle properties [7, 62, 91]. Observations indicate that, in geological time scales, the mantle deforms like a fluid. If the mantle is treated as such, it is necessary to model properties such as thermal conductivity, density or viscosity. For instance, in mantle convection viscosity has typically been considered to depend strongly on temperature, although it may also be dependent on another magnitudes such as depth [11], a combination of both depth and temperature [6], or pressure. In addition to viscosity, other fluid properties may depend on temperature such as density, thermal diffusivity or thermal conductivity. However, since consideration of the effect of simultaneous variations on all the properties fails to provide a clear understanding of the exact role played by each one of these properties, in our study we consider solely the effects due to the variability of viscosity.

Geophysical applications arising from the numerical study of convection problems with viscosity strongly dependent on temperature make it a subject of great interest. Furthermore from the mathematical point of view it has recently been proven that this is a well-posed problem [50, 112] for viscosities which are smooth bounded positive analytical functions of temperature, and therefore stands a good chance of solution on a computer using a stable algorithm.

1.2. The geophysical point of view

In the classical Rayleigh-Bénard convection problem, heat is applied uniformly from below and the conductive solution (also called the basic solution), which is the simplest stationary solution to the problem, is characterized by a fluid at rest with a constant gradient of temperature. This solution becomes unstable for a vertical gradient of temperature beyond a critical threshold. Above this threshold, the convective motion settles in and new patterns are observed; the fluid begins to move and form convection rolls that circulate alternately in a clockwise or a counterclockwise direction (see Figure 1.1).

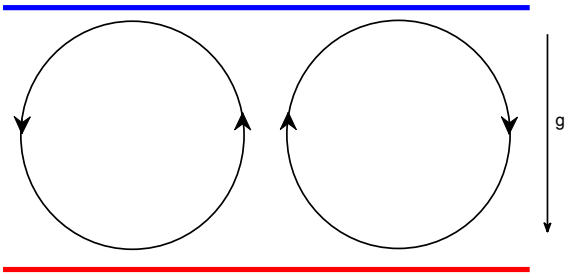

Figure 1.1. Rayleigh-Bénard convection.

The Earth's interior behaves as a convective fluid on geological scales. However, in some aspects it differs from classical Rayleigh-Bénard convection. For instance, the physical properties of the mantle include a complex rheology and variable viscosity that may depend on temperature or other magnitudes such as depth [11], a combination of both depth and temperature [6], or pressure. The variability of the viscosity introduces strong couplings between the momentum and heat equations, as well as important nonlinearities into the whole problem. Transitions in the viscosity are important for describing melting and solidification processes which are significant in magma chamber dynamics [8, 9], in volcanic conduits [35, 75], in the formation of chimneys in mushy layers [21], in metal processing in industry (see [95], for example), and so on. In phase transitions, in addition to viscosity, other fluid properties such as density or thermal diffusivity may change abruptly.

Most studies on convection in the Earth's mantle employ the Boussinesq approximation, which assumes an incompressible mantle. However, the mantle is compressible due to changes in the density, which increases towards the Earth interior. Typically, density may depend on depth, temperature and/or pressure. Studies in which numerical analysis of compressible convection are performed indicate that density stratification has a stabilizing effect [61], producing upwelling plumes weaker than downwelling plumes and influencing the thermal boundary layer [67]. Thermal conductivity may also be variable, but this dependence has generally received less attention than that of viscosity, as the latter is much stronger in the Earth's mantle. The dependence of conductivity on temperature introduces new nonlinearities into the heat equation, which may lead to diverse dynamics [55]. Conductivity that decreases with temperature makes convection more chaotic and time dependent [34, 115].

The variety of physical properties causes diverse types of convection. Layered convection is due to endothermic phase changes in the minerals that constitute the mantle's interior [73]. Large viscosity contrasts in fluids with temperature-dependent viscosity lead to stagnant lid convection [81, 99], such as that presented in the lithosphere of other bodies in the solar system such as the Moon, Venus or Mars [100, 101]. Regarding the subduction initiation, numerical results [5, 98, 104, 106] suggest that this is only possible if the stiff upper layers of the lithosphere are weakened by brittle fracture. Several mechanisms have been proposed for driving the motion of the lithospheric plates. Forsyth and Uyeda [38], for instance, conclude that plate-like motion is produced by the sinking slab that pulls the plate in the subduction process due to an excess of lithosphere density.

In this work, we consider solely the effects due to the variability of viscosity. Viscosity is a measure of the resistance of a fluid to gradual deformation, and in this sense very viscous fluids have a more rigid behavior than less viscous fluids. When examining the transition of viscosity with temperature, we focus on the global fluid motion when some parts of it tend to be more rigid than others. Disregarding the variations on density in this transition moves us away from instabilities caused by abrupt density changes, such as the Rayleigh-Taylor instability in which a denser fluid over a lighter one tends to penetrate it by forming a fingering pattern.

The study of symmetries in classical convection (*i.e.* in fluids with constant viscosity and thermal diffusivity) has been the object of much attention [3, 29, 45, 63, 64, 65, 79, 84], because symmetric systems typically exhibit more complicated behavior than non-symmetric systems, and there exist numerous novel dynamical phenomena whose presence is fundamentally related to the presence of symmetry, such as traveling waves or stable heteroclinic cycles [2, 29, 31, 49]. The counterpart of this problem in fluids with viscosity depending on temperature has received less consideration. Our focus is on a convection problem in a 2D domain, in which viscosity depends on temperature in the presence of the O(2) symmetry and infinite Prandtl number. Our problem is idealized with respect to realistic geophysical flows occurring in the Earth's interior, since these are 3D flows moving in spherical shells [12, 13]. Under these conditions, the symmetry present in the problem is formed by all the orientation, preserving rigid motions of $\mathbb{R}^3$ that fix the origin, which is the SO(3) group [18, 44, 59]. The effects of the Earth's rotation are negligible in this respect and do not break this symmetry, since the high viscosity of the mantle renders the Coriolis number insignificant. The link between our simplified problem and these realistic setups is that the O(2) symmetry is isomorphic to the rotations along the azimuthal coordinate, which form a closed subgroup of SO(3). In addition, the O(2) symmetry is present in systems with cylindrical geometry, which provide an idealized setting for volcanic conduits and magma chambers. SO(2) symmetry is also present in 3D flows moving in spherical shells which rotate around an axis. The interest of 2D numerical studies for representing 3D time-dependent thermal convection with constant viscosity is addressed in [96]. These authors report that in turbulent regimes at high Rayleigh numbers the flow structure and global quantities such as the Nusselt number and the Reynolds number show a similar behaviour in 3D and 2D simulations in which high values of the Prandtl number are concerned. These results therefore suggest that our simulations may well be illustrative for the 3D case, since although they are far from a turbulent regime and do not correspond to the case of constant viscosity, they have been performed according to the infinite Prandtl number approach. The impact of the symmetry on the solutions displayed in convection problems with viscosity dependent on temperature is addressed in Sections 3.1, 3.2 and 3.3.

Convective instabilities are also crucial in other geophysical contexts such as the atmosphere and the ocean. Motivated by the interest of studying the rotational effect (gravitational and centrifugal buoyancy force), which is negligible in the Earth's interior, we study confined rotating convection in 3D fluids in which viscosity weakly depends on temperature at large Prandtl number. Rotating Rayleigh-Bénard convection is currently the object of much additional attention due to the availability of new modern experimental facilities and significant advances in its numerical simulation [66, 103, 116]. For the most part, these studies are focused on low and moderate Prandtl numbers, motivated primarily by astrophysical interests [102]. Large Prandtl number systems are also of much interest, particularly when the working fluids are alcohols, silicone oils and exotic gases under high pressure. For this reason it is desirable to access high-Prandtl number regimes both in laboratory experiments and in numerical or theoretical models in order to gain insight into some of the physical processes involved. Some theoretical studies have been conducted in the limit of infinite Prandtl number [20, 33, 114], but these neglect two aspects of rotating convection which may be dominant, especially in a realistic physical setting; namely, confinement and centrifugal buoyancy [4, 53, 56, 68, 74, 92]. In our study we focus on examining rotating effects in a 3D cylinder containing aqueous mixtures of glycerine with large Prandtl number. The Prandtl number is large because the viscosity in these fluids is also very large. In the particular physical setting considered, which fixes the Coriolis number (see definition in (1.10)), centrifugal effects (represented by the Froude number) are specially important, because they increase with the viscosity precisely because the Coriolis number is fixed. We study the centrifugal effects on the wall-modes regime. These are pairs of hot and cold thermal plumes which ascend and descend in the cylinder sidewall boundary layer, essentially forming a one-dimensional pattern characterized by the number of hot/cold plume pairs. These results are presented and discussed in Section 3.4.

1.3. The mathematical point of view

The ocean, the atmosphere and the interior of the planets can be described by the equations of fluid dynamics because they behave as fluids. Although the equations of fluid mechanics were formulated more than two centuries ago, the structure of their solutions still remains one of the most studied problems in mathematics, due to the difficulties introduced by their nonlinear terms.

The existence of critical conditions giving rise to an instability is related to the presence of a bifurcation. Bifurcation theory provides a theoretical framework for describing a range of solutions to nonlinear dynamical systems that depend upon physical parameters that may vary causing the system to show different states. Let us denote by μ a vector of scalars that represent these physical parameters. A local bifurcations point can be detected from a stability change. Let us consider the evolution problem $u' = G(\mu, u)$, for a certain class of operators G, which depend on μ, the scalars related to physical parameters, and acts on u, the physical state. Let us consider u_0, an equilibrium solution that satisfies $G(\mu, u_0) = 0$. The principle of linearized stability states that for a fixed μ if all eigenvalues λ of the linearized operator $G'(\mu, u_0)$ (linearized with respect to u) satisfy $\Re(\lambda) \leq a < 0$ for some a independent of λ, then the equilibrium solution u_0 of the equation $u' = G(\mu, u)$ is stable. The principle is well-established for finite systems of ordinary differential equations, corresponding to the equation $u' = G(\mu, u)$ on a finite-dimensional space; the result is known as Lyapounov's Theorem. In this case, the condition $\Re(\lambda) \leq a < 0$ can be replaced by the simpler condition $\Re(\lambda) < 0$ for all λ. The two conditions are equivalent because there is a finite number of eigenvalues. Thus if they all have negative real parts, there is an eigenvalue λ_0 with the

largest real part, and we have $\Re(\lambda) \leq \Re(\lambda_0) < 0$ for all λ. For operators on infinite-dimensional spaces, the condition $\Re(\lambda) \leq a < 0$ is stronger than $\Re(\lambda) < 0$, since there may be a sequence of eigenvalues tending to zero from below; the stronger condition is needed to exclude "marginal stability" (eigenvalues with $|\Re(\lambda)|$ arbitrarily small), which can be turned into instability by small perturbations.

In this thesis, we work with partial differential equations, and thus with infinite-dimensional spaces. However the considered system is highly dissipative and in a finite-sized domain, and for this reason it behaves as a finite dimensional system. We approach the stationary solutions u_0 in our setup by means of a spectral collocation technique in a spatial grid. We analyse the stability of these solutions by means of a linear stability analysis, the purpose of which is to determine the sign of the real part of the eigenvalue λ. If it is negative, the perturbation decays and the stationary solution is stable, while if it is positive, the perturbation increases and the stationary solution is unstable. The bifurcation point corresponds to the parameter set μ, in which $\Re(\lambda) = 0$, and $\Im(\lambda) = 0$ (stationary bifurcation) or $\Im(\lambda) \neq 0$ (Hopf bifurcation). Representations of different types of stationary bifurcations can be seen in Figure 1.2. In our setting, due to the presence of the symmetry there always exists a zero eigenvalue which is related to a neutral dynamically non active direction [31].

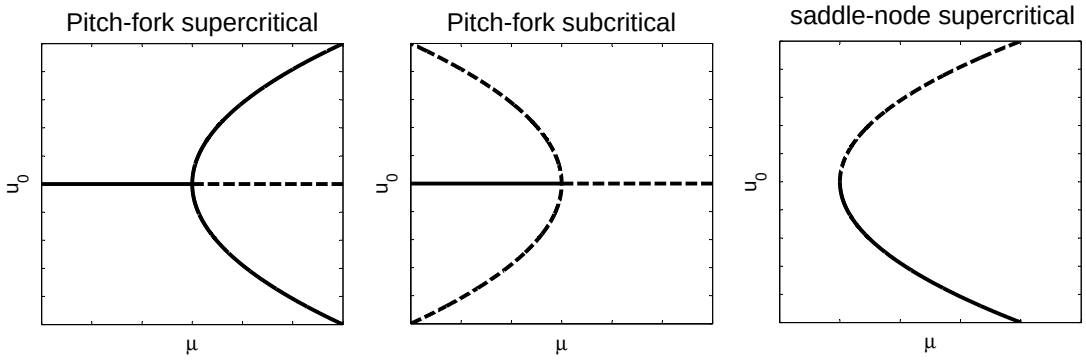

Figure 1.2. Branching diagrams of local Bifurcations. The dashed branches correspond to unstable equilibrium solutions, while the solid ones are stable equilibrium solutions.

Although rigorous results exist on local bifurcation theory in PDE (see [22, 89]), in practice it appears difficult to use such results to answer specific questions about the solutions, e.g. to determine the number of non-constant co-existing steady states. Rigorous computational methods have recently attempted to fill the gap between the above-mentioned theoretical and computational advances. For instance, Park [87, 88] examines the bifurcation and structure of the solutions using the theory of *attractor bifurcation* developed by Ma and Wang [71, 72]. Other rigorous approaches to this problem by Lessard *et al.* [10, 32, 39, 109], employ finite dimensional projections by using spectral expansions, and then approximations to construct a global continuous curve, eventually applying the uniform contraction principle on tubes to reach a conclusion on the existence of a unique smooth solution curve. Typically, the systems analyzed with these techniques are simpler than ours. Non rigorous numerics is the first step to take in the analysis of the problems under consideration, which have not been studied before and have a higher degree of complexity.

We conduct our study by combining bifurcation techniques with time-evolution simulations. For the 2D problem, it has been proven in in recent works [50, 112] that, from the mathematical point of view, the convection problem that concerns us in Sections 3.1, 3.2 and 3.3 is a well-posed problem. Well-posedness has been proven for dependences of viscosity with temperature that are bounded positive analytic functions. Thus, we expect a stable algorithm that approaches the time-evolution problem to exist.

The problem discussed in Sections 3.1, 3.2 and 3.3 is very stiff, since it is in fact a set of differential algebraic equations, and for this reason it is a partial differential system for which certain numerical methods for solving the equations are numerically unstable, unless the step size is taken to be extremely small. The term "stiff" first appeared in the paper by Curtiss and Hirschfelder [28] on problems in chemical kinetics. Without giving a precise definition, they call a differential equation stiff if the implicit Euler method performs much better than the explicit Euler method. This article is also famous because it introduces the backward differentiation formulas (BDF). The presence of different time scales in the time evolution is a distinctive feature of stiff problems. Application of standard methods for the solution of these problems, for example, the Euler method, explicit Runge-Kutta methods, or Adams-Bashforth can exhibit instability though other methods may produce stable solutions. Methods intended to solve stiff problems efficiently do more work per step than nonstiff methods and usually, they are implicit. Currently, the most widely used methods for solving stiff problems are the linear multistep methods. In particular, as reported in Section 3.1, we have successfully implemented a semi-implicit BDF scheme to deal with the problem under consideration.

Our numerical approach uses spectral methods to expand the solution in the spatial coordinates. These methods are extensively used in the numerical simulation of convection problems, since they are highly accurate, although they are not very popular in the simulation of convection problems with temperature-dependent viscosity [60], especially when this dependence is very strong, as is the case in our first setup, because they are reported to have limitations when handling lateral variations in viscosity. Alternatively, preferred schemes exist in which the basis functions are local; for example, finite difference, finite element and finite volume methods. The works by [6, 42], for instance, have treated this problem in a finite element discretization in primitive variables, while in [23, 80] finite differences or finite elements are used in the stream-function vorticity approach. Spectral methods have been successfully applied to model mantle convection with moderate viscosity variations in, for instance, [14, 19]. These works do not use the primitive variables formulation, and deal with the variations in viscosity by decomposing it into a mean (horizontally averaged) part and a fluctuating (laterally varying) part. Our approach to the first setup, described next, addresses the variable viscosity problem by proposing a spectral approximation in primitive variables without any decomposition on the viscosity. The main novelty in this study is the extension of the spectral methodology discussed in [90], valid only for stationary problems, for solving the time-dependent problem.

In Section 3.1, the use of spectral techniques to solve the proposed problem numerically is justified, and the motivation for the use of these techniques in preference to others is discurred. Spectral methods may be particularly suitable for dealing with problems involving symmetries, as some solutions with approaches based on other spatial discretizations might be overlooked. In Section 3.2, the full partial differential equations system is analyzed by means of direct numer-

ical simulations and bifurcation analysis techniques, and we also show that typical solutions of systems with symmetries, as previously reported in diverse contexts [2, 31, 110], are also present in convection with temperature-dependent viscosity. We report the presence of travelling waves and limit cycles near heteroclinic connections after a Hopf bifurcation. The viscosity law (1.8) considered in Section 3.3 is similar to (1.7) studied in Section 3.2, the main difference being the size of the temperature gap in which the viscosity changes. The results described in Section 3.3 confirm the role of symmetry in the physical configuration of the problem. We show that in our setting convective processes exists which include plate-like motions that alternate in time with stagnant-lid regimes. Some of these transitions include bursts in which the solution releases energy to accommodate different spatial patterns.

The spectral techniques also are used in Section 3.4 in a rotation convection problem. This problem, is not so stiff as the one discussed in the previous sections and is solved with the second-order time-splitting method proposed in [58]. The spatial discretization of this fully 3D problem utilizes a Galerkin–Fourier expansion in the azimuthal coordinate and a Chebyshev collocation method in radial and vertical directions. See Section 3.4, Chapter 4 or reference [77] for more numerical details.

1.4. Problems Setups

We study two thermal convection problems: the first one is a 2D rectangular domain with infinite Prandtl number and viscosity strongly dependent on temperature, while the second, is a Rayleigh-Bénard convection problem in a 3D circular rotating cylinder with finite but large Prandtl and weak dependence of viscosity on temperature.

1.4.1. Convection with viscosity strongly dependent on temperature (2D)

First we consider a two-dimensional fluid layer of depth d (z coordinate) placed between two parallel plates of length L. The bottom plate is at temperature T_1 and the upper plate is at T_0, where $T_0 = T_1 - \Delta T$ and ΔT is the vertical temperature difference, which is positive. See Figure 1.3.

In the equations governing the system, $\mathbf{u} = (u_x, u_z)$ is the velocity field , T is the temperature, P is the pressure, x and z are the spatial coordinates and t is the time, respectively. Equations are simplified by taking into account the Boussinesq approximation, in which the density ρ is considered constant everywhere except in the external forcing term, and where a dependence on temperature is assumed as follows $\rho = \rho_0(1 - \alpha(T - T_0))$. Here α is the thermal expansion coefficient and ρ_0 is the mean density at temperature T_1.

The magnitudes are expressed in dimensionless form after rescaling as follows: $(x', z') = (x, z)/d$, $t' = \kappa t/d^2$, $\mathbf{u}' = d\mathbf{u}/\kappa$, $P' = d^2P/(\rho_0\kappa\nu_0)$, $\theta' = (T - T_0)/(\Delta T)$. Here, κ is the thermal diffusivity and ν_0 is the viscosity at temperature T_0. After rescaling the domain, $\Omega_1 = [0, L)\times[0, d]$ is transformed into $\Omega_2 = [0, \Gamma) \times [0, 1]$, where $\Gamma = L/d$ is the aspect ratio. The system evolves according to the momentum and the mass balance equations, as well as to the energy conservation

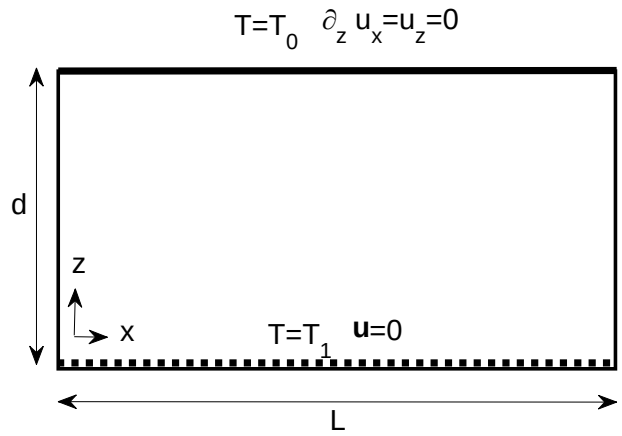

Figure 1.3. Problem setup. A 2D container of length L and depth d with periodic lateral boundary conditions. The bottom plate (dashed line) is rigid and is at temperature T_1; the upper plate (thick line) is free slip and is at temperature T_0 ($T_0 < T_1$).

principle. The non-dimensional equations are:

$$\nabla \cdot \mathbf{u} = 0, \tag{1.1}$$

$$\frac{1}{Pr}(\partial_t \mathbf{u} + \mathbf{u} \cdot \nabla \mathbf{u}) = Ra\theta \vec{e}_3 - \nabla P + \operatorname{div}\left(\frac{\nu(\theta)}{\nu_0}(\nabla \mathbf{u} + (\nabla \mathbf{u})^T)\right), \tag{1.2}$$

$$\partial_t \theta + \mathbf{u} \cdot \nabla \theta = \Delta \theta. \tag{1.3}$$

Here $\vec{e}_3$ represents the unitary vector in the vertical direction, $Ra = d^3 \alpha g \Delta T/(\nu_0 \kappa)$ is the Rayleigh number, g is the gravity acceleration and $Pr = \nu_0/\kappa$ is the Prandtl number, respectively. Typically for rocks Pr, is very large, since they present low thermal diffusivity (approximately $10^{-6} m^2/s$) and large viscosity (of the order $10^{20} Ns/m^2$) [30]. For this reason, Pr can be considered as infinite and the left hand side term in (1.2) can be made equal to zero. This transforms the problem into a differential algebraic equation (DAE), which is very stiff. The viscosity $\nu(\theta)$ is a smooth positive bounded function of θ. With these assumptions, the problem under study is a well-posed problem [50, 112] and thus there is a good chance of solving the time evolution problem with a stable algorithm.

Our setting is a 2D domain with periodic boundary conditions along the horizontal coordinate. We consider that the bottom plate is rigid and the upper surface is non-deformable and free slip. The dimensionless boundary conditions are expressed as,

$$\theta = 1, \ \mathbf{u} = \vec{0}, \ \text{on } z = 0 \text{ and } \ \theta = \partial_z u_x = u_z = 0, \ \text{on } z = 1. \tag{1.4}$$

Jointly with equations (1.1)-(1.3), lateral boundary conditions are invariant under translations along the x-coordinate, which introduces the symmetry SO(2) into the problem. In convection problems with constant viscosity, the reflexion symmetry $x \to -x$ is also present insofar as the fields are conveniently transformed as follows $(\theta, u_x, u_z, P) \to (\theta, -u_x, u_z, P)$. In this case, the O(2) group expresses the full problem symmetry. The new terms introduced by the temperature dependent viscosity in (1.2) maintain the reflexion symmetry, and thus the full symmetry group

is O(2).

In this work, we use several temperature viscosity laws for different purposes as, detailed below:

- Exponential law, according to previous results by [90]

$$\frac{\nu(\theta)}{\nu_0} = \exp(-\mu Ra\theta) \tag{1.5}$$

  where μ is the exponential rate and ν_0 is the maximum viscosity in the fluid layer. If $\mu = 0$, dependence on (1.5) reduces to that of constant viscosity. For the temperature-dependent viscosity case we consider $\mu = 0.0862$. This law is used in Section 3.1 for testing and verifying the spectral numerical approach, as typically spectral methods are not used in this context.

- Exponential law proposed by Torrance and Turcotte [105],

$$\frac{\nu(\theta)}{\nu_0} = \exp[c(1/2 - \theta)] \tag{1.6}$$

  where $c = \ln(\nu_{max}/\nu_{min})$. This law is only used for benchmark purposes in Section 3.1.

- "Smooth" arctangent law:

$$\begin{aligned} \frac{\nu(\theta)}{\nu_0} =& C_1 \arctan(\beta(Ra\theta\mu - b)) + C_2 \\ C_1 =& \frac{(1-a)}{\arctan(-\beta b) - \arctan(\beta(2500 - b))} \\ C_2 =& 1 - C_1 \arctan(-b\beta) \end{aligned} \tag{1.7}$$

  The arc-tangent law models a transition in the viscosity within a narrow temperature gap which is controlled by β. The parameter β controls how abrupt the viscosity transition with temperature is and is kept as 0.9. The temperature at which the transition occurs is controlled by b, the parameter related to the Rayleigh transition Ra_t which is described and used in the following law of viscosity, and a is related to the inverse of the maximum viscosity contrast. The parameter μ, related to physical constants in the system, is fixed to $\mu = 0.0146$.

  Figure 1.4 shows a representation of the law (1.7) for several parameter values. Figure 1.4(a) shows the dependence on the Ra number. At low Ra, the viscosity is almost uniform across the fluid layer, and it is only beyond $Ra = 1000$ that the sharp change in the viscosity is perceived. In Figure 1.4(b), dependance on the b number may be observed. For b as small as 1, the transition occurs close to $\theta = 1$ and most of the fluid layer has low viscosity, while if b is very large at this Ra number most of the fluid has constant viscosity ν_0. The critical Ra number is approximately $Ra_c \sim 1100$, thus if b is large, the viscosity near the critical Rayleigh number is almost constant across the fluid layer. In this case, the phase transition is noticed in the fluid at large Ra numbers, well above $Ra = 1300$, in a convection state in which vigorous plumes are already formed. Finally, Figure 1.4(c) shows the influence of different viscosity contrasts.

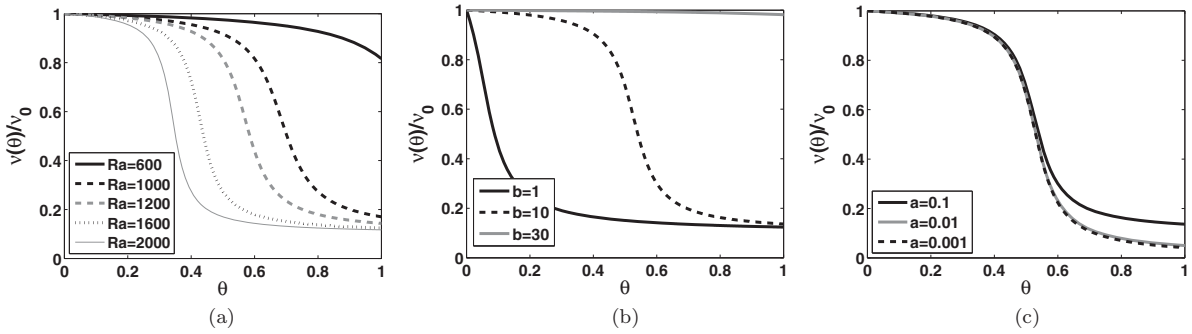

Figure 1.4. Representation of the arctangent viscosity law versus the dimensionless temperature for different parameters values; a) $b = 10$, $a = 0.1$ and different Ra values; b) $a = 0.1$, $Ra = 1300$ and different b values; c) $b = 10$, $Ra = 1300$ and different a values.

- "Sharp" arctangent law:

$$\frac{\nu(\theta)}{\nu_0} = -\left(\frac{1-a}{\pi}\right)\arctan(\beta\mu(Ra\theta - Ra_t)) + \left(\frac{1+a}{2}\right) \tag{1.8}$$

  This arctangent law models a transition in the viscosity which is controlled by β. The transition is now much sharper than before because β is fixed to 100. The constant μ is also fixed to $\mu = 0.0146$ and the temperature at which the transition occurs is adjusted by the transition Rayleigh Ra_t. This law is used in Section 3.3.

Figure 1.5 shows how the viscosity varies with temperature for several of the considered laws in the parameter ranges used in this study. The variability in viscosity introduces strong couplings between the momentum and heat equations, as well as introducing important nonlinearities into the whole problem. For the arctangent dependence of viscosity with temperature according to (1.7) or (1.8), we observe a fluid in which the viscosity changes abruptly in a temperature interval around a temperature of transition. This defines a phase change over a mushy region, which expresses the melting of minerals or other components.

The simplest stationary solution to the problem described by equations (1.1)-(1.3) with boundary conditions (1.4), is the conductive solution which satisfies $\mathbf{u}_c = 0$ and $\theta_c = -z+1$. This solution is stable only for a range of vertical temperature gradients which are represented by small enough Rayleigh numbers. Beyond the critical threshold Ra_c, a convective motion settles in and new structures are observed which may be either time-dependent or stationary. The stationary equations in the latter case, obtained by canceling the time derivatives in the system (1.1)-(1.3), are satisfied by the bifurcating solutions. As in the conductive solution the new solutions depend on the external physical parameters, and new critical thresholds exist at which they lose their stability, thereby giving rise to new bifurcated structures. Conditions exist in which time-dependent regimes are found in the neighborhood of branches which are unstable, as for instance after a Hopf bifurcation. In these cases, the time-dependent numerical simulations are performed with initial data in the unstable equilibrium solution, plus a small perturbation.

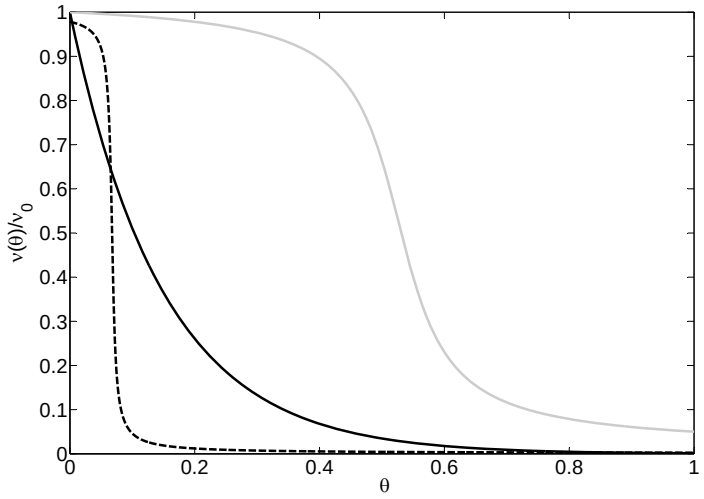

Figure 1.5. Representation of different viscosity law versus the dimensionless temperature. The solid black line corresponds to exponencial law (1.5) with $\mu = 0.0862$ and $Ra = 78$ used in Section 3.1; while the solid gray line corresponds to arctangent law (1.7) with $\mu = 0.0146$, $Ra = 1300$, $b = 10$ and $a = 0.01$ used in the Section 3.2, and the dashed line corresponds to the arctangent law (1.8) with $\mu = 0.0146$, $Ra = 148$, $\beta = 100$, $Ra_t = 10$ and $a = 0.001$.

1.4.2. Confined rotating convection (3D)

Secondly, we study centrifugal effects in a convection problem with viscosity weakly dependently on temperature at large Prandtl number. In particular we seek to gain insights into convection processes that involve aqueous mixtures of glycerine, which are chosen because of their use in many fluid mechanical settings [16], as well as in heat-transfer and chemical kinetics applications. We consider a flow in a circular cylinder of radius r_0 and depth d, rotating at a constant rate ω rad/s. The governing equations are written in the rotating frame of reference using the Boussinesq approximation, in which all fluid properties are considered constant, except for the density in the gravitational and centrifugal buoyancy terms. The governing equations are non-dimensionalized in a slightly differently way than before. We use d as the length scale, d^2/κ as the time scale, $\nu_0^2\rho_0/d^2$ as the pressure scale (where ρ_0 is now the density at temperature T_0 and ν_0 is the kinematic viscosity at temperature T_0) and ΔT as the temperature scale, respectively. They are explicitly expressed as:

$$
\begin{aligned}
&(\partial_t + \mathbf{u}\cdot\nabla)\mathbf{u} = -\nabla p + \sigma Ra T\hat{z} + 2\sigma\Omega\mathbf{u}\times\hat{z} - \frac{\sigma Fr Ra}{\Gamma}T\mathbf{r} + \sigma\nabla\cdot\left[\frac{\nu}{\nu_0}(\nabla\mathbf{u} + (\nabla\mathbf{u})^T)\right], \\
&(\partial_t + \mathbf{u}\cdot\nabla)T = \nabla^2 T, \qquad\qquad \nabla\cdot\mathbf{u} = 0.
\end{aligned} \tag{1.9}
$$

Here, T is the non-dimensional temperature with origin at T_0 ($T = (T_{\text{phys}} - T_0)/\Delta T$), $\mathbf{u}$ is the velocity field in the rotating frame, (u, v, w) are the components of $\mathbf{u}$ in cylindrical coordinates (r, θ, z), p is the kinematic pressure (including gravitational and centrifugal contributions), $\hat{z}$ the unit vector in the vertical direction z, and $\mathbf{r}$ is the radial vector in cylindrical coordinates. The top and bottom endwalls are maintained at constant temperatures $T_0 - 0.5\Delta T$ and $T_0 + 0.5\Delta T$, respectively, where T_0 is the reference temperature and ΔT is the temperature difference between the endwalls. The non-dimensional parameters are:

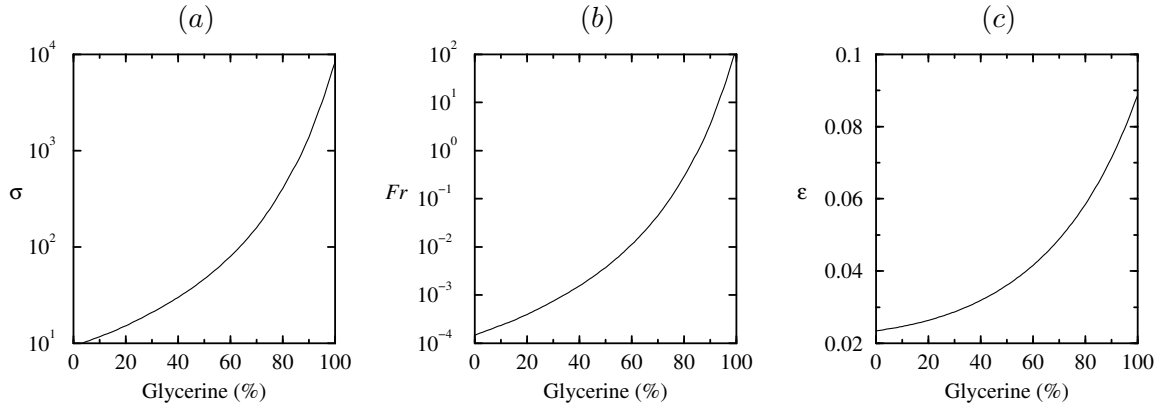

Figure 1.6. Variations of σ, Fr and ε for aqueous mixtures of glycerine at 22.4°C.

$$\begin{array}{ll} \text{Rayleigh number} & Ra = \alpha g d^3 \Delta T/\kappa\nu_0, \\ \text{Coriolis number} & \Omega = \omega d^2/\nu_0, \\ \text{Froude number} & Fr = \omega^2 r_0/g, \\ \text{Prandtl number} & \sigma = \nu_0/\kappa, \\ \text{aspect ratio} & \Gamma = r_0/d. \end{array} \tag{1.10}$$

In order to keep the Coriolis number fixed (it depends on the viscosity) whilst increasing the Prandtl number, the rotation rate of the cylinder ω must increase, and thus the Froude number Fr also increases. For large Prandtl numbers the Froude number becomes large enough to strongly influence the dynamics.

The boundary conditions for $\mathbf{u}$ and T are:

$$\begin{aligned} r = \Gamma: &\quad u = v = w = 0, \quad T = 0, \\ z = \pm 1/2: &\quad u = v = w = 0, \quad T = \mp 1/2. \end{aligned} \tag{1.11}$$

In order to gain insights into convection processes involving mixtures of glycerine, it is desirable to perform numerical simulations that involve large Pr numbers. In particular, in our simulations we use physical parameters that correspond to aqueous mixtures of glycerine with mass concentration in the range of 60–90% glycerine. In this range of concentrations *i.e.* glycerine concentration above 60%, the Froude number ($Fr = \omega^2 r_0/g$) is greater than 0.01, and the effects of this parameter, and thus centrifugal effects, are significant.

We study temperature-dependent viscosity effects by assuming that the viscosity depends linearly on temperature. Cheng [17] provides a formula that approximates the dependence of viscosity with temperature for the glycerine-water mixtures. Since in our setting the temperature range is small, we assume that the viscosity depends linearly on temperature, given by the tangent to the curve reported by [17] at the reference temperature T_0. In dimensionless form, it is given by

$$\nu(T) = \nu_0(1 - \gamma T), \tag{1.12}$$

where γ is a linear rate given by

$$\gamma = \varepsilon \Delta T, \quad \varepsilon = -\frac{\nu'_{\text{Cheng}}(T_0)}{\nu_0}. \tag{1.13}$$

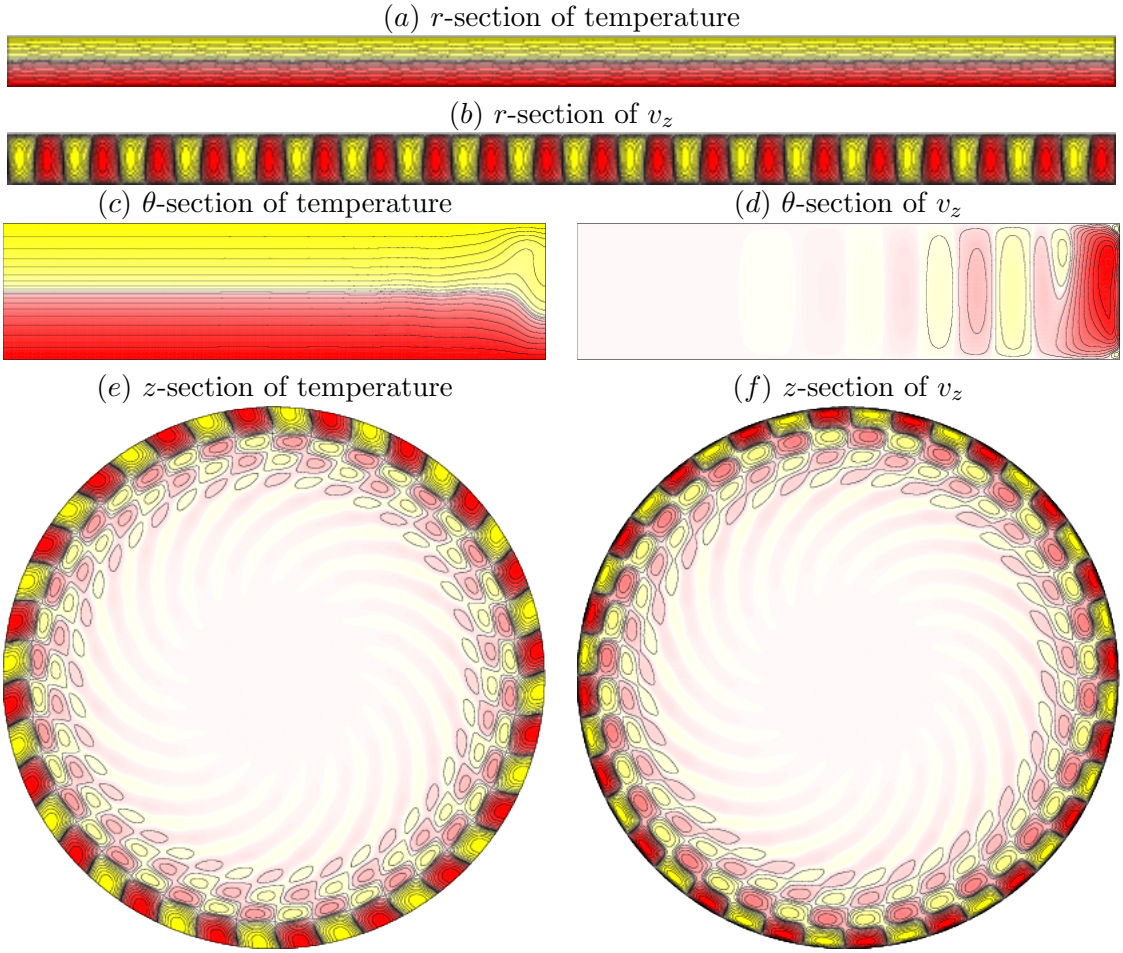

Figure 1.7. Different sections of temperature and vertical velocity for the equilibrium wall-mode state at $\Omega = 625$, $\Gamma = 4$, $\sigma = 7$, $Ra = 9 \times 10^4$ and $Fr = 0$.

Figure 1.6 shows the variations of σ, Fr and ε for aqueous mixtures of glycerine at 22.4°C. The density and dynamic viscosity of the aqueous glycerine mixtures, required to calculate σ and Fr, are obtained from [46], and ε is determined from (1.13). For the range of glycerine concentrations considered, the Prandtl number increases by about one order of magnitude, while the Froude number increases by almost two orders of magnitude.

After setting γ equal to the values that correspond to the various glycerine concentrations considered, we find that the effects of temperature-dependent viscosity are negligible , as reported in the Section 4.2.2 and computationally quite expensive to incorporate. For this reason, we keep the viscosity constant in the results reported in the main body of Section 3.4. Thus the problem

studied is the following:

$$
\begin{aligned}
&(\partial_t + \mathbf{u}\cdot\nabla)\mathbf{u} = -\nabla p + \sigma Ra T\hat{z} + 2\sigma\Omega\mathbf{u}\times\hat{z} - \frac{\sigma Fr Ra}{\Gamma}T\mathbf{r} + \sigma\nabla^2\mathbf{u},\\
&(\partial_t + \mathbf{u}\cdot\nabla)T = \nabla^2 T, \qquad\qquad \nabla\cdot\mathbf{u} = 0,
\end{aligned}
\tag{1.14}
$$

In this section, analysis of the solutions is explored solely from the perspective of their time evolution, and then the initial data is described. The wall-modes regime are pairs of hot and cold thermal plumes that ascend and descend in the cylinder sidewall boundary layer, forming an essentially one-dimensional pattern characterized by the number of hot/cold plume pairs. Thus, the initial condition is a wall-mode solution with wavenumber $m = 20$, *i.e.*, twenty pairs of hot and cold thermal plumes ascending and descending in the cylinder sidewall boundary layer. This condition is a stable solution obtained according to [93], with parameters $\Omega = 625$, $\Gamma = 4$, $\sigma = 7$, $Ra = 9 \times 10^4$ and $Fr = 0$ and mode $m = 20$. The different sections of temperature and vertical velocity for this initial data can be seen in Figure 1.7. In the present study, the aspect ratio $\Gamma = 4$ and Coriolis number $\Omega = 625$ are fixed to correspond to those in previous studies [69, 70], and we consider variations in σ, Ra and Fr. The results corresponding to this setting are presented in Section 3.4.

CHAPTER 2

Objectives

The objective of this work is to explore numerically the solutions of several convection problems in diverse contexts of interest in geophysics. We conduct the study by combining bifurcation analysis and time-evolution simulations.

The breakdown of work into specific objectives is as follows:

1. Development of spectral numerical methods to solve the time dependent regime in a convection problem with viscosity strongly dependent on temperature at infinite Prandtl number.

Prior to exploring new numerical approaches, existing numerical methods of classical convection problems are implemented, and we have verified that they can not be used to solve the time-evolution problem of our interest in which viscosity strongly depends on temperature and the Prandtl number is infinite (see Section 3.1, "*Other semi-implicit scheme*" and "*Results*").

We propose spectral numerical methods based on a primitive variable formulation which overcome the shortcomings of existing techniques and succeed in solving the time evolution problem (Section 3.1, "*Numerical schemes for time dependent solutions*").

2. Numerical analysis of the solutions of a convection problem in which the viscosity strongly depends on temperature in the presence of the O(2) symmetry.

Our purpose is to describe the variety of stationary solutions depending on the viscosity laws under consideration, thereby exploring transitions from stationary regimes towards time-dependent regimes and analyzing the impact of the symmetry on the time-dependent regimes. We arrange these goals in the following steps:

- Linear Stability Analysis: The primary instability thresholds of the conductive solution are calculated with different viscosity laws: Exponential law (Section 3.1, "*The conductive solution*"), "smooth" arctangent law (Section 3.2, "*The viscosity law* ") and "sharp" arctangent law (Section 3.3, "*Stationary solutions and their stability* ").
- Bifurcations Diagrams: Bifurcation diagrams as a function of the Rayleigh number, Ra, for different viscosity laws are obtained. (Section 3.1, "*Stationary solutions and their stability*"

for the exponential law, Section 3.2, "*Bifurcation diagrams and time-dependent solutions*" for the "smooth" arctangent law and Section 3.3, "*Results and discussion*" for the "sharp" arctangent law).

- Morphology of the plumes: The influence on the morphology of the plumes of several viscosity laws and a range of parameters is explored in Section 3.1, "*Time dependent and transitory regimes*", Section 3.2, "*Results*" and Section 3.3, "*Results and discussion*".

- Transitions to time-dependent regimes: Several time-dependent regimes are described, among which solutions that are fundamentally related to the presence of the O(2) symmetry are recognized. Of particular interest are those in which plate-like convection emerges. (Section 3.2, "*Bifurcation diagrams and time-dependent solutions*", Section 3.3, "*Results and discussion*").

3. Numerical analysis of the time evolution of a convection problem in which the viscosity weakly depends on temperature in the presence of rotation and considering centrifugal effects.

Our principal objective here is to investigate the centrifugal effects in a rotating convection problem at large Prandtl number and viscosity weakly dependent on temperature. The numerical approach solves the time-evolution with spectral second-order time-splitting method. The Coriolis force is relatively large and the onset of thermal convection is in the so-called wall modes regime (see Section 3.4, "*Results*").

We explore the impact on the solutions of the viscosity dependence on temperature and of the Prandtl number, and we find that these effects are small when compared with the centrifugal ones (Section 3.4, "*Results*" and "*Appendix A: Temperature-dependent viscosity*").

CHAPTER 3

Results

The results obtained are presented by *compendium of articles*. I have written four papers which have already been published in journals.

The first one, entitled "Spectral numerical schemes for time-dependent convection with viscosity dependent on temperature" is co-authored by my advisor A.M. Mancho and is published in *Communications in Nonlinear Science and Numerical Simulation* **19** (4) 538-553 (2014). In this article, spectral numerical methods based on a primitive variable formulation are proposed to solve the time evolution of a convection problem in a 2D domain with viscosity strongly depending on temperature at infinite Prandtl number. We examine the scope of our techniques by exploring transitions from stationary regimes towards time-dependent regimes. We also compare the output and performance of these methods with other schemes.

The second article, entitled "Bifurcations and dynamics of a convection problem with temperature dependent viscosity under the presence of the O(2) symmetry", is co-authored by A. M. Mancho and is published in *Physical Review E* **88**, 043005 (2013). In this paper, with the same setup as in the first, we study the influence on the morphology of the plumes of a particular viscosity law in a range of parameter values, and explore the impact of symmetry on the time evolution of the solutions. We report that at a large aspect ratio and high Rayleigh numbers, travelling waves, heteroclinic connections and chaotic regimes are found. These solutions are greatly influenced by the presence of the symmetry and have not previously been described in the context of temperature dependent viscosities.

The third paper, entitled "Symmetry and plate-like convection in fluids with temperature-dependent viscosity" is also co-authored by A. M. Mancho and is published in *Physics of Fluids* **26**, 016602 (2014). This article has been featured as one of the Editor's Picks at the main journal web page. This selection highlights the best articles published in the journal during the year according to the editor judgement. This paper considers the same setup as in the first two articles and addresses a viscosity dependence on temperature that models a very viscous (and thus rather rigid) lithosphere over a convecting mantle. Here we find solutions such as limit cycles that are fundamentally related to the presence of symmetry. Spontaneous plate-like behaviors that rapidly evolve towards a stagnant lid regime emerge sporadically through abrupt bursts during these cy-

cles. The plate-like evolution alternates motions towards either right or left, thereby introducing temporary asymmetries on the convecting styles.

The fourth paper is coauthored by J. M. Lopez, A.M. Mancho and F. Marques. Its title is "Confined rotating convection with large Prandtl number: Centrifugal effects on wall modes" and is published in *Physical Review E* **89**, 013019 (2014). Therein, for a thermal convection problem in a 3D rotating cylinder, and in order to investigate the centrifugal buoyancy effects, we use the physical parameters corresponding to an aqueous mixture of glycerine, with mass concentration in the range of 60-90%. Our findings are that the centrifugal buoyancy term has a significant impact on the structure and dynamics of the sidewall boundary layer as well as on the bulk convection. The effects of the Froude number cannot be ignored for rotating convection at large Prandtl numbers.

3.1. Spectral numerical schemes for time-dependent convection with viscosity dependent on temperature

Coauthors: Ana M. Mancho

Abstract: This article proposes spectral numerical methods to solve the time evolution of convection problems with viscosity strongly dependent on temperature at infinite Prandtl number. Although we verify the proposed techniques solely for viscosities that depend exponentially on temperature, the methods are extensible to other dependence laws. The setup is a 2D domain with periodic boundary conditions along the horizontal coordinate which introduces a symmetry in the problem. This is the O(2) symmetry, which is particularly well described by spectral methods and motivates the use of these methods in this context. We examine the scope of our techniques by exploring transitions from stationary regimes towards time dependent regimes. At a given aspect ratio, stable stationary solutions become unstable through a Hopf bifurcation, after which the time-dependent regime is solved by the spectral techniques proposed in this article.

Reference: [26] J. Curbelo, A. M. Mancho. Spectral numerical schemes for time-dependent convection with viscosity dependent on temperature. Communications in Nonlinear Science and Numerical Simulation, **19** (2014) 3, 538-553

Commun Nonlinear Sci Numer Simulat 19 (2014) 538–553

Contents lists available at ScienceDirect

Commun Nonlinear Sci Numer Simulat

journal homepage: www.elsevier.com/locate/cnsns

Spectral numerical schemes for time-dependent convection with viscosity dependent on temperature

J. Curbelo [a,b], A.M. Mancho [a,*]

[a] Instituto de Ciencias Matemáticas (CSIC-UAM-UCM-UC3M), Nicolás Cabrera, 13-15, Campus Cantoblanco UAM, 28049 Madrid, Spain
[b] Departamento de Matemáticas de la Universidad Autónoma de Madrid, Facultad de Ciencias, Módulo 17, 28049 Madrid, Spain

ARTICLE INFO

Article history:
Received 20 November 2012
Received in revised form 1 April 2013
Accepted 2 April 2013
Available online 17 April 2013

Keywords:
Spectral semi-implicit method
Numerical analysis
Convection with viscosity dependent on temperature
Infinite Prandtl number

ABSTRACT

This article proposes spectral numerical methods to solve the time evolution of convection problems with viscosity strongly dependent on temperature at infinite Prandtl number. Although we verify the proposed techniques solely for viscosities that depend exponentially on temperature, the methods are extensible to other dependence laws. The set-up is a 2D domain with periodic boundary conditions along the horizontal coordinate which introduces a symmetry in the problem. This is the O(2) symmetry, which is particularly well described by spectral methods and motivates the use of these methods in this context. We examine the scope of our techniques by exploring transitions from stationary regimes towards time dependent regimes. At a given aspect ratio, stable stationary solutions become unstable through a Hopf bifurcation, after which the time-dependent regime is solved by the spectral techniques proposed in this article.

1. Introduction

Thermal convection in fluids in which viscosity depends on temperature plays an important role in many geophysical and technical processes. This problem is addressed in the literature by considering diverse laws. For instance, an Arrhenius-type viscosity law is a common approach to describing upper mantle convection problems [1–4]. Other studies such as [3, 5–8] consider fluids in which viscosity depends exponentially on temperature. In [6], an exponential law is chosen to fit the experimental data for the temperature dependence of viscosity in glycerol. In [3], the exponential dependence is discussed as an approach to the Arrhenius law by means of a Taylor series around a reference temperature. This is also called the Frank–Kamenetskii approximation (see [9]). In [8], extremely large viscosity variations such as those expected in the mantle are investigated by means of an exponential law. More recently, [10,11] have considered the hyperbolic tangent or the arctangent as viscosity laws since they model a viscosity transition in a narrow temperature gap. Further studies have treated other weaker dependencies such as linear [12,13] or quadratic ones [14,15].

From the mathematical point of view it has recently been proven that convection problems in which viscosity is a function of temperature is a well posed problem [16,17] for dependences which are smooth bounded positive analytical functions, so it stands a good chance of solution on a computer using a stable algorithm. The variability in viscosity introduces strong couplings between the momentum and heat equations, as well as introducing important nonlinearities into the whole problem. On the other hand, it is of particular interest for mantle convection problems, to consider the fact that the Prandtl number, which is the quotient of viscosity and thermal diffusivity, is virtually infinite. This limit transforms the set of equations describing the time-dependent problem into a differential algebraic problem (DAE), which is very stiff.

* Corresponding author. Tel.: +34 912999762.
E-mail addresses: jezabel.curbelo@icmat.es (J. Curbelo), a.m.mancho@icmat.es (A.M. Mancho).

1007-5704/$ - see front matter © 2013 Elsevier B.V. All rights reserved.
http://dx.doi.org/10.1016/j.cnsns.2013.04.005

Spectral numerical schemes for time-dependent convection with viscosity dependent on temperature.

J. Curbelo, A.M. Mancho

Abstract

This article proposes spectral numerical methods to solve the time evolution of convection problems with viscosity strongly depending on temperature at infinite Prandtl number. Although we verify the proposed techniques just for viscosities that depend exponentially on temperature, the methods are extensible to other dependence laws. The set-up is a 2D domain with periodic boundary conditions along the horizontal coordinate. This introduces a symmetry in the problem, the O(2) symmetry, which is particularly well described by spectral methods and motivates the use of these methods in this context. We examine the scope of our techniques by exploring transitions from stationary regimes towards time dependent regimes. At a given aspect ratio stable stationary solutions become unstable through a Hopf bifurcation, after which the time-dependent regime is solved by the spectral techniques proposed in this article.

1 Introduction

Thermal convection in fluids in which viscosity depends on temperature plays an important role in many geophysical and technical processes. This problem has been addressed in the literature by considering diverse laws. For instance an Arrhenius-type viscosity law is a usual approach to describe upper mantle convection problems [1, 2, 3, 4]. Other studies such as [5, 6, 7, 3, 8] have considered fluids in which viscosity depends exponentially on temperature. In [6] an exponential law is chosen to fit the experimental data for the temperature dependence of viscosity in glycerol. In [3] it is discussed the exponential dependence as an approach to the Arrhenius law by means of a Taylor series around a reference temperature, also called the Frank-Kamenetskii approximation (see [9]). In [8] extremely large viscosity variations as those expected in the mantle are investigated by means of an exponential law. More recently [10, 11] have considered the hyperbolic tangent or the arctangent as viscosity laws for they model a viscosity transition in a narrow temperature gap. Other studies have treated other weaker dependencies such as linear [12, 13] or quadratic ones [14, 15].

From the mathematical point of view it has recently been proven that convection problems in which viscosity is a function of temperature is a well posed problem [16, 17] for dependences which are smooth bounded positive analytical functions, so it stands a good chance of solution on a computer using a stable algorithm. The variability in viscosity introduces strong couplings between the momentum and heat equations, as well as introducing important nonlinearities into the whole problem. On the other hand, it is of major interest, in particular for mantle convection problems, to consider the fact that the Prandtl number, which is the quotient of viscosity and thermal diffusivity, is virtually infinite. This limit transforms the set of equations describing the time-dependent problem into a differential algebraic problem (DAE), which is very stiff.

In this context, this article discusses the performance of several time evolution spectral schemes for convection problems in which the viscosity depends on temperature and the Prandtl number is infinite. We focus the analysis by choosing an exponential law similar to that discussed in [18]. We characterize time-dependent solutions demonstrating the efficiency of the time-dependent scheme to describe the solutions beyond the stationary regime. Our setting is a 2D domain with periodic boundary conditions along the horizontal coordinate. The equations with periodic boundary conditions are invariant under horizontal translations, thus the problem has a symmetry represented by the SO(2) group. Additionally, if the reflection symmetry exists, the full symmetry group is the O(2) group. Symmetric systems typically exhibit more complicated behavior than non-symmetric systems and there exist numerous novel dynamical phenomena whose existence is fundamentally related to the presence of symmetry, such as traveling waves or stable heteroclinic cycles [19, 20, 21]. The numerical simulation of dynamics under the presence of symmetry has been usually addressed by spectral techniques [21, 22]. In the context of convection problems with constant viscosity in cylindrical containers that posses the O(2) symmetry, the existence of heteroclinic cycles have been reported both experimentally [23] and numerically with a fully spectral approach [24]. However Assemat and co-authors [25] who have used high order finite element methods to solve a similar set-up notice the absence of the heteroclinic cycles in their simulations. Additionally they notice the influence of the computational grid on the breaking of the O(2) symmetry, by producing pinning effects on the solution. These

reasons suggest that spectral methods might be particularly suitable to deal with problems with symmetries as some solutions might be overlooked with approaches based on other spatial discretizations.

Spectral methods are not very popular in the simulation of convection problems with temperature-dependent viscosity [26], as they are reported to have limitations when handling lateral variations in viscosity. Alternatively, preferred schemes exist in which the basis functions are local; for example, finite difference, finite element and finite volume methods. For instance, the works by [27, 28] have treated this problem in a finite element discretization in primitive variables, while in [29, 30] finite differences or finite elements are used in the stream-function vorticity approach. Spectral methods have been successfully applied to model mantle convection with moderate viscosity variations in, for instance, [31, 32]. These works do not use the primitive variables formulation, and deal with the variations in viscosity by decomposing it into a mean (horizontally averaged) part and a fluctuating (laterally varying) part. Our approach addresses the variable viscosity problem by proposing a spectral approximation in primitive variables without any decomposition on the viscosity. The main novelty in this paper is the extension of the spectral methodology discussed in [18], valid only for stationary problems, for solving the time-dependent problem, and the extension of the results to describe time-dependent solutions.

As regards temporal discretization, backward differentiation formulas (BDF's) are widely used in convection problems. This is the case of the work discussed in [33], which following ideas proposed in [34] uses a fixed time step second-order-accurate which combines Adams-Bashforth and BDF schemes. A recent article by García and co-authors [35] compares the performance of several semi-implicit and implicit time integrations methods based on BDF and extrapolation formulas. The physical set-ups discussed in these papers are for convection problems with constant viscosity and finite Prandtl number. In contrast, this article focuses on convection problems with viscosity strongly dependent on temperature and infinite Prandtl number that lead to a differential algebraic problem. We will see that the semi-implicit methods discussed in [34, 33] do not work in this context. BDFs and implicit methods are known to be an appropriate choice [36, 37] for efficiently tackling very stiff problems. According to [36, 35], for the time discretization scheme we propose several high order backward differentiation formulas which are ready for an automatic stepsize adjustment. Furthermore, we solve the fully implicit problem and also propose a semi-implicit approach. The output and performance of this option are compared with those of the implicit scheme. It is found that the semi-implicit approach presents some advantages in terms of computational performance.

The article is organized as follows: In Section 2, we formulate the problem, providing a description of the physical set-up, the basic equations and the boundary conditions. Section 3 describes a spectral scheme for stationary solutions which will be useful for benchmarking the time dependent numerical schemes. First the conductive solution and its stability is determined. Other stationary solutions appear above the instability threshold, which are computed by means of a Newton-Raphson method using a collocation method. The stability of the stationary solutions is predicted by means of a linear stability analysis and is also solved with the spectral technique. Section 4 discusses several time-dependent schemes, which include implicit and semi-implicit schemes. Section 5 reports the results at a fixed aspect ratio in a range of Rayleigh numbers. Stationary and time-dependent solutions are found and different morphologies of the thermal plumes are described. Some computational advantages of some schemes versus others are discussed. Finally, Section 6 presents the conclusions.

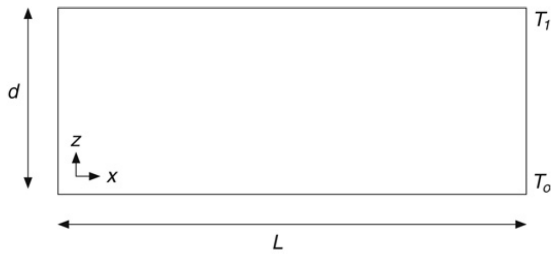

Figure 1: Problem set-up.

2 Formulation of the problem

The physical set-up, shown in Fig.1, consists of a two dimensional fluid layer of depth d (z coordinate) placed between two parallel plates of length L. The bottom plate is at temperature T_0 and the upper plate is at T_1, where $T_1 = T_0 - \Delta T$ and ΔT is the vertical temperature difference, which is positive, *i.e*, $T_1 < T_0$.

In the equations governing the system, $\mathbf{u} = (u_x, u_z)$ is the velocity field, T is the temperature, P is the pressure, x and z are the spatial coordinates and t is the time. Equations are simplified by taking into account the Boussinesq

approximation, where the density ρ is considered constant everywhere except in the external forcing term, where a dependence on temperature is assumed as follows $\rho = \rho_0(1-\alpha(T-T_1))$. Here ρ_0 is the mean density at temperature T_1 and α the thermal expansion coefficient.

We express the equations with magnitudes in dimensionless form after rescaling as follows: $(x', z') = (x, z)/d$, $t' = \kappa t/d^2$, $\mathbf{u}' = d\mathbf{u}/\kappa$, $P' = d^2P/(\rho_0\kappa\nu_0)$, $\theta' = (T - T_1)/(\Delta T)$. Here κ is the thermal diffusivity and ν_0 is the maximum viscosity of the fluid, which is the viscosity at temperature T_1. After rescaling the domain, $\Omega_1 = [0, L) \times [0, d]$ is transformed into $\Omega_2 = [0, \Gamma) \times [0, 1]$, where $\Gamma = L/d$ is the aspect ratio. The system evolves according to the momentum and the mass balance equations, as well as to the energy conservation principle. The non-dimensional equations are (after dropping the primes in the fields):

$$\nabla \cdot \mathbf{u} = 0, \tag{1}$$

$$\frac{1}{Pr}(\partial_t \mathbf{u} + \mathbf{u} \cdot \nabla \mathbf{u}) = R\theta\vec{e}_3 - \nabla P + \operatorname{div}\left(\frac{\nu(\theta)}{\nu_0}(\nabla \mathbf{u} + (\nabla \mathbf{u})^T)\right), \tag{2}$$

$$\partial_t \theta + \mathbf{u} \cdot \nabla\theta = \Delta\theta. \tag{3}$$

Here $\vec{e}_3$ represents the unitary vector in the vertical direction, $R = d^3\alpha g\Delta T/(\nu_0\kappa)$ is the Rayleigh number, g is the gravity acceleration and $Pr = \nu_0/\kappa$ is the Prandtl number. We consider that the Pr is infinite, as is the case in mantle convection problems, and thus the term on the left-hand side in (2) can be made equal to zero. This transforms the problem into a differential algebraic equation (DAE), which is very stiff.

The viscosity $\nu(\theta)$ is a smooth positive bounded function of θ. In order to test the performance of the proposed schemes $\nu(\theta)$ is chosen to be an exponential law following previous results by [18]. The dimensional form of this law is as follows:

$$\frac{\nu(T)}{\nu_0} = \exp(-\gamma(T - T_1)) \tag{4}$$

where γ is an exponential rate and ν_0 is the largest viscosity at the upper surface. The dimensionless expression is:

$$\frac{\nu(\theta)}{\nu_0} = \exp(-\mu R\theta) \tag{5}$$

where $\mu = \gamma\nu_0\kappa/(d^3\alpha g)$. The presence of the R number in the exponent of the viscosity law is uncommon among the literature that considers this viscosity dependence. However it formulates better laboratory experiments in which the increment of the R number is done by increasing the temperature at the bottom surface. This procedure ties the viscosity to change with the Rayleigh number. Dependence on Eq. (5) reduces to that of constant viscosity if $\mu = 0$, while for temperature-dependent viscosity we consider $\mu = 0.0862$. The viscosity contrast in equation (5) for Rayleigh numbers up to $R = 120$ –as employed in this article– is $3.1 \cdot 10^4$.

Additionally for benchmark purposes in section 3.1 the exponential law proposed by [5] has been considered:

$$\frac{\nu(\theta)}{\nu_0} = \exp[c(\frac{1}{2} - \theta)] \tag{6}$$

where $c = \ln(\nu_{max}/\nu_{min})$. In this law ν_0 is the viscosity involved in the definition of the dimensionless R number but it is not longer the maximum viscosity but the viscosity at $\theta = 1/2$.

For boundary conditions, we consider that the bottom plate is rigid and that the upper surface is non deformable and free slip. The dimensionless boundary conditions are expressed as,

$$\theta = 1,\ \mathbf{u} = \vec{0},\ \text{on } z = 0 \text{ and } \ \theta = \partial_z u_x = u_z = 0,\ \text{on } z = 1. \tag{7}$$

Lateral boundary conditions are periodic. Jointly with equations (1)-(3), these conditions are invariant under translations along the x-coordinate, which introduces the symmetry SO(2) into the problem. In convection problems with constant viscosity, the reflexion symmetry $x \to -x$ is also present insofar as the fields are conveniently transformed as follows $(\theta, u_x, u_z, p) \to (\theta, -u_x, u_z, p)$. In this case, the O(2) group expresses the full problem symmetry. The new terms introduced by the temperature dependent viscosity, in the current set-up Eq. (2) maintain the reflexion symmetry, and the symmetry group is O(2).

3 Numerical schemes for stationary solutions

The numerical codes proposed in this article for the time-dependent problem requiere *a priori* known solutions for benchmark. In the set-up under consideration, both stationary and time-dependent solutions exist. Some of the stationary solutions have simple analytical expressions which are known *a priori*, but there are others which

are not so simple and must be found numerically. Stationary solutions are not stable in the full parameter space, and after becoming unstable either other stationary solutions may become stable or a time-dependent regime is observed. In order to verify our methods, the self-consistency of results provided by a different kind of analysis is required. In this context, this section describes stationary solutions to the system (1)-(3) and their stability. This description, together with the fact that the problem is well-posed [17], provide a required *a priori* knowledge that will assist in the examination of the validity of different time-dependent numerical schemes.

3.1 The conductive solution

The simplest stationary solution to the problem described by equations (1)-(3) with boundary conditions (7) is the conductive solution which satisfies $\mathbf{u}_c = 0$ and $\theta_c = -z + 1$. This solution is stable only for a range of vertical temperature gradients which are represented by small enough Rayleigh numbers. Beyond the critical threshold R_c, a convective motion settles in and new structures are observed which may be either time dependent or stationary. The stationary equations in the latter case, obtained by canceling the time derivatives in the system (1)-(3), are satisfied by the bifurcating solutions. As in the conductive solution the new solutions depend on the external physical parameters, and new critical thresholds exist at which they lose their stability, thereby giving rise to new bifurcated structures.

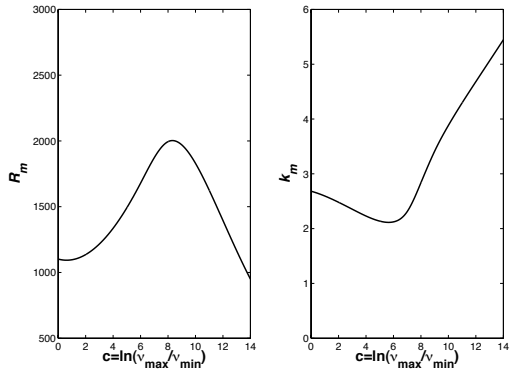

Figure 2: Critical curves according to the exponential law given in (6). a) R_m versus c; b) k_m versus c.

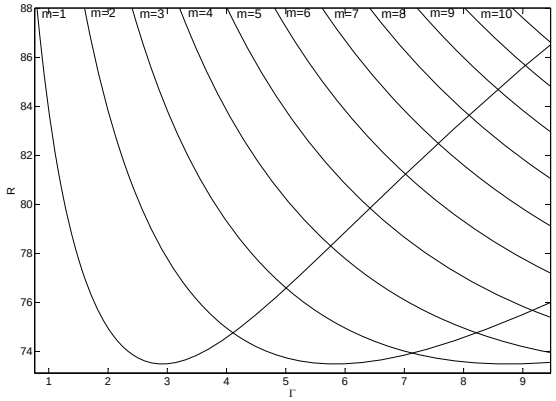

Figure 3: Critical instability curves $R(m, \Gamma)$ for a fluid layer with temperature dependent viscosity $\mu = 0.0862$ according to the exponential law given in (5).

In this section, we first describe the instability thresholds for the conductive solution. For this purpose small

perturbations are added to it:

$$\begin{aligned} \mathbf{u}(x,z,t) &= 0 + \tilde{\mathbf{u}}(z)\mathrm{e}^{\lambda t+ikx}, & (8)\\ \theta(x,z,t) &= -z+1+\tilde{\theta}(z)\mathrm{e}^{\lambda t+ikx}, & (9)\\ P(x,z,t) &= -Rz^2/2 + Rz + C + \tilde{P}(z)\mathrm{e}^{\lambda t+ikx}. & (10)\end{aligned}$$

The sign in the real part of the eigenvalue λ determines the stability of the solution: if it is negative the perturbation decays and the stationary solution is stable, while if it is positive the perturbation grows in time and the conductive solution is unstable. If these expressions are introduced into the system (1)-(3), and both the nonlinear terms in the perturbations and their tildas are dropped, the system becomes:

$$\begin{aligned} 0 &= iku_x + \partial_z u_z,\\ 0 &= ikP - \left[\frac{\partial_z\nu(\theta_c)}{\nu_0}(iku_z+\partial_z u_x) + \frac{\nu(\theta_c)}{\nu_0}(\partial^2_{zz}-k^2)u_x\right],\\ 0 &= \partial_z P - \left[2\frac{\partial_z\nu(\theta_c)}{\nu_0}\partial_z u_z + \frac{\nu(\theta_c)}{\nu_0}(\partial^2_{zz}-k^2)u_z\right] - R\theta,\\ \lambda\theta &= (\partial^2_{zz}-k^2)\theta + u_z.\end{aligned}$$

The boundary conditions for the perturbation fields are:

$$\theta = 0,\ \mathbf{u} = \vec{0},\ \text{on } z=0 \text{ and } \ \theta = \partial_z u_x = u_z = 0,\ \text{on } z=1. \tag{11}$$

Stability analysis of the conductive solution for viscosity dependent on temperature is numerically addressed in [6, 18, 38]. For the results reported in this section we follow the spectral scheme presented in [39]. Appropriate expansions in Chebyshev polynomials of the unknown fields $(\mathbf{u},\theta,P)$ along the vertical coordinate transform the eigenvalue problem into its discrete form:

$$Aw = \lambda Bw,$$

where the expansion coefficients are stored in the vector w. This generalized eigenvalue problem supplies the dispersion relation $R = R(k)$ at the bifurcation point ($\mathrm{Re}(\lambda) = 0$). $R(k)$ is an upwards concave curve that reaches a minimum at R_m, k_m. In an infinite domain. R_m and k_m are referred respectively as the critical Rayleigh number and the critical wave number because above R_m the conductive solution losses its stability and a new pattern grows with wave number k_m. For the viscosity law (6) Stengel and co-authors [6] have computed the values of R_m, k_m as a function of the viscosity contrast $c = \ln(\nu_{max}/\nu_{min})$ ranging from 0 to 14. For free slip conditions at the top and rigid conditions at the bottom, their Figure 2 shows a curve that we reproduce with our spectral scheme also in our Figure 2. The agreement among them is excellent and this provides a first benchmark for our calculations.

In finite domains the wavenumber k that appears in the dispersion relation cannot be arbitrary but must meet the periodic boundary conditions, *i. e.*:

$$k\,\Gamma = 2\pi m, \ \text{ with } \ m = 1,2,3\ldots \tag{12}$$

Here, m is the number of wavelengths of the unstable structure growing in the finite domain. Restrictions to k given by condition (12) are replaced in the dispersion relation $R = R(k)$, thereby providing a critical curve for each integer m as a function of the aspect ratio Γ, $R = R(m,\Gamma)$. Figure 3 displays critical Rayleigh numbers R_c on the vertical axis as a function of the aspect ratio Γ on the horizontal axis for the viscosity law (5), which is the one we keep in the remaining analysis. The conductive solution is stable below the critical curves, which means that in a box with a given aspect ratio, Γ, if $R < R_c$ then initial conditions near to the conductive solution evolve in time approaching it. Alternatively, if at that aspect ratio $R > R_c$, then initial conditions which are near to the conductive solution evolve in time away from it, towards a different solution. This new solution may be stationary or time-dependent. Figure 3 confirms that for increasing aspect ratios the most unstable spatial eigenfunction increases its wavenumber m.

3.2 Numerical stationary solutions

There exist stationary solutions to the system (1)-(3) that bifurcate from the conductive solution above the instability thresholds displayed in Figure 3 and may be computed numerically. They are stationary because they satisfy the stationary version of equations (1)-(3), which are obtained by canceling the partial derivatives with respect to time. These solutions may be numerically obtained by using a variant of the iterative Newton-Raphson method, similar to that in [18]. This method starts with an approximate solution at step $s = 0$, to which is added a small correction in tilda:

$$(\mathbf{u}^s + \tilde{\mathbf{u}}, \theta^s + \tilde{\theta}, P^s + \tilde{P}). \tag{13}$$

These expressions are introduced into the system (1)-(3), and after canceling the nonlinear terms in tilda, the following equations are obtained:

$$0 = \nabla \cdot \tilde{\mathbf{u}} + \nabla \cdot \mathbf{u}^s, \tag{14}$$

$$\begin{aligned} 0 = &- \partial_x \tilde{P} - \partial_x P^s + \frac{1}{\nu_0}[L_{11}(\theta^s, u_x^s, u_z^s) + L_{12}(\theta^s)\tilde{u}_x \\ &+ L_{13}(\theta^s)\tilde{u}_z + L_{14}(\theta^s, u_x^s, u_z^s)\tilde{\theta}], \end{aligned} \tag{15}$$

$$\begin{aligned} 0 = &- \partial_z \tilde{P} - \partial_z P^s + \frac{1}{\nu_0}[L_{21}(\theta^s, u_x^s, u_z^s) + L_{22}(\theta^s)\tilde{u}_x \\ &+ L_{23}(\theta^s)\tilde{u}_z + (L_{24}(\theta^s, u_x^s, u_z^s) + R)\tilde{\theta}], \end{aligned} \tag{16}$$

$$0 = \tilde{\mathbf{u}} \cdot \nabla\theta^s + \mathbf{u}^s \cdot \nabla\tilde{\theta} + \mathbf{u}^s \cdot \nabla\theta^s - \Delta\tilde{\theta} - \Delta\theta^s. \tag{17}$$

Here, L_{ij} $(i = 1, 2,\ j = 1, 2, 3, 4)$ are linear operators with non constant coefficients which are defined as follows:

$$\begin{aligned} L_{11}(\theta, u_x, u_z) = &2\partial_\theta\nu(\theta)\partial_x\theta\partial_x u_x + \nu(\theta)\Delta u_x \\ &+ \partial_\theta\nu(\theta)\partial_z\theta(\partial_x u_z + \partial_z u_x), \end{aligned} \tag{18}$$

$$L_{12}(\theta) = 2\partial_\theta\nu(\theta)\partial_x\theta\partial_x + \nu(\theta)\Delta + \partial_\theta\nu(\theta)\partial_z\theta\partial_x, \tag{19}$$

$$L_{13}(\theta) = \partial_\theta\nu(\theta)\partial_z\theta\partial_x, \tag{20}$$

$$\begin{aligned} L_{14}(\theta, u_x, u_z) = &2\partial_\theta\nu(\theta)\partial_x u_x\partial_x + 2\partial^2_{\theta\theta}\nu(\theta)\partial_x\theta\partial_x u_x + \partial_\theta\nu(\theta)\Delta u_x \\ &+ (\partial_x u_z + \partial_z u_x)(\partial_\theta\nu(\theta)\partial_z + \partial^2_{\theta\theta}\nu(\theta)\partial_z\theta), \end{aligned} \tag{21}$$

$$\begin{aligned} L_{21}(\theta, u_x, u_z) = &2\partial_\theta\nu(\theta)\partial_z\theta\partial_z u_z + \nu(\theta)\Delta u_z \\ &+ \partial_\theta\nu(\theta)\partial_x\theta(\partial_z u_x + \partial_x u_z), \end{aligned} \tag{22}$$

$$L_{22}(\theta) = \partial_\theta\nu(\theta)\partial_x\theta\partial_z, \tag{23}$$

$$L_{23}(\theta, u_x, u_z) = 2\partial_\theta\nu(\theta)\partial_z\theta\partial_z + \nu(\theta)\Delta + \partial_\theta\nu(\theta)\partial_x\theta\partial_z, \tag{24}$$

$$\begin{aligned} L_{24}(\theta, u_x, u_z) = &2\partial_\theta\nu(\theta)\partial_z u_z\partial_z + 2\partial_{\theta\theta}\nu(\theta)\partial_z\theta\partial_z u_z + \partial_\theta\nu(\theta)\Delta u_z \\ &+ (\partial_z u_x + \partial_x u_z)(\partial_\theta\nu(\theta)\partial_x + \partial_{\theta\theta}\nu(\theta)\partial_x\theta). \end{aligned} \tag{25}$$

In the above expressions spatial derivatives of the viscosity function $\nu(\theta)$ are computed through the chain rule as numerically this provides more accurate results. The unknown fields $\tilde{\mathbf{u}},\ \tilde{P},\ \tilde{\theta}$ are found by solving the linear system with the boundary conditions (11) and the new approximate solution $s + 1$ is set to

$$\mathbf{u}^{s+1} = \mathbf{u}^s + \tilde{\mathbf{u}},\ \theta^{s+1} = \theta^s + \tilde{\theta},\ P^{s+1} = P^s + \tilde{P}.$$

The whole procedure is repeated for $s + 1$ until a convergence criterion is fulfilled. In particular, we consider that the l^2 norm of the computed perturbation should be less than 10^{-9}.

At each step, the resulting linear system is solved by expanding any unknown perturbation field Y, in Chebyshev polynomials in the vertical direction and Fourier modes along the horizontal axis:

$$Y(x, z) = \sum_{l=1}^{\lceil L/2 \rceil} \sum_{m=0}^{M-1} a^Y_{lm} T_m(z) e^{i(l-1)x} + \sum_{l=\lceil L/2 \rceil+1}^{L} \sum_{m=0}^{M-1} a^Y_{lm} T_m(z) e^{i(l-1-L)x}. \tag{26}$$

In this notation, $\lceil \cdot \rceil$ represents the nearest integer towards infinity. Here L and M are the number of nodes in the horizontal and vertical directions, respectively. Chebyshev polynomials are defined in the interval $[-1, 1]$ and Fourier modes in the interval $[0, 2\pi]$. Therefore, for computational convenience, the domain $\Omega = [0, \Gamma) \times [0, 1]$ is transformed into $[0, 2\pi) \times [-1, 1]$. This change in coordinates introduces scaling factors into equations and boundary conditions which are not explicitly given here. There are $4 \times L \times M$ unknown coefficients which are determined by a collocation method in which equations (14)-(16) and boundary conditions are posed at the collocation points (x_j, z_i),

$$\text{Uniform grid:} \quad x_j = (j-1)\frac{2\pi}{L}, \qquad j = 1, \ldots, L;$$

$$\text{Gauss–Lobatto:} \quad z_i = \cos\left(\left(\frac{i-1}{M-1} - 1\right)\pi\right), \qquad i = 1, \ldots, M;$$

After replacing expression (26) in equations (14)-(16), the partial derivatives are evaluated on the basis of functions. Derivatives of the Chebyshev polynomials at the collocation points are evaluated *a priori* according to the ideas

reported in [40]. The expansion (26) is an interpolator outside the collocation points, which when restricted to these points may be rewritten as:

$$Y(x_j, z_i) = \sum_{l=1}^{L} \sum_{m=0}^{M-1} a_{lm}^{Y} T_m(z_i) e^{i(l-1)x_j}, \tag{27}$$

due to the aliasing effect of the functions $e^{i(l-1)x_j}$ and $e^{i(l-1-L)x_j}$ for $l > L/2$ at the collocation points. However, this expression is not valid for computing the spatial derivatives of the fields, for which purpose expansion (26) should be used. Although in practice Eq. (26) is correct and provides good results, we do not employ it in this work because it involves complex functions and complex unknowns a_{lm}^{Y}, eventually leading to the inversion of complex matrices which computationally are more costly than real matrices. On the other hand since the unknown functions Y are real, they admit expansions with real functions and real unknowns. In order to obtain these functions, we take into account Euler's formula $e^{ilx} = \cos(lx) + i\sin(lx)$, which is replaced in (26). We also note that the coefficients are given by conjugated pairs in such a way that, for instance, $a_{2m}^{Y} = a_{Lm}^{Y*}$. Strictly speaking, expansion (26) is a real function only if every coefficient in the first summatory for $l \geq 2$ has a conjugate pair in the second summatory. This implies that L must be an odd number; thus in what follows we restrict ourselves to odd L values. With these considerations the following equations are obtained:

$$\begin{aligned} Y(x, z) = &\sum_{l=1}^{\lceil L/2 \rceil} \sum_{m=0}^{M-1} b_{lm}^{Y} T_m(z) \cos((l-1)x) \\ &+ \sum_{l=2}^{\lceil L/2 \rceil} \sum_{m=0}^{M-1} c_{lm}^{Y} T_m(z) \sin((l-1)x). \end{aligned} \tag{28}$$

Some relations among the real and complex coefficients are: $b_{1m}^{Y} = a_{1m}^{Y}$ and $b_{lm}^{Y} = 2\Re(a_{lm}^{Y})$ and $c_{lm}^{Y} = -2\Im(a_{lm}^{Y})$, for $l = 2, \ldots, \lceil L/2 \rceil$.

The rules followed to obtain as many equations as unknowns are described next. Equations (14)–(17) are evaluated at nodes $i = 2, \ldots, M-1$, $j = 1, \ldots, L$. This provides $4 \times (M-2) \times L$ equations; the boundary conditions (7) are evaluated at $i = 1, M$, $j = 1, \ldots, L$. This supplies additional $4 \times L \times M - 2L$ equations. In order to obtain the remaining $2L$ equations, we complete the system with extra boundary conditions which eliminate spurious modes for pressure [39, 41] projecting the equation of motion in the upper and lower plate of the domain *i.e.* the equation (16) is evaluated at nodes $i = 1, M$, $j = 1, \ldots, L$. This choice has been reported to be successful for many convection problems [39, 42, 43]. However, in the present set-up, results are improved if, for the equation (16) imposed at the upper boundary, the continuity equation is assumed and $\partial_{zz}^2 u_z$ is replaced with $-\partial_{xz} u_x$. With these rules we obtain a linear system of the form $AX = b$ in which X contains the unknowns. However, the matrix A is singular due to the fact that pressure with the imposed conditions is defined up to an additive constant. According to[39, 42, 43], we fix the constant by removing equation (16) at node $j = 1$, $i = 2$ and adding at this point the equation $b_{10}^{P} = 0$. This is computationally cheaper than the pseudo-inverse method. However, in the problem under study, dropping the equation (16) at one point introduces weakly oscillating structures on this side of the pressure field. To overcome this drawback, in the final step of the iterative procedure, once the tolerance is attained, we proceed alternatively by computing a pseudoinverse of the matrix A by using the singular value decomposition (SVD). Let $A = U\Sigma V^*$ be the singular value decomposition of A; $V\Sigma^+ U^*$ is the pseudoinverse of A, where Σ^+ is the pseudoinverse of a diagonal matrix, i.e. it takes the reciprocal of each non-zero element on the diagonal, and transposes the resulting matrix.

The study of the stability of the numerical stationary solutions under consideration is addressed by means of a linear stability analysis. Now perturbations are added to a general stationary solution, labeled with superindex b:

$$\mathbf{u}(x, z, t) = \mathbf{u}^b(x, z) + \tilde{\mathbf{u}}(x, z)\mathrm{e}^{\lambda t}, \tag{29}$$

$$\theta(x, z, t) = \theta^b(x, z) + \tilde{\theta}(x, z)\mathrm{e}^{\lambda t}, \tag{30}$$

$$P(x, z, t) = P^b(x, z) + \tilde{P}(x, z)\mathrm{e}^{\lambda t}. \tag{31}$$

The linearized equations are:

$$0 = \nabla \cdot \tilde{\mathbf{u}} \tag{32}$$

$$0 = -\partial_x \tilde{P} + \frac{1}{\nu_0}[L_{12}(\theta^b)\tilde{u}_x + L_{13}(\theta^b)\tilde{u}_z + L_{14}(\theta^b, u_x^b, u_z^b)\tilde{\theta}] \tag{33}$$

$$0 = -\partial_z \tilde{P} + \frac{1}{\nu_0}[L_{22}(\theta^b)\tilde{u}_x + L_{23}(\theta^b)\tilde{u}_z + (L_{24}(\theta^b, u_x^b, u_z^b) + R)\tilde{\theta}] \tag{34}$$

$$0 = \tilde{\mathbf{u}} \cdot \nabla\theta^b + \mathbf{u}^b \cdot \nabla\tilde{\theta} + \mathbf{u}^b \cdot \nabla\theta^b - \Delta\tilde{\theta} + \lambda\tilde{\theta}, \tag{35}$$

where the operators L_{ij} are the same as those defined in Eqs. (18)-(25). The stability of the stationary solutions is approached with the collocation method used for the Newton-Raphson iterative method. Expansions of the fields (28) are replaced in equations (32)-(35), and they and the boundary conditions (11) are evaluated at the collocation nodes following the same rules as before. As a result, the discrete form of the generalized eigenvalue problem is obtained:

$$Aw = \lambda Bw, \tag{36}$$

where w is a vector containing unknowns.

In order to solve the generalized eigenvalue problem, we use a generalized Arnoldi method, which is described in [44]. The numerical approach uses the idea of preconditioning the eigenvalue problem with a modified Caley transformation, which transforms the problem (36) and which admits infinite eigenvalues into another one with all its eigenvalues finite. Afterwards, the Arnoldi method is applied.

4 Numerical schemes for time dependent solutions

The governing equations (1)–(3), together with boundary conditions (7), define a time-dependent problem for which we discuss temporal schemes based on a primitive variables formulation. The spatial discretization is analogous to that proposed in the previous section, thus the focus in this section is to discuss the time discretization of the problem.

To integrate in time, we use a third order multistep scheme. In particular, we use a backward differentiation formula (BDF), since as discussed in [36, 37] these are highly appropriate for very stiff problems such as ours. The BDF evaluates the time derivative in Eq. (3) by differentiating the formula that extrapolates the field θ^{n+1} with a third order Lagrange polynomial that uses fields at times $\theta^n, \theta^{n-1}, \theta^{n-2}$, *i.e.*:

$$\theta(t) := \ell_{n+1}(t)\theta^{n+1} + \ell_n(t)\theta^n + \ell_{n-1}(t)\theta^{n-1} + \ell_{n-2}(t)\theta^{n-2}$$

ℓ_k being a Lagrange polinomial of order 3:

$$\ell_k(t) = \prod_{\substack{n-2 \le m \le n+1 \\ m \neq k}} \frac{t - t_m}{t_k - t_m}, \quad n-2 \le k \le n+1$$

Then,

$$\partial_t \theta^{n+1} = \ell'_{n+1}(t_{n+1})\theta^{n+1} + \ell'_n(t_{n+1})\theta^n + \ell'_{n-1}(t_{n+1})\theta^{n-1} + \ell'_{n-2}(t_{n+1})\theta^{n-2} \tag{37}$$

For the fixed time step case, the time differentiation simplifies to the equation:

$$\partial_t \theta^{n+1} = \frac{11\theta^{n+1} - 18\theta^n + 9\theta^{n-1} - 2\theta^{n-2}}{6\Delta t} \tag{38}$$

In stiff problems, a variable time step scheme with an adaptative step control that adjusts itself conveniently to the different regimes is advisable. The expressions for the time derivative (37) for the variable time step case are:

$$\begin{aligned}
\ell'_{n+1}(t_{n+1}) =& \frac{\Delta t_n^2 + 4\Delta t_{n+1}\Delta t_n + \Delta t_n \Delta t_{n-1} + 3\Delta t_{n+1}^2 + 2\Delta t_{n-1}\Delta t_{n+1}}{(\Delta t_n + \Delta t_{n+1} + \Delta t_{n-1})(\Delta t_n + \Delta t_{n+1})\Delta t_{n+1}} \\
\ell'_n(t_{n+1}) =& \frac{\Delta t_n^2 + \Delta t_n \Delta t_{n-1} + \Delta t_{n-1}\Delta t_{n+1} + \Delta t_{n+1}^2 + 2\Delta t_n \Delta t_{n+1}}{(\Delta t_n + \Delta t_{n-1})\Delta t_n \Delta t_{n+1}} \\
\ell'_{n-1}(t_{n+1}) =& \frac{\Delta t_{n+1}(\Delta t_n + \Delta t_{n+1} + \Delta t_{n-1})}{(\Delta t_n + \Delta t_{n+1})\Delta t_n \Delta t_{n-1}} \\
\ell'_{n-2}(t_{n+1}) =& \frac{\Delta t_{n+1}(\Delta t_n + \Delta t_{n+1})}{((\Delta t_n + \Delta t_{n-1})^2 + \Delta t_n \Delta t_{n+1} + \Delta t_{n-1}\Delta t_{n+1})\Delta t_{n-1}},
\end{aligned}$$

where $\Delta t_n = t_n - t_{n-1}$.

The variable time step scheme controls the step size according to the general ideas proposed by [45, 36], and adapted to our particular case with parameters taken from [46]. The result of an integration at time $n+1$ is accepted, depending on the estimated error E for the fields. The error estimation E is based on the difference between the solution obtained with a third and a second order scheme. Then essentially the new time step is evaluated as follows:

$$h_{new} = s \left(\frac{E}{\text{tolerance}} \right)^{-1/(q+1)} h_{old}.$$

In practice, this expression is tuned and a maximum increase of the step size is allowed. Here s is a safety factor, and q is the order of the numerical scheme. Acceptance of the result of an integration means that E is below a certain tolerance, which is explained in the subsection 4.2. If the result is accepted, a new time step is proposed according to the law:

$$h_{new} = \begin{cases} sh_{old}\left(\frac{E}{\text{tolerance}}\right)^p, & E > \text{tolerance} \cdot \left(\frac{5}{s}\right)^{1/p} \\ 5h_{old}, & E \leq \text{tolerance} \cdot \left(\frac{5}{s}\right)^{1/p}, \end{cases}$$

where h is the size of the time step and $s = 0.9$, $p = -0.33$ ($q = 2$). In case of rejection, the step is decreased as follows:

$$h_{new} = s\left(\frac{E}{\text{tolerance}}\right)^{-1/(q+1)} h_{old},$$

with $q = 3$.

4.1 The fully implicit method

BDFs are a particular case of multistep formulas which are *implicit*, thus the BDF scheme implies solving at each time step the problem (see [36]):

$$\partial_t \mathbf{y}^{n+1} = \mathbf{f}(\mathbf{y}^{n+1}),$$

which in the particular problem under consideration becomes:

$$0 = \nabla \cdot \mathbf{u}^{n+1} \tag{39}$$

$$0 = R\theta^{n+1}\vec{e_3} - \nabla P^{n+1} + \text{div}\left(\frac{\nu(\theta^{n+1})}{\nu_0}(\nabla \mathbf{u}^{n+1} + (\nabla \mathbf{u}^{n+1})^T)\right) \tag{40}$$

$$\partial_t \theta^{n+1} = -\mathbf{u}^{n+1} \cdot \nabla \theta^{n+1} + \Delta \theta^{n+1}, \tag{41}$$

where $\partial_t \theta^{n+1}$ is replaced by the expression (37). The solution to the system (39)-(41) is our benchmark for transitory and time-dependent regimes.

The nonlinear terms on the right-hand side of these equations are approached at each time step, $n+1$, by a Newton-Raphson method similar to the one described before to find numerical stationary solutions. We assume that the solution at time $n+1$ is a small perturbation $\tilde{Y}$ of an approximate solution. Linear equations for $\tilde{Y}$ are derived by introducing the analogue of expression (13) into the nonlinear terms of equations (39)-(41) and cancelling all the nonlinear terms in tilda. The resulting linearized terms are the same as those appearing in Eqs. (14)-(17). For the first step $s = 0$, we take as an approximate solution the solution at time n. The unknown perturbation fields $\tilde{Y}$ are expanded by Eq. (28), which is replaced in the equations and boundary conditions at the collocation points according to the rules described in the previous section. In particular, the improved boundary conditions for pressure, previously described, are used. A linear system is obtained:

$$Ay = b \tag{42}$$

which is iteratively solved at each time step $n+1$ until the perturbation $\tilde{Y}$ is below a tolerance. Here, A is a matrix of order $4 \times L \times M$ and y is the vector containing the unknown coefficients of the fields $\tilde{Y}$. As previously performed the matrix A is converted into a full rank matrix by removing the projection of equation (40) at node $j = 1$, $i = 2$, and fixing the pressure by adding at this point the equation $b_{10}^P = 0$. This provides accurate results and is computationally cheaper than the pseudoinverse method.

4.2 The semi-implicit method

Implicit methods are a robust and numerically stable choice for stiff problems. However, they may be rather demanding computationally, since at each time step they require several matrix inversions to solve the system (42) at successive iterations. This subsection proposes an alternative semi-implicit scheme that is computationally less demanding than the fully implicit scheme.

Similarly to the fully implicit method, the semi-implicit scheme approaches the nonlinear terms in Eqs. (39)-(41) by assuming that the solution at time $n+1$ is a small perturbation $\tilde{Z}$ of the solution at time n; thus, $\mathbf{z}^{n+1} = \mathbf{z}^n + \tilde{Z}$. Once linear equations for $\tilde{Z}$ are derived, the equations are rewritten by replacing $\tilde{Z} = \mathbf{z}^{n+1} - \mathbf{z}^n$. Additionally, the linear system is completed by using expression (37) for the time derivative of the temperature. The solution is obtained at each step by solving the resulting linear equation for variables in time $n+1$. As before, the unknown fields are expanded by Eq. (28), which is replaced in the equations and boundary conditions at the collocation points according to the rules described in the previous section. At each time step the linear system:

$$Ay = b \tag{43}$$

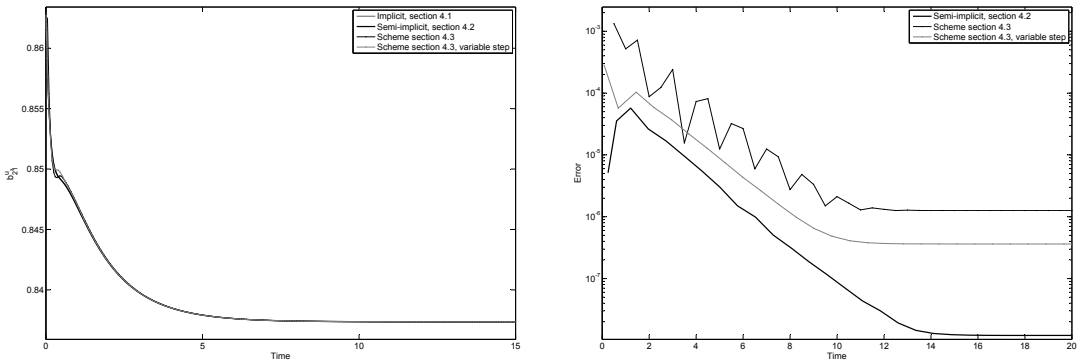

(a) Time evolution of a transitory regime

(b) Evolutions of the error versus time

Figure 4: Transition of an initial data to a stationary solution with $\Gamma = 3.4$, $R = 75$ for the exponential viscosity law (5).

	M=36	M=38	M=40	M=42
L=29	0.0030 - 0.0002i	0.0046	0.0046	0.0047
	-8.2205	-8.4419	-8.4419	-8.4419
L=31	0.0017	-0.0019	0.0017	0.0017
	-8.4418	-8.4417	-8.4418	-8.4418
L=33	0.0011	0.0011	-5.79e-4 -1.11e-4i	7.95e-4 + 6.30e-5i
	-8.4418	-8.4418	-8.4417	-8.4418

Table 1: Computation of the two eigenvalues with largest real part for the stationary solution obtained at $\Gamma = 3.4$, $R = 78$ at different expansions $L \times M$.

is solved, where A is a matrix of order $4 \times L \times M$ and y is the vector containing the unknown coefficients of the expansions of the $\mathbf{z}^{n+1}$ fields. The matrix is transformed into a full rank matrix with the same procedure used for the fully implicit case.

The fully implicit and the semi-implicit methods are implemented with a variable time step scheme that requires an error estimation based on the difference between the solution obtained with a third and a second order scheme. The second order scheme approaches the time derivative of the temperature as follows:

$$\partial_t \theta^{n+1} = \frac{(\Delta t_n^2 + 2\Delta t_n \Delta t_{n+1})\theta^{n+1} - (\Delta t_n + \Delta t_{n+1})^2 \theta^n + \Delta t_{n+1}^2 \theta^{n-1}}{\Delta t_n \Delta t_{n+1}(\Delta t_{n+1} + \Delta t_n)}, \tag{44}$$

where $\Delta t_n = t_n - t_{n-1}$. In practice, this changes the linear system to be solved at each step, as follows:

$$\widetilde{A}\widetilde{y} = \widetilde{b}$$

The computation of the second order solution thus leads to an additional matrix inversion at each time step, and as a consequence the full calculation is slowed down considerably. To avoid this additional inversion, we estimate the error by measuring instead how well the third order solution y satisfies the second order system, i.e.:

$$E = \frac{\|\widetilde{b} - \widetilde{A}y\|}{\|b\|} \tag{45}$$

where $\|\cdot\|$ represents the l^2 norm. Acceptance of the result of an integration means that E is below a tolerance that we fix at $5 \cdot 10^{-6}$. Once the error is estimated, the step size is determined as explained at the beginning of Section 4.

4.3 Other semi-implicit schemes

For completeness, we describe here alternative semi-implicit schemes that have been successfully used in fluid mechanics and convection problems with constant viscosity and finite Prandtl number. Despite its success in many fluid mechanics set-ups, this scheme is insufficient for our problem.

	M=30	M=40	M=50	M=60	M=70	M=80
L=31	0.9433 + 0.7023i 0.9433 - 0.7023i	0.2227 -2.9525	0.5829 + 0.4345i 0.5829 - 0.4345i	0.3926 -2.3225 + 0.7449i	0.4217 -2.1744 + 0.7450i	0.2265 -2.6555 + 0.7536i
L=37	0.3564 -2.1572 + 0.0829i	0.1837 -2.1273 + 0.0843i	0.1369 -2.6814	0.1318 -2.0368 + 0.0843i	0.1834 -2.1427 + 0.0841i	0.0946 -2.1495+ 0.0964i
L=43	-0.2039 + 0.0913i -0.2039 - 0.0913i	0.1767 -2.7849 + 0.0546i	0.0773 +0.0371i 0.0773 -0.0371i	-0.0289 + 0.0886i -0.0289 - 0.0886i	0.0585 -2.1576+9.7059e-3i	0.0464 -2.1308
L=49	-0.1436 -2.4633 +0.8885i	0.0836 -2.8147 + 0.0127i	0.0705 -2.3698	0.0379 -2.3625	9.7501e-3 -2.1391+ 6.3240e-4i	4.7754e-3 -2.1482
L=55	-0.1382 -2.5619 + 0.8760i	0.0571 -2.1569	0.0315 -2.1893 + 1.0669e-3i	5.8407e-3 -2.1618 + 6.7549e-4i	3.7262e-3 -2.1597	7.8574e-4 -2.1598
L=61	0.0913 -2.6323 + 0.1950i	0.0261 -2.1623	4.5781e-3 -2.1606	1.5021e-3 -2.1603	6.4589e-4 -2.1599	9.8951e-5 -2.1599

Table 2: Computation of the two eigenvalues with largest real part for the stationary solution obtained at $\Gamma = 3.4$, $R = 110$ at different expansions $L \times M$.

The adaptation of the numerical scheme described in [34, 33] to the problem under study is as follows; the semi-implicit scheme at each time step decouples the heat (3) and the momentum equations (2). The time discretization of the heat equation is as follows:

$$\frac{3\theta^{n+1} - 4\theta^n + \theta^{n-1}}{2\Delta t} + 2\mathbf{u}^n \cdot \nabla\theta^n - \mathbf{u}^{n-1} \cdot \nabla\theta^{n-1} = \Delta\theta^{n+1}, \tag{46}$$

where the time derivative of the temperature field has been evaluated with a second order fixed step BDF formula. Once θ^{n+1}, is known the velocity and pressure at time t_{n+1}, are obtained by solving the following linear system in the unknown fields:

$$\begin{aligned} &\nabla \cdot \mathbf{u}^{n+1} = 0, \\ &\nabla P^{n+1} = R\theta^{n+1}\vec{e_3} + \operatorname{div}\left(\frac{\nu(\theta^{n+1})}{\nu_0}\left(\nabla\mathbf{u}^{n+1} + (\nabla\mathbf{u}^{n+1})^T\right)\right). \end{aligned} \tag{47}$$

We implement this scheme by expanding the unknown fields in the equations (46) and (47) with Eq. (28). They are solved at successive times t_n. The discrete version of (46) is a linear system with $L \times M$ unknowns, while the discrete version of (47) has $3 \times L \times M$ unknowns. The decoupled nature of the procedure gives a certain speed advantage to this method as compared with the previous one. However, the results presented in the next section confirm that this method is not robust when applied to the differential algebraic equations under study. Increasing the order of the method or using a variable step technique does not improve the output provided by this approach.

5 Results

This section completes the description provided in [18] on the solutions of the convection problem in which the viscosity depends exponentially on temperature. By describing stationary, transitory and time dependent regimes for the problem under study, the consistency between the reported numerical procedures is confirmed.

5.1 Stationary solutions and their stability

Figure 5 displays the bifurcation diagram obtained from the analysis of a fluid layer in a finite domain with aspect ratio $\Gamma = 3.4$. Viscosity depends on the temperature according to the exponential law (5), with $\mu = 0.0862$. The viscosity contrast across the fluid layer depends on R in such a way that at the instability threshold this contrast is around $6 \cdot 10^2$, while at the maximum Rayleigh numbers displayed in Figure 5 it is of the order of $3.1 \cdot 10^4$. Stable branches are displayed as solid lines, while unstable branches are dashed.

The diagram displayed in Fig. 5 is obtained by branch continuation techniques, as explained in [18]. The solutions are obtained with the procedure described in Section 3.2. The vertical axis represents the sum $|b^\theta_{11}|+|b^\theta_{12}|$. These are coefficients obtained from the expansion of the temperature field:

$$\begin{aligned} \theta(x,z,t) = &\sum_{l=1}^{\lceil L/2 \rceil}\sum_{m=0}^{M-1} b^\theta_{lm}(t)T_m(z)\cos((l-1)x) \\ &+ \sum_{l=2}^{\lceil L/2 \rceil}\sum_{m=0}^{M-1} c^\theta_{lm}(t)T_m(z)\sin((l-1)x). \end{aligned}$$

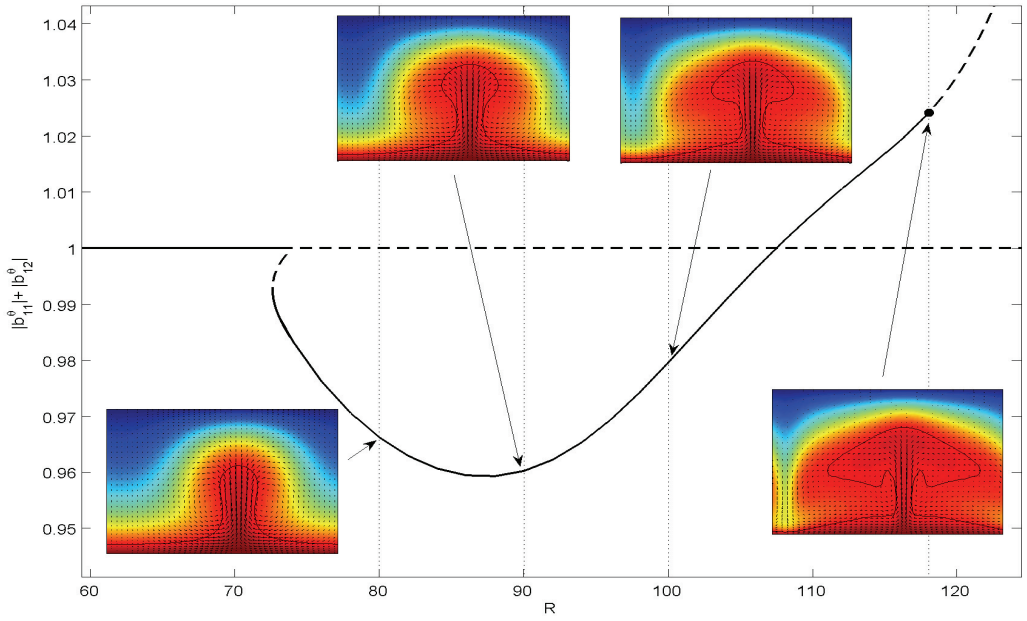

Figure 5: Bifurcation diagram for a fluid with viscosity dependent exponentially on temperature ($\mu = 0.0862$ in law (5)) at $\Gamma = 3.4$. Stable branches are solid while unstable branches are dashed. Solutions are displayed at the R numbers highlighted with vertical dashed lines.

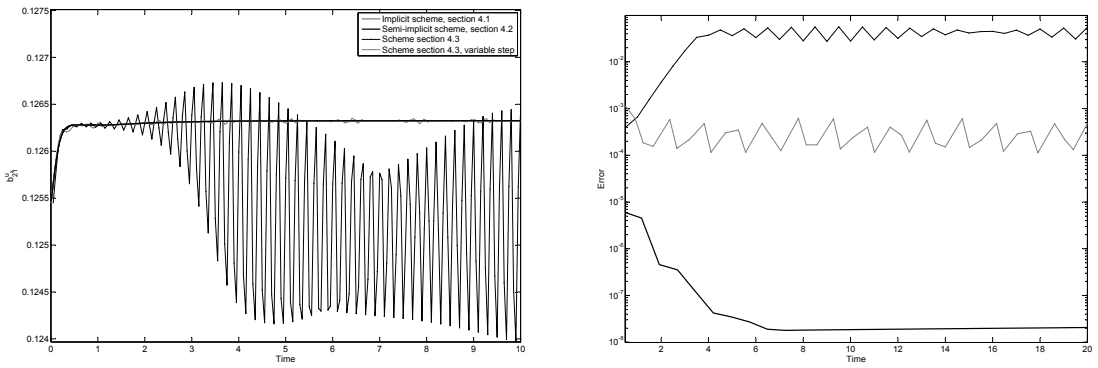

(a) Time evolution of a transitory regime

(b) Evolutions of the error versus time

Figure 6: Transition of an initial data to a stationary solution with $\Gamma = 3.4$, $R = 78$ for the exponential viscosity law (5).

Most of the coefficients $b^\theta_{lm}(t), c^\theta_{lm}(t)$ in this expansion are approximately zero, but others are not. As a representation of the whole spatial function, we select the sum of the significant coefficients $|b^\theta_{11}|$ and $|b^\theta_{12}|$.

Table 1 confirms the convergence of the eigenvalues for a stationary solution obtained at $\Gamma = 3.4$, $R = 78$. At this low R number, results have two significant decimal digits for expansions $L = 29 \times M = 38$ onwards. The results confirm that this is a stable solution. The presence of a zero eigenvalue is expected due to the symmetry SO(2) derived from the periodic boundary conditions. Periodic boundary conditions imply that arbitrary translations of the solutions along the x-coordinate must also be solutions to the system. Thus, instead of an isolated fixed point at the bifurcation threshold a circle of fixed points emerges[47]. The neutral direction is the direction connecting fixed points on this circle. Table 2 shows the convergence results obtained for $R = 110$. At this larger R number higher expansions are required; this is also expected because at large R numbers the viscosity contrast across the

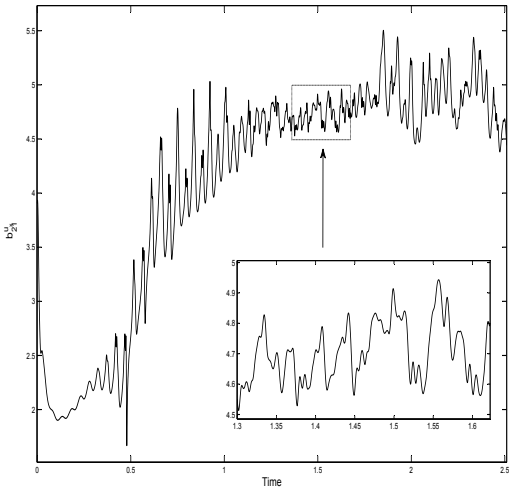

(a) Time evolution

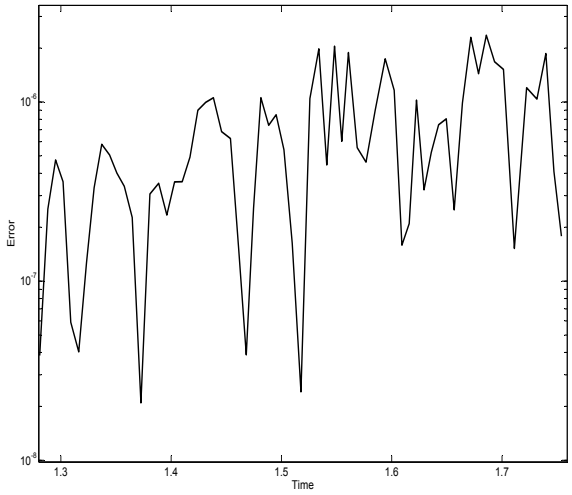

(b) Evolution of the error versus time

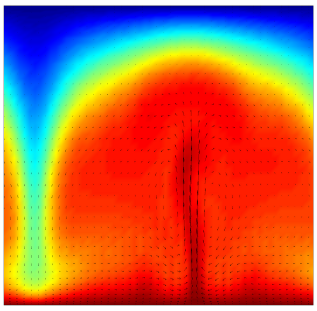

(c) Time $t = 1$

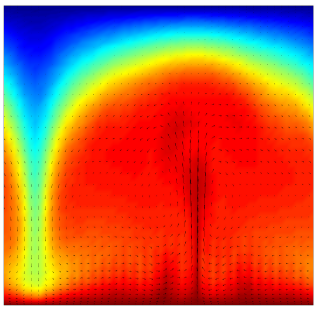

(d) Time $t = 1.1$

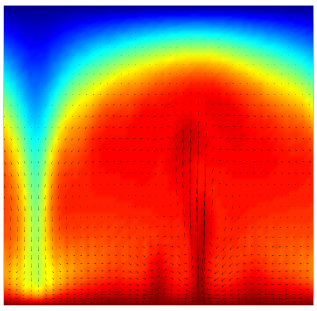

(e) Time $t = 1.2$

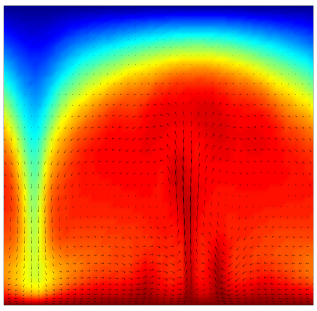

(f) Time $t = 1.3$

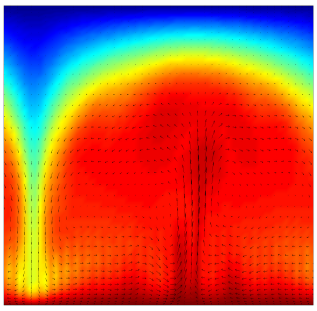

(g) Time $t = 1.4$

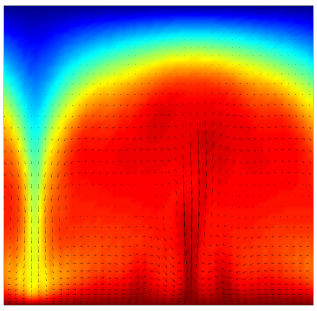

(h) Time $t = 1.5$

Figure 7: Temporal evolution of time dependent solution at $\Gamma = 3.4$ and $R = 120$ for the exponential viscosity law (5).

fluid layer increases. For expansions $L = 55 \times M = 60$ onwards, a significant number of decimal digits is obtained.

Results displayed in Figure 5 are interpreted as follows: at the bifurcation threshold the fluid undergoes a subcritical bifurcation, as reported in [48, 6, 18, 49]. The instability threshold of the unstable branch from the conductive solution occurs at $R = 73.7544$ which coincides with the prediction of the linear theory $R = 73.7501$ within a 0.006%. These results confirm the high accuracy of spectral methods which is above for instance the outcome reported in [3] where using finite volume methods obtain on similar thresholds an accuracy of 0.4%. The

unstable branch bifurcates at $R \sim 74$, below the critical threshold for the conductive solution, in a saddle-node bifurcation at which a stable stationary branch emerges. The pattern of the plume at this aspect ratio, consistent with diagram 3 has wave number $m = 1$. The stable branch becomes unstable at $R \sim 118$ through a Hopf bifurcation. Stationary solutions are displayed at the different R numbers highlighted with vertical dashed lines. These results extend those reported in [18], where the morphology of the plume has not been discussed. Images in Fig. 5 show the evolution of the plume with the Rayleigh number. As reported in [1], three idealized shapes for plumes are typically found: spout-shaped, where the tail of the plume is nearly as large as the head; mushroom-shaped; and balloon-shaped. Figure 5 confirms that at low R numbers ($R = 80$) the plume is spout-shaped. At higher $R = 90, 100$ the plume is more rounded at the top and becomes closer to a balloon-shaped plume while at $R = 118$ the plume becomes closer to a mushroom-shaped one. Regarding the velocity field, Moresi and Solomatov report in [8] that from $10^4 - 10^5$ viscosity contrasts a stagnant lid develops, and the upper part of the fluid, where the viscosity is much larger, does not move. The velocity fields overlapping the temperature patterns in Figure 5 confirm that at the larger viscosity contrasts obtained at $R = 118$, the velocity in the upper part of the fluid is almost null.

The set of stationary solutions obtained with the techniques reported in Section 3, as already noted by Plá et al. in [18] is more comprehensive than what one would expect from mere direct time evolution simulations, because the latter do not prove anything about the asymptotic regime. However, as also noted by these authors, simulations of the evolution in time are also necessary to describe time-dependent regimes which are present at high R numbers. From the computational point of view, the Newton-Raphson method is more advantageous than the time evolution schemes, as it finds a stationary solution in less than 50 iterations, while the semi-implicit scheme needs around 200 iterations (matrix inversions) to find the same solution beginning from the same initial data.

5.2 Time dependent and transitory regimes

Figure 4(a) represents the time evolution of the coefficient $b_{21}^{u_x}$ in a transitory regime towards a fixed point. A rescaled Time$= 10t$ is represented on the horizontal axis, where t is the dimensionless time. The simulation is produced at $R = 75$, which is above the instability threshold of the conductive solution, as confirmed in Figures 3 and 5. The results displayed in Figure 4(a) are obtained with all the numerical schemes described in Section 4. Figure 4(b) represents the evolution of the error versus time for the different schemes. The error is defined with respect to the benchmark solution obtained with the fully implicit approach.

Despite the good performance of all schemes at low R number, at higher R numbers the semi-implicit scheme reported in Section 4.3 breaks. Fig 6(a) confirms this point by depicting at $R = 78$ the time evolution of the coefficient $b_{21}^{u_x}$ in a transitory regime towards a fixed point. The schemes in Section 4.3 fail to solve the transition with fixed and variable time steps, which is nevertheless well determined with the implicit and semi-implicit scheme in Section 4.2. Fig 6(b) reports the evolution of the error with respect the benchmark solution for the different schemes.

Figure 7 confirms the existence of time-dependent convection after the Hopf bifurcation occurred at $R = 118$. Fig 7(a) displays the time evolution of the coefficient $b_{2m}^{u_x}$ versus time. The dynamics is rather chaotic as is foreseen for high Rayleigh numbers. This is truly the case as in our study as the viscosity ν_0 used to define R is the maximum viscosity in the fluid layer. A redefined R number from the smallest viscosity, as used other studies, would be four order of magnitudes bigger than this one. Snapshots of the plume in the time-dependent regime are shown in Figures 7(c)–7(h). In this time series, hot blobs ascend in the central part of the plume and these are released in the upper part of the fluid. Fig 7(b) shows the evolution of the error for the semi-implicit scheme.

The time dependent solutions displayed in Figure 7 although confirms the validity of the method do not particularly exhibit the influence of the symmetry, and thus the proposed spectral scheme does not show its power on this respect for the chosen test problem. However for other viscosity dependencies as the ones reported in [11] the current spectral method has successfully described solutions whose existence is related to the presence of the symmetry.

As regards computational performance, the semi-implicit scheme requires higher expansions than the fully implicit scheme in order to achieve stability, but as it eventually requires fewer matrix inversions –both because it requires only one inversion at each time step and because larger step sizes are allowed– it is slightly faster than the fully implicit scheme. On average, for the simulations reported in this article the semi-implicit scheme requires 80 time units of time for doing what the fully implicit scheme takes 100 time units. Thus regarding CPU time the semi-implict method is more advantageous.

6 Conclusions

This paper addresses the numerical simulation of time-dependent solutions of a convection problem with viscosity strongly dependent on temperature at infinite Prandtl number. We propose a spectral method which deals with

the primitive variables formulation. Time derivatives are evaluated by backwards differentiation formulas (BDFs), which are adapted to perform with variable time step. BDFs are a particular case of multistep formulas which are implicit. We solve the fully implicit problem and compare it with a semi-implicit method. For the problem under study, the proposed semi-implicit method is shown to be accurate and to have a slightly faster performance than the fully implicit scheme. We further show that other semi-implicit schemes, which provide a good performance in classical convection problems with constant viscosity and finite Pr number, do not succeed in this set-up.

The time-dependent scheme succeeds in completing the results reported for this problem by [18]. Assisted by bifurcation techniques, we have gained insight into the possible stationary solutions satisfied by the basic equations. The morphology of the plume is described and compared with others obtained in the literature. Stable stationary solutions become unstable through a Hopf bifurcation, after which the time-dependent regime is solved by the spectral techniques proposed in this article.

The time dependent solutions found for the exponential viscosity law do not evidence the influence of the symmetry. However in [11] for different viscosity dependences, at high-moderate viscosity contrasts, it is reported that the proposed scheme is successful to this end. Finite element methods and finite volume methods have proven to be successful to reach extremely large viscosity contrasts up to 10^{10}-10^{20} and we have not improved these limits with spectral methods. However at moderate viscosity contrasts the purpose of later techniques seems to be justified by novel dynamical evolutions derived from the presence of symmetries where they can play a better role than other discretizations and become the standard method as has been the case in classical convection problems with constant viscosity [50, 33, 35, 51].

Acknowledgements

We thank A. Rucklidge and J. Palmer for useful comments and suggestions. We are grateful to CESGA and to CCC of Universidad Autónoma de Madrid for computing facilities. This research is supported by the Spanish Ministry of Science under grants MTM2008-03754, MTM2011-26696 and MINECO: ICMAT Severo Ochoa project SEV-2011-0087.

References

[1] L. H. Kellogg and S. D. King. The effect of temperature dependent viscosity on the structure of new plumes in the mantle: Results of a finite element model in a spherical, axisymmetric shell. *Earth and Planetary Science Letters*, 148:13–26, 1997.

[2] S. E. Zaranek and E. Parmentier. The onset of convection in fluids with strongly temperature-dependent viscosity cooled from above with implications for planetary lithospheres. *Earth and Planetary Science Letters*, 224:371–386, 2004.

[3] A. Bottaro, P. Metzener, and M. Matalon. Onset and two-dimensional patterns of convection with strongly temperature-dependent viscosity. *Physics of Fluids*, 4(655-663), 1992.

[4] G.F. Davies. *Dynamic Earth. Plates, Plumes and Mantle convection.* Cambridge University Press, 2001.

[5] K. E. Torrance and D. L. Turcotte. Thermal convection wiith large viscosity variations. *J. Fluid Mech.*, 47(113), 1971.

[6] K. C. Stengel, D. S. Olivier, and J. R. Booker. Onset of convection in a variable-viscosity fluid. *J. Fluid Mech.*, 129:411–431, 1982.

[7] S. Morris. The effects of strongly temperature-dependent viscosity on slow flow past a hot sphere. *J. Fluid Mech.*, 124(1-26), 1982.

[8] L. N. Moresi and V. S. Solomatov. Numerical investigation of 2D convection with extremely large viscosity variations. *Physics of Fluids*, 7(9):2154–2162, 1995.

[9] G. R. Fulford and P. Broadbridge. *Industrial Mathematics.* Australian Mathematical Society Lecture Series 16. Cambridge University Press, 2002.

[10] M. Ulvrová, S. Labrosse, N. Coltice, P. Raback, and P.J. Tackley. Numerical modelling of convection interacting with a melting and solidification front: Application to the thermal evolution of the basal magma ocean. *Physics of the Earth and Planetary Interiors*, 206-207:51–66, 2012.

[11] J. Curbelo and A. M. Mancho. Bifurcations and dynamics in convection with temperature-dependent viscosity in the presence of the O(2) symmetry. *Phys. Rev. E*, 88:043005, 2013.

[12] E. Palm, T. Ellingsen, and B. Gjevik. On the occurrence of cellular motion in bénard convection. *J. Fluid Mech.*, 30(651-661), 1967.

[13] L. Richardson and B. Straughan. A nonlinear stability analysis for convection with temperature–dependent viscosity. *Acta Mechanica*, 97:41–49, 1993.

[14] J. I. Diaz and B. Straughan. Global stability for convection when the viscosity has a maximum. *Continuum Mech. Thermodyn.*, 16:347–352, 2004.

[15] A. Vaidya and R. Wulandana. Non-linear stability for convection with quadratic temperature dependent viscosity. *Math. Meth. Appl. Sci.*, 29:1555–1561, 2006.

[16] M. Gunzburger, Y. Saka, and X. Wang. Well-posedness of the infinite Prandtl number model for convection with temperature-dependent viscosity. *Anal. Appl.*, 7:297–308, 2009.

[17] C. Wang and Z. Zhang. Global well-posedness for the 2-D Boussinesq system with the temperature- dependent viscosity and thermal diffusivity. *Advances in Mathematics*, 228:43–62, 2011.

[18] F. Pla, A. M. Mancho, and H. Herrero. Bifurcation phenomena in a convection problem with temperature dependent viscosity at low aspect ratio. *Physica D: Nonlinear Phenomena*, 238(5):572–580, 2009.

[19] J. Guckenheimer and P. Holmes. Structurally stable heteroclinic cycles. *Math. Proc. Cambridge Philos. Soc.*, 103(189-192), 1988.

[20] D. Armbruster, J. Guckenheimer, and P. Holmes. Heteroclinic cycles and modulated travelling waves in systems with O(2) symmetry. *Physica D*, 29:257–282, 1988.

[21] S. P. Dawson and A. M. Mancho. Collections of heteroclinic cycles in the Kuramoto-Sivashinsky equation. *Physica D: Nonlinear Phenomena*, 100(3-4):231–256, 1997.

[22] P. Holmes, J. L. Lumley, and G. Berkooz. *Turbulence, Coherent Structures, Dynamical Systems and Symmetry.* Cambridge Monographs and Mechanics. Cambridge University Press, 1996.

[23] D. Johnson and R. Narayanan. Experimental observation of dynamic mode switching in interfacial-tension-driven convection near a codimension-two point. *Phys. Rev. E*, 54:R3102, 1996.

[24] P.C. Dauby, P. Colinet, and D. Johnson. Theoretical analysis of a dynamic thermoconvective pattern in a circular container. *Phys. Rev. E*, 61:2663, 2000.

[25] P. Assemat, A. Bergeon, and E. Knobloch. Nonlinear marangoni convection in circular and elliptical cylinders. *Physics of Fluids*, 19:104101, 2007.

[26] A. Ismail-Zadeh and P.J. Tackley. *Computational Methods for Geodynamics.* Cambridge University Press, 2010.

[27] D. Gartling. *NACHOS– A finite element computer program for incompressible flow problems, Parts I and II.* Sand 77-1333, Sand 77-1334. Sandia National Laboratories, Albuquerque, NM, USA., 1977.

[28] B. Blankebach, F. Busse, U. Christensen, L. Cserepes, D. Gunkel, U. Hansen, H. Harder, G. Jarvis, M. Koch, G. Marquart, D. Moore, P. Olson, H. Schmeling, and T. Schnaubelt. A benchmark comparison for mantle convection codes. *Geophysical Journal International*, 98:23–38, 1989.

[29] L. Cserepes. On different numerical solutions of the equations of mantle convection. *Annales Universitatis Scientarum Budapestinensis*, Section of Geophysics and Metorology(ed. Stegena, Eötvös Univesity, Budapest):52–67, 1985.

[30] D. R. Moore, R. R. Peckover, and N. O. Weiss. Difference methods for two-dimensional convection. *Computer Phys. Communs.*, 6:198–220, 1974.

[31] U. Christensen, , and H. Harder. 3-d convection with variable viscosity. *Geophysical Journal International*, 104:213–226, 1991.

[32] O. Cadek and L. Fleitout. Effect of lateral viscosity variations in the top 300 km on the geoid and dynamic topography. *Geophysical Journal International*, 152:566–580, 2003.

[33] I. Mercader, O. Batiste, and A. Alonso. An efficient spectral code for incompressible flows in cylindrical geometries. *Computers & Fluids*, 39(2):215–224, 2010.

[34] S. Hugues and A. Randriamampianina. An improved projection scheme applied to pseudospectral methods for the incompressible Navier–Stokes equations. *International Journal for Numerical Methods in Fluids*, 28(3):501–521, 1998.

[35] F. García, M. Net, B. García-Archilla, and J. Sánchez. A comparison of high-order time integrators for thermal convection in rotating spherical shells. *J. Comput. Phys.*, 229:7997–8010, 2010.

[36] E. Hairer, S.P. Norsett, and G. Wanner. *Solving Ordinary Differential Equations I. Nonstiff Problems*. Springer, 2009.

[37] E. Hairer and G. Wanner. *Solving Ordinary Differential Equations. II. Stiff and Differential Algebraic Problems*. Springer, 1991.

[38] F. Pla, H. Herrero, and O. Lafitte. Theoretical and numerical study of a thermal convection problem with temperature-dependent viscosity in an infinite layer. *Physica D: Nonlinear Phenomena*, 239(13):1108–1119, 2010.

[39] H. Herrero and A. M. Mancho. On pressure boundary conditions for thermoconvective problems. *International Journal for Numerical Methods in Fluids*, 39(5):391–402, 2002.

[40] H. Herrero and A.M. Mancho. Numerical modeling in chebyshev collocation methods applied to stability analysis of convection problems. *Applied Numerical Mathematics*, 33:161–166, 2000.

[41] H. Herrero, S. Hoyas, A. Donoso, A. M. Mancho, J. M. Chacón, R. F. Portugués, and B. Yeste. Chebyshev collocation for a convective problem in primitive variable formulation. *Journal of scientific computing*, 18(3):315–328, 2003.

[42] S. Hoyas, H. Herrero, and AM Mancho. Thermal convection in a cylindrical annulus heated laterally. *Journal of Physics A: Mathematical and General*, 35:4067, 2002.

[43] M. C. Navarro, A. M. Mancho, and H. Herrero. Instabilities in buoyant flows under localized heating. *Chaos: An Interdisciplinary Journal of Nonlinear Science*, 17:023105, 2007.

[44] M. C. Navarro, H. Herrero, A. M. Mancho, and A. Wathen. Efficient solution of generalized eigenvalue problem arising in a thermoconvective instability. *Communications in Computational Physics*, 3:308–329, 2008.

[45] F. Ceschino. *Modification de la longeur du pas dans l'intégration numérique par les méthodes a pas liés*. Chiffres, 1961.

[46] W.H. Press, B.P. Flannery, S.A. Teukolsky, and W.T. Vetterling. *Numerical Recipes in Fortran 77: The Art of Scientific Computing*. Cambridge University Press, 1992.

[47] S. P. Dawson and A. M. Mancho. Collections of heteroclinic cycles in the kuramoto-sivashinsky equation. *Physica D*, 100:231–256, 1997.

[48] D. B. White. The planforms and onset of convection with a temperature dependent viscosity. *J. Fluid. Mech.*, 191:247–286, 1988.

[49] V.S. Solomatov. Localized subcritical convective cells in temperature-dependent viscosity fluids. *Phys. Earth Planet. Inter.*, 200-201:63–71, 2012.

[50] L. S. Tuckerman. Divergence-free velocity fields in nonperiodic geometries. *Journal of Computational Physics*, 80(2):403–441, 1989.

[51] A. M. Mancho, H. Herrero, and J. Burguete. Primary instabilities in convective cells due to nonuniform heating. *Physical Review E*, 56(3):2916, 1997.

3.2. Bifurcations and dynamics of a convection problem with temperature dependent viscosity under the presence of the O(2) symmetry

Coauthors: Ana M. Mancho

Abstract: We is focus on the study of a convection problem in a two-dimensional setup in the presence of the O(2) symmetry. In the fluid, the viscosity depends on the temperature by changing its value abruptly in an interval around a temperature of transition. The influence of the viscosity law on the morphology of the plumes is examined for several parameter settings and it is found a variety of shapes ranging from spout to mushroom shaped. We explore the impact of the symmetry on the time evolution of this type of fluid, and find solutions which are greatly influenced by its presence: at a large aspect ratio and high Rayleigh numbers, travelling waves, heteroclinic connections and chaotic regimes are found. These solutions, which are due to the symmetry presence, have not been previously described in the context of temperature dependent viscosities, however similarities are found with solutions described in other contexts such as flame propagation problems or convection problems with constant viscosity also under the presence of the O(2) symmetry, thus confirming the determining role of the symmetry in the dynamics.

Reference: [25] J. Curbelo , A. M. Mancho. Bifurcations and dynamics of a convection problem with temperature-dependent viscosity under the presence of the O(2) symmetry. Physical Review E **88**, 043005 (2013).

PHYSICAL REVIEW E **88**, 043005 (2013)

Bifurcations and dynamics in convection with temperature-dependent viscosity in the presence of the O(2) symmetry

J. Curbelo[1,2] and A. M. Mancho[1]

[1]*Instituto de Ciencias Matemáticas (CSIC-UAM-UCM-UC3M), Nicolás Cabrera, 13-15, 28049 Madrid, Spain*

[2]*Departamento de Matemáticas, Facultad de Ciencias, Universidad Autónoma de Madrid, 28049 Madrid, Spain*

(Received 16 May 2013; published 14 October 2013)

We focus on the study of a convection problem in a two-dimensional setup in the presence of the O(2) symmetry. The viscosity in the fluid depends on the temperature as it changes its value abruptly in an interval around a temperature of transition. The influence of the viscosity law on the morphology of the plumes is examined for several parameter settings, and a variety of shapes ranging from spout- to mushroom-shaped are found. We explore the impact of the symmetry on the time evolution of this type of fluid, and we find solutions which are greatly influenced by its presence: at a large aspect ratio and high Rayleigh numbers, traveling waves, heteroclinic connections, and chaotic regimes are found. These solutions, which are due to the presence of symmetry, have not been previously described in the context of temperature-dependent viscosities. However, similarities are found with solutions described in other contexts such as flame propagation problems or convection problems with constant viscosity also in the presence of the O(2) symmetry, thus confirming the determining role of the symmetry in the dynamics.

DOI: 10.1103/PhysRevE.88.043005 PACS number(s): 47.20.Ky, 05.45.−a

I. INTRODUCTION

This paper addresses the numerical study of convection at infinite Prandtl number in fluids in which viscosity strongly depends on temperature in the presence of the O(2) symmetry. Convection in fluids with temperature-dependent viscosity is of interest because of its importance in engineering and geophysics. Linear and quadratic dependencies of the viscosity on temperature have been discussed [1–4], but in order to address the Earth's upper mantle convection, in which viscosity contrasts are of several orders of magnitude, a stronger dependence with temperature must be considered. This problem has been approached both in experiments [5–8] and in theory [9–14]. In these contexts, the dependence of viscosity with temperature is expressed by means of an Arrhenius law. In [10], the exponential dependence is discussed as an approach to the Arrhenius law by means of a Taylor series around a reference temperature. This is also called the Frank-Kamenetskii approximation (see [15]). Viscosity has also been considered when it depends on other magnitudes such as depth [16,17], a combination of both depth and temperature [17], or pressure [18]. However, it is commonly accepted [18,19] that in the Earth's interior, viscosity depends most significantly on temperature. The usual approach in numerical models of the mantle [12,17,20] is to consider constant thermal conductivity. This approach has also been verified in fluid experiments seeking to model mantle convection [7]. However, studies also exist in which variations on thermal conductivity are considered [21–23].

Here, we focus on the study of a fluid in which the viscosity changes abruptly in a temperature interval around a temperature of transition. This defines a phase change over a mushy region, which expresses the melting of minerals or other components. Melting and solidification processes are important in magma chamber dynamics [24,25], in volcanic conduits [26,27], in the formation of chimneys in mushy layers [28], in metal processing in industry (see, for example, [29]), etc. In phase transitions, other fluid properties in addition to viscosity may change abruptly, such as density or thermal diffusivity. However, in this study we consider solely the study of effects due to the variability of viscosity, since consideration of the effect of simultaneous variations on all the properties prevents a focused understanding of the exact role played by each one of these properties. Viscosity is a measure of fluid resistance to gradual deformation, and in this sense very viscous fluids are more likely to behave rigidly when compared to less viscous fluids. When examining the proposed transition with temperature, we focus on the global fluid motion when some parts of it tend to be more rigid than others. Disregarding the variations on density in this transition moves us away from instabilities caused by abrupt density changes such as the Rayleigh-Taylor instability, in which a denser fluid over a lighter one tends to penetrate it by forming a fingering pattern. A recent article by Ulvrová *et al.* [30] deals with a problem similar to ours, but takes into account variations both in density and in viscosity. Thermal conductivity effects are related to the relative importance of heat advection versus diffusion. In this way, diffusive effects are important at large conductivity, while heat advection by fluid particles is dominant at low conductivity. The contrasts arising from these variations are beyond the scope of our work and thus are disregarded here.

This paper addresses the convection of a two-dimensional (2D) fluid layer with temperature-dependent viscosity and periodic boundary conditions *possessing the O(2) symmetry*. The motivation arises from the fact that symmetric systems typically exhibit more complicated bifurcations than nonsymmetric systems and introduce conditions and degeneracies in bifurcation analysis. There exist numerous novel dynamical phenomena whose existence is fundamentally related to the presence of symmetry [31–34]. Solutions related to the presence of symmetry include rotating waves [35], modulated waves [36,37], slow "phase" drifts along directions of broken symmetry [38], and stable heteroclinic cycles [37,39,40]. SO(2) symmetry is present in problems described by the Navier-Stokes [41,42] or the Kuramoto-Sivashinsky [40,43] equations with periodic boundary conditions, since the

Bifurcations and dynamics in convection with temperature-dependent viscosity in the presence of the O(2) symmetry

J. Curbelo[1,2], A. M. Mancho[1]
[1]Instituto de Ciencias Matemáticas (CSIC-UAM-UCM-UC3M),
Nicolás Cabrera, 13-15, 28049 Madrid, Spain
[2]Departamento de Matemáticas, Facultad de Ciencias,
Universidad Autónoma de Madrid, 28049 Madrid, Spain

February 10, 2014

Abstract

We focus the study of a convection problem in a 2D set–up in the presence of the O(2) symmetry. The viscosity in the fluid depends on the temperature as it changes its value abruptly in an interval around a temperature of transition. The influence of the viscosity law on the morphology of the plumes is examined for several parameter settings, and a variety of shapes ranging from spout to mushroom shaped is found. We explore the impact of the symmetry on the time evolution of this type of fluid, and find solutions which are greatly influenced by its presence: at a large aspect ratio and high Rayleigh numbers, traveling waves, heteroclinic connections and chaotic regimes are found. These solutions, which are due to the symmetry presence, have not been previously described in the context of temperature dependent viscosities. However, similarities are found with solutions described in other contexts such as flame propagation problems or convection problems with constant viscosity also under the presence of the O(2) symmetry, thus confirming the determining role of the symmetry in the dynamics.

1 Introduction

This paper addresses the numerical study of convection at infinite Prandtl number in fluids in which viscosity strongly depends on temperature in the presence of O(2) symmetry. Convection in fluids with temperature-dependent viscosity is of interest because of its importance in engineering and geophysics. Linear and quadratic dependencies of the viscosity on temperature have been discussed [47, 52, 22, 65], but in order to address the Earth's upper mantle convection, in which viscosity contrasts are of several orders of magnitude, a stronger dependence with temperature must be considered. This problem has been approached both in experiments [53, 13, 6, 67] and in theory [45, 7, 50, 44, 60, 61]. In these contexts, the dependence of viscosity with temperature is expressed by means of an Arrhenius law. In [7], the exponential dependence is discussed as an approach to the Arrhenius law by means of a Taylor series around a reference temperature. This is also called the Frank-Kamenetskii approximation (see [27]). Viscosity has also been considered when it depends on other magnitudes such as depth [10, 5], a combination of both depth and temperature [5] or pressure [51]. However, it is commonly accepted [20, 51] that in the Earth's interior, viscosity depends most significantly on temperature. The usual approach in numerical models of the mantle [44, 5, 63] is to consider constant thermal conductivity. This approach has also been verified in fluid experiments seeking to model mantle convection [6]. However, studies also exist which consider variations on thermal conductivity [23, 24, 68].

Here, we focus on the study of a fluid in which the viscosity changes abruptly in a temperature interval around a temperature of transition. This defines a phase change over a mushy region, which expresses the melting of minerals or other components. Melting and solidification processes are important in magma chamber dynamics [8, 9], in volcanic conduits [25, 42], in the formation of chimneys in mushy layers [15], in metal processing in industry (see, for example, [55]), etc. In phase transitions, other fluid properties in addition to viscosity may change abruptly, such as density or thermal diffusivity. However, in this study we consider solely the study of effects due to the variability of viscosity, since consideration of the effect of simultaneous variations on all the properties prevents a focused understanding of the exact role played by each one of these properties. Viscosity is a measure of fluid resistance to gradual deformation, and in this sense very viscous fluids are more likely to behave rigidly when compared to less viscous fluids. When examining the proposed transition with temperature, we focus on the global fluid motion when some parts of it tend to be more rigid

than others. Disregarding the variations on density in this transition moves us away from instabilities caused by abrupt density changes such as the Rayleigh Taylor instability, in which a denser fluid over a lighter one tends to penetrate it by forming a fingering pattern. A recent article by M. Ulvrová *et al.* [64] deals with a similar problem to ours, but takes into account both variations in density and in viscosity. Thermal conductivity effects are related to the relative importance of heat advection versus diffusion. In this way, diffusive effects are important at large conductivity, while heat advection by fluid particles is dominant at low conductivity. The contrasts arising from these variations are beyond the scope of our work and thus are disregarded here.

This paper addresses the convection of a 2D fluid layer with temperature-dependent viscosity and periodic boundary conditions *possessing the O(2) symmetry*. The motivation arises from the fact that symmetric systems typically exhibit more complicated bifurcations than non-symmetric systems and introduce conditions and degeneracies in bifurcation analysis. There exist numerous novel dynamical phenomena whose existence is fundamentally related to the presence of symmetry [16, 29, 31, 26]. Solutions related to the presence of symmetry, include rotating waves [54], modulated waves [49, 2], slow "phase" drifts along directions of broken symmetry [41], and stable heteroclinic cycles [2, 33, 21]. The SO(2) symmetry is present in problems described by the Navier-Stokes [30, 62] or the Kuramoto-Sivashinsky [21, 3] equations with periodic boundary conditions, since the equations are invariant under translations and the boundary conditions do not break this invariance. Additionally, if the reflection symmetry exists, the full symmetry group is the O(2) group. While in classical convection problems (with constant viscosity), the study of the solutions and bifurcations in the presence of symmetries has been the object of much attention [38, 32, 46, 43, 40, 39, 19, 4], its counterpart in fluids with viscosity depending on temperature has received less consideration. Our 2D physical set-up is idealized with respect to realistic geophysical flows occurring in the Earth's interior, as these are 3D flows moving in spherical shells [11, 12]. Under these conditions, the symmetry present in the problem is formed by all the orientation preserving rigid motions of $\mathbb{R}^3$ that fix the origin,which is the SO(3) group [14, 28, 36]. The effects of the Earth's rotation are negligible in this respect and do not break this symmetry, since the high viscosity of the mantle makes the Coriolis number insignificant. The link between our simplified problem and these realistic set-ups is that the O(2) symmetry is isomorphic to the rotations along the azimuthal coordinate, which form a closed subgroup of SO(3). Additionally, the O(2) symmetry is present in systems with cylindrical geometry, which provide an idealized setting for volcanic conduits and magma chambers. The SO(2) symmetry is also present in 3D flows moving in spherical shells which rotate around an axis.

In this way, specific symmetry-related solutions found in our setting are expected to be present in these other contexts. The interest of 2D numerical studies for representing 3D time-dependent thermal convection with constant viscosity has been addressed in [56]. The authors report that in turbulent regimes at high Rayleigh numbers, the flow structure and global quantities such as the Nusselt number and the Reynolds number show a similar behaviour in 3D and 2D simulations as far as high values of the Prandtl number are concerned. In some sense, these results suggest that our simulations might be illustrative for the 3D case, since although they are far from a turbulent regime and do not correspond to the case of constant viscosity, they have been performed according to the infinite Prandtl number approach. In this article we show that typical solutions of systems with symmetries, as previously reported in diverse contexts [2, 21, 66], are also present in mantle convection and magma-related problems. We report the presence of traveling waves and limit cycles near heteroclinic connections after a Hopf bifurcation. We do this by means of bifurcation analysis techniques an direct numerical simulations and of the full partial differential equations system.

The article is organized as follows: In Section 2, we formulate the problem, providing the description of the physical set-up, the basic equations and boundary conditions. In Section 3 we present the viscosity law under consideration and discuss several limits in which previously studied dependencies are recovered. Section 4 summarizes the numerical methods used to sketch an outlook of the solutions displayed by the system. Section 5 discusses the solutions obtained for a broad parameter set. Finally Section 6 presents the conclusions.

2 Formulation of the problem

As shown in Figure 1 we consider a fluid layer, placed in a 2D container of length L (x coordinate) and depth d (z coordinate). The bottom plate is at temperature T_0 and the upper plate is at T_1, where $T_1 = T_0 - \Delta T$ and ΔT is the vertical temperature difference, which is positive, *i.e*, $T_1 < T_0$.

The magnitudes involved in the equations governing the system are the velocity field $\mathbf{u} = (u_x, u_z)$, the temperature T, and the pressure P. The spatial coordinates are x and z and the time is denoted by t. Equations are simplified by taking into account the Boussinesq approximation, where the density ρ is considered as constant everywhere except in the external forcing term, where a dependence on temperature is assumed, as follows $\rho = \rho_0(1 - \alpha(T - T_1))$. Here ρ_0 is the mean density at temperature T_1 and α the thermal expansion coefficient.

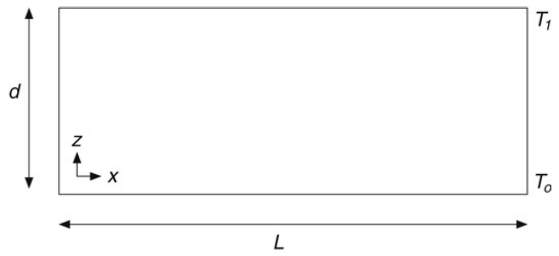

Figure 1: Problem set-up. A 2D container of length L and depth d with periodic lateral boundary conditions. The bottom plate plate is at temperature T_0 and is rigid, while at the upper plate the temperature is T_1 ($T_1 < T_0$) and free slip.

The equations are expressed with magnitudes in dimensionless form after rescaling as follows: $(x', z') = (x, z)/d$, $t' = \kappa t/d^2$, $\mathbf{u}' = d\mathbf{u}/\kappa$, $P' = d^2P/(\rho_0\kappa\nu_0)$, $\theta' = (T - T_1)/(\Delta T)$. Here, κ is the thermal diffusivity and ν_0 is the maximum viscosity of the fluid, which is viscosity at temperature T_1. After rescaling the domain, $\Omega_1 = [0, L) \times [0, d]$ is transformed into $\Omega_2 = [0, \Gamma) \times [0, 1]$ where $\Gamma = L/d$ is the aspect ratio. The system evolves according to the momentum and the mass balance equations, as well a to the energy conservation principle. The non-dimensional equations are (after dropping the primes in the fields):

$$\nabla \cdot \mathbf{u} = 0, \tag{1}$$

$$\frac{1}{\mathrm{Pr}}(\partial_t \mathbf{u} + \mathbf{u} \cdot \nabla \mathbf{u}) = \mathrm{Ra}\theta\vec{e_3} - \nabla P + \mathrm{div}\left(\frac{\nu(\theta)}{\nu_0}(\nabla \mathbf{u} + (\nabla \mathbf{u})^T)\right), \tag{2}$$

$$\partial_t \theta + \mathbf{u} \cdot \nabla \theta = \Delta \theta. \tag{3}$$

Here, $\vec{e_3}$ represents the unitary vector in the vertical direction, $\mathrm{Ra} = d^4\alpha g\Delta T/(\nu_0\kappa)$ is the Rayleigh number, g is the gravity acceleration, $\mathrm{Pr} = \nu_0/\kappa$ is the Prandtl number. Typically for rocks Pr, is very large, since they present low thermal conductivity (approximately $10^{-6}m^2/s$) and very large viscosity (of the order $10^{20}Ns/m^2$) [20]. Thus, for the problem under consideration, Pr can be considered as infinite and the left-hand side term in (2) can be made equal to zero. The viscosity $\nu(\theta)$ is a smooth positive bounded function of θ, which in our set-up represents a transition in the fluid, due for instance to the melting of minerals caused by an abrupt change in viscosity at a certain temperature. This is discussed in detail in the following section.

For the boundary conditions, we consider that the bottom plate is rigid and that the upper surface is non-deformable and free slip. The dimensionless boundary conditions are expressed as,

$$\theta = 1,\ \mathbf{u} = \vec{0},\ \text{on } z = 0 \text{ and } \ \theta = \partial_z u_x = u_z = 0,\ \text{on } z = 1. \tag{4}$$

Lateral boundary conditions are periodic. Jointly with equations (1)-(3), these conditions are invariant under translations along the x-coordinate, which introduces the symmetry SO(2) into the problem. In convection problems with constant viscosity, the reflexion symmetry $x \to -x$ is also present insofar as the fields are conveniently transformed as follows $(\theta, u_x, u_z, p) \to (\theta, -u_x, u_z, p)$. In this case, the O(2) group expresses the full problem symmetry. The new terms introduced by the temperature dependent viscosity, in the current set-up equation (2) maintain the reflexion symmetry, and the symmetry group is O(2).

3 The viscosity law

We consider that the viscosity depends on temperature, and that it changes more or less abruptly at a certain temperature interval centered at a temperature of transition. This is expressed with an arctangent law which reads as follows:

$$\nu(T) = A_1 \arctan(\beta\{(T - T_1) - b\}) + A_2 \tag{5}$$

The parameter β controls how abrupt the transition of the viscosity with temperature is. Very high β values imply that the viscosity transition occurs within a very narrow temperature gap, while a finite and not too large value β assumes that the phase change happens over a mushy region of finite thickness [64]. For the results reported in this article, we have fixed $\beta = 0.9$. As β is fixed, the viscosity transition always occurs in a temperature interval with constant thickness $\Delta\theta \sim 0.23$. The temperature at which the transition occurs is controled by b. The constants A_1 and A_2 are adjusted by imposing that at the reference temperature T_1 the

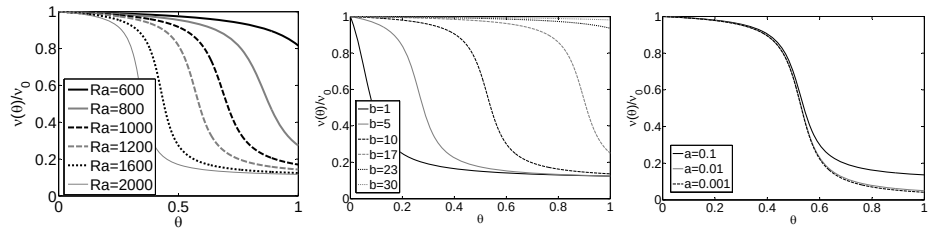

(a) (b) (c)

Figure 2: Representation of the arctangent viscosity law versus the dimensionless temperature for different parameters values; a) $b = 10$, $a = 0.1$ and different Ra values; b) $a = 0.1$, Ra $= 1300$ and different b values; c) $b = 10$, Ra $= 1300$ and different a values.

viscosity law (5) must be ν_0. On the other hand, in the limit $T >> T_1$, for instance $T - T_1 = 2500$, the viscosity is fixed to a fraction a of the viscosity ν_0. These conditions supply the system:

$$\begin{aligned} \nu_0 &= A_1 \arctan(-\beta b) + A_2 \\ \nu_0 a &= A_1 \arctan(\beta\{2500 - b\}) + A_2 \end{aligned}$$

which has the solution:

$$\begin{aligned} A_1 &= \frac{\nu_0(1-a)}{\arctan(-\beta b) - \arctan(\beta(2500-b))}, \\ A_2 &= \nu_0 - A_1 \arctan(-b\beta). \end{aligned}$$

In dimensionless form, the viscosity law becomes:

$$\frac{\nu(\theta)}{\nu_0} = C_1 \arctan(\beta(\mathrm{Ra}\theta\mu - b)) + C_2 \tag{6}$$

where $C_1 = A_1/\nu_0$ and $C_2 = A_2/\nu_0$. In this expression, Ra is the Rayleigh number, θ is the dimensionless temperature, which takes values between 0 at the upper surface and 1 at the bottom. The parameter μ, defined as $\mu = \nu_0\kappa/(d^3\alpha g)$, is in this study fixed to $\mu = 0.0146$. The parameter a is related to the inverse of the maximum viscosity contrast on the fluid layer, although the viscosity $\nu_0 a$ may not correspond to any element of the fluid layer. For instance Figure 2(a) shows the viscosity variation with temperature for different Rayleigh numbers at $a = 0.1$ and $b = 10$. It is observed that at low Ra, Ra $= 600$, the viscosity is almost uniform in the fluid layer, and it is only beyond Ra $= 1000$ that the sharp change in the viscosity is perceived. Figure 2(b) shows the effect of varying b at Ra $= 1300$ and $a = 0.1$. If b is as small as 1, the transition occurs close to $\theta = 1$ and most of the layer has low viscosity, while if b is very large at this Ra number most of the fluid has constant viscosity ν_0. It is interesting to relate the viscosity law as represented in these figures with the linear stability analysis of a fluid layer with constant viscosity ν_0, as presented in Figure 3. In this figure, one may observe that the critical Ra number is approximately $\mathrm{Ra}_c \sim 1100$. On the other hand, in Figure 2(b) one may observe that if b is large, the viscosity near the critical Rayleigh number is almost constant across the fluid layer. In this case, the phase transition is noticed in the fluid at large Ra numbers, well above Ra $= 1300$, in a convection state in which vigorous plumes are already formed, as may be deduced from Figure 2(a). Figure 3(a) confirms that at this limit the instability threshold of the conductive state remains unchanged with respect to that obtained with constant viscosity. On the other hand, if b is small, changes in the fluid viscosity are noticed at low Ra numbers –below the critical threshold of a fluid with constant viscosity– and in this case the instability threshold of the conductive state is affected by the phase transition. This is illustrated, for instance, in Figures 2(a) and 3(b). For $b = 10$ and $a = 0.1$, the changes in the viscosity across the fluid layer are noticed from Ra $= 800$ onwards, which is below the instability threshold obtained for constant viscosity. In this case, the instability thresholds for the conductive solution are as those displayed in Figure 4, and thus the phase transition is perceived from the beginning by weakly convective states.

We now discuss the relation between the arctangent law and an Arrhenius type law frequently used in the literature to model mantle convection problems. This viscosity law is expressed according to [37, 20] as:

$$\nu(\theta) = \nu_0 \exp\left[\frac{E^*}{\overline{R}\Delta\theta}\left(\frac{1}{\theta + t_1} - \frac{1}{1 + t_1}\right)\right] \tag{7}$$

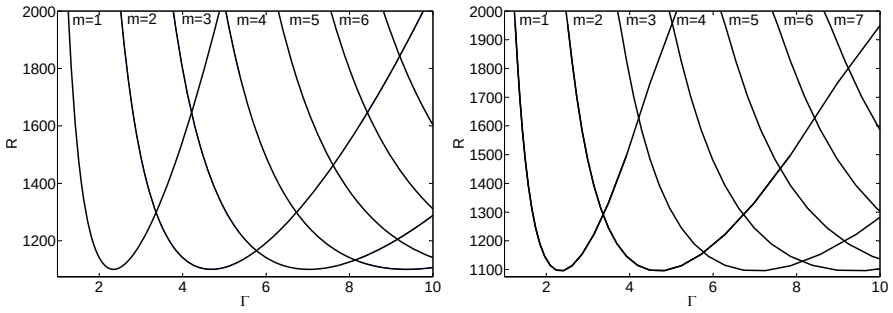

(a) (b)

Figure 3: Critical instability curves of the Rayleigh number, Ra, versus the aspect ratio Γ at different wave numbers m. The results are for a fluid layer a) with constant viscosity; b) with temperature dependent viscosity $\mu = 0.0146$ $a = 0.1$ and $b = 30$.

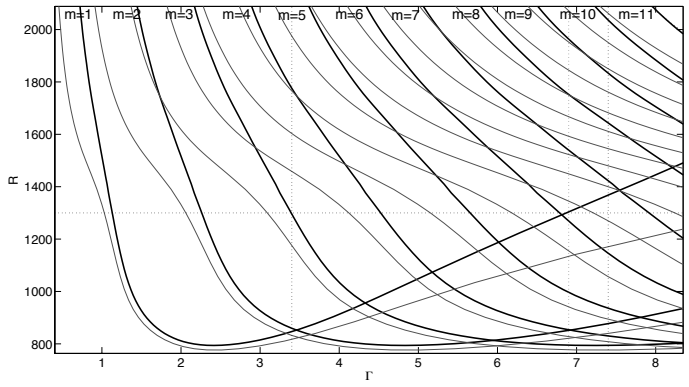

Figure 4: Critical instability curves of the Rayleigh number, Ra, versus the aspect ratio Γ at different wave numbers m. The results are for a fluid layer with temperature dependent viscosity $\mu = 0.0146$, $b = 10$ and $a = 0.1$ (thick line) or $a = 0.01$ (thin line).

where E^* is the activation energy, $\overline{R}$ is the universal gas constant, $\Delta\theta$ is the temperature drop across the fluid layer and t_1 is the surface temperature divided by the temperature drop across the layer. Figure 5 represents the viscosity (7) versus the dimensionless temperature for $\frac{E^*}{\overline{R}\Delta\theta} = 0.25328$ and $t_1 = 0.1$ as considered by [37]. Additionally, several arctangent laws with different b values are displayed. In this representation, one may observe the great similitude between the Arrhenius law and the arctangent law for $b = 1$. At larger b values, the decaying rate between viscosities is still similar to an Arrhenius law; however, temperature intervals exist with approximately constant viscosities ν_0 and $\nu_0 a$.

One of the effects of the viscosity contrasts in the fluid motion is that if they are very large, as achieved for instance with the exponential or the Arrhenius law, they lead to a stagnant lid convection regime [44, 58, 59], in which there exists a non mobile cap where heat is dissipated mainly by conduction over a convecting flow. In [64, 17] a similar stagnant regime is obtained for a viscosity law similar to the one presented in this section. In our setting, we have considered a free slip boundary at the top boundary, thus quiescence is not imposed. This condition enables us to consider spontaneous transitions from stagnant to non stagnant regimes.

4 Numerical methods

Analysis of the solutions to the problem described by equations (1)-(3) and boundary conditions (4) is assisted by time dependent numerical simulations and bifurcation techniques such as branch continuation. As highlighted by [18, 48], the combination of both techniques provide a thorough insight into the solutions observed in the system. A full discussion on the spectral numerical schemes used is given in [18]. For completeness, we now

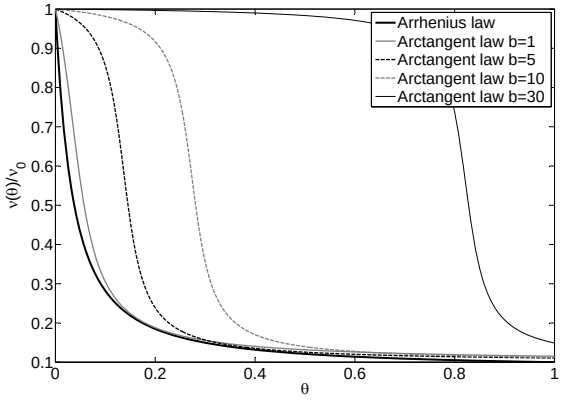

Figure 5: The law of the viscosity dependent on the temperature used in [37] with viscosity contrast of factor 10 against the arctangent law (6) with parameters $b = 1, 5, 10, 30$, Ra $= 2500$ and $a = 0.1$

summarize the essential elements of the numerical approach.

4.1 Stationary solutions and their stability

The simplest stationary solution to the problem described by equations (1)-(3) with boundary conditions (4) is the conductive solution which satisfies $\mathbf{u}_c = 0$ and $\theta_c = -z+1$. This solution is stable only for a range of vertical temperature gradients which are represented by small enough Rayleigh numbers. Beyond the critical threshold Ra_c, a convective motion settles in and new structures are observed which may be either time dependent or stationary. In the latter case, the stationary equations, obtained by canceling the time derivatives in the system (1)-(3) are satisfied by the bifurcating solutions. At the instability threshold of the conductive state, the growing solutions are periodic and correspond to sine or cosine eigenfunctions with wave number m. Figures 3 and 4 display the critical instability curves for different m values as a function of the aspect ratio. The new solutions depend on the external physical parameters, and new critical thresholds exist at which stability is lost, thereby giving rise to new bifurcated structures. These solutions are numerically obtained by using an iterative Newton-Raphson method. This method starts with an approximate solution at step $s = 0$, to which is added a small correction in tilde:

$$(\mathbf{u}^s + \tilde{\mathbf{u}}, \theta^s + \tilde{\theta}, P^s + \tilde{P}). \tag{8}$$

These expressions are introduced into the system (1)-(3), and after canceling the nonlinear terms in tilde, the following equations are obtained:

$$0 = \nabla \cdot \tilde{\mathbf{u}} + \nabla \cdot \mathbf{u}^s, \tag{9}$$

$$\begin{aligned} 0 = &- \partial_x \tilde{P} - \partial_x P^s + \frac{1}{\nu_0}[L_{11}(\theta^s, u_x^s, u_z^s) + L_{12}(\theta^s)\tilde{u}_x \\ &+ L_{13}(\theta^s)\tilde{u}_z + L_{14}(\theta^s, u_x^s, u_z^s)\tilde{\theta}], \end{aligned} \tag{10}$$

$$\begin{aligned} 0 = &- \partial_z \tilde{P} - \partial_z P^s + \frac{1}{\nu_0}[L_{21}(\theta^s, u_x^s, u_z^s) + L_{22}(\theta^s)\tilde{u}_x \\ &+ L_{23}(\theta^s)\tilde{u}_z + (L_{24}(\theta^s, u_x^s, u_z^s) + \mathrm{Ra})\tilde{\theta}], \end{aligned} \tag{11}$$

$$0 = \tilde{\mathbf{u}} \cdot \nabla\theta^s + \mathbf{u}^s \cdot \nabla\tilde{\theta} + \mathbf{u}^s \cdot \nabla\theta^s - \Delta\tilde{\theta} - \Delta\theta^s. \tag{12}$$

Here, L_{ij} $(i = 1, 2,\ j = 1, 2, 3, 4)$ are linear operators with non-constant coefficients, which are defined as follows:

$$\begin{aligned}
L_{11}(\theta, u_x, u_z) =& 2\partial_\theta\nu(\theta)\partial_x\theta\partial_x u_x + \nu(\theta)\Delta u_x + \partial_\theta\nu(\theta)\partial_z\theta(\partial_x u_z + \partial_z u_x), && (13)\\
L_{12}(\theta) =& 2\partial_\theta\nu(\theta)\partial_x\theta\partial_x + \nu(\theta)\Delta + \partial_\theta\nu(\theta)\partial_z\theta\partial_x, && (14)\\
L_{13}(\theta) =& \partial_\theta\nu(\theta)\partial_z\theta\partial_x, && (15)\\
L_{14}(\theta, u_x, u_z) =& 2\partial_\theta\nu(\theta)\partial_x u_x\partial_x + 2\partial^2_{\theta\theta}\nu(\theta)\partial_x\theta\partial_x u_x + \partial_\theta\nu(\theta)\Delta u_x\\
&+ (\partial_x u_z + \partial_z u_x)(\partial_\theta\nu(\theta)\partial_z + \partial^2_{\theta\theta}\nu(\theta)\partial_z\theta), && (16)\\
L_{21}(\theta, u_x, u_z) =& 2\partial_\theta\nu(\theta)\partial_z\theta\partial_z u_z + \nu(\theta)\Delta u_z + \partial_\theta\nu(\theta)\partial_x\theta(\partial_z u_x + \partial_x u_z), && (17)\\
L_{22}(\theta) =& \partial_\theta\nu(\theta)\partial_x\theta\partial_z, && (18)\\
L_{23}(\theta, u_x, u_z) =& 2\partial_\theta\nu(\theta)\partial_z\theta\partial_z + \nu(\theta)\Delta + \partial_\theta\nu(\theta)\partial_x\theta\partial_z, && (19)\\
L_{24}(\theta, u_x, u_z) =& 2\partial_\theta\nu(\theta)\partial_z u_z\partial_z + 2\partial_{\theta\theta}\nu(\theta)\partial_z\theta\partial_z u_z + \partial_\theta\nu(\theta)\Delta u_z\\
&+ (\partial_z u_x + \partial_x u_z)(\partial_\theta\nu(\theta)\partial_x + \partial_{\theta\theta}\nu(\theta)\partial_x\theta). && (20)
\end{aligned}$$

The unknown fields $\tilde{\mathbf{u}},\ \tilde{P},\ \tilde{\theta}$ are found by solving the linear system with the boundary conditions:

$$\tilde{\theta} = 0,\ \tilde{\mathbf{u}} = \vec{0},\ \text{on } z = 0 \text{ and } \tilde{\theta} = \partial_z\tilde{u_x} = \tilde{u_z} = 0,\ \text{on } z = 1. \quad (21)$$

Then the new approximate solution $s + 1$ is set to

$$\mathbf{u}^{s+1} = \mathbf{u}^s + \tilde{\mathbf{u}},\ \theta^{s+1} = \theta^s + \tilde{\theta},\ P^{s+1} = P^s + \tilde{P}.$$

The whole procedure is repeated for $s + 1$ until a convergence criterion is fulfilled. In particular, we consider that the l^2 norm of the computed perturbation should be less than 10^{-9}.

The study of the stability of the stationary solutions under consideration is addressed by means of a linear stability analysis. Now perturbations are added to a general stationary solution, labeled with superindex b:

$$\begin{aligned}
\mathbf{u}(x, z, t) &= \mathbf{u}^b(x, z) + \tilde{\mathbf{u}}(x, z)\mathrm{e}^{\lambda t}, && (22)\\
\theta(x, z, t) &= \theta^b(x, z) + \tilde{\theta}(x, z)\mathrm{e}^{\lambda t}, && (23)\\
P(x, z, t) &= P^b(x, z) + \tilde{P}(x, z)\mathrm{e}^{\lambda t}. && (24)
\end{aligned}$$

The sign in the real part of the eigenvalue λ determines the stability of the solution: if it is negative, the perturbation decays and the stationary solution is stable, while if it is positive the perturbation grows over time and the conductive solution is unstable. The linearized equations are:

$$\begin{aligned}
0 =& \nabla\cdot\tilde{\mathbf{u}} && (25)\\
0 =& -\partial_x\tilde{P} + \frac{1}{\nu_0}[L_{12}(\theta^b)\tilde{u}_x + L_{13}(\theta^b)\tilde{u}_z + L_{14}(\theta^b, u^b_x, u^b_z)\tilde{\theta}] && (26)\\
0 =& -\partial_z\tilde{P} + \frac{1}{\nu_0}[L_{22}(\theta^b)\tilde{u}_x + L_{23}(\theta^b)\tilde{u}_z + (L_{24}(\theta^b, u^b_x, u^b_z) + \mathrm{Ra})\tilde{\theta}] && (27)\\
0 =& \tilde{\mathbf{u}}\cdot\nabla\theta^b + \mathbf{u}^b\cdot\nabla\tilde{\theta} + \mathbf{u}^b\cdot\nabla\theta^b - \Delta\tilde{\theta} + \lambda\tilde{\theta}, && (28)
\end{aligned}$$

where the operators L_{ij} are the same as those defined in equations (13)-(20). Equations (25)-(28) jointly with its boundary conditions (identical to (21)) define a generalized eigenvalue problem.

The unknown fields Y of the stationary (9)-(12) and eigenvalue problems (25)-(28) are approached by means of a spectral method according to the expansion:

$$Y(x, z) = \sum_{l=1}^{\lceil L/2\rceil}\sum_{m=0}^{M-1} b^Y_{lm}T_m(z)\cos((l-1)x) + \sum_{l=2}^{\lceil L/2\rceil}\sum_{m=0}^{M-1} c^Y_{lm}T_m(z)\sin((l-1)x). \quad (29)$$

In this notation, $\lceil\cdot\rceil$ represents the nearest integer towards infinity. Here L is an odd number as justified in [18]. $4 \times L \times M$ unknown coefficients exist which are determined by a collocation method in which equations and boundary conditions are imposed at the collocation points (x_j, z_i),

$$\begin{aligned}
&\text{Uniform grid:} && x_j = (j-1)\frac{2\pi}{L}, && j = 1, \ldots, L;\\
&\text{Gauss–Lobatto:} && z_i = \cos\left(\left(\frac{i-1}{M-1} - 1\right)\pi\right), && i = 1, \ldots, M;
\end{aligned}$$

according to the rules detailed in [18]. Expansion orders L and M are taken to ensure accuracy on the results: details on their values are provided in the Results section.

4.2 Time dependent schemes

Together with boundary conditions (4), the governing equations (1)–(3) define a time-dependent problem for which we propose a temporal scheme based on a spectral spatial discretization analogous to that proposed in the previous section. As before, expansion orders L and M are such that they ensure accuracy on the results and details on their values are given in the following section. To integrate in time, we use a third order multistep scheme. In particular, we use a backward differentiation formula (BDF), adapted for use with a variable time step. The variable time step scheme controls the step size according to an estimated error E for the fields. The error estimation E is based on the difference between the solution obtained with a third and a second order scheme. The result of an integration at time $n+1$ is accepted if E is below a certain tolerance. Details on the step adjustment are found in [18].

BDFs are a particular case of multistep formulas which are *implicit*, thus the BDF scheme implies solving at each time step the problem (see [34]):

$$0 = \nabla \cdot \mathbf{u}^{n+1} \tag{30}$$

$$0 = \mathrm{Ra}\theta^{n+1}\vec{e_3} - \nabla P^{n+1} + \mathrm{div}\left(\frac{\nu(\theta^{n+1})}{\nu_0}(\nabla \mathbf{u}^{n+1} + (\nabla \mathbf{u}^{n+1})^T)\right) \tag{31}$$

$$\partial_t \theta^{n+1} = -\mathbf{u}^{n+1} \cdot \nabla \theta^{n+1} + \Delta \theta^{n+1}, \tag{32}$$

where $\partial_t \theta^{n+1}$ is replaced by a backward differentiation formula.

In [18], it has been proved that instead of solving the fully implicit scheme (30)-(32), a semi-implicit scheme can produce results with a similar accuracy and fewer CPU time requirements. The semi-implicit scheme approaches the nonlinear terms in equations (30)-(32) by assuming that the solution at time $n+1$ is a small perturbation $\tilde{Z}$ of the solution at time n; thus, $\mathbf{z}^{n+1} = \mathbf{z}^n + \tilde{Z}$. Once linear equations for $\tilde{Z}$ are derived, the equations are rewritten by replacing $\tilde{Z} = \mathbf{z}^{n+1} - \mathbf{z}^n$. The solution is obtained at each step by solving the resulting linear equation for variables in time $n+1$.

5 Results

5.1 Exploration of stationary solutions in the parameter space

In this section we explore how stationary solutions obtained at a low aspect ratio $\Gamma = 3.4$ for the system (1)-(3) depend on the parameters a and b of the viscosity law (6). We examine the shape and structure of the plumes in a range of Rayleigh numbers from $\mathrm{Ra} = 2500$ to $\mathrm{Ra} = 3500$.

We first consider that the parameter b is large: for instance, as large as 30. In this case, Figure 2(b) confirms that at the instability threshold the viscosity across the fluid layer is almost constant and equal to ν_0, no matter what the value of a may be. Thus, the viscosity transition becomes evident in the fluid once convection has settled in at Ra numbers well above the instability threshold. Figure 6(a) shows the plume pattern observed at $\mathrm{Ra} = 2500$ for $a = 0.1$; although values $a = 0.01$ and $a = 0.001$ are not displayed, they provide a very similar output. The plume is spout-shaped, with the tail of the plume nearly as large as the head. In the pattern, the two black contour lines mark temperatures between which the viscosity decays most rapidly. These correspond to the transition region in which the gradient of the viscosity law (6) is large. Thus one of the contours, the coldest one, fits the temperature θ_1 at which the viscosity has decayed by 5% from the maximum, *i.e.*, $\nu = 0.95\,\nu_0$, while the second addresses $\theta_2 = \theta_1 + \Delta\theta$ with temperature increment $\Delta\theta = 0.23$. The maximum viscosity decay rate always takes place at a constant temperature increment, since the decaying rate of the law (6) β, is the same through out all this study. At larger Rayleigh numbers, $\mathrm{Ra} = 3500$, Figure 6(b) shows that the head of the plume becomes more prominent. A comparison between Figure 6(b) and Figure 6(c) indicates that the large viscosity contrast favors the formation of a balloon-shaped plume, with a thinner tail and more prominent and rounded head. As regards the velocity fields, none of these patterns develop a stagnant lid at the surface for any of the viscosity contrasts a considered, even though the upper part corresponds to the region with maximum viscosity. This result is dissimilar to what is obtained in [64, 17]. In [17] it is argued that the cause of these differences could be attributed to the transition sharpness controled by β, which in this work has been considered to be smoother. Additionally, the results reported in [64] are obtained at larger viscosity contrasts, and the fact that these need to be large enough for the development of a stagnant lid has been addressed.

We now consider that the parameter b is small. As explained in Section 3, in this case the viscosity transition occurs at low Ra numbers, below the instability threshold of the fluid with constant viscosity ν_0. As low viscosity also implies diminishing the critical Ra number, the overall effect is that for small b the instability threshold is below that with constant viscosity ν_0, and the phase transition is perceived by weakly convective states. Figure

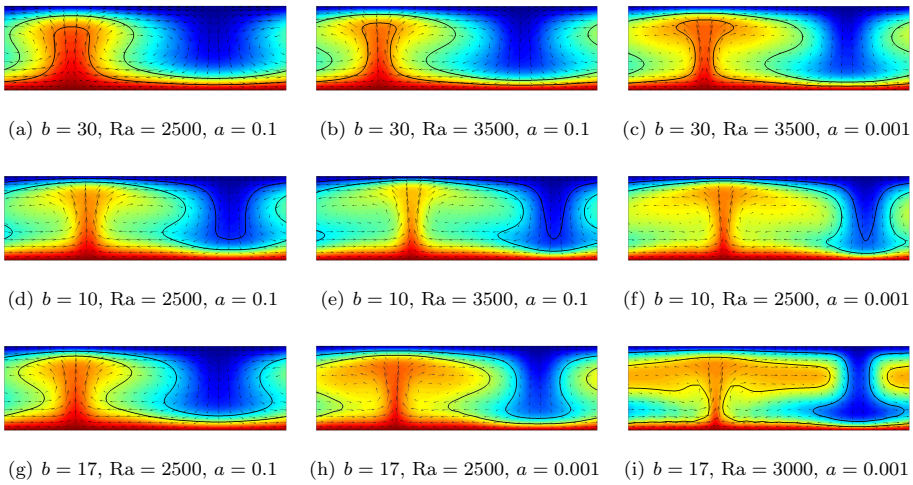

(a) $b = 30$, Ra $= 2500$, $a = 0.1$ (b) $b = 30$, Ra $= 3500$, $a = 0.1$ (c) $b = 30$, Ra $= 3500$, $a = 0.001$

(d) $b = 10$, Ra $= 2500$, $a = 0.1$ (e) $b = 10$, Ra $= 3500$, $a = 0.1$ (f) $b = 10$, Ra $= 2500$, $a = 0.001$

(g) $b = 17$, Ra $= 2500$, $a = 0.1$ (h) $b = 17$, Ra $= 2500$, $a = 0.001$ (i) $b = 17$, Ra $= 3000$, $a = 0.001$

Figure 6: (Color online). Plumes obtained for several values of the viscosity parameter b. The arrows indicate the velocity field, while the contour colors represent the temperature ranging from hot (bottom plate) to cold (upper plate). The two black contour lines indicate the temperatures between which viscosity decays most rapidly.

6(d) shows the structure of the plume obtained for $b = 10$ and $a = 0.1$ at Ra $= 2500$. The head tends to be spread over a wide area and the viscosity transition occurs at cold fluid zones away from the main plume. This pattern is rather similar to those obtained with $b = 5$ or $b = 1$, except that for smaller b values the tail of the plume tends to be thinner. Increasing the Ra number makes the tail of the plume thinner and spreads the head of the plume in the upper part, as reflected in Figure 6(e). On the other hand, high Ra numbers shift the viscosity transition towards colder temperature contours. As expected from the viscosity law (6), there is no Ra number at which the whole fluid layer is "melted", since this law always imposes that a transition occurs across the fluid layer. Figure 6(f) reports the effect of diminishing the viscosity contrast a to $a = 0.001$ at Ra $= 2500$. A mushroom-shaped plume with a thin tail and prominent head is observed. As before, none of these solutions develop a stagnant lid at the surface for any of the examined viscosity contrasts a.

Intermediate values such as $b = 17$ interpolate these extreme patterns. Figure 6(g) shows the evolution from Figure 6(d) to Figure 6(a) in which the black contour lines indicating the position of maximum viscosity decay converge towards the ascending plume boundary, thus highlighting its shape. The head of the plume shrinks and the tail strengthens. Diminishing a to the contrast 0.001 transforms the structure into a balloon-shaped plume (Figure 6(h)), while an increase in the Ra number spreads the head of the plume in the upper fluid towards a mushroom-shaped plume.

The structure of the observed plumes as a spout, balloon or mushroom shape follows the schematic profiles reported in [37]. In the limit of low b, our viscosity law –as reported in Section 3– converges towards the Arrehnius law used by these authors, and the plume shapes reported there are similar to ours. However, a detailed comparison between both works is not possible as unlike these authors we include the Ra number in the viscosity law, since this provides a better expression of the realistic situation in which the increment of the Ra number is performed by increasing the temperature differences between the bottom and upper surfaces. Other viscosity laws, such as the exponential law reported in [18] provide different plume structures, which are mainly spout shaped.

The results reported in this section are obtained with expansions ($L \times M = 37 \times 44$) except that in Figure 6(c), which corresponds to ($L \times M = 47 \times 42$). Similarly to what is reported in [18]. The validity of these expansions is decided by ensuring that it provides accuracy in the eigenvalue along the neutral direction due to the SO(2) symmetry, which is always 0. This eigenvalue is lost if the expansions employed are insufficiently large, because badly resolved basic states present noisy structures either at the fields themselves or at their derivatives, and both contribute to the stability problem (26)-(28).

5.2 Bifurcation diagrams and time dependent solutions

Solutions to the system (1)-(3) experience bifurcations depending on the aspect ratio and on the Rayleigh number. We now describe how these solutions vary along the dotted lines enhanced in Figure 4 for parameters

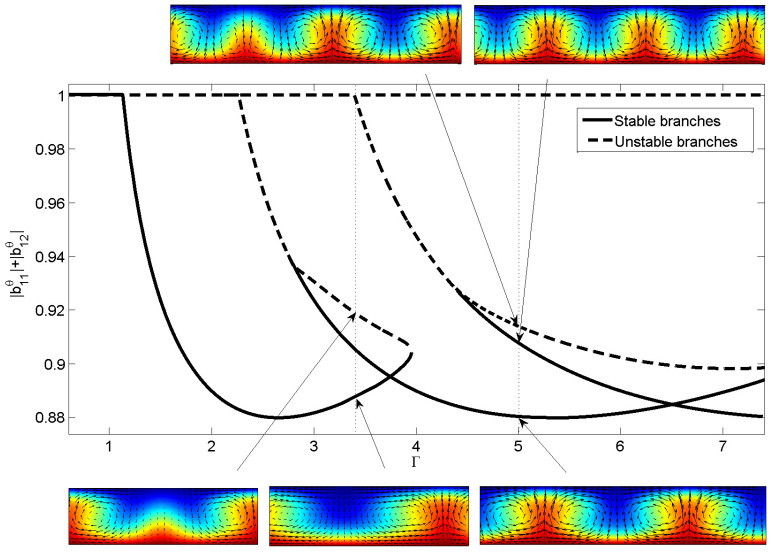

Figure 7: (Color online). Bifurcation diagram as a function of the aspect ratio at Ra = 1300 for a fluid with viscosity dependent on temperature ($b = 10$, $a = 0.1$). Stationary solutions are displayed at different Ra numbers, which are highlighted by vertical lines. The arrows tag the branch points corresponding to the disclosed patterns. The dashed branches are unstable, while the solid ones are stable.

$\mu = 0.0146$ and $b = 10$. We consider for a the choices 0.1 and 0.01.

Figure 7 shows the branch bifurcation diagram as a function of the aspect ratio for Rayleigh number Ra = 1300 and $a = 0.1$. Branches are obtained by representing along the vertical axis the sum of the absolute value of two relevant coefficients in the expansion of the temperature field, b^θ_{11} and b^θ_{12}. Solid lines stand for stable branches, while dashed lines are the unstable ones. The horizontal line at $|b^\theta_{11}| + |b^\theta_{12}| = 1$ corresponds to the trivial conductive solution. At a low aspect ratio, the stable branch is that with wave number $m = 1$, and at a higher aspect ratio the stable solutions increase their wave number to $m = 2$ and $m = 3$. The unstable branch ending up with a saddle-node bifurcation and connecting the $m = 1$ with the $m = 2$ branch corresponds to a mixed mode.

Stationary stable and unstable solutions, obtained at the positions indicated by arrows, are pictured. No stagnant lid appears at the surface for any of the aspect ratios considered. The expansion orders required by this figure to ensure accuracy are not the same along all branches. We have guaranteed that for successive orders expansions the amplitude values displayed on the vertical axis of the bifurcation diagrams are preserved. A rule of thumb is that high modes obtained at larger aspect ratios require higher expansions. Thus while for mode $m = 1$ expansions ($L \times M = 37 \times 44$) are sufficient, for $m = 2$ and $m = 3$ at larger aspect ratios expansions are increased up to ($L \times M = 61 \times 44$).

Bifurcations are further analyzed at three different aspect ratios as a function of the Rayleigh number. Among the many possible choices for the aspect ratios, we consider occurrences at which the existence of solutions related to symmetries are found, such choices thereby serving our purpose of highlighting the importance of symmetries in fluids with viscosity dependent on temperature. Figure 8 represents the branching obtained at $\Gamma = 3.4$ for $a = 0.1$. The pictured plumes, which are computed for a rather low Rayleigh number, Ra = 1500, are spout-shaped, with the tail of the plume nearly as large as the head. As already reported in the previous section for increasing Ra numbers, plumes become balloon-shaped and beyond that mushroom-shaped. No stagnant lid is observed at any Ra number. Several branches are distinguished. The branch related to mode $m = 1$ arises at the lowest Ra number and is stable in the whole range displayed. Mode $m = 2$ emerges at Ra ~ 860 from the unstable conductive solution through an unstable branch, which becomes stable through a pitchfork bifurcation at Ra ~ 890. Results at this aspect ratio are obtained with expansions ($L \times M = 37 \times 44$).

This simple diagram with simple stationary solutions obtained at a low aspect ratio is in contrast to those with more complex solutions obtained at a larger aspect ratio. Figure 9 represents the bifurcations obtained at $\Gamma = 6.9$ as a function of Ra for $a = 0.01$. Figure 9(a) examines the Ra interval from 800 to 1300. In this range several stationary solutions are portrayed both stable and unstable. At Ra ~ 1290, a Hopf bifurcation

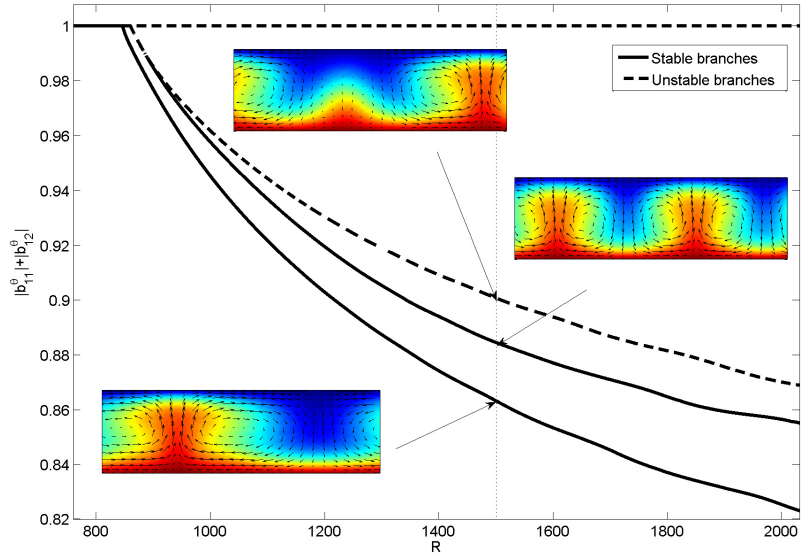

Figure 8: (Color online). Bifurcation diagram as a function of the Rayleigh number for a fluid with viscosity dependent on temperature ($b = 10$, $a = 0.1$) at $\Gamma = 3.4$. Stationary solutions are displayed at the Ra number, which is highlighted with the vertical line. The arrows tag the branch points corresponding to the disclosed patterns.The dashed branches are unstable, while the solid ones are stable.

occurs at the branch of mode $m = 3$ (see Figure 9(b)). After the bifurcation, a traveling wave is found, as illustrated in the phase portrait represented at Ra = 1300. The solution evolves in time by traveling towards the left. This breaks the symmetry $x \to -x$. However, the right traveling solution obtained by the symmetry transformation also exists, as expected from equivariant bifurcation theory [16]. See [1] for further details. The presence of traveling waves after a Hopf bifurcation has been reported in diverse contexts in under the presence of the O(2) symmetry [2, 66, 21, 16], and here they are reported in the context of convection with variable viscosity. At larger Ra numbers, up to Ra $\sim$ 1320, the traveling wave persists, while its frequency increases. A stable fixed point with wavenumber $m = 3$ is found in the range Ra $\sim 1340 - 1380$. A cycle limit appears at around Ra $\sim$ 1400. In this regime, the time-dependent solution consists of plumes that weakly oscillate in the horizontal direction around their vertical axis of symmetry. See [1] for further details. Close to Ra $\sim$ 1416, a stable branch of fixed points emerges, which is visualized at Ra $\sim$ 1525. It shows the presence of plumes that are non-uniformly distributed along the horizontal coordinate: two close plumes, which are asymmetric around their vertical axis, and a third one that maintains its symmetry. None of the described solutions develop stagnant lids at the surface. At low Ra numbers (*i.e.* Figure 9(a)) results are obtained with expansions ($L \times M = 47 \times 44$), while for higher Ra numbers (*i.e.* Figure 9(b)) results are obtained with expansions ($L \times M = 61 \times 44$).

Figure 10 shows the bifurcation diagram obtained at $\Gamma = 7.4$ as a function of Ra for $a = 0.1$. The mode $m = 3$ branch, marked with a solid black line, emerges at Ra $\sim$ 794. Figure 10(b) shows that at $R \sim 2190$ the branch undergoes a Hopf bifurcation. Beyond this point, solutions embedded in a projection over the coefficient space are represented at the R values marked with vertical dotted lines. A limit cycle is observed at Ra = 2210 just above the bifurcation point. Its projection over the coefficient space displays a point at every time step of the time series. The solution appears to reside in the neighbourhood of a heteroclinic connection between two fixed points as it evolves into a quasi-stationary regime –near the large density of points– followed by a rapid transition to a new quasi-stationary regime. The two fixed points between which the solution oscillates are similar to the non-uniformly distributed plumes described in the previous paragraph (see [1] for further details). A solution is found at Ra = 2300 that has a time-dependence in which the block of plumes shifts irregularly along the horizontal direction, towards both the left and the right (see [1]). For increasing Ra numbers, the horizontal motion persists, but the oscillation becomes more regular and pattern displacements along the $x-$coordinate are gradually reduced. This is verified through simulations at Ra = 2350 and at Ra = 2400 (see [1]). The diagram displayed in Figure 10(a) shows a gray solid line associated to a mode $m = 2$ stable branch that emerges by means of a saddle node bifurcation jointly with an unstable branch. An irregular pattern obtained at Ra = 1800 for the unstable branch is included in this diagram. Once again, none of the solutions described at this aspect

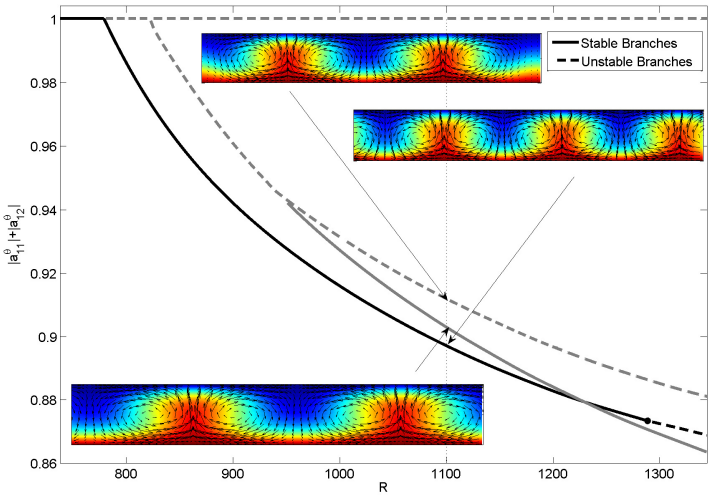

(a)

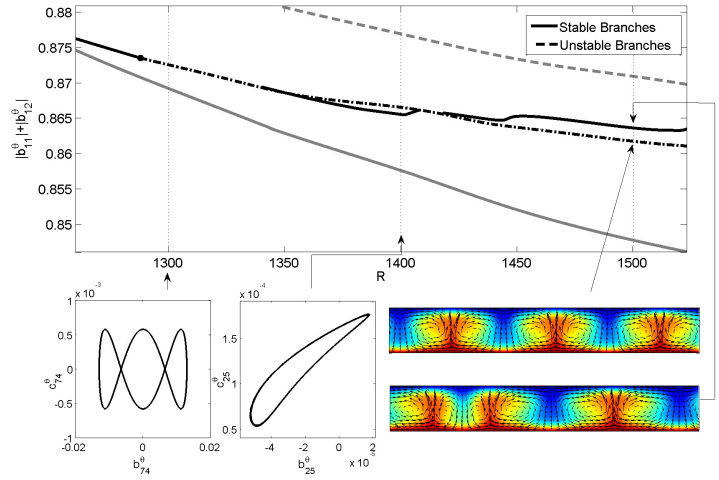

(b)

Figure 9: (Color online). Bifurcation diagrams as a function of the Rayleigh number for a fluid with viscosity dependent on temperature ($b = 10$, $a = 0.01$) at $\Gamma = 6.9$. The dashed branches correspond to stationary unstable solutions, while solid branches correspond to stationary stable ones. The gray lines indicate spatial patterns with period 2, while the black ones are for period 3 patterns. a) Rayleigh number in the range 800-1300. Stationary solutions are displayed at the Ra number highlighted with the vertical line. Arrows tag the branch points corresponding to the disclosed patterns; b) Rayleigh number in the range 1250-1500. Stationary solutions are displayed at the Ra number, which is highlighted by the vertical line. The arrows tag the branch points corresponding to the disclosed patterns. Two additional vertical lines highlight the Ra = 1300 and Ra = 1400 numbers at which time dependent solutions are found. These are displayed as a time series projected on the coefficient space (for a description see the text and [1]).

ratio has a stagnant lid at the surface. Results in this figure are obtained with different order expansions. At low R number expansions ($L \times M = 47 \times 42$) are sufficient while for higher Ra numbers they are increased up to ($L \times M = 61 \times 44$) and even to ($L \times M = 101 \times 44$).

The time dependent solutions reported in Figures 9 and 10 in many respects resemble those described for the Kuramoto-Sivashinsky (KS) equation [21, 35] in the presence of the O(2) symmetry, which also report

the presence of traveling waves and heteroclinic cycles. The KS equation is proposed in order to describe thermal diffusive instabilities in flame fronts [57], and while apparently this setting is rather different to ours, the similitude between solutions suggest that the abrupt changes in the viscosity could define a similar kind of front to those observed in flame propagation phenomena. On the other hand, similar solutions have been found in 3D convection with constant viscosity in the presence of the O(2) symmetry [39, 19], thus confirming the determining role of the symmetry in the dynamics.

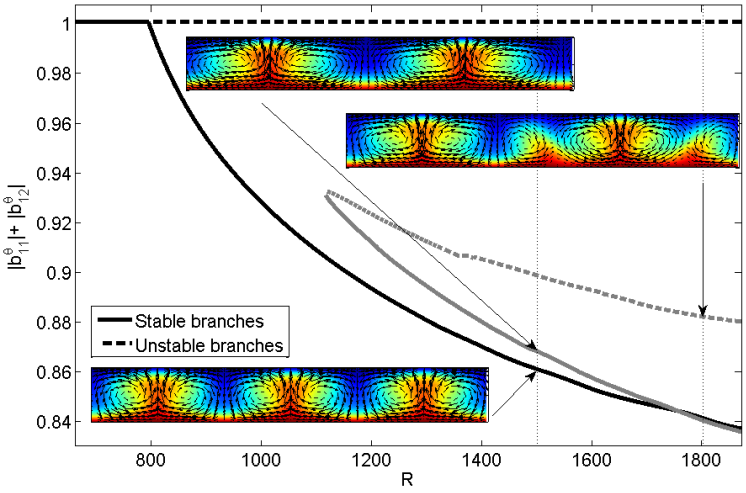

(a)

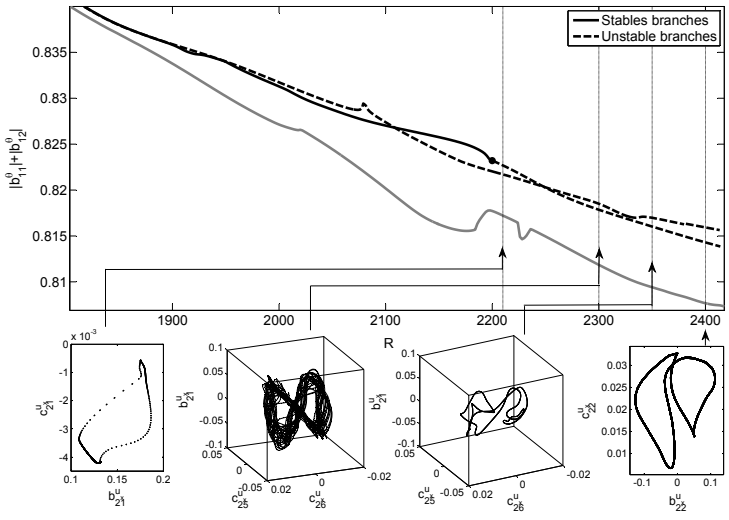

(b)

Figure 10: (Color online). Bifurcation diagrams as a function of the Rayleigh number for a fluid with viscosity dependent on temperature ($b = 10$, $a = 0.1$) at $\Gamma = 7.4$. The dashed branches correspond to stationary unstable solutions, while solid branches correspond to stationary stable ones. The gray lines stand for spatial patterns with period 2 while the black ones are for period 3 patterns. a) Rayleigh number in the range 700-1800. Stationary solutions are displayed at the Ra number, which is highlighted by the vertical line. The arrows tag the branch points corresponding to the disclosed patterns; b) Rayleigh number in the range 1800-2500. Vertical lines highlight the Ra numbers at which time dependent solutions are found. These are 2210, 2300, 2350 and 2400. These are displayed as a time series projected on the coefficients space (for a description see the text and [1]).

6 Conclusions

This article addresses the study of a convection problem with temperature-dependent viscosity in the presence of the O(2) symmetry. In particular, the considered viscosity law represents a viscosity transition at a certain temperature interval around a temperature of transition. This is a problem of great interest for its many applications in geophysical and industrial flows and in this work the focus is on exploring the impact of symmetry on the solutions displayed by system.

Our results report the influence on parameters a and b of the viscosity law on the morphology of the plumes at a low aspect ratio ($\Gamma = 3.4$). It is shown that if the temperature of transition is well above the instability threshold of a fluid with constant viscosity ν_0, *i.e*, b is large, plumes tend to be thicker and show spout-like shapes. Increasing the Ra number induces their evolution towards balloon-shaped plumes, and this effect is more pronounced for high viscosity contrasts (small a). At low b values plumes are thinner, and the head of the plume tends to spread in a mushroom-like shape in the upper part of the fluid.

We explore bifurcations both for a fixed Ra number as a function of the aspect ratio, and bifurcations at three fixed aspect ratios as a function of the Ra number. No stagnant lid regime is observed in any of the physical conditions analyzed. Among the stationary solutions obtained along the bifurcation branches, one of the more interesting stable patterns consists of the non-uniformly distributed plumes that break symmetry along their vertical axis.

We also find that, for the higher Rayleigh numbers explored, at a high aspect ratio several rich dynamics appear. As already reported in classical convection problems, we find dynamical phenomena fundamentally related to the presence of symmetry, such as traveling waves, oscillating solutions in the neighborhood of heteroclinic connections and chaotic regimes characterized by "phase" drifts along the horizontal direction linked to the SO(2) symmetry.

Acknowledgements

We are grateful to CESGA and to CCC of Universidad Autónoma de Madrid for computing facilities. This research is supported by the Spanish Ministry of Science under grants MTM2008-03754, MTM2011-26696 and MINECO: ICMAT Severo Ochoa project SEV-2011-0087.

References

[1] See supplemental material. `http://link.aps.org/supplemental/10.1103/PhysRevE.88.043005`.

[2] D. Armbruster, J. Guckenheimer, and P. Holmes. Heteroclinic cycles and modulated travelling waves in systems with o(2) symmetry. *Physica D*, 29(257-282), 1988.

[3] D. Armbruster, J. Guckenheimer, and P. Holmes. Kuramoto-sivashinsky dynamics on the center-unstable manifold. *SIAM Journal on Applied Mathematics*, 49(3):676–691, 1989.

[4] P. Assemat, A. Bergeon, and E. Knobloch. Nonlinear marangoni convection in circular and elliptical cylinders. *Physics of Fluids*, 19:104101, 2007.

[5] B. Blankenbach, F. H. Busse, U. Christensen, L. Cserepes, D. Gunkel, U. Hansen, H. Harder, G. Jarvis, M. Koch, G. Marquart, D. Moore, P. Olson, H.Schmeling, and M. Schnaubelt. A benchmark comparison for mantle convection codes. *Geophys. J. Int.*, 98:23–38, 1989.

[6] J. R. Booker. Thermal convection with strongly temperature-dependent viscosity. *J. Fluid Mech.*, 76:741–754, 1976.

[7] A. Bottaro, P. Metzener, and M. Matalon. Onset and two-dimensional patterns of convection with strongly temperature-dependent viscosity. *Physics of Fluids*, 4(655-663), 1992.

[8] G. Brandeis and C. Jaupert. On the interaction between convection and crystallization in cooling magma chambers. *Earth Planet. Sci. Lett.*, 77:345–361, 1986.

[9] G. Brandeis and B. D. Marsh. The convective liquidus in a solidifying magma chamber: a fluid dynamic investigation. *Nature*, 339:613–616, 1989.

[10] H. P. Bunge, M. A. Richards, and J. R. Baumgardner. Effect of depth-dependent viscosity on the planform of mantle convection. *Nature*, 436:436–438, 1996.

[11] F. H. Busse. Pattern of convection in spherical shells. *J. Fluid Mech.*, 72:65–85, 1975.

[12] F. H. Busse and N. Riahi. Pattern of convection in spherical shells ii. *J. Fluid Mech.*, 123:283–391, 1982.

[13] F. Capone and M. Gentile. Nonlinear stability analysis of convection for fluids with exponentially temperature-dependent viscosity. *Acta Mechanica*, 107:53–64, 1994.

[14] P. Chossat. Bifurcation and stability of convective flows in a rotating or not rotating spherical shell. *SIAM Journal on Applied Mathematics*, 37:624–647, 1975.

[15] S. M. Copley, A. F. Giamel, S. M. Johnson, and M. F. Hornbecker. The origin of freckles in unidirectionally solidified castings. *Metall. Trans.*, 1:2193–2204, 1970.

[16] J. D. Crawford and E. Knobloch. Symmetry and symmetry-breaking bifurcations in fluid dynamics. *Annu. Rev. Fluid Mech.*, 23(341-387), 1991.

[17] J. Curbelo and A. M. Mancho. Plate-like convection induced by symmetries in fluids with temperature-dependent viscosity. *Preprint. arxiv: 1306.2921*, 2013.

[18] J. Curbelo and A. M. Mancho. Spectral numerical schemes for time-dependent convection with viscosity dependent on temperature. *Communications in Nonlinear Science and Numerical Simulations*, 19, 2014.

[19] P.C. Dauby, P. Colinet, and D. Johnson. Theoretical analysis of a dynamic thermoconvective pattern in a circular container. *Phys. Rev. E*, 61:2663, 2000.

[20] G.F. Davies. *Dynamic Earth. Plates, Plumes and Mantle convection.* Cambridge University Press, 2001.

[21] S. P. Dawson and A. M. Mancho. Collections of heteroclinic cycles in the Kuramoto-Sivashinsky equation. *Physica D: Nonlinear Phenomena*, 100(3-4):231–256, 1997.

[22] J. I. Diaz and B. Straughan. Global stability for convection when the viscosity has a maximum. *Continuum Mech. Thermodyn.*, 16:347–352, 2004.

[23] F. Dubuffet, D. A. Yuen, and M. Rabinowicz. Effects of a realistic mantle thermal conductivity on the patterns of 3d convection. *Earth Planet. Sci. Lett.*, 171:401–409., 1999.

[24] F. Dubuffet, D. A. Yuen, and T. K. B. Yanagawa. Feedback effects of variable thermal conductivity on the cold downwellings in high rayleigh number convection. *Geophys. Res. Lett.*, 27:2981–2984, 2000.

[25] J. D. Dufek and G. W. Bergantz. Transient two-dimensional dynamics in the upper conduit of a rhyolitic eruption: A comparison of the closure models for the granular stress. *J. Volcanol. Geotherm. Res*, 143:113–132, 2005.

[26] M. Field. Equivariant dynamical systems. *Trans. Am. Math. Soc.*, 259(185-205), 1980.

[27] G. R. Fulford and P. Broadbridge. *Industrial Mathematics.* Australian Mathematical Society Lecture Series 16. Cambridge University Press, 2002.

[28] M. Golubitsky and D.G. Schaeffer. Bifurcation with o(3) symmetry including applications to the benard problem. *Communs. Pure. Appl. Math.*, 35:81–11, 1982.

[29] M. Golubitsky and D.G. Schaeffer. *Singularities and Groups in Bifurcation Theory*, volume 1. Springer, 1985.

[30] M. Golubitsky and I. Stewart. Symmetry and stability in taylor-couette flow. *SIAM J. Math. Anal.*, 17(249-288), 1986.

[31] M. Golubitsky, I. Stewart, and D.G. Schaeffer. *Singularities and Groups in Bifurcation Theory*, volume 2. Springer, 2nd edition, 2000.

[32] M. Golubitsky, J. W. Swift, and E. Knobloch. Symmetries and pattern selection in rayleigh-benard convection. *Physica D*, 10:249–276, 1984.

[33] J. Guckenheimer and P. Holmes. Structurally stable heteroclinic cycles. *Math. Proc. Cambridge Philos. Soc.*, 103(189-192), 1988.

[34] E. Hairer, S.P. Norsett, and G. Wanner. *Solving Ordinary Differential Equations I. Nonstiff Problems.* Springer, 2009.

[35] J. M. Hyman, B. Nicoalaenko, and S. Zaleski. Order and complexity in the kuramoto-sivansinsky model of weakly turbulent interfaces. *Physica D*, 23(1-3):265–292, 1986.

[36] E. Ihrig and M. Golubitsky. Pattern selection with o(3) symmetry. *Physica D*, 12:1–33, 1984.

[37] L. H. Kellogg and S. D. King. The effect of temperature dependent viscosity on the structure of new plumes in the mantle: Results of a finite element model in a spherical, axisymmetric shell. *Earth and Planetary Science Letters*, 148:13–26, 1997.

[38] P. Kolodner, D. Bensimon, and C. M. Surko. Traveling-wave convection in an annulus. *Phys. Rev. Lett.*, 60(1):723–726, 1988.

[39] D. Krmpotic, B. Echebarria, and C. Perez-Garcia. Resonant interactions in benard-marangoni convection in cylindrical containers. *Physica D*, 99(4):487–502, 1997.

[40] D. Krmpotic, G. B. Mindlin, and C. Perez-Garcia. Benard-marangoni convection in square containers. *Phys. Rev. E*, 54(4):3609–3613, 1996.

[41] M. Krupa. Bifurcations of relative equilibria. *SIAM J. Math. Anal.*, 21:1453–1486, 1990.

[42] L. G. Mastin. Insights into volcanic conduit flow from an open-source numerical model. *Geochem. Geophys. Geosyst.*, 3:1037, 2002.

[43] G. B. Mindlin, T. Ondarcuhu, H. L. Mancini, C. Perez-Garcia, and A. Garcimartin. Comparison of data from bernard-marangoni convection in a square container with a model-based on symmetry arguments. *International Journal of Bifurcation and Chaos*, 4(5):1121–1133, 1994.

[44] L. N. Moresi and V. S. Solomatov. Numerical investigation of 2D convection with extremely large viscosity variations. *Physics of Fluids*, 7(9):2154–2162, 1995.

[45] M. Ogawa, G. Schubert, and A. Zebib. Numerical simulations of three-dimensional convection in a fluid with strongly temperature dependent viscosity. *J. Fluid Mech.*, 233:299–328, 1991.

[46] T. Ondarcuhu, G. B. Mindlin, H. L. Mancini, and C. Perez-Garcia. Dynamic patterns in bernard-marangoni convection in a square container dynamic patterns in bernard-marangoni convection in a square container dynamic patterns in bernard-marangoni convection in a square container dynamic patterns in bernard-marangoni convection in a square container. *Phys. Rev. Lett.*, 70(25):3892–3895, 1993.

[47] E. Palm, T. Ellingsen, and B. Gjevik. On the occurrence of cellular motion in bénard convection. *J. Fluid Mech.*, 30(651-661), 1967.

[48] F. Pla, A. M. Mancho, and H. Herrero. Bifurcation phenomena in a convection problem with temperature dependent viscosity at low aspect ratio. *Physica D: Nonlinear Phenomena*, 238(5):572–580, 2009.

[49] D. Rand. Dynamics and symmetry: predictions for modulated waves in rotating fluids. *Arch. Ration. Mech. Anal.*, 79(1):1–38, 1982.

[50] J. T Ratcliff, P.J. Tacley, G. Schubert, and A. Zebib. Transitions in thermal convection with strongly variable viscosity. *Physics of the Earth and Planetary Interiors*, 102:201–202, 1997.

[51] J. Revenaugh and B. Parsons. Dynamic topography and gravity anomalies for fluid layers whose viscosity varies exponencially with depht. *Geophys. J. R Astrr. Soc.*, 90:349–368, 1987.

[52] L. Richardson and B. Straughan. A nonlinear stability analysis for convection with temperature–dependent viscosity. *Acta Mechanica*, 97:41–49, 1993.

[53] F. M. Richter, H. C. Nataf, and S.F. Daly. Heat transfer and horizontally averaged temperature of convection with large viscosity variation. *J. Fluid Mech*, 129:173–192, 1983.

[54] D. Ruelle. Bifurcations in the presence of a symmetry group. *Arch. Ration. Mech. Anal.*, 51:136–152, 1973.

[55] J. R. Sarazin and A. Hellawell. Channel formation in pb-sn, pb-sb and pb-sn-sb alloys and comparison with the system nh4cl-h2o. *Metall. Trans.*, 19A:1861–1871, 1988.

[56] J. Schmalzl, M. Breuer, and U. Hansen. On the validity of two-dimensional numerical approaches to time-dependent thermal convection. *Europhysics Letters*, 67(3):390–396, 2004.

[57] G. I. Sivashinky. On flame propagation under conditions of stoichiometry. *SIAM Journal on Applied Mathematics*, 39(1):67–82, 1980.

[58] V. S. Solomatov and L. N. Moresi. Stagnant lid convection on Venus. *J. Geophys. Res*, 101:4737–4753, 1996.

[59] V. S. Solomatov and L. N. Moresi. Three regimes of mantle convection with non-newtonian viscosity and stagnant lid convection on the terrestrial planets. *Geophysical Research Letters*, 24(15):1907–1910, 1997.

[60] V.S. Solomatov. Localized subcritical convective cells in temperature-dependent viscosity fluids. *Phys. Earth Planet. Inter.*, 200-201:63–71, 2012.

[61] V.S. Solomatov and A.C. Barr. Onset of convection in fluids with strongly temperature-dependent, power-law viscosity 2. dependence on the initial perturbation. *Phys. Earth Planet. Inter.*, 165(1-2):1–13, 2007.

[62] I. Stewart and A. S. Hill. Three-mode interactions with o(2) symmetry and a model for taylor-couette flow. *Dyn. Stab. Sys.*, 6:267–339, 1991.

[63] K. E. Torrance and D. L. Turcotte. Thermal convection wiith large viscosity variations. *J. Fluid Mech.*, 47(113), 1971.

[64] M. Ulvrová, S. Labrosse, N. Coltice, P. Raback, and P.J. Tackley. Numerical modelling of convection interacting with a melting and solidification front: Application to the thermal evolution of the basal magma ocean. *Physics of the Earth and Planetary Interiors*, 206-207:51–66, 2012.

[65] A. Vaidya and R. Wulandana. Non-linear stability for convection with quadratic temperature dependent viscosity. *Math. Meth. Appl. Sci.*, 29:1555–1561, 2006.

[66] S. A. van Gilsa and J. Mallet-Paret. Hopf bifurcation and symmetry: travelling and standing waves on the circle. *Proceedings of the Royal Society of Edinburgh: Section A*, 104(3-4):279–307, 1986.

[67] D. B. White. The planforms and onset of convection with a temperature dependent viscosity. *J. Fluid. Mech.*, 191:247–286, 1988.

[68] T.K.B. Yanagawa, M. Nakada, and D.A. Yuen. A simplified mantle convection model for thermal conductivity stratification. *Phys. Earth Planet. Inter.*, 146:163–177, 2004.

3.3. Symmetry and plate-like convection in fluids with temperature-dependent viscosity

Coauthors: Ana M. Mancho

Abstract: We explore the instabilities developed in a fluid in which viscosity depends on temperature. In particular, we consider a dependency that models a very viscous (and thus rather rigid) lithosphere over a convecting mantle. To this end, we study a 2D convection problem in which viscosity depends on temperature by abruptly changing its value by a factor of 400 within a narrow temperature gap. We conduct a study which combines bifurcation analysis and time-dependent simulations. Solutions such as limit cycles are found that are fundamentally related to the presence of symmetry. Spontaneous plate-like behaviors that rapidly evolve towards a stagnant lid regime emerge sporadically through abrupt bursts during these cycles. The plate-like evolution alternates motions towards either the right or the left, thereby introducing temporary asymmetries on the convecting styles. Further time-dependent regimes with stagnant and plate-like lids are found and described.

Reference: (Editor's Pick) [27] J. Curbelo , A. M. Mancho. Symmetry and plate-like convection in fluids with temperature-dependent viscosity. Physics of Fluids **26**, 016602 (2014)

PHYSICS OF FLUIDS **26**, 016602 (2014)

Symmetry and plate-like convection in fluids with temperature-dependent viscosity

Jezabel Curbelo[1,2] and Ana M. Mancho[1]
[1]*Instituto de Ciencias Matemáticas (CSIC-UAM-UCM-UC3M), C/ Nicolás Cabrera, 13-15, 28049 Madrid, Spain*
[2]*Departamento de Matemáticas, Universidad Autónoma de Madrid, Facultad de Ciencias, módulo 17, 28049 Madrid, Spain*

(Received 12 June 2013; accepted 22 November 2013; published online 10 January 2014)

We explore the instabilities developed in a fluid in which viscosity depends on temperature. In particular, we consider a dependency that models a very viscous (and thus rather rigid) lithosphere over a convecting mantle. To this end, we study a 2D convection problem in which viscosity depends on temperature by abruptly changing its value by a factor of 400 within a narrow temperature gap. We conduct a study which combines bifurcation analysis and time-dependent simulations. Solutions such as limit cycles are found that are fundamentally related to the presence of symmetry. Spontaneous plate-like behaviors that rapidly evolve towards a stagnant lid regime emerge sporadically through abrupt bursts during these cycles. The plate-like evolution alternates motions towards either the right or the left, thereby introducing temporary asymmetries on the convecting styles. Further time-dependent regimes with stagnant and plate-like lids are found and described. © *2014 AIP Publishing LLC*. [http://dx.doi.org/10.1063/1.4850296]

I. INTRODUCTION

Rayleigh-Bénard convection is the classic example of thermal convection.[1] In these systems, under certain critical conditions, small fluctuations lead to massive reorganization of the convective motions.[2–5] This is a characteristic phenomenon of open systems that transfer energy and that are modelled by nonlinear equations.

The internal energy of the planetary interiors is dissipated by convective processes, thus convection plays a crucial role in the evolution of the planet. Convective styles in planetary interiors are different from Rayleigh-Bénard convection. For instance, plate tectonics, which is distinctive of the Earth,[6] is the surface manifestation of convection in the Earth's mantle. Other bodies in the solar system, such as the Moon, Venus or Mars do not exhibit plate tectonics and present other convection expressions with a stagnant lithosphere.[7,8] Different physical justifications exist for the diverse types of convection: layered convection, for instance, is due to endothermic phase changes in the minerals that constitute the mantle interior.[9] The mantle is compressible due to changes in density, which increases towards the Earth interior. Numerical analysis of compressible convection indicates that density stratification has a stabilizing effect,[10] produces upwelling plumes weaker than those downwelling and influences the thermal boundary layer.[11] The dependence of conductivity on temperature introduces new nonlinearities into the heat equation, which may lead to diverse dynamics.[12] When conductivity decreases with temperature, convection becomes more chaotic and time-dependent.[13,14] Thermal conductivity variation has generally been less studied than that of viscosity, as the latter is much stronger in the Earth's mantle. Large viscosity contrasts in fluids with temperature-dependent viscosity lead to stagnant lid convection.[15,16] Regarding the subduction initiation, numerical results[17–20] suggest that this is only possible if the stiff upper layers of the lithosphere are weakened by brittle fracture. Several mechanisms have been proposed for driving the motion of the lithospheric plates. Forsyth and Uyeda,[21] for instance, conclude that plate-like motion

Symmetry and plate-like convection in fluids with temperature-dependent viscosity

Jezabel Curbelo[1,2], Ana M. Mancho[1]
[1]Instituto de Ciencias Matemáticas (CSIC-UAM-UCM-UC3M),
C/ Nicolás Cabrera, 13-15, 28049 Madrid, Spain
[2]Departamento de Matemáticas, Universidad Autónoma de Madrid,
Facultad de Ciencias, módulo 17, 28049, Madrid, Spain

February 10, 2014

Abstract

We explore the instabilities developed in a fluid in which viscosity depends on temperature. In particular, we consider a dependency that models a very viscous (and thus rather rigid) lithosphere over a convecting mantle. To this end, we study a 2D convection problem in which viscosity depends on temperature by abruptly changing its value by a factor of 400 within a narrow temperature gap. We conduct a study which combines bifurcation analysis and time-dependent simulations. Solutions such as limit cycles are found that are fundamentally related to the presence of symmetry. Spontaneous plate-like behaviors that rapidly evolve towards a stagnant lid regime emerge sporadically through abrupt bursts during these cycles. The plate-like evolution alternates motions towards either the right or the left, thereby introducing temporary asymmetries on the convecting styles. Further time-dependent regimes with stagnant and plate-like lids are found and described.

1 Introduction

Rayleigh-Bénard convection is the classic example of thermal convection [1]. In these systems, under certain critical conditions, small fluctuations lead to massive reorganization of the convective motions [2, 3, 4, 5]. This is a characteristic phenomenon of open systems that transfer energy and that are modelled by nonlinear equations. The internal energy of the planetary interiors is dissipated by convective processes, thus convection plays a crucial role in the evolution of the planet. Convective styles in planetary interiors are different from Rayleigh-Bénard convection. For instance, plate tectonics, which is distinctive of the Earth [6], is the surface manifestation of convection in the Earth's mantle. Other bodies in the solar system, such as the Moon, Venus or Mars do not exhibit plate tectonics and present other convection expressions with a stagnant lithosphere [7, 8]. Different physical

justifications exist for the diverse types of convection: layered convection, for instance, is due to endothermic phase changes in the minerals that constitute the mantle interior [9]. The mantle is compressible due to changes in density, which increases towards the Earth interior. Numerical analysis of compressible convection indicates that density stratification has a stabilizing effect [10], produces upwelling plumes weaker than those downwelling and influences the thermal boundary layer [11] . The dependence of conductivity on temperature introduces new nonlinearities into the heat equation, which may lead to diverse dynamics [12]. When conductivity decreases with temperature, convection becomes more chaotic and time-dependent [13, 14]. Thermal conductivity variation has generally been less studied than that of viscosity, as the latter is much stronger in the Earth's mantle. Large viscosity contrasts in fluids with temperature-dependent viscosity lead to stagnant lid convection [15, 16]. Regarding the subduction initiation, numerical results [17, 18, 19, 20] suggest that this is only possible if the stiff upper layers of the lithosphere are weakened by brittle fracture. Several mechanisms have been proposed for driving the motion of the lithospheric plates. Forsyth and Uyeda [21], for instance, conclude that plate-like motion is produced by the sinking slab that pulls the plate in the subduction process due to an excess of lithosphere density.

Finding the impact of the different physical properties present in the mantle on its convection styles is an important goal of research into planetary interiors. In this context, our focus is on examining the instabilities found in a 2D fluid in the presence of the O(2) symmetry which contemplates a phase transition similar to a melting-solidification processes. In particular, we consider a highly viscous layer (lithosphere) over a fluid mantle which is modeled with a viscosity that changes abruptly by a factor of 400, in a narrow temperature gap at which magma melts. In phase transitions, other fluid properties in addition to viscosity may change abruptly, such as density or thermal diffusivity. However, in this study we confine ourselves solely to the effects due to the variability of viscosity, since consideration of the effect of simultaneous variations on all the properties prevents a focused understanding of the exact role played by each one of these properties. Viscosity is a measure of fluid resistance to gradual deformation, and in this sense highly viscous fluids are more likely to behave rigidly when compared to less viscous fluids. When examining the proposed transition with temperature, we focus on the global fluid motion when some parts of this motion tend to be more rigid than others. By disregarding the variations on density in this transition, we move away from instabilities caused by abrupt density changes such as the Rayleigh Taylor instability, in which a denser fluid over a lighter one tends to penetrate it by forming a fingering pattern. A recent article by M. Ulvrová *et al.* [22] deals with a problem similar to the one we address here, but takes into account variations in both density and viscosity. Thermal conductivity effects are related to the relative importance of heat advection versus diffusion. Diffusive effects are therefore important at large conductivity, while heat advection by fluid particles is dominant at low conductivity. The contrasts arising from these variations are beyond the scope of our work and are thus disregarded herein.

In our setting we show that convective processes exist which include plate-like motions that alternate in time with stagnant-lid regimes. Some of these transitions include bursts in which the solution releases energy to accommodate different spatial patterns. These solutions are mathematically related to limit cycles, which are persistent solutions in the presence of the O(2) symmetry [23, 24, 25] which is also found in this problem. There exist numerous novel dynamical phenomena in fluids that are fundamentally related to the presence of symmetries [26]: these include rotating waves [27], modulated waves [23, 28] and stable heteroclinic cycles [23, 24, 25]. The SO(2) symmetry is present in the problem under consideration, because the equations are invariant under translations and periodic boundary conditions do not break this invariance. Additionally, if the reflection symmetry exists, the full group of symmetry is the O(2) group.

The impact of the symmetry on the solutions displayed in convection problems with temperature-dependent viscosity has been addressed in [29, 30], where a 2D physical set-up similar to ours is analyzed. The viscosity law considered in this work is similar to the one studied in [30], the main difference being that the viscosity change in our current setting is achieved within a narrower temperature gap. Our problem is idealized in terms of realistic geophysical flows occurring in the Earth's interior, as these are 3D flows moving in spherical shells [31, 32]. Under these conditions, the symmetry present in the problem is formed by all the orientation, preserving rigid motions of $\mathbb{R}^3$ that fix the origin, which is the SO(3) group [33, 34, 35]. The effects of the Earth's rotation are negligible in this respect and do not break this symmetry, as the high viscosity of the mantle renders the Coriolis number insignificant. The link between our simplified problem and these realistic set-ups is that the O(2) symmetry is isomorphic to the rotations along the azimuthal coordinate, which form a closed subgroup of SO(3). Furthermore the O(2) symmetry is present in systems with cylindrical geometry, which provide an idealized setting for volcanic conduits and magma chambers. The results described in this paper confirm the symmetry role in the solutions that under the physical conditions considered exhibit plate-like dynamics and energy bursts.

The article is organized as follows. Section 2 describes the physical set-up and provides the governing equations as well as a detailed characterization of the viscosity law. Section 3 briefly introduces the numerical methods used to obtain the solutions. The results are presented in Section 4. Finally, Section 5 details the conclusions.

2 The physical set-up and the governing equations

We consider a convection problem in a fluid layer of thickness d placed in a 2D finite container of size L as shown in Fig 1. The bottom plate is rigid, *i.e.* $\mathbf{u} = 0$, and it is at temperature T_1. The upper plate is non-deformable and free slip and is at temperature T_0, where $T_0 = T_1 - \Delta T$ and ΔT is the vertical temperature difference, which is positive, *i.e*, $T_0 < T_1$. The lateral boundary conditions are periodic.

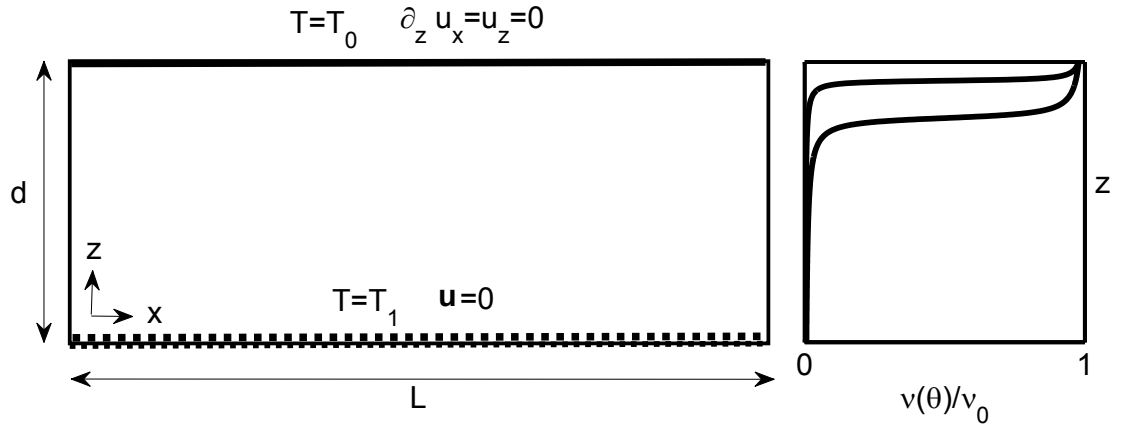

Figure 1: Problem set-up. A 2D container of length L and depth d with periodic lateral boundary conditions. The bottom plate (dashed line) is rigid and is at temperature T_1; the upper plate (thick line) is free slip and is at temperature T_0 ($T_0 < T_1$). The viscosity transitions versus the depth z for the conductive temperature and Ra = 50 and 150 are depicted on the right.

The equations governing the system are expressed with magnitudes in dimensionless form after rescaling as follows: $(x', z') = (x, z)/d$, $t' = \kappa t/d^2$, $\mathbf{u}' = d\mathbf{u}/\kappa$, $P' = d^2P/(\rho_0\kappa\nu_0)$, $\theta' = (T - T_0)/(\Delta T)$. Here, κ is the thermal diffusivity, ρ_0 is the mean density at temperature T_0 and ν_0 is the reference viscosity. After rescaling the domain, $\Omega_1 = [0, L) \times [0, d]$ is transformed into $\Omega_2 = [0, \Gamma) \times [0, 1]$ where $\Gamma = L/d$ is the aspect ratio. The non-dimensional equations are (after dropping the primes in the fields):

$$\nabla \cdot \mathbf{u} = 0, \tag{1}$$

$$\frac{1}{Pr}(\partial_t \mathbf{u} + \mathbf{u} \cdot \nabla \mathbf{u}) = \mathrm{Ra}\theta\vec{e}_3 - \nabla P + \mathrm{div}\left(\frac{\nu(\theta)}{\nu_0}(\nabla \mathbf{u} + (\nabla \mathbf{u})^T)\right), \tag{2}$$

$$\partial_t \theta + \mathbf{u} \cdot \nabla \theta = \Delta\theta. \tag{3}$$

Here, $\vec{e}_3$ represents the unitary vector in the vertical direction; $\mathrm{Ra} = d^4\alpha g\Delta T/(\nu_0\kappa)$ is the Rayleigh number; g is the gravity acceleration; α the thermal expansion coefficient and $Pr = \nu_0/\kappa$ is the Prandtl number. Typically for rocks, Pr is very large, since they present low thermal conductivity (approximately $10^{-6}m^2/s$) and very large viscosity (of the order $10^{20}Ns/m^2$) [36]. Thus, for the problem under consideration, Pr can be considered as infinite and the left-hand side term in (2) can be made equal to zero. These equations use the Boussinesq approximation in which the density is considered constant everywhere except in the buoyant term of Eq. (2) where a dependence on temperature is assumed, as follows $\rho = \rho_0(1-\alpha(T-T_0))$. Thus, no change in the density at the melting temperature is considered and is assumed to be small. Jointly with equations (1)-(3), the lateral periodic

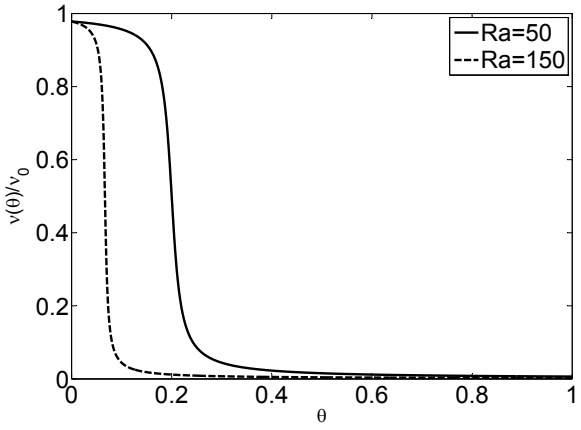

Figure 2: Viscosity law and its dependence on the Rayleigh number.

conditions are invariant under translations along the x-coordinate, which introduces the symmetry SO(2) into the problem. The reflexion symmetry $x \to -x$ is also present insofar as the fields are conveniently transformed as follows: $(\theta, u_x, u_z, p) \to (\theta, -u_x, u_z, p)$. In this case, the O(2) group expresses the full symmetry of the problem.

The viscosity $\nu(\theta)$ is a smooth, positive and bounded function of θ. We use a law that represents the melting by means of an abrupt change in the viscosity at a small temperature gap defining the melting transition. In dimensionless form, this law is,

$$\frac{\nu(\theta)}{\nu_0} = -\left(\frac{1-a}{\pi}\right)\arctan(\beta\mu(\mathrm{Ra}\theta - \mathrm{Ra}_t)) + \left(\frac{1+a}{2}\right) \tag{4}$$

Here, the temperature at which the transition occurs is adjusted by the transition Rayleigh Ra_t which in our case is $\mathrm{Ra}_t = 10$. The choice of a positive value for Ra_t imposes that there exists a viscosity transition in the interior of the fluid layer, even if Ra is very large. The parameter β controls the abruptness of the viscosity transition on θ. Throughout this study we take $\beta = 100$. The constant μ, fixed to $\mu = 0.0146$, expresses fluid properties. The presence of the Ra number in the viscosity law is uncommon among the literature dealing with viscosity dependent on temperature. However, it expresses better what happens in laboratory experiments in which the increment of the Ra number is performed by increasing the temperature T_1 at the lower boundary. This procedure ties the viscosity to changes in the Rayleigh number, which is the parameter that we vary in our study. Changes in the Ra number, as it appears in the viscosity law, necessarily imply changes in the viscosity contrasts. This is explored in further detail. The maximum viscosity in the fluid layer is ν_0, and this is the viscosity value used to define the dimensionless Rayleigh number Ra in Eq. (2). In practice, ν_0 is a viscosity only taken by the fluid at the upper surface where $\theta = 0$ (*i.e*, at temperature T_0), in the limit of large Ra_t and small Ra. The parameter a

is related to the inverse of the maximum viscosity contrast and is fixed at 10^{-3}. In the range of Ra numbers considered in this study, we obtain viscosity contrasts of the order of $3 \cdot 10^2 - 4 \cdot 10^2$. Figure 2 represents the viscosity law at different Ra numbers within the range considered in this work. It is observed that as the Ra number increases the viscosity transition occurs in a temperature gap closer to $\theta = 0$, and therefore closer to the upper surface. The conductive solution (i.e. $\mathbf{u}_c = 0$) to the problem described by equations (1)-(3) corresponds to the linear temperature $\theta_c = -z + 1$. Fig. 1 shows two viscosity profiles as a function of the depth z for this particular temperature solution. These profiles are obtained at the same Ra numbers as in Figure 2, i.e. $\mathrm{Ra} = 50, 150$, and they confirm that the viscosity transition occurs close to the upper surface.

A viscosity law similar to that expressed in Eq. (4) has been proposed in [22, 30]. The study in [22] also considers a change in the density at the temperature of transition, while in [30] the viscosity change occurs within a broader temperature gap.

3 Numerical methods

The results presented in this work are obtained by solving the basic equations and boundary conditions with the numerical techniques reported in [29]. Our analysis is assisted by time-dependent numerical simulations and bifurcation techniques such as branch continuation. These schemes are briefly described below.

3.1 Stationary solutions and their stability

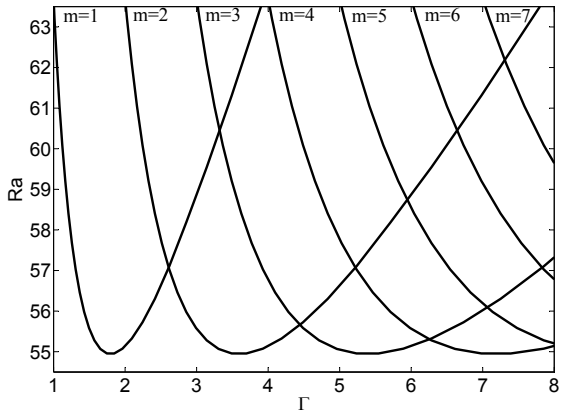

Figure 3: Critical instability curves $\mathrm{Ra}(m, \Gamma)$ for a fluid layer with temperature dependent viscosity taking $\mu = 0.0146$, $a = 0.001$, $\mathrm{Ra}_t = 10$ and $\beta = 100$.

The simplest stationary solution to the problem described by equations (1)-(3) and their boundary conditions is the conductive solution that satisfies $\mathbf{u}_c = 0$ and $\theta_c = -z + 1$. This solution is stable only for a range of vertical temperature gradients that are represented by small enough Rayleigh numbers. Beyond the critical threshold Ra_c, a convective motion settles in and new structures are observed, which may be either time-dependent or stationary. In the latter case, the stationary equations, obtained by cancelling the time derivatives in the system (1)-(3) are satisfied by the bifurcating solutions. At the instability threshold of the conductive state, the growing solutions are periodic and correspond to sine or cosine eigenfunctions with wave number m. Figure 3 displays the critical instability curves for different m values as a function of the aspect ratio. These curves are obtained by means of a simplified linear stability analysis for the conductive solution, as reported in [29]. At the instability threshold around $\mathrm{Ra} \sim 55$, the viscosity law indicates (see Figure 2) that the viscosity transition takes place at the lowest temperatures across the fluid layer, which is near the fluid surface. Thus, at this threshold the fluid consists of a highly viscous layer over a fluid that is not so viscous and is starting its convection.

Beyond the instability thresholds displayed in Figure 3, new branches of stationary solutions arise that evolve with the external physical parameters. There also exist new critical thresholds at which stability is lost, thereby giving rise to new bifurcated structures. These stationary solutions are numerically obtained by using an iterative Newton-Raphson method as reported in [29, 30].

The study of the stability of the stationary solutions under consideration is addressed by means of a linear stability analysis. To this end, a field Y representing the unknown physical magnitudes is decomposed into its stationary solution Y^b and a perturbation $\tilde{y}$ as follows:

$$Y(x, z, t) = Y^b(x, z) + \tilde{y}(x, z)\mathrm{e}^{\lambda t}. \tag{5}$$

The sign in the real part of the eigenvalue λ determines the stability of the solution: if it is negative, the perturbation decays and the stationary solution is stable, while if it is positive the perturbation grows over time and the stationary solution is unstable.

For each unknown field expression, (5) is introduced into the system (1)-(3) and the equations are linearized in $\tilde{y}$, which are assumed to be small (see [29, 30] for details). Together with their boundary conditions, the equations define a generalized eigenvalue problem. The unknown perturbation fields $\tilde{y}$ of the linear equations are approached by means of a spectral method according to the expansion:

$$\tilde{y}(x, z) = \sum_{l=1}^{\lceil L/2 \rceil} \sum_{m=0}^{M-1} b_{lm}^{\tilde{y}} T_m(z) \cos((l-1)x) + \sum_{l=2}^{\lceil L/2 \rceil} \sum_{m=0}^{M-1} c_{lm}^{\tilde{y}} T_m(z) \sin((l-1)x). \tag{6}$$

In this notation, $\lceil \cdot \rceil$ represents the nearest integer towards infinity. Here, L is an odd number as justified in [29]. $4 \times L \times M$ unknown coefficients exist that are determined

by a collocation method in which equations and boundary conditions are imposed at the collocation points, according to the rules detailed in [29]. Expansion orders L and M are taken to ensure accuracy on the results: details of their values are provided in the Section 4.

3.2 Time-dependent schemes

The governing equations (1)–(3) and their boundary conditions define a time-dependent problem for which we propose a temporal scheme based on a spectral spatial discretization analogous to that proposed in the previous section. As before, expansion orders L and M are such that they ensure accuracy on the results; details on their values are given in the following section. In order to integrate in time, we use a third order multistep scheme. In particular, we use a backward differentiation formula (BDF) that is adapted for use with a variable time step. Details on the step adjustment are found in [29]. BDFs are a particular case of multistep formulas which are *implicit*. In [29], it is reported that instead of solving the fully implicit scheme, a semi-implicit scheme is able to provide results with a similar accuracy and fewer CPU time requirements, and this is the method we employ to obtain the time-dependent solutions.

4 Results and discussion

Our study is focused on the solutions displayed by this system at a fixed aspect ratio $\Gamma = 2.166$. As the system is forced to transport more energy by increasing the Ra number, the conductive solution becomes unstable, and new convective solutions are observed. The bifurcation point for this primary event occurs at Ra ~ 55. Furthermore, beyond this point a sequence of bifurcations occur when Ra increases, which is described below.

Figures 4 and 5 show the bifurcating branches captured at different Ra ranges. In the diagrams, the horizontal axis represents the Ra number, while on the vertical axis the system state is represented by a scalar given by the sum of two coefficients in the expansion (6) of a stationary solution:

$$|b^{\theta}_{24}| + |b^{\theta}_{34}|. \tag{7}$$

This amplitude is related to the energy in the temperature field. The horizontal line at 0 corresponds to the conductive solution which is always a stationary solution of the system. In these figures, stable branches are represented by solid lines, while unstable branches are shown with dashed lines. The lines in black correspond to solutions with periodicity $m = 2$ and the lines in gray are for those with $m = 1$. The validity of these bifurcation diagrams is decided by ensuring that for successive order expansions the amplitude values displayed on the vertical axis of the bifurcation diagrams are preserved. Most of the results reported in these diagrams are obtained with expansions $L \times M = 47 \times 50$ although these are increased up to $L \times M = 50 \times 100$ when required (especially at high Ra numbers).

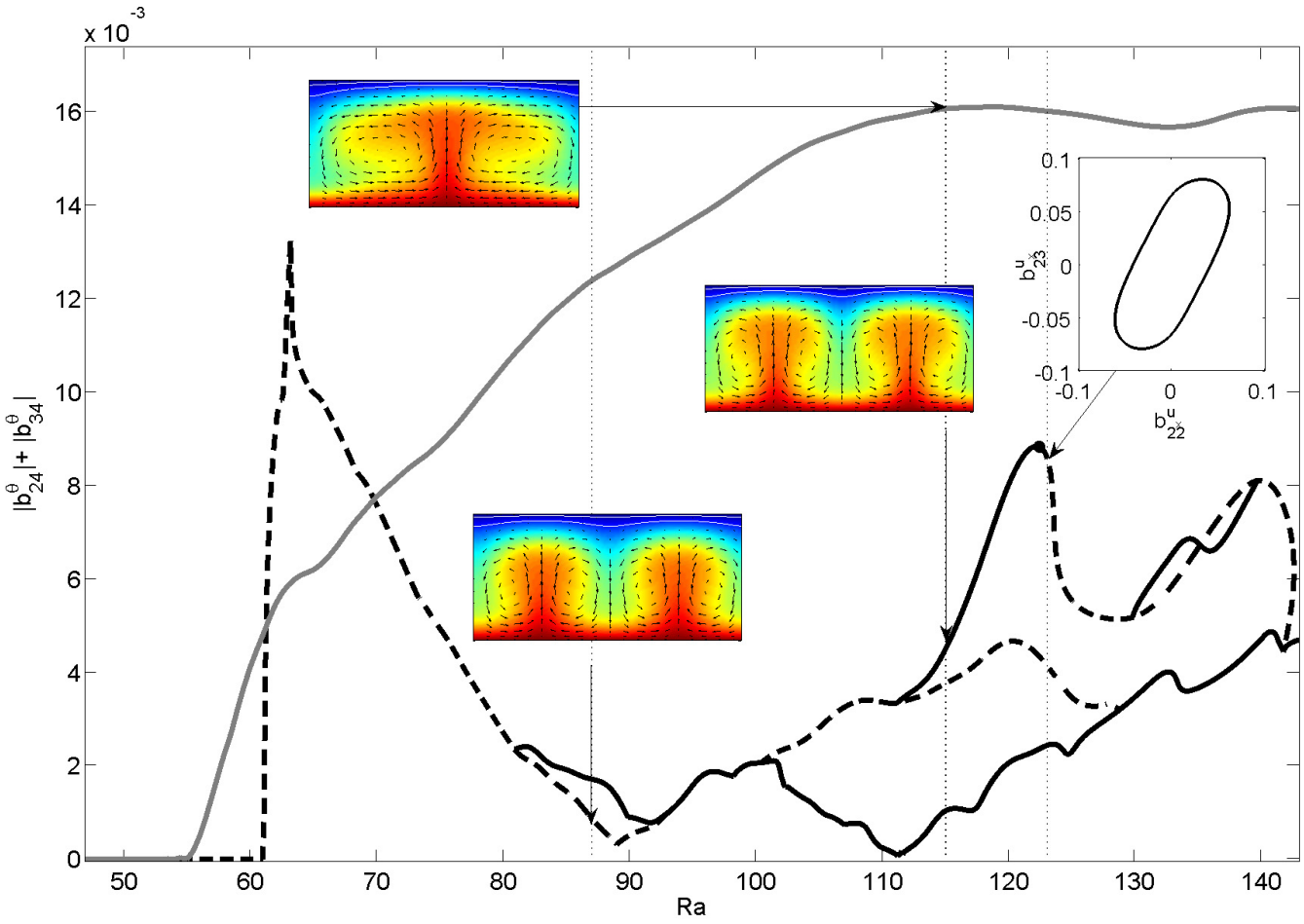

Figure 4: Bifurcation diagram at $\Gamma = 2.166$ for the fluid under consideration in the range $\mathrm{Ra} \in [45, 143]$. This is obtained by representing the amplitude $|b^{\theta}_{24}| + |b^{\theta}_{34}|$ versus the Ra number. Solid lines represent stable branches, while dashed lines stand for the unstable ones.

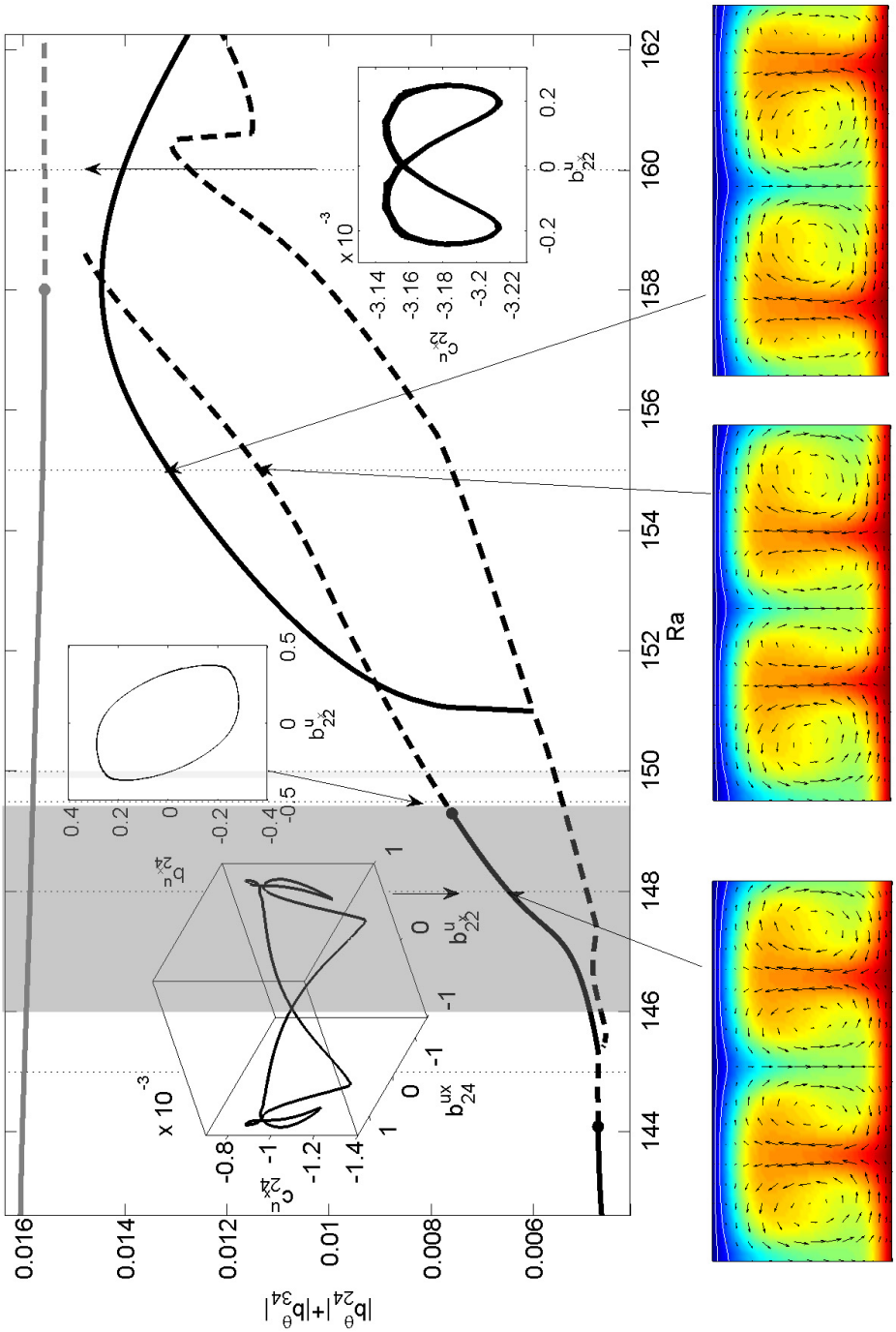

Figure 5: Bifurcation diagram at $\Gamma = 2.166$ for the fluid under consideration in the range $\mathrm{Ra} \in [143, 162]$. This is obtained by representing the amplitude $|b^{\theta}_{24}| + |b^{\theta}_{34}|$ versus the Ra number. Solid lines represent stable branches, while dashed lines stand for the unstable ones. Shaded regions limit the parameter values Ra, between which the time-dependent solutions described in Figure 7 are observed.

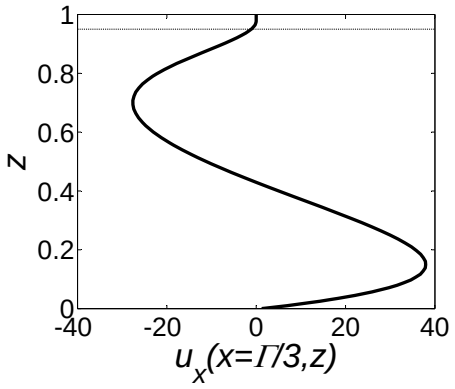

Figure 6: Representation of u_x versus z for the stationary one plume pattern obtained at $\Gamma = 2.166$ and $\mathrm{Ra} = 115$. The horizontal line highlights the stagnant upper lid.

Figure 4 is focused on the Ra interval $\mathrm{Ra} \in [45, 143]$ and reveals that several stable solutions are possible under the same physical conditions. The patterns observed in the physical variables, temperature and velocity, are plotted at different Rayleigh numbers. For instance, at $\mathrm{Ra} = 115$ the solution for the solid grey branch is displayed, which corresponds to a pattern with one plume. Two white lines indicate the temperature contours at which the viscosity mostly decay. Figure 6 displays the horizontal component of the velocity versus the z-coordinate for this solution. The highlighted thin layer at the upper part confirms the existence of a stagnant lid at the surface. At $\mathrm{Ra} = 87$ a two-plume solution in an unstable branch is represented. Several pitchfork bifurcations occur from which stable branches emerge. At $\mathrm{Ra} = 115$ the pattern of a two-plume stable solution is shown; as in the one-plume solution, it has a stagnant upper surface. This stable branch undergoes a Hopf bifurcation at $\mathrm{Ra} \sim 123$, after which time-dependent solutions are found. A projection on the expansion coefficients space of this time-dependent solution is displayed at $\mathrm{Ra} \sim 123$. This solution consists of two plumes each slightly oscillating around their axis below a stagnant lid. After the Hopf bifurcation, the unstable branch undergoes a pitchfork bifurcation at $\mathrm{Ra} \sim 130$ and a stable branch emerges. This branch merges again with the unstable branch at $\mathrm{Ra} \sim 140$. The crossing of branches at $\mathrm{Ra} \sim 135$ is an effect of the projection taken and does not represent any transcritical bifurcation.

When the system is forced to transfer higher energy rates, further time-dependent solutions are observed. This is confirmed in Figure 5, which describes a bifurcation diagram similar to the previous one but at higher Rayleigh numbers $\mathrm{Ra} \in [143, 162]$. The black branch bifurcates through a Hopf bifurcation at $\mathrm{Ra} \sim 144$ towards time-dependent regimes that coexist with the grey stable branch. Hopf bifurcations also occur for a different black stable branch at $\mathrm{Ra} \sim 149.3$, as well as for the grey solid branch at $\mathrm{Ra} \sim 158$. Figure 5 shows several stationary solutions: at $\mathrm{Ra} \sim 148$ it displays a two-plume structure obtained

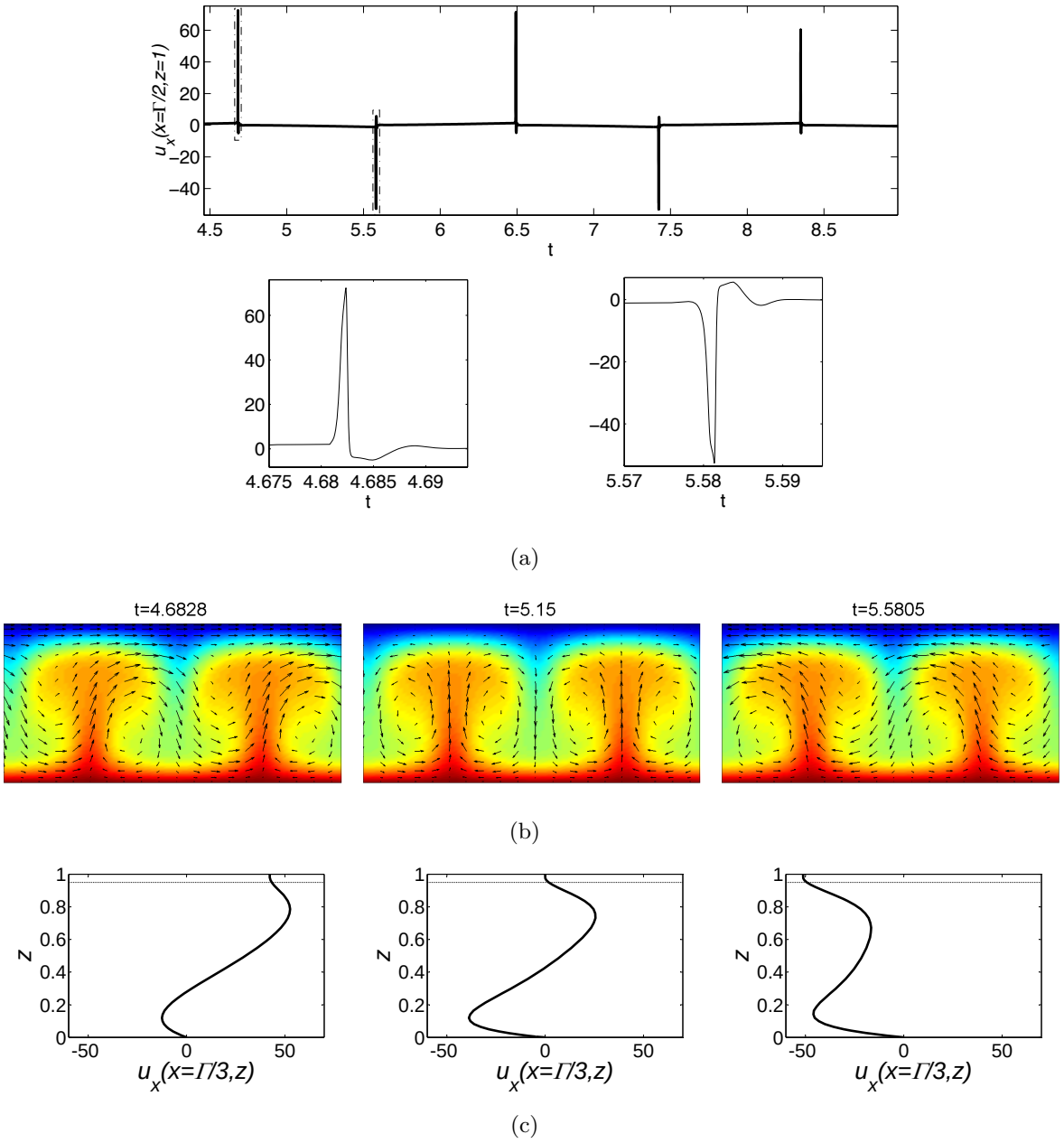

Figure 7: Time-dependent regime of a two-plume pattern at $\Gamma = 2.166$ and $\mathrm{Ra} = 148$ in the Ra range highlighted with the shaded region in Figure 5. a) Time series of the horizontal component of the velocity at the surface point $(z = 1, x = \Gamma/2)$ on $\mathrm{Ra} = 148$. Two zooms are represented for the bursts at around times $t \sim 4.7$ and $t \sim 5.6$; b) spatial patterns during the bursts at times $t = 4.6828$ and $t = 5.5805$ and in the quiescent state at $t = 5.15$. c) the horizontal component of the velocity u_x versus the z-coordinate at fixed $x = \Gamma/3$ at times $t = 4.6828$, $t = 5.15$ and $t = 5.5805$. The horizontal line highlights the moving upper lid that switches with a stagnant lid.

over the marked branch. This solution coexists with a time-dependent solution observed over the entire shaded region, of which we provide a projection of the time series obtained at Ra = 148, which is explained in detail below. An unstable stationary solution over this branch is displayed at Ra $\sim$ 155. The pattern is asymmetric, with the plumes more prominent outwards. At this Ra number, the structure of a stationary solution on the stable branch also exhibits asymmetry, but with the heads more prominent inwards. All the stationary solutions have a stagnant upper surface.

We next describe the temporal evolution observed in the shaded region of Figure 5. A summary of what is obtained at Ra = 148 is given in Figure 7. The system evolves as a limit cycle in a type of evolution similar to that close to heteroclinic cycles, a typical object of systems with the O(2) symmetry [23, 25]. Over time, the system stays close to two quiescent states, which are distinguished in Figure 7(a) by the zero upper velocity for long periods. These states are interrupted by bursts in which energy at the upper surface is abruptly released. One of the two quiescent states is represented in the center panel of Figure 7(b). In these almost stationary positions, the system presents two plumes that oscillate very slightly and have a stagnant lid at the upper surface. The two states are distinguished by the fact that the plumes are slightly shifted along the horizontal direction. Figure 7(c) represents the horizontal component of the velocity u_x versus the depth z for a quiescent state at time $t = 0.14482$. In the center panel one may observe the stagnant upper lid. The quasi-stationary regimes are connected by rapidly evolving transitions which release the energy very rapidly. The solution during these crises has the interesting characteristic that in these episodes it consists of "plate-like" convective styles. By "plate-like" motion we refer to the fact that the stagnant lid at the upper surface drifts alternately towards the right or the left as a block. The first and third panels in Figure 7(c) show a moving upper layer by displaying the horizontal component of the velocity u_x versus the depth z. A thin lid is observed which moves like a rigid body without internal shear either to the right or to the left. We have verified that variations of the velocity within this thin layer are below 0.05%, and for this reason it has the appearance of a moving plate. In these short time intervals (short when compared to the duration of the quiescent states), a meandering jet develops simultaneously below the drifting surface, in which sinking and upwards currents are observable (see Figure 7(b)).

It is clear that the lateral boundary conditions (*i.e.* the symmetry) are important for this behaviour because they allow upper drift motions. Moreover, the shifted inactive states between which the alternancy appears are possible only in this scenario. On the other hand, in a recent work by Ulvrová et al. [22] the authors study a law similar to ours, although symmetry effects are absent and this type of transition is not reported. Nevertheless, it should be noted that symmetry is not a sufficient condition for this kind of behavior: for instance, previous results discussed in [30], also in the presence of the O(2) symmetry, and in a similar setting to ours, make no reference to "plate-like" convection nor stagnant lids, although symmetries do exert an influence on the described solutions. The main difference between the setting considered in this work and that presented in

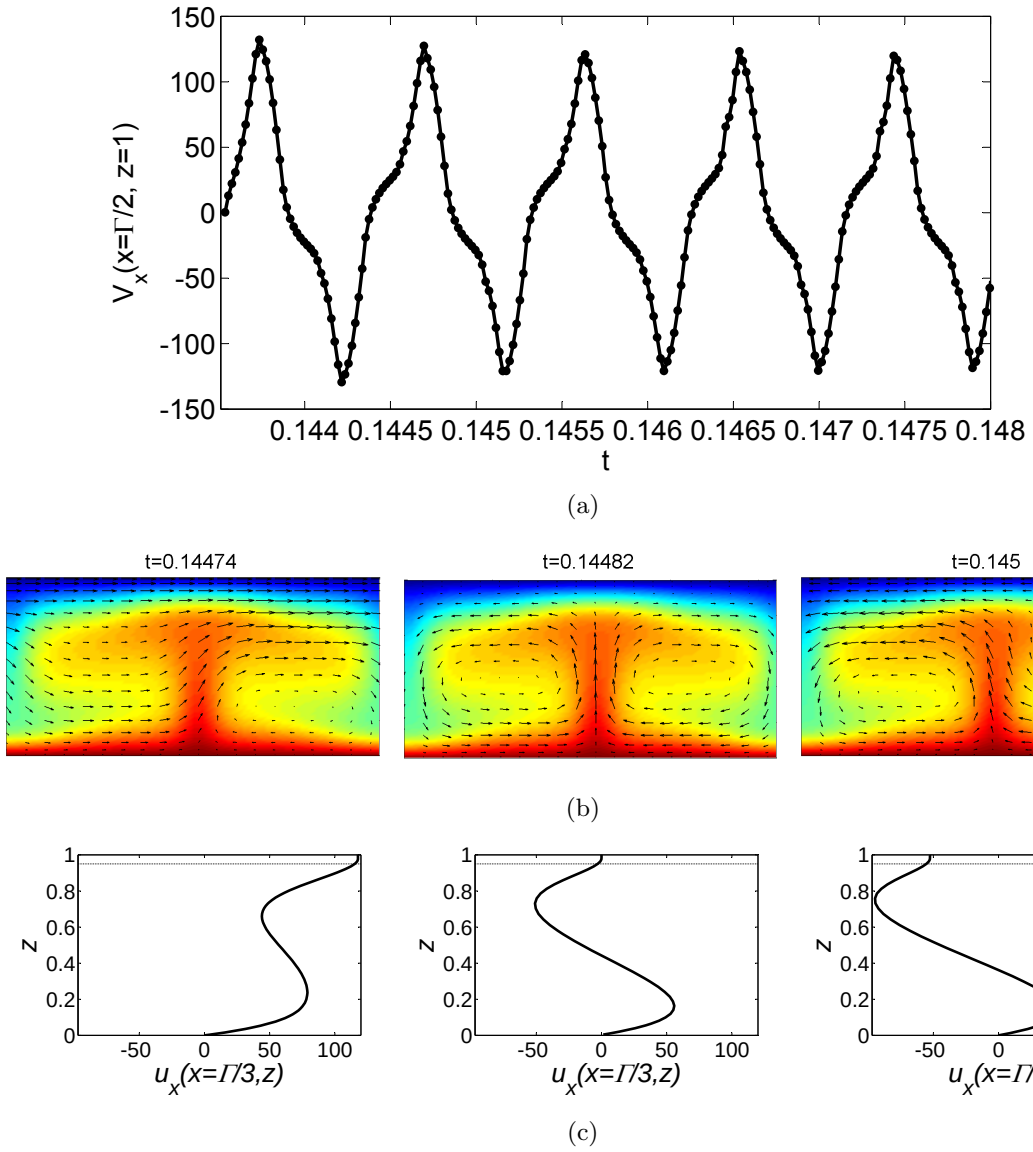

Figure 8: Time-dependent regime of a one-plume pattern at $\Gamma = 2.166$ and $\mathrm{Ra} = 160$. a) Time series of the horizontal component of the velocity at the surface point $(z = 1, x = \Gamma/2)$ at $\mathrm{Ra} = 160$; b) spatial patterns at times $t = 0.14474$ and $t = 0.14482$ and $t = 0.145$.; c) the horizontal component of the velocity u_x versus the z-coordinate at fixed $x = \Gamma/3$ at times $t = 0.14474$, $t = 0.14482$ and $t = 0.145$. The horizontal line highlights the moving upper lid.

[30] is that the transition of the viscosity with temperature is less abrupt than in our study. Furthermore results reported in [29], also in the presence of the O(2) symmetry and viscosity according to exponential law, indicate the existence of a stagnant lid, although no impact of the symmetry on the time evolution is found.

The bursting solutions obtained in this study are justified in the framework of the symmetry presence, but this does not imply that episodic solutions cannot be obtained in other settings in which the symmetry is absent. For instance, in the numerical work by [37], catastrophic events in Earth's mantle are reported. However, these bursting solutions are rather different to ours insofar as they do not connect almost quasi-stationary states and the solutions are not linked to any plate-like behaviour. The work by [6] is connected to episodic plate reorganizations, although the authors obtain time series in which transitions are not so dramatic as ours. However, in their problem they consider a square box with periodic boundary conditions, so they have the symmetry $\mathrm{O}(2)\times\mathrm{O}(2)$. Unfortunately, they provide no discussion on the impact of the underlying symmetry on their solutions.

Our simulations indicate that the solution described in Fig. 7 becomes non-attractive at $\mathrm{Ra} \sim 149.5$. At this point, an initial data starting near this regime evolves towards a periodic solution, a projection of which is shown in Figure 5. This motion consists of slightly asymmetrical plumes, each one rapidly vibrating around its central vertical axis. This is a time-dependent solution in which the surface fluid remains stagnant. At $\mathrm{Ra} \sim 160$, Figure 5 shows the projection on the coefficient space of a time series obtained for the asymptotic time-dependent regime of one plume. Figure 8 shows the time evolution in detail. The system evolves in a periodic motion in which the upper surface drifts alternately towards the right and the left, which is confirmed by a time series of the horizontal velocity component at the surface. Long quiescent states between the drift motions are no longer observed, only a continuously oscillating motion. In Figure 8(b), snapshots of the temperature and velocity fields obtained at times $t = 0.14474, 0.14482, 0.145$ show the plate-like motion. Figure 8(c) enforces this vision by displaying the horizontal component of the velocity u_x versus the depth z at the same selected times. A thin upper lid which moves consistently is observed. As in the previously described plate motion, a meandering jet develops below the drifting surface in which sinking and upwards currents are observable (see Figure 8(b)). These time-dependent solutions are obtained with expansions $L \times M = 47 \times 50$.

5 Conclusions

In this paper we address the subject of a convecting fluid in which viscosity depends on temperature. We examine a dependency which models an abrupt change in the viscosity in a gap around a temperature of transition. We explore the space of solutions at a fixed aspect ratio by means of bifurcation diagrams and time-dependent numerical simulations. We find time-dependent convection in which the symmetry plays an important role. In particular, we describe limit cycles and time periodic solutions which are similar to others

found in several contexts in the literature (see [23, 24, 25]) in the presence of the O(2) symmetry.

The time evolution during the limit cycles presents two peculiarities: first of all, they are bursting solutions that release energy abruptly in time and secondly plate-like convection is observed during the bursts. Additionally, time-periodic solutions are found that have a similar plate-like dynamic with a smoother time evolution. No plate-like dynamics have hitherto been observed in this type of convection problem. For viscosity dependencies according to the Arrhenius law, or its approach by means of an exponential law, no temporal transitions between stagnant lids and drifting lids have been reported. Recent studies by Ulvrová et al. [22], who use a law similar to ours, do not report this type of transitions either, although symmetry effects are not considered in their study.

Forsyth and Uyeda [21] propose that plate-like motion is produced by sinking slabs that pull the plates in the subduction process. The results reported in our study are obtained for constant density within the Boussinesq approximation, and provide convection examples of moving plates that coexist with subsurface upwards and downwards meandering jets, but without a proper subduction. Obviously, these examples do not rule out the existence of subduction in the Earth, but rather propose a role played by the symmetry which can be particularly illustrative for understanding convective styles of the Earth prior to subduction, or that of other planetary bodies.

Acknowledgements

We thank CESGA for computing facilities. This research is supported by the Spanish Ministry of Science under grant MTM2011-26696 and MINECO: ICMAT Severo Ochoa project SEV-2011-0087.

References

[1] H. Benard. Les tourbillons cellulaires dans une nappe liquide author(s): Benard, h. source: Rev. gen. sci. pures appl. volume: 11 pages: 1261-1271 published: 1900 times cited: 589 (from web of science). *Rev. Gen. Sci. Pures Appl.*, 11:1261–1271, 1900.

[2] A. M. Mancho, H. Herrero, and J. Burguete. Primary instabilities in convective cells due to nonuniform heating. *Physical Review E*, 56(3):2916, 1997.

[3] S. Hoyas, H. Herrero, and A. M. Mancho. Bifurcation diversity of dynamic thermocapillary liquid layers. *Physical Review E*, 66(5):057301, 2002.

[4] S. Hoyas, A. M. Mancho, H. Herrero, N. Garnier, and A. Chiffaudel. Bénard–Marangoni convection in a differentially heated cylindrical cavity. *Physics of Fluids*, 17:054104, 2005.

[5] M. C. Navarro, A. M. Mancho, and H. Herrero. Instabilities in buoyant flows under localized heating. *Chaos: An Interdisciplinary Journal of Nonlinear Science*, 17:023105, 2007.

[6] S. D. King, J. P. Lowman, and C. W. Gable. Episodic tectonic plate reorganizations driven by mantle convection. *Earth and Planetary Science Letters*, 203:83–91, 2002.

[7] V. S. Solomatov and L. N. Moresi. Three regimes of mantle convection with non-newtonian viscosity and stagnant lid convection on the terrestrial planets. *Geophysical Research Letters*, 24(15):1907–1910, 1997.

[8] S. C. Solomon, S. E. Smrekar, D. L. Bindschadler, R. E. Grimm, W. M . Kaula, R. J. Phillips, R. S. Saunders, G. Schubert, S. W. Squyres, and E. R. Stofan. Venus tectonics: An overview of Magellan observations. *J. Geophys. Res*, 97(13199-132555), 1992.

[9] P. Machetel and P. Weber. Intermittent layered convection in a model mantle with an endothermic phase change at 670 km. *Nature*, 350:55–57, 1991.

[10] G. T. Jarvis and D. P. Mckenzie. Convection in a compressible fluid with infinite prandtl number. *J. Fluid Mech.*, 96(03):515–583, 1980.

[11] X. Liu and S. Zhong. Analyses of marginal stability, heat transfer and boundary layer properties for thermal convection in a compressible fluid with infinite prandtl number. *Geophys. J. Int.*, 194:125–144, 2013.

[12] A. M. Hofmeister and D. Yuen. Critical phenomena in thermal conductivity: Implications for lower mantle dynamics. *Journal of Geodynamics*, 44:186–199, 2007.

[13] F. Dubuffet, D. A. Yuan, and E. S. G. Rainey. Controlling thermal chaos in the mantle by positive feedback from radiative thermal conductivity. *Nonlinear Proc. Geophys.*, 9(1-13), 2002.

[14] T. K. B. Yanagawa, M. Nakada, and D. A. Yuan. The influence of lattice thermal conductivity on thermal convection with strongly temperature-dependent viscosity. *Earth Space Sci.*, 57(15-28), 2005.

[15] L. N. Moresi and V. S. Solomatov. Numerical investigation of 2D convection with extremely large viscosity variations. *Physics of Fluids*, 7(9):2154–2162, 1995.

[16] V. S. Solomatov and L. N. Moresi. Stagnant lid convection on Venus. *J. Geophys. Res*, 101:4737–4753, 1996.

[17] P. J. Tackley. Self-consistent generation of tectonic plates in three dimensional mantle convection. *Earth and Planetary Science Letters*, 157:9–22, 1998.

[18] R.Trompert and U. Hansen. Mantle convection simulations with reologies that generate plate-like behaviour. *Nature*, 395(686-689), 1998.

[19] D. Bercovici. The generation of plate tectonics from mantle convection. *Earth and Planetary Science Letters*, 205(107-121), 2003.

[20] V. S. Solomatov. Initiation of subduction by small-scale convection. *J. Geophys. Res*, 109:B01412, 2004.

[21] D. Forsyth and S. Uyeda. On the relative importance of the driving forces of plate motion. *Geophys. J. R Astr. Soc.*, 43:163–200, 1975.

[22] M. Ulvrová, S. Labrosse, N. Coltice, P. Raback, and P.J. Tackley. Numerical modelling of convection interacting with a melting and solidification front: Application to the thermal evolution of the basal magma ocean. *Physics of the Earth and Planetary Interiors*, 206-207:51–66, 2012.

[23] D. Armbruster, J. Guckenheimer, and P. Holmes. Heteroclinic cycles and modulated travelling waves in systems with O(2) symmetry. *Physica D*, 29(257-282), 1988.

[24] J. Guckenheimer and P. Holmes. Structurally stable heteroclinic cycles. *Math. Proc. Cambridge Philos. Soc.*, 103(189-192), 1988.

[25] S. P. Dawson and A. M. Mancho. Collections of heteroclinic cycles in the Kuramoto-Sivashinsky equation. *Physica D: Nonlinear Phenomena*, 100(3-4):231–256, 1997.

[26] J. D. Crawford and E. Knobloch. Symmetry and symmetry-breaking bifurcations in fluid dynamics. *Annu. Rev. Fluid Mech.*, 23(341-387), 1991.

[27] D. Ruelle. Bifurcations in the presence of a symmetry group. *Arch. Ration. Mech. Anal.*, 51:136–152, 1973.

[28] D. Rand. Dynamics and symmetry: predictions for modulated waves in rotating fluids. *Arch. Ration. Mech. Anal.*, 79(1):1–38, 1982.

[29] J. Curbelo and A. M. Mancho. Spectral numerical schemes for time-dependent convection with viscosity dependent on temperature. *Communications in Nonlinear Science and Numerical Simulations*, 19(2), 2014.

[30] J. Curbelo and A. M. Mancho. Bifurcations and dynamics in convection with temperature-dependent viscosity under the presence of the O(2) symmetry. *Physical Review E*, 2013.

[31] F. H. Busse. Pattern of convection in spherical shells. *J. Fluid Mech.*, 72:65–85, 1975.

[32] F. H. Busse and N. Riahi. Pattern of convection in spherical shells II. *J. Fluid Mech.*, 123:283–391, 1982.

[33] P. Chossat. Bifurcation and stability of convective flows in a rotating or not rotating spherical shell. *SIAM Journal on Applied Mathematics*, 37:624–647, 1975.

[34] M. Golubitsky and D.G. Schaeffer. Bifurcation with O(3) symmetry including applications to the benard problem. *Communs. Pure. Appl. Math.*, 35:81–11, 1982.

[35] E. Ihrig and M. Golubitsky. Pattern selection with O(3) symmetry. *Physica D*, 12:1–33, 1984.

[36] G.F. Davies. *Dynamic Earth. Plates, Plumes and Mantle convection.* Cambridge University Press, Cambridge, England, 2001.

[37] S. A. Weinstein. Catastrophic overturn of the earth's mantle driven by multiple phase changes and internal heat generation. *Geophysical Research Letters*, 20(321-324), 1993.

3.4. Confined rotating convection with large Prandtl number: Centrifugal effects on wall modes

Coauthors: Juan López, Ana M. Mancho, Francisco Marqués

Abstract: Thermal convection in a rotating cylinder with a radius-to-height aspect ratio of $\Gamma = 4$ for fluids with large Prandtl number is studied numerically. Centrifugal buoyancy effects are investigated in a regime where the Coriolis force is relatively large and the onset of thermal convection is in the so-called wall modes regime, where pairs of hot and cold thermal plumes ascend and descend in the cylinder sidewall boundary layer, forming an essentially one-dimensional pattern characterized by the number of hot and cold plume pairs. In our numerical study, we use the physical parameters corresponding to aqueous mixtures of glycerine with mass concentration in the range of 60–90% glycerine and a Rayleigh number range that extends from the threshold for wall modes up to values where the bulk fluid region is also convecting. The study shows that for the range of Rayleigh numbers considered, the local variations in viscosity due to temperature variation in the flow are negligible. However, the mean viscosity, which varies faster than exponentially with variations in the percentage of glycerine, leads to a faster than exponential increase in the Froude number for a fixed Coriolis force, and hence an enhancement of the centrifugal buoyancy effects with significant dynamical consequences, which are detailed.

Reference: [24] Jezabel Curbelo, Juan López, Ana M. Mancho, Francisco Marqués. Confined rotating convection with large Prandtl number: Centrifugal effects on wall modes. Physical Review E **89**, 013019 (2014).

PHYSICAL REVIEW E **89**, 013019 (2014)

Confined rotating convection with large Prandtl number: Centrifugal effects on wall modes

Jezabel Curbelo
Instituto de Ciencias Matemáticas (CSIC-UAM-UC3M-UCM), Nicolás Cabrera, 15, Madrid 28049, Spain and Departamento de Matemáticas, Universidad Autónoma de Madrid, Madrid 28049, Spain

Juan M. Lopez*
School of Mathematical and Statistical Sciences, Arizona State University, Tempe, Arizona 85287, USA

Ana M. Mancho
Instituto de Ciencias Matemáticas (CSIC-UAM-UC3M-UCM), Nicolás Cabrera, 15, Madrid 28049, Spain

Francisco Marques
Department of Física Aplicada, Universitat Politècnica de Catalanya, Girona s/n, Mòdul B4 Campus Nord, 08034 Barcelona, Spain
(Received 29 October 2013; published 23 January 2014)

Thermal convection in a rotating cylinder with a radius-to-height aspect ratio of $\Gamma = 4$ for fluids with large Prandtl number is studied numerically. Centrifugal buoyancy effects are investigated in a regime where the Coriolis force is relatively large and the onset of thermal convection is in the so-called wall modes regime, where pairs of hot and cold thermal plumes ascend and descend in the cylinder sidewall boundary layer, forming an essentially one-dimensional pattern characterized by the number of hot and cold plume pairs. In our numerical study, we use the physical parameters corresponding to aqueous mixtures of glycerine with mass concentration in the range of 60%–90% glycerine and a Rayleigh number range that extends from the threshold for wall modes up to values where the bulk fluid region is also convecting. The study shows that for the range of Rayleigh numbers considered, the local variations in viscosity due to temperature variation in the flow are negligible. However, the mean viscosity, which varies faster than exponentially with variations in the percentage of glycerine, leads to a faster than exponential increase in the Froude number for a fixed Coriolis force, and hence an enhancement of the centrifugal buoyancy effects with significant dynamical consequences, which are detailed.

DOI: 10.1103/PhysRevE.89.013019 PACS number(s): 47.32.Ef, 47.55.pb

I. INTRODUCTION

Rotating Rayleigh-Bénard convection in a circular cylinder is a classical canonical system that has been receiving much additional attention recently due to the availability of new modern experimental facilities and significant advances in its numerical simulation [1]. For the most part, studies have focused on Prandtl numbers (the ratio of thermal to viscous time scales of the problem) of order 10 and smaller, motivated primarily by astrophysical interests [2]. Large Prandtl number systems are also of much interest, particularly when the working fluids are various alcohols, silicone oils, and exotic gases under high pressure. For this reason it is desirable to access high-Prandtl number regimes both in laboratory experiments and in numerical or theoretical models in order to gain insight into some of the physical processes involved. Conducting laboratory experiments over a range of large Prandtl numbers requires the choice of appropriate fluids. Aqueous mixtures of glycerine are one such choice which has been used in many fluid mechanical settings [3], as well as in heat-transfer and chemical kinetics applications. However, these have a temperature-dependent viscosity which may need to be accounted for.

In rotating convection, recent experiments [4] have reported significant qualitative differences between the states found for Prandtl numbers bigger than one and smaller than one. In Ref. [5] heat flux enhancements due to rotation were investigated, and it was noted that there is a lack of experimental and numerical studies that address Prandtl number effects for rotating convection. For Prandtl numbers greater than 100, there are few studies in rotating convection. There exist some theoretical studies in the limit of infinite Prandtl number [6–8], but these neglect two aspects of rotating convection which can be dominant, especially in a realistic physical setting, namely, confinement and centrifugal buoyancy [9–14]. Experiments are often designed to operate in parameter regimes where the Froude number Fr is small so that centrifugal effects can be neglected [15]. Neglecting centrifugal buoyancy in a large Prandtl number setting can be especially problematic since reaching a large Prandtl number requires a large viscosity fluid, such as highly concentrated aqueous mixtures of glycerine. As the Coriolis number (ratio of viscous time to system rotation period) also depends on the viscosity, in order to keep this number fixed while increasing the Prandtl number, the rotation of the system must be increased. This increment also augments the Froude number, which depends, quadratically, on the rotation rate. So, for small Prandtl numbers the Froude number is small and generally negligible, but for large Prandtl numbers the Froude number becomes large enough to strongly influence the dynamics.

In this paper, we conduct numerical simulations in a rotating cylinder of radius-to-depth ratio equal to 4 with fluids covering a large range of Prandtl and Froude numbers. The precise parameter regimes are described below, together with the description of the governing equations and their numerical

*jmlopez@asu.edu

Large Prandtl number confined rotating convection: centrifugal effects on wall modes

J. Curbelo

Instituto de Ciencias Matemáticas (CSIC-UAM-UC3M-UCM),

Nicolás Cabrera, 15, Madrid 28049, Spain

Departamento de Matemáticas, Universidad Autónoma de Madrid, Madrid 28049, Spain

J. M. Lopez*

School of Mathematical and Statistical Sciences,

Arizona State University, Tempe, Arizona 85287, USA

A. M. Mancho

Instituto de Ciencias Matemáticas (CSIC-UAM-UC3M-UCM),

Nicolás Cabrera, 15, Madrid 28049, Spain

F. Marques

Department of Física Aplicada, Universitat Politècnica de Catalanya,

Girona s/n, Mòdul B4 Campus Nord, 08034 Barcelona, Spain

(Dated: October 29, 2013)

Abstract

Thermal convection in a rotating cylinder with a radius-to-height aspect ratio of $\Gamma = 4$ for fluids with large Prandtl number is studied numerically. Centrifugal buoyancy effects are investigated in a regime where the Coriolis force is relatively large and the onset of thermal convection is in the so-called wall modes regime, where pairs of hot and cold thermal plumes ascend and descend in the cylinder sidewall boundary layer, forming an essentially one-dimensional pattern characterized by the number of hot/cold plume pairs. In our numerical study, we use the physical parameters corresponding to aqueous mixtures of glycerine with mass concentration in the range of 60–90% glycerine and a Rayleigh number range that extends from the threshold for wall modes up to values where the bulk fluid region is also convecting. The study shows that for the range of Rayleigh numbers considered, the local variations in viscosity due to temperature variation in the flow are negligible. However the mean viscosity, which varies faster than exponentially with variations in the percentage of glycerine, leads to a faster than exponential increase in the Froude number for a fixed Coriolis force, and hence an enhancement of the centrifugal buoyancy effects with significant dynamical consequences which are detailed.

*Electronic address: jmlopez@asu.edu

I. INTRODUCTION

Rotating Rayleigh-Bénard convection in a circular cylinder is a classical canonical system that has been receiving much additional attention recently due to the availability of new modern experimental facilities and significant advances in its numerical simulation [1]. For the most part, studies have focused on Prandtl numbers (the ratio of thermal to viscous time scales of the problem) of order 10 and smaller, motivated primarily by astrophysical interests [2]. Large Prandtl number systems are also of much interest, particularly when the working fluids are various alcohols, silcone oils and exotic gases under high pressure. For this reason it is desirable to access high-Prandtl number regimes both in laboratory experiments and in numerical or theoretical models in order to gain insight into some of the physical processes involved. Conducting laboratory experiments over a range of large Prandtl numbers requires the choice of appropriate fluids. Aqueous mixtures of glycerine are one such choice which has been used in many fluid mechanical settings [3], as well as in heat-transfer and chemical kinetics applications. However these have a temperature dependent viscosity which may need to be accounted for.

In rotating convection, recent experiments [4] have reported significant qualitative differences between the states found for Prandtl numbers bigger than one and smaller than one. In [5], heat flux enhancements due to rotation were investigated, and it was noted that there is a lack of experimental and numerical studies that address Prandtl number effects for rotating convection. For Prandtl numbers greater than 100, there are few studies in rotating convection. There exist some theoretical studies in the limit of infinite Prandtl number [6–8], but these neglect two aspects of rotating convection which can be dominant, especially in a realistic physical setting, namely confinement and centrifugal buoyancy [9–14]. Experiments are often designed to operate in parameter regimes where the Froude number, Fr, is small so that centrifugal effects can be neglected [15]. Neglecting centrifugal buoyancy in a large Prandtl number setting can be especially problematic since reaching a large Prandtl number requires a large viscosity fluid, such as highly concentrated aqueous mixtures of glycerine. As the Coriolis number (ratio of viscous time to system rotation period) also depends on the viscosity, in order to keep this number fixed whilst increasing the Prandtl number, the rotation of the system must be increased. This increment also augments the Froude number which depends, quadratically, on the rotation rate. So, for small Prandtl numbers the

Froude number is small and generally negligible, but for large Prandtl numbers the Froude number becomes large enough to strongly influence the dynamics.

In this paper, we conduct numerical simulations in a rotating cylinder of radius-to-depth ratio equal to 4 with fluids covering a large range of Prandtl and Froude numbers. The precise parameter regimes are described below, together with the description of the governing equations and their numerical resolution. We find that for moderate Rayleigh numbers (up to and a little beyond where the bulk begins to convect), the local variations in viscosity due to temperature variations in the flow are negligible, especially when compared to the centrifugal effects.

II. THE PHYSICAL SET-UP, THE GOVERNING EQUATIONS AND THE NUMERICAL SCHEME

Consider the flow in a circular cylinder of radius r_0 and depth d, rotating at a constant rate ω rad/s. The top and bottom endwalls are maintained at constant temperatures $T_0 - 0.5\Delta T$ and $T_0 + 0.5\Delta T$, respectively, where T_0 is the reference temperature and ΔT is the temperature difference between the endwalls. The sidewall is assumed to be insulating. The governing equations are written in the rotating frame of reference, using the Boussinesq approximation in which all fluid properties are considered constant, except for the density in the gravitational and centrifugal buoyancy terms. Using d as the length scale, d^2/κ as the time scale, $\nu^2\rho_0/d^2$ as the pressure scale (ρ_0 is the density at temperature T_0) and ΔT as the temperature scale, the non-dimensional governing equations are:

$$(\partial_t + \boldsymbol{u}\cdot\nabla)\boldsymbol{u} = -\nabla p + \sigma Ra T\hat{z} + 2\sigma\Omega\boldsymbol{u}\times\hat{z} - \frac{\sigma Fr Ra}{\Gamma}T\boldsymbol{r} + \sigma\nabla^2\boldsymbol{u}, \tag{1}$$

$$(\partial_t + \boldsymbol{u}\cdot\nabla)T = \nabla^2 T, \qquad \nabla\cdot\boldsymbol{u} = 0, \tag{2}$$

where the non-dimensional temperature is $T = (T_{\rm phys} - T_0)/\Delta T$, $\boldsymbol{u}$ is the velocity field in the rotating frame, (u, v, w) are the components of $\boldsymbol{u}$ in cylindrical coordinates (r, θ, z), p is the kinematic pressure (including gravitational and centrifugal contributions), $\hat{z}$ the unit vector in the vertical direction z, and $\boldsymbol{r}$ is the radial vector in cylindrical coordinates. There

are five non-dimensional parameters:

$$\begin{aligned} &\text{Rayleigh number} && Ra = \alpha g d^3 \Delta T/\kappa\nu_0, \\ &\text{Coriolis number} && \Omega = \omega d^2/\nu_0, \\ &\text{Froude number} && Fr = \omega^2 r_0/g, \\ &\text{Prandtl number} && \sigma = \nu_0/\kappa, \\ &\text{aspect ratio} && \Gamma = r_0/d, \end{aligned} \tag{3}$$

where α is the coefficient of volume expansion, g is the gravitational acceleration, κ is the thermal diffusivity, and ν_0 is the kinematic viscosity at temperature T_0. The boundary conditions for $\boldsymbol{u}$ and T are:

$$r = \Gamma: \qquad u = v = w = 0, \quad T_r = 0, \tag{4}$$

$$z = \pm 1/2: \quad u = v = w = 0, \quad T = \mp 1/2. \tag{5}$$

The dimensionless form of the temperature-dependent density used in (1) is:

$$\rho(T) = \rho_0(1 - \alpha T). \tag{6}$$

The validity of the Boussinesq approximation requires $\alpha\Delta T \ll 1$. Expressing this value in terms of the non-dimensional parameters of the problem gives

$$\alpha\Delta T = RaFr/\Omega^2\sigma\Gamma. \tag{7}$$

For the range of parameters considered in this study, $\alpha\Delta T$ is indeed small ($< 10^{-3}$). This criterion is often quoted as being a sufficient criterion to validate the Boussinesq approximation, although [16, 17] introduced additional conditions under which the Boussinesq approximation can be applied. These include certain factors related to the temperature dependence of the material properties which should be smaller than a certain tolerance for a required level of accuracy. For the parameter regimes considered in this study, since ΔT is small, these requirements are also satisfied.

In our numerical experiments, we have considered glycerine-water mixtures. The aspect ratio is fixed to $\Gamma = 4$ and the Coriolis number to $\Omega = 625$, corresponding to values used in previous studies where onset was dominated by wall modes [18, 19]. Figure 1 shows the variations of σ and Fr for aqueous mixtures of glycerine at 22.4°C. The density and dynamic

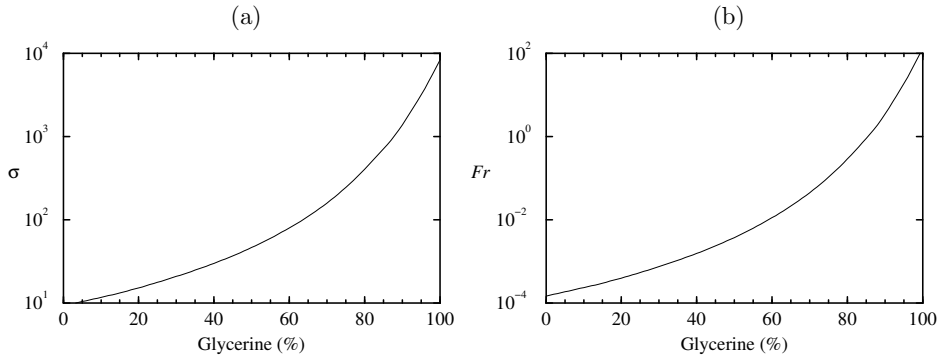

FIG. 1: Variations of σ and Fr for aqueous mixtures of glycerine at 22.4°C.

viscosity of the aqueous glycerine mixtures, required to calculate σ and Fr, have been obtained from [20]. We have focused our attention on the concentration range 60–90%, as we are interested in examining centrifugal effects and for glycerine concentrations less than 60%, $Fr < 0.01$, and the effects of this parameter are negligible. For the range of glycerine concentrations considered, the Prandtl number increases by about one order of magnitude while the Froude number increases by almost two orders of magnitude. Temperature-dependent viscosity effects are negligible in the parameter range analyzed in this study. For completeness, these are briefly discussed in the Appendix A, which also details how the governing equations change due to temperature-dependent viscosity, and how these are solved numerically.

The governing equations have been solved using the second-order time-splitting method proposed in [21] combined with a pseudo-spectral method for the spatial discretization, utilizing a Galerkin–Fourier expansion in the azimuthal coordinate θ and Chebyshev collocation in $x = r/\Gamma$ and $y = 2z$ of the form

$$F(r,\theta,z) = \sum_{l=0}^{L}\sum_{n=0}^{N}\sum_{m=-M}^{M} a_{l,n,m}\Xi_l(x)\Xi_n(y)e^{\mathrm{i}m\theta}. \tag{8}$$

The velocity components, temperature and pressure are the real or imaginary parts of F. The radial dependence of the variables is approximated by Chebyshev expansions with appropriate parities of their azimuthal Fourier components [22]. To avoid including the origin in the collocation mesh, an odd number of Gauss–Lobatto points in r is used and the equations are solved only in the interval $r \in (0, \Gamma]$. Following [23], we have used the combinations $u_+ = u + iv$ and $u_- = u - iv$ in order to decouple the linear diffusion terms in

the momentum equations. For each Fourier mode, the resulting Helmholtz equations for T, w, u_+ and u_- have been solved using a diagonalization technique in the two coordinates r and z. The imposed parity of the Fourier modes guarantees the regularity conditions at the origin needed to solve the Helmholtz equations [24]. Further details of the numerical code can be found in [25]. We have used $L = 48$ spectral modes in r, $N = 24$ in z, $M = 184$ in θ and a time-step $dt \in [2.5 \times 10^{-7}, 5 \times 10^{-6}]$ thermal time units. The time-step used depends on the Prandtl number and to a lesser extent the Froude number. When these are large, the time-step used needs to be decreased.

III. RESULTS

The present study is focused on examining how the wall modes in rotating convection are quenched in a regime dominated by Coriolis force and large Prandtl number. For a fixed Coriolis number, we consider a variety of aqueous mixtures of glycerine, thus setting the Froude and Prandtl numbers of each mixture, and increase the Rayleigh number from below the onset of the wall modes to beyond values at which bulk convection occurs.

Our results can be characterized by the Nusselt number Nu, the ratio of the vertical heat flux of the flow state to the vertical heat flux due solely to conduction:

$$Nu(r, \theta, z) = -\partial_z T(r, \theta, z). \tag{9}$$

It is also useful to consider the azimuthally averaged Nusselt number given by:

$$\overline{Nu}(r, z) = -\int_0^{2\pi} \partial_z T(r, \theta, z)\, \mathrm{d}\theta\,, \tag{10}$$

and the horizontally averaged Nusselt number $\langle Nu \rangle$ at any height z, given by:

$$\langle Nu \rangle(z) = -\int_0^{\Gamma}\int_0^{2\pi} \partial_z T(r, \theta, z)\, r \mathrm{d}r\mathrm{d}\theta = \int_0^{\Gamma} \overline{Nu}(r, z)\, r\mathrm{d}r. \tag{11}$$

We begin by examening the effects of increasing the Prandtl number whilst ignoring the centrifugal buoyancy (artificially setting $Fr = 0$), as this corresponds to a setting closer to previous studies on Prandtl number effects and provides a case to compare with when centrifugal buoyancy is accounted for.

We set $Ra = 9 \times 10^4$, which is well above the critical Rayleigh number for the onset of wall modes, $Ra_c \sim 4 \times 10^4$, when $\Omega = 625$ and $\Gamma = 4$. In this parameter regime, the wall

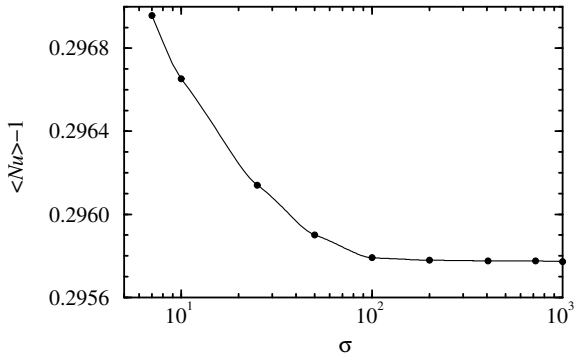

FIG. 2: Variation of the Nusselt number with σ for $\Omega = 625$, $Ra = 9 \times 10^4$, $\Gamma = 4$ and $Fr = 0$.

modes are stable and there is no bulk convection. The wall modes are rotating waves whose spatial structure simply precesses without change (in the rotating frame of reference), thus leading to a time-independent Nusselt number [26]. This Rayleigh number is close to but below the value for which bulk convection occurs. The wall mode structure is maintained for all values of σ without any significant differences for solutions with $\sigma > 100$.

Figure 2 shows how the Nusselt number varies with $\sigma \in [7, 1000]$. The Nusselt number diminishes slightly with increasing σ until $\sigma \sim 100$ and from then on it is independent of σ. The temperature and velocity throughout the cylinder does not vary with Prandtl number for $\sigma > 100$. This is consistent with what is found generally in non-rotating convection, but as we shall now see, is a result of ignoring centrifugal buoyancy effects.

Typically, in rotating convection studies, the Coriolis term is taken into account but the Froude number is artificially set to zero, ignoring the centrifugal buoyancy term. [12, 27] have shown that centrifugal buoyancy plays a significant dynamic role and changes the problem in a fundamental manner. The total buoyancy force (gravitational plus centrifugal) no longer points in the vertical direction, but now also has a radial component which varies with radial distance from the rotation axis. This destroys the horizontal translation invariance that is inherent in the horizontally unbounded theoretical treatments of the problem [7, 28–32]. Furthermore, the reflection symmetry about the cylinder mid-height (the so-called up-down symmetry) is also destroyed. Figure 1 strongly suggests that for the fixed Coriolis number $\Omega = 625$, one cannot ignore centrifugal buoyancy because for the glycerine mixtures

considered, the corresponding Froude number is not small ($0.01 \lesssim Fr \lesssim 10$).

For $Ra \in [2 \times 10^4, 9 \times 10^4]$, we now study the effects of $Fr \neq 0$. We do this by increasing the mass concentration of glycerine in aqueous mixtures, which also increases the viscosity of the fluid. In order to keep the Coriolis number the same for all aqueous mixtures, the rotation rate of the cylinder ω must increase with the viscosity, i.e. the concentration of glycerine, and hence the Froude number Fr also increases. We have considered several glycerine concentrations. For glycerine concentration of about 60%, $Fr \sim 10^{-2}$ is small and negligible and $\sigma \sim 100$, and so we set the test case with which to compare the results for larger glycerine concentrations to be $Fr = 0$ and $\sigma = 100$, nominally corresponding to a 60% glycerine mixture. Figure 3 shows isotherms in a horizontal section of the cylinder at $z = 0.2$ for $\Omega = 625$ and $\Gamma = 4$, for four representative cases at Ra as indicated. In the first row, we have the nominal cases for 60% glycerine mixture with artificially set $Fr = 0$ and $\sigma = 100$. In fact, with $Fr = 0$, there are no discernable changes in the solutions for $\sigma > 100$ over the range of Ra considered in this paper. The other three rows in the figure are for increasing percentages of glycerine in the mixture and are computed with the corresponding physical values of Fr and σ, as indicated. In all simulations, we begin with the lowest value of Ra and use as initial condition the wall mode with azimuthal wavenumber $m = 20$ computed for $Fr = 0$, $\sigma = 7$, $\Gamma = 4$ and $\Omega = 625$. In this parameter regime there is a large Eckhaus-stable band of wall modes with azimuthal wavenumbers varying from about 12 to 36 [18, 19]. By using the same initial condition for low Ra and continuing the resulting wall mode state to higher Ra, we are able to continue the same wall mode branch for the different glycerine concentrations.

The wall-mode structure is maintained for small values of the Froude number, it becomes weaker at intermediate Fr and is quenched for large Fr, where axisymmetric target-like patterns are found. As Fr increases, the precession frequency also changes, as shown in Fig. 4. The precession of the wall modes is retrograde in all cases considered, and increases in absolute value when Fr increases, and the increase is larger for increasing Ra. As the percentage of glycerine is reduced, the precession frequencies ω_p approach those reported in [19], who considered the case of pure water with $Fr = 0$ and $\sigma = 7$. The precession frequencies ω_p reported here and in [19] correspond to the frequencies obtained via FFT of the temperature at a fixed point; the rotation frequency of the pattern, ω_{pattern}, differs from ω_p by a factor of m (the azimuthal wavenumber $m = 20$ in the case considered here):

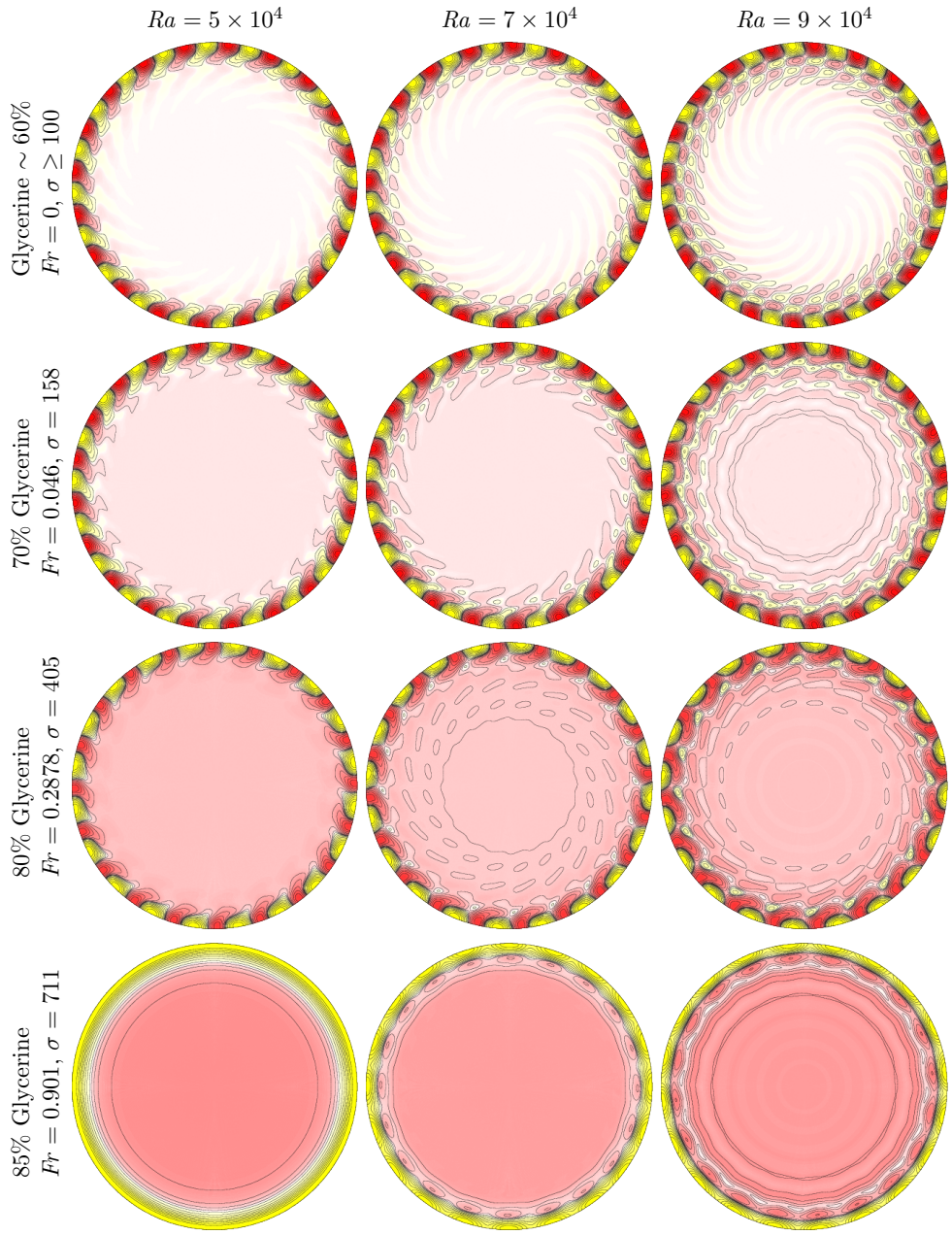

FIG. 3: (Color online) Isotherms at height $z = 0.2$ for $\Omega = 625$, $\Gamma = 4$ and Ra as indicated for $\sigma = 100$ ignoring centrifugal buoyancy (top row with $Fr = 0$), and with the values of Fr and σ corresponding to aqueous mixtures of glycerine at 70% (second row), 80% (third row) and 85% (bottom row) of mass at 22.4°C. There are 10 positive (red/dark gray) and 10 negative (yellow/light gray) isotherms in the range $T \in [-0.5, 0.5]$.

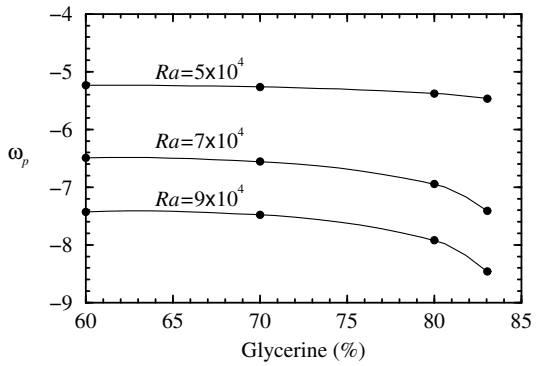

FIG. 4: Variation of the precession frequency of the wall modes with glycerine concentration for various Ra with $\Omega = 625$ and $\Gamma = 4$; the values of σ and Fr used are for the corresponding glycerine mixture at 22.4°C.

$\omega_{\text{pattern}} = \omega_p/m$.

Figure 5(a) shows how $\langle Nu \rangle - 1$, computed at the top endwall $z = 0.5$, varies with the glycerine concentration for various $Ra \leq 9 \times 10^4$, for which the Nusselt number remains time independent. Figures 5(b) and (c) show the same result but as functions of the corresponding values of Fr and σ. The minima in the curves correspond to the glycerine concentrations (and Fr and σ) at which the wall modes are quenched for the given Ra. To the left of these minima (light gray shaded area), wall modes are present, and to the right (dark gray shaded area) the wall modes are not present and the centrifugal buoyancy driven target patterns are observed. For low glycerine concentrations, Fr is small and as the concentration is increased the centrifugal buoyancy strength increases, acting most strongly at large radii where the wall mode plumes reside; it acts to diminish the strength of the wall modes so that they transport less heat. At the same time, the centrifugal buoyancy is also driving an axisymmetric large scale meridional circulation that is enhancing the heat transport, and is responsible for the rapid increase in the Nusselt number at large glycerine concentrations where Fr is also large. Above $Ra = 9 \times 10^4$, the onset of bulk convection is observed.

Figure 6 is the continuation of Fig. 3 to higher Rayleigh numbers. As expected, for fixed glycerine concentration (or fixed Fr and σ), as the Rayleigh number is increased the bulk interior fluid starts to convect. On the other hand, for Ra fixed, an increase in the glycerine concentration enhances the centrifugal buoyancy, and not only are the wall modes

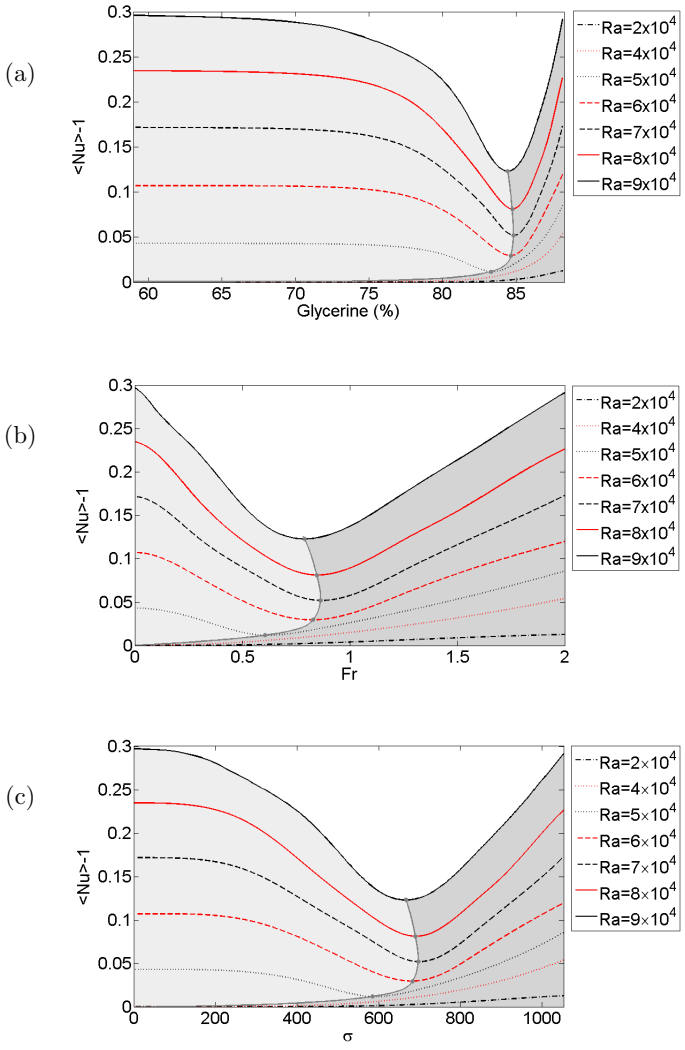

FIG. 5: (Color online) Nusselt number versus (a) glycerine concentration, (b) Froude number and (c) Prandtl number for $\Omega = 625$ and $\Gamma = 4$ and various Ra as indicated. The values of σ and Fr used are for the corresponding glycerine mixture at 22.4°C.

quenched but so too is the bulk convection. When there is bulk convection at low glycerine concentrations, the time evolution of the patterns is of Küppers-Lortz type [33], with rolls changing their orientation in time (see [13, 19] for similar simulations with $Fr = 0$). However, this dynamic is destroyed for high glycerine concentrations as centrifugal buoyancy effects

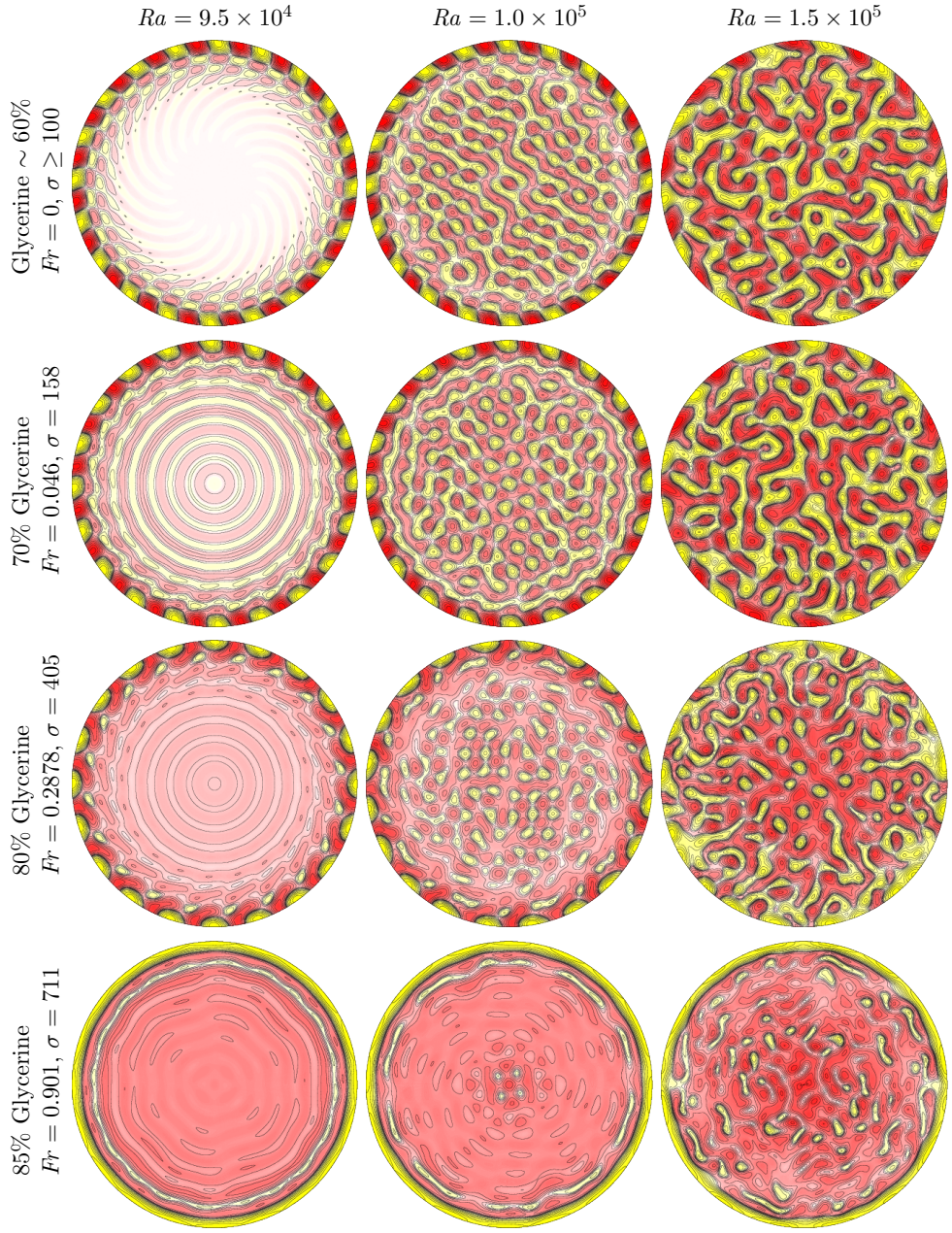

FIG. 6: (Color online) Isotherms at $\theta = 0, \pi/20$ for $\Omega = 625$, $\Gamma = 4$ and Ra as indicated for $\sigma = 100$ ignoring centrifugal buoyancy (top row with $Fr = 0$), and with the values of Fr and σ corresponding to aqueous mixtures of glycerine at 70% (second row), 80% (third row) and 85% (bottom row) of mass at 22.4°C. There are 10 positive (red/dark gray) and 10 negative (yellow/light gray) isotherms in the range $T \in [-0.5, 0.5]$.

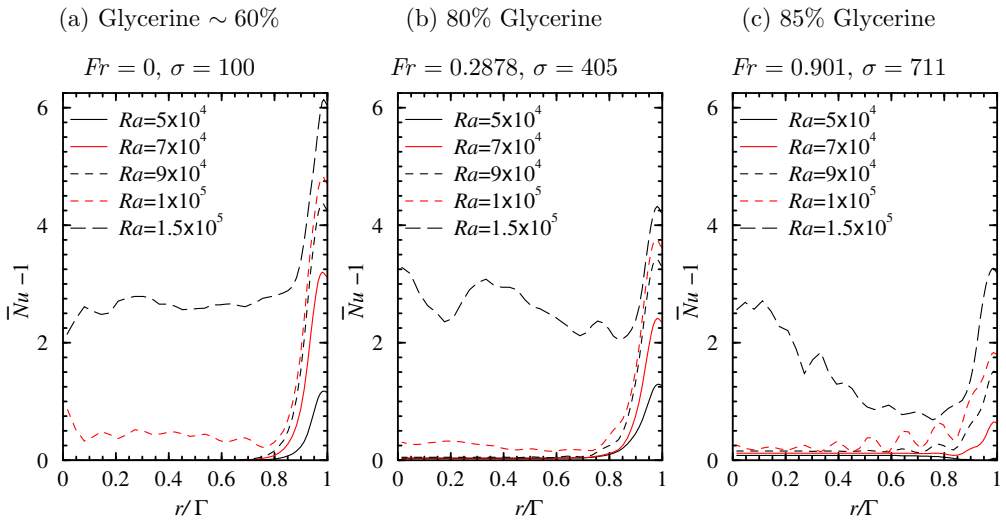

FIG. 7: (Color online) Radial variations of the azimuthally averaged Nusselt number for $\Omega = 625$, $\Gamma = 4$, and various Ra, Fr and σ as indicated.

become more dominant.

Figure 7 depicts the azimuthally averaged Nusselt number $\overline{Nu}(r, z)$ defined in (10), versus the radial distance r at the upper plate ($z = 0.5$). We observe that most of the heat flux occurs in the sidewall boundary layer where either the wall mode plumes reside when Fr is small, or the target pattern rings have the strongest circulation when Fr is large. The Nusselt number increases with the Rayleigh number, but is always localized in the sidewall boundary layer until Ra is increased above the onset of bulk convection. In the highest glycerine concentration case with $Fr = 0.901$, for $Ra = 10^5$, just as the bulk is about to convect, we see that there is a strong correlation between the heat flux radial distribution and the strength of the circulation in the target pattern rings.

IV. CONCLUSIONS

This article addresses the study of rotating convection at large Prandtl numbers, focusing on centrifugal buoyancy effects that are usually neglected when using the Boussinesq approximation. The presence of the centrifugal term means that horizontal periodicity is lost; this is a major set back for analytic and asymptotic studies, as well as numerically, as

Fourier basis functions in the horizontal directions cannot be used. However, the centrifugal buoyancy term is readily accommodated in appropriate numerical treatments, for example using a Chebyshev basis in the radial direction.

Large Prandtl numbers are easily obtained using different concentrations of glycerine in aqueous mixtures, making the parameter ranges investigated in this study readily accessible in laboratory experiments. An additional advantage of using glycerine solutions is that the range of Prandtl and Froude numbers accessible is large: one and two orders of magnitudes respectively, for the numerical simulations reported here.

We have analyzed the flow structure in the Rayleigh number range $5 \times 10^4 \leq Ra \leq 1.5 \times 10^5$, i.e. from the onset of wall modes up to convection in the bulk. We have found that the centrifugal buoyancy term has a large impact on the structure and dynamics of the sidewall boundary layer and also on the bulk convection.

In the absence of rotation, the flow characteristics change with increasing Prandtl number, and at about $\sigma = 100$ an asymptotic regime is reached where there are no further changes in the flow. However in the presence of rotation, increasing σ is linked to increments in Fr and new dynamics result. At low Ra, increasing the glycerine concentration results in the wall modes losing angular velocity in the laboratory frame of reference (i.e. the retrograde rotation rate increases) due to the large scale circulation induced by the centrifugal buoyancy which eventually drives the wall modes towards target patterns with increasing Fr. For larger Ra, the wall modes are quenched and if Fr is large enough the wall modes completely disappear. At large Ra, bulk convection appears in most of the cell, and if $Fr = 0$ is artificially set in the governing equations, the dynamics is related to the Küppers-Lortz dynamics. At higher Fr, the dynamics change as random narrow cold plumes emerging from the top lid emerge. These changes in the flow structure have a direct impact on the heat transfer. For small Fr, most of the heat transport is due to the wall mode plumes. As Fr increases and the wall modes are quenched, the heat transport is reduced, until Fr is large enough so that the centrifugal buoyancy driven large scale circulation leading to the axisymmetric target pattern flow is strong and accounts for the heat transport.

A major conclusion of the present study is that Fr effects cannot be ignored for rotating convection at large Prandtl numbers. The simulations at the largest Ra numbers explored show that the structure and dynamics of the plumes emerging from the top and bottom endwall boundary layers are significantly altered when Fr effects are included. The dynamics

are very different from the Küppers-Lortz dynamics that are observed when $Fr \approx 0$. This aspect warrants further detailed study both from the experimental and the numerical point of view.

Acknowledgments

This work was supported in part by the U.S. National Science Foundation grants DMS-0922864 and CBET-1336410, the Spanish Ministry of Education and Science grants FIS2009-08821, MTM2011-26696, and MINECO: ICMAT Severo Ochoa project SEV-2011-0087.

APPENDIX A: TEMPERATURE-DEPENDENT VISCOSITY

The non-dimensional governing equations including temperature-dependent viscosity are:

$$(\partial_t + \boldsymbol{u}\cdot\nabla)\boldsymbol{u} = -\nabla p + \sigma Ra T\hat{z} + 2\sigma\Omega\boldsymbol{u}\times\hat{z} - \frac{\sigma Fr Ra}{\Gamma}T\boldsymbol{r} + \sigma\nabla\cdot\left[\frac{\nu}{\nu_0}(\nabla\boldsymbol{u} + (\nabla\boldsymbol{u})^T)\right],$$
$$(\partial_t + \boldsymbol{u}\cdot\nabla)T = \nabla^2 T, \qquad \nabla\cdot\boldsymbol{u} = 0. \tag{A1}$$

The equation $\nu_C(T)$ that approximates the dependence of viscosity with temperature for glycerine-water mixtures from [34] is used. Since in our setting the temperature range is small, we use a linear approximation for the temperature dependence of viscosity, given by the tangent to the curve reported by [34] at the reference temperature T_0. In dimensionless form, it is given by

$$\nu(T) = \nu_0(1-\gamma T), \tag{A2}$$

where γ is a linear rate given by

$$\gamma = \varepsilon\Delta T, \quad \varepsilon = -\frac{1}{\nu_0}\frac{\mathrm{d}\nu_C}{\mathrm{d}T}\Big|_{T=T_0}. \tag{A3}$$

The viscous term in (A1), $\sigma\nabla\cdot\left[\frac{\nu(T)}{\nu_0}(\nabla\boldsymbol{u} + (\nabla\boldsymbol{u})^T)\right]$, that depends on the velocity, is expanded in a part that is independent of the temperature and is treated implicitly, and another part that explicitly depends on T and is proportional to γ, that is treated explicitly in the same way as the Coriolis term, $\sigma\Omega\boldsymbol{u}\times\hat{z}$. This scheme works well for a weak dependency of viscosity on temperature and the set of Prandtl numbers considered in our study. However,

it is not stable for stronger viscosity dependencies on temperature or infinite Prandtl number (see [35] for further details).

We have studied temperature-dependent viscosity effects by setting γ equal to the values corresponding to the various glycerine concentrations considered. Fixing $\sigma = 100$ and $Ra = 9 \times 10^4$, we tested this effect with and without centrifugal buoyancy, i.e. with $Fr = 0$ and Fr corresponding to various glycerine mixtures. We found that the relative differences in the horizontally averaged Nusselt number at either the bottom or top endwall obtained with constant viscosity ($\gamma = 0$) and with temperature-dependent viscosity are less than 0.2%. Moreover, in all of the cases tested, the relative differences between the temperature fields at the point $(r, \theta, z) = (3.2, 0, 0)$ are below 5%. Even at the largest Fr, the temperature-dependent viscosity case does not produce significant changes in the solution with respect to the case of constant viscosity. The same was observed at larger $Ra = 10^5$. These results are as to be expected given that for the parameter regimes used, $\alpha \Delta T < 10^{-3}$, as noted earlier. Hence, since the effects of temperature-dependent viscosity are negligible and yet quite expensive to incorporate computationally, we have keep the viscosity constant for the result in the main body of this paper.

[1] M. Lappa, *Rotating Thermal Flows in Natural and Industrial Processes* (Wiley, 2012).

[2] E. A. Spiegel, Annu. Rev. Astron. Astrophys. **9**, 323 (1971).

[3] C. F. Chen and S. Thangam, J. Fluid Mech. **161**, 161 (1985).

[4] E. M. King and J. M. Aurnou, Proc. Nat. Acad. Sci. USA **110**, 6688 (2013).

[5] R. J. A. M. Stevens, H. J. H. Clercx, and D. Lohse, Phys. Rev. E **86**, 056311 (2012).

[6] P. Constantin, C. Hallstrom, and V. Poutkaradze, J. Math. Phys. **42**, 773 (2001).

[7] C. R. Doering and P. Constantin, J. Math. Phys. **42**, 784 (2001).

[8] X. Yan, J. Math. Phys. **45**, 2718 (2004).

[9] G. M. Homsy and J. L. Hudson, J. Fluid Mech. **35**, 33 (1969).

[10] J. E. Hart, J. Fluid Mech. **403**, 133 (2000).

[11] N. Becker, J. D. Scheel, M. C. Cross, and G. Ahlers, Phys. Rev. E **73**, 066309 (2006).

[12] F. Marques, I. Mercader, O. Batiste, and J. M. Lopez, J. Fluid Mech. **580**, 303 (2007).

[13] A. Rubio, J. M. Lopez, and F. Marques, J. Fluid Mech. **644**, 337 (2010).

[14] J. M. Lopez and F. Marques, J. Fluid Mech. **628**, 269 (2009).

[15] R. J. A. M. Stevens, H. J. H. Clercx, and D. Lohse, Eur. J. Mech. B-Fluids **40**, 41 (2013).

[16] D. D. Gray and A. Giorgini, Intnl J. Heat Mass Transfer **19**, 545 (1976).

[17] F. H. Busse, J. Fluid Mech. **30**, 625 (1967).

[18] J. M. Lopez, F. Marques, I. Mercader, and O. Batiste, J. Fluid Mech. **590**, 187 (2007).

[19] F. Marques and J. M. Lopez, Phys. Fluids **20**, 024109 (2008).

[20] S. P. Gregory, in *Glycerine: A Key Cosmetic Ingredient*, edited by E. Jungermann and N. O. V. Sonntag (Marcel Dekker, New York, 1991) pp. 113–156.

[21] S. Hughes and A. Randriamampianina, Intnl J. Num. Meth. Fluids **28**, 501 (1998).

[22] B. Fornberg, *A Practical Guide to Pseudospectral Methods* (Cambridge Univ. Press, 1998).

[23] S. A. Orszag and A. T. Patera, J. Fluid Mech. **128**, 347 (1983).

[24] I. Mercader, M. Net, and A. Falqués, Comp. Meth. Appl. Mech. & Engng **91**, 1245 (1991).

[25] I. Mercader, O. Batiste, and A. Alonso, Computers & Fluids **39**, 215 (2010).

[26] H. F. Goldstein, E. Knobloch, I. Mercader, and M. Net, J. Fluid Mech. **248**, 583 (1993).

[27] J. M. Lopez, A. Rubio, and F. Marques, J. Fluid Mech. **569**, 331 (2006).

[28] S. Chandrasekhar, *Hydrodynamic and Hydromagnetic Stability* (Oxford Univ. Press, 1961).

[29] J. H. P. Dawes, J. Fluid Mech. **428**, 61 (2001).

[30] R. C. Kloosterziel and G. F. Carnevale, J. Fluid Mech. **480**, 25 (2003).

[31] K. Julien and E. Knobloch, J. Math. Phys. **48**, 065405 (2007).

[32] A. Prosperetti, Phys. Fluids **24**, 114101 (2012).

[33] G. Küppers and D. Lortz, J. Fluid Mech. **35**, 609 (1969).

[34] N. S. Cheng, Ind. Eng. Chem. Res. **47**, 3285 (2008).

[35] J. Curbelo and A. M. Mancho, Commun. Nonlinear Sci. Numer. Simulat. **19**, 538 (2014).

CHAPTER 4

Discussion

This thesis addresses the numerical analysis of several convection problems through spectral techniques. A first problem involves a viscosity which strongly depends on temperature in the infinite Prandtl number limit, in a 2D domain in the presence of the O(2) symmetry. We propose a numerical scheme in order to solve the time-dependent problem in this context. A second problem involves a 3D domain in a cylindrical geometry, and here we consider the dynamics of a fluid in the presence of rotation with viscosity weakly dependent on temperature and large Prandtl number.

This chapter extends the discussion regarding technical details about numerical aspects as well as the description of solutions that have not been addressed before.

4.1. Convection problem with viscosity strongly dependent on temperature (2D)

4.1.1. Numerical Methods

Stationary solutions and the spatial discretization

We now provide details on the numerical computation of stationary solution to equations (1.1)-(1.3). For this purpose, we approximate the unknown fields by using a collocation method with expansions that consider Chebyshev polynomials along the vertical direction and Fourier modes along the horizontal coordinate. Chebyshev polynomials are eigenfunctions of a singular Sturm Liouville problem. For this reason they form a complete basis of a Hilbert space and are suitable for approaching functions with no *a priori* restrictions in the boundary conditions [15]. In the horizontal direction we use Fourier modes, which are convenient because they verify the periodic boundary conditions present in the problem.

Our Fourier expansions are linked to the discrete Fourier transform. These are the coefficients

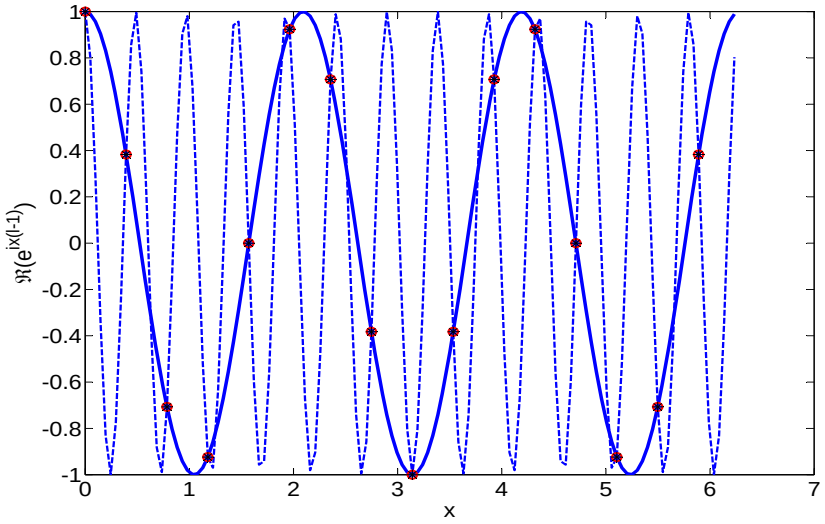

Figure 4.1. The functions $f(x) = \Re(e^{ix(l-1)})$ with $l = 14$ (red circ) is indistinguishable from the same function with $l = 14 - L$, where $L = 16$ (black asterisks) when it is evaluated in certain x_j.

$\{\tilde{u}_j\}$ with $j = 0, \ldots, L-1$ in the expression:

$$u(x_j) = \sum_{l=0}^{L-1} \tilde{u_j} e^{ilx_j}, \quad j = 0, \ldots, L-1, \tag{4.1}$$

where we consider the uniform grid $x_j = 2\pi j/L$, $j = 0, \ldots, L-1$. The expression (4.1) is not a good interpolant for the function $u(x_j)$, since it is a complex function (the function u is real) outside the grid nodes x_j and its real part oscillates very rapidly. According to [94] a true interpolant that uses the coefficients of the discrete Fourier transform takes into account the phenomenon of aliasing. Aliasing implies that one may add L to any of the complex-sinusoid frequencies without changing the values in the x_j points. In this way, this phenomenon allows the replacement of e^{ilx_j} with $e^{i(l-1-L)x_j}$, for $L/2 + 1 \leq l \leq L$, since these two functions are the same at the nodes x_j (see Figure 4.1). A good Fourier interpolant thus has the form:

$$u(x_j) = \sum_{l=0}^{L/2} \tilde{u_j} e^{ilx_j} + \sum_{l=L/2+1}^{L-1} \tilde{u_j} e^{i(l-1-L)x_j}, \quad j = 0, \ldots, L-1. \tag{4.2}$$

This is a good interpolant for the function $u(x_j)$ because outside the grid points it is a real function (for every function e^{ilx_j} in the first summation there exist its complex conjugate in the second summation) and it does not oscillate wildly. This interpolant is for 1D functions, while the problem given by equations (1.1)-(1.3), together with the boundary conditions (1.4), is 2D. Thus, in this case, the spatial expansions for an unknown perturbation field Y is:

$$Y(x,z) = \sum_{l=1}^{\lceil L/2 \rceil} \sum_{m=0}^{M-1} a_{lm}^{Y} T_m(z) e^{i(l-1)x} + \sum_{l=\lceil L/2 \rceil+1}^{L} \sum_{m=0}^{M-1} a_{lm}^{Y} T_m(z) e^{i(l-1-L)x}. \tag{4.3}$$

In this notation, $\lceil\cdot\rceil$ represents the nearest integer towards infinity. Here L and M are the number of nodes in the horizontal and vertical directions, respectively. In the horizontal direction, these nodes are at the uniform grid x_j, while in the vertical direction z_j are at the collocation Gauss Lobato points:

$$\begin{aligned} \text{Uniform grid:} \quad & x_j = (j-1)\frac{2\pi}{L}, && j = 1, \ldots, L; \\ \text{Gauss–Lobatto:} \quad & z_i = \cos\left(\left(\frac{i-1}{M-1} - 1\right)\pi\right), && i = 1, \ldots, M. \end{aligned} \tag{4.4}$$

The coefficients of this expansion a^Y_{lm} are complex numbers and are given by conjugated pairs in such a way that, for instance, $a^Y_{2m} = a^{Y*}_{Lm}$. As the unknown functions Y are real, they admit expansions with real functions and real unknowns. In order to obtain these functions, we take into account Euler's formula $e^{ilx} = \cos(lx) + i\sin(lx)$, which is replaced in (4.3). In accordance with these considerations, the following equations are obtained:

$$Y(x,z) = \sum_{l=1}^{\lceil L/2\rceil}\sum_{m=0}^{M-1} b^Y_{lm} T_m(z)\cos((l-1)x) + \sum_{l=2}^{\lceil L/2\rceil}\sum_{m=0}^{M-1} c^Y_{lm} T_m(z)\sin((l-1)x). \tag{4.5}$$

The relations among the real and complex coefficients are:

$$\begin{aligned} & b^Y_{1m} = a^Y_{1m} \\ & b^Y_{lm} = 2\Re(a^Y_{lm}), \quad c^Y_{lm} = -2\Im(a^Y_{lm}), \quad \text{for } l = 2, \ldots, \lceil L/2\rceil. \end{aligned} \tag{4.6}$$

Note that, strictly speaking, expansion (4.3) is a real function only if every coefficient in the first summatory for $l \geq 2$ has a conjugate pair in the second summatory. This implies that L must be an odd number; thus, in what follows we restrict ourselves to odd L values.

In order to obtain the stationary solutions (satisfying the stationary version of equations (1.1)-(1.3) and which are obtained by canceling the partial derivatives with respect to time) we use a variant of the iterative Newton-Raphson methods. This method starts with an approximate solution at step $s = 0$, to which is added a small correction in tilde:

$$(\mathbf{u}^s + \tilde{\mathbf{u}}, \theta^s + \tilde{\theta}, P^s + \tilde{P}). \tag{4.7}$$

These expressions are introduced into the system (1.1)-(1.3), and after canceling the nonlinear terms in tilde, the following equations are obtained:

$$0 = \nabla\cdot\tilde{\mathbf{u}} + \nabla\cdot\mathbf{u}^s, \tag{4.8}$$

$$0 = -\partial_x\tilde{P} - \partial_x P^s + \frac{1}{\nu_0}[L_{11}(\theta^s, u^s_x, u^s_z) + L_{12}(\theta^s)\tilde{u}_x + L_{13}(\theta^s)\tilde{u}_z + L_{14}(\theta^s, u^s_x, u^s_z)\tilde{\theta}], \tag{4.9}$$

$$0 = -\partial_z\tilde{P} - \partial_z P^s + \frac{1}{\nu_0}[L_{21}(\theta^s, u^s_x, u^s_z) + L_{22}(\theta^s)\tilde{u}_x + L_{23}(\theta^s)\tilde{u}_z + (L_{24}(\theta^s, u^s_x, u^s_z) + Ra)\tilde{\theta}], \tag{4.10}$$

$$0 = \tilde{\mathbf{u}}\cdot\nabla\theta^s + \mathbf{u}^s\cdot\nabla\tilde{\theta} + \mathbf{u}^s\cdot\nabla\theta^s - \Delta\tilde{\theta} - \Delta\theta^s. \tag{4.11}$$

Here, L_{ij} $(i = 1, 2,\ j = 1, 2, 3, 4)$ are linear operators with non-constant coefficients, which are defined as follows:

$$L_{11}(\theta, u_x, u_z) = 2\partial_\theta\nu(\theta)\partial_x\theta\partial_x u_x + \nu(\theta)\Delta u_x + \partial_\theta\nu(\theta)\partial_z\theta(\partial_x u_z + \partial_z u_x), \tag{4.12}$$

$$L_{12}(\theta) = 2\partial_\theta\nu(\theta)\partial_x\theta\partial_x + \nu(\theta)\Delta + \partial_\theta\nu(\theta)\partial_z\theta\partial_x, \tag{4.13}$$

$$L_{13}(\theta) = \partial_\theta\nu(\theta)\partial_z\theta\partial_x, \tag{4.14}$$

$$\begin{aligned} L_{14}(\theta, u_x, u_z) =& 2\partial_\theta\nu(\theta)\partial_x u_x\partial_x + 2\partial^2_{\theta\theta}\nu(\theta)\partial_x\theta\partial_x u_x + \partial_\theta\nu(\theta)\Delta u_x \\ &+ (\partial_x u_z + \partial_z u_x)(\partial_\theta\nu(\theta)\partial_z + \partial^2_{\theta\theta}\nu(\theta)\partial_z\theta), \end{aligned} \tag{4.15}$$

$$L_{21}(\theta, u_x, u_z) = 2\partial_\theta\nu(\theta)\partial_z\theta\partial_z u_z + \nu(\theta)\Delta u_z + \partial_\theta\nu(\theta)\partial_x\theta(\partial_z u_x + \partial_x u_z), \tag{4.16}$$

$$L_{22}(\theta) = \partial_\theta\nu(\theta)\partial_x\theta\partial_z, \tag{4.17}$$

$$L_{23}(\theta) = 2\partial_\theta\nu(\theta)\partial_z\theta\partial_z + \nu(\theta)\Delta + \partial_\theta\nu(\theta)\partial_x\theta\partial_z, \tag{4.18}$$

$$\begin{aligned} L_{24}(\theta, u_x, u_z) =& 2\partial_\theta\nu(\theta)\partial_z u_z\partial_z + 2\partial_{\theta\theta}\nu(\theta)\partial_z\theta\partial_z u_z + \partial_\theta\nu(\theta)\Delta u_z \\ &+ (\partial_z u_x + \partial_x u_z)(\partial_\theta\nu(\theta)\partial_x + \partial_{\theta\theta}\nu(\theta)\partial_x\theta). \end{aligned} \tag{4.19}$$

The unknown fields $\tilde{\mathbf{u}},\ \tilde{P},\ \tilde{\theta}$ are found by solving the linear system with the boundary conditions (1.4), and the new approximate solution $s+1$ is set to

$$\mathbf{u}^{s+1} = \mathbf{u}^s + \tilde{\mathbf{u}},\ \theta^{s+1} = \theta^s + \tilde{\theta},\ P^{s+1} = P^s + \tilde{P}.$$

The whole procedure is repeated for $s+1$ until a convergence criterion is fulfilled.

At each step, after replacing the expression (4.5) in this set of equations, we obtain a the linear system

$$AX = b, \tag{4.20}$$

where X contains the coefficients of the expansion (4.5) of the unknown fields. Although (4.3) is correct and provides good results, we do not employ it in this work because it involves complex functions and complex unknowns a^Y_{lm}, eventually leading to the inversion of complex matrices which computationally are more costly than real matrices. We have verified that in our problem the time taken to solve the linear system (4.20) increases by a factor of three when it is complex rather than when it is real. The resulting system is evaluated at the collocation points according to the rules given in Section 3.1. This procedure has been successfully performed in [54, 57, 83, 90]; however, in our setup, results are improved if, for the equation (4.10) imposed at the upper boundary, the continuity equation is assumed and the term $\partial^2_{zz}u_z$ is replaced by $-\partial_{xz}u_x$. According to the method discussed in the references [54, 57, 83, 90], this equation is imposed at the collocation points $i = M, j = 1, \ldots, L$. We fix the constant by removing equation (4.10) on node $i = 2, j = 1$, which is used to fix the additive arbitrary constant for the pressure. This is done by adding the equation $b^P_{10} = 0$ at this point. Fixing the constant for the pressure field determines the linear system (4.20), which otherwise is undetermined. However, we have observed that in problems with viscosity strongly dependent on temperature, as in the case of arctangent viscosity laws, this method gives rise to inaccuracies in the pressure field, which are detailed below. Figure 4.2(a) and the blue line in Figure 4.2(d) show the effects of such replacement in a stationary solution obtained for the "smooth" viscosity law at parameters $b = 10, a = 0.1$ with $Ra = 1300$ and $\Gamma = 3.4$. The inaccuracies are mainly observed at the upper boundary. Figure 4.2(a) and 4.2(b) compare the effect with/without replacing $\partial^2_{zz}u_z$ by $-\partial^2_{xz}u_x$. The difference is best seen in Figure 4.2(d). The direct application of the methodology reported in references [54, 57, 83, 90] introduces weakly

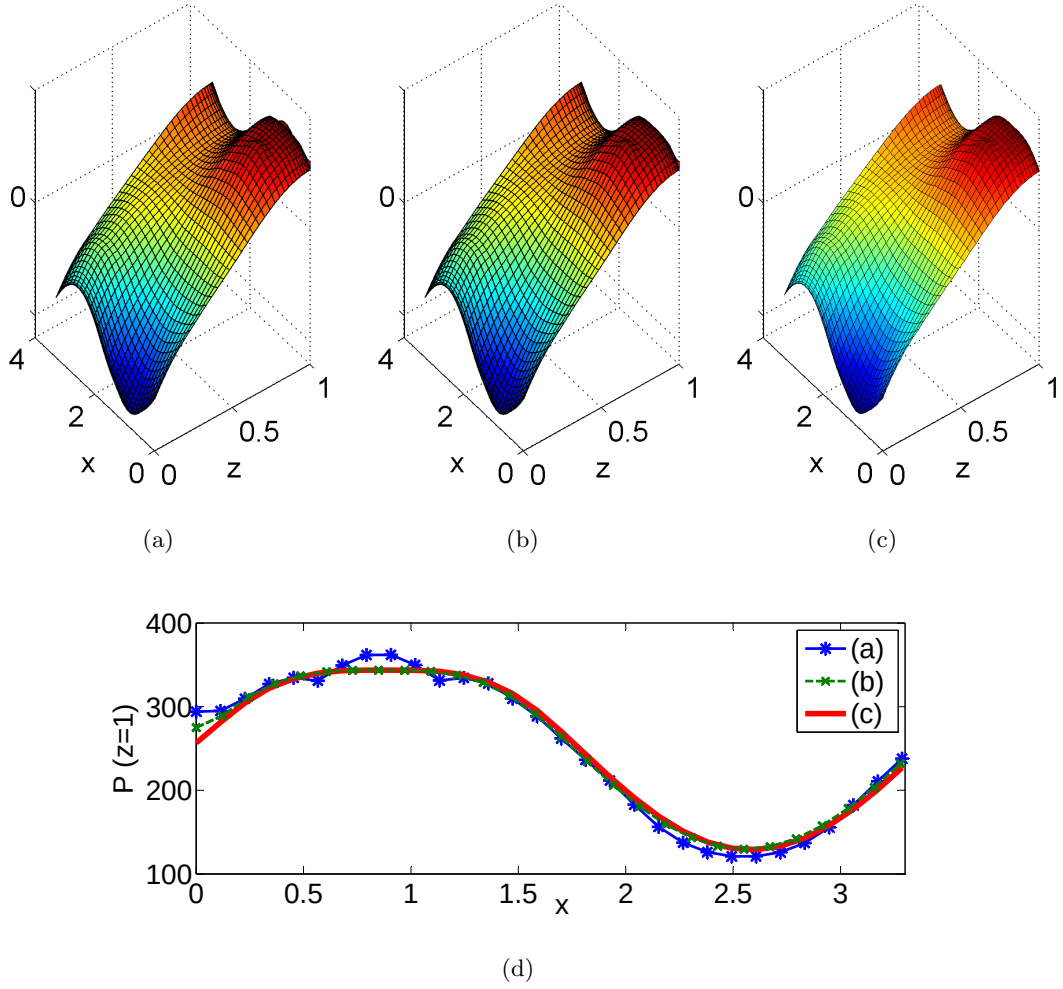

Figure 4.2. Pressure field for a stationary solution obtained with the "smooth" arctangent viscosity law (1.7) using $b = 10, a = 0.1$ with $Ra = 1300$ and $\Gamma = 3.4$; a) Shows the pressure obtained without replacing $\partial^2_{zz} u_z$ by $-\partial^2_{xz} u_x$ in the equation (4.10); b) Shows the pressure replacing $\partial^2_{zz} u_z$ by $-\partial^2_{xz} u_x$ in the equation (4.10) without using SVD; c) Shows the pressure replacing $\partial^2_{zz} u_z$ by $-\partial^2_{xz} u_x$ in the equation (4.10) using SVD; d) Shows a comparison of previous cases in the boundary $z = 1$.

oscillating structures on the pressure field, and these diminish with the alternative method, the output of which is displayed in Figure 4.2(b) and by the green line in Figure 4.2(d).

We have observed that the positions at which the oscillations appear are directly related to the position in which equation (4.10) is substituted by the equation which fixes the arbitrary additive constant in the pressure field. As previously noted, this step is necessary to obtain a determined system in (4.20), but on the other hand, as we note here, this method may cause oscillations in the pressure field. In order to overcome this drawback, instead of fixing the pressure constant, we opt for computing a pseudo-inverse of the matrix A by using the singular value decomposition (SVD). Let $A = U\Sigma V^*$ be the singular value decomposition of A; Σ being a rectangular diagonal matrix with diagonal entries that are the singular values of A in decreasing order, and unitary ma-

trices U and V. From this decomposition, the pseudo-inverse is $V\Sigma^{+}U^{*}$. Here U^{*} is the conjugate transpose of U and Σ^{+} is the pseudoinverse of a diagonal matrix, *i.e.* it takes the reciprocal of each non-zero element on the diagonal, and transposes the resulting matrix. Finding the solution of the system (4.20) in this way eliminates spurious oscillations of the pressure field (see Figure 4.2(c) and the red line in Figure 4.2(d)). Computationally, however this is much more expensive than solving the determined linear system (4.20) with standard MATLAB techniques such as the command $A \backslash b$, which optimizes the solution of the linear system by choosing the most appropiate method according to the structure of matrix A (see MATLAB manual). For this reason, our final choice uses a combination of both methods. The iterative procedure is implemented by fixing the constant for pressure, and once the tolerance is attained one extra iteration is performed using the pseudo-inverse matrix.

Linear Stability

Completing the description of the stationary solutions found at different values of the parameter space requires analysis of their stability properties. Time-dependent regimes will then be explored in the regions in which unstable branches emerge.

The stability of stationary states, u^b, θ^b, P^b, is analyzed by adding a perturbation to them as follows:

$$\begin{aligned}
\mathbf{u}(x,z,t) =& \mathbf{u}^b(x,z) + \tilde{\mathbf{u}}(x,z)\mathrm{e}^{\lambda t},\\
\theta(x,z,t) =& \theta^b(x,z) + \tilde{\theta}(x,z)\mathrm{e}^{\lambda t},\\
P(x,z,t) =& P^b(x,z) + \tilde{P}(x,z)\mathrm{e}^{\lambda t}.
\end{aligned} \tag{4.21}$$

The expressions are introduced into the equations (1.1)-(1.3), and after dropping the nonlinear terms the linearized equations are obtained:

$$0 = \nabla \cdot \tilde{\mathbf{u}} \tag{4.22}$$

$$0 = -\partial_x \tilde{P} + \frac{1}{\nu_0}[L_{12}(\theta^b)\tilde{u}_x + L_{13}(\theta^b)\tilde{u}_z + L_{14}(\theta^b, u_x^b, u_z^b)\tilde{\theta}] \tag{4.23}$$

$$0 = -\partial_z \tilde{P} + \frac{1}{\nu_0}[L_{22}(\theta^b)\tilde{u}_x + L_{23}(\theta^b)\tilde{u}_z + (L_{24}(\theta^b, u_x^b, u_z^b) + Ra)\tilde{\theta}] \tag{4.24}$$

$$0 = \tilde{\mathbf{u}} \cdot \nabla\theta^b + \mathbf{u}^b \cdot \nabla\tilde{\theta} + \mathbf{u}^b \cdot \nabla\theta^b - \Delta\tilde{\theta} + \lambda\tilde{\theta}, \tag{4.25}$$

where the operators L_{ij} are the same as those defined in (4.12)-(4.19). Together with their boundary conditions, equations (4.22)-(4.25) define a generalized eigenvalue problem. The sign in the real part of the eigenvalue λ determines the stability of the solution: if it is negative, the perturbation decays and the stationary solution is stable, while if it is positive the perturbation grows over time and the stationary solution is unstable.

Any unknown field Y in the generalized eigenvalue problem (4.22)-(4.25) is approached by means of a spectral method according to the expansion given in (4.5). The eigenvalue problem is thus transformed into one of the form:

$$Aw = \lambda Bw \tag{4.26}$$

in which w contains the coefficients of the eigenfunction and λ is the eigenvalue. The matrices A and B are expressed as follows:

$$A = \begin{pmatrix} K & C \\ \widehat{C}^T & 0 \end{pmatrix}; \quad B = \begin{pmatrix} M & 0 \\ 0 & 0 \end{pmatrix}, \tag{4.27}$$

where K and M are matrices of size $\bar{n} \times \bar{n}$ and C and $\hat{C}$ are $\bar{n} \times \bar{m}$ matrices with $\bar{n} > \bar{m}$. Here $\bar{n} = 3 \times L \times M$ and $\bar{m} = L \times M$.

In this section we explain in detail some transformations that we apply in order to solve this generalized eigenvalue problem efficiently from the computational point of view. Our procedure is taken from [82] and has been adapted to our setting. The eigenvalues of the problem (4.26) can be infinite, because B is singular and this prevents us from employing the *eigs* subroutine of MATLAB that uses the Arnoldi for computing just a reduced number of eigenvalues, which are those of interest in our problem. In order to overcome this difficulty, in the work [82] the use of a modified Cayley transformation is proposed, which preconditions the eigenvalue problem and transforms it into another one with all its eigenvalues finite.

The transformation is performed in such a way that an infinite eigenvalue of the original problem corresponds to a concrete and known finite eigenvalue for the new eigenvalue problem. Denote by λ_i, $i = 1, \ldots, \bar{r}$, the $\bar{r}$ finite eigenvalues of (4.26) and by $\sigma(A, B)$ the set of these eigenvalues. We consider the following direct extension of the Cayley transform. For $\alpha_1, \alpha_2 \in \mathbb{R}$ with $\alpha_2 < \alpha_1 < 0$ and $\alpha_1 \notin \sigma(A, B)$, consider

$$(A - \alpha_2 B)w = \mu(A - \alpha_1 B)w. \tag{4.28}$$

It is not difficult to show that the eigenvalues of this problem are given by

$$\begin{aligned} \mu_i &= \frac{\lambda_i - \alpha_2}{\lambda_i - \alpha_1}, && i = 1, \ldots, \bar{r}, \\ \mu_i &= 1, && i = \bar{r} + 1, \ldots, \bar{n} + \bar{m}, \end{aligned} \tag{4.29}$$

in which, the eigenvalue equal to 1, of multiplicity $\bar{n} + \bar{m} - \bar{r}$, arises from the infinite eigenvalue of (4.26). For $\lambda \in \mathbb{C}$, the equation

$$\mu = C(\lambda) = \frac{\lambda - \alpha_2}{\lambda - \alpha_1} \tag{4.30}$$

represents a conformal transformation between the λ and μ planes.

We then introduce the following eigenvalue problem

$$\hat{A}w = \mu \hat{B}w, \tag{4.31}$$

where

$$\hat{A} = \begin{pmatrix} K - \alpha_2 & \alpha_3 C \\ \alpha_3 \widehat{C}^T & 0 \end{pmatrix}, \quad \hat{B} = \begin{pmatrix} K - \alpha_1 M & C \\ \hat{C}^T & 0 \end{pmatrix}, \tag{4.32}$$

with $\alpha_3 \notin \{C(\lambda)\}_1^{\bar{r}}$. Thus, the algorithm for solving the eigenvalue problem (4.26) is as follows: first we solve the system $\hat{A}X = \hat{B}$. After computing X, the Arnoldi method (MATLAB function *eigs*) is used for calculating s eigenvalues of X with the largest magnitude: $\mu_i, i = 1 \ldots, s$. If the

number of these eigenvalues with $|\mu_i| < 1$ is zero, α_2 is increased (if $\alpha_2 > \alpha_1$ the values of α_1, α_2 are exchanged) we define the matrices $\hat{A}$ and $\hat{B}$ again and the process is repeated. Finally the λ_i, $i = 1, \ldots, \bar{s}$ are calculated using (4.30). We take as starting values $\alpha_3 = 0$, $\alpha_2 = -6$ and $\alpha_1 = -0.1$.

As reported in [82], this procedure accelerates enormously the calculation of the generalized eigenvalue problem with respect to the direct use of the standard MATLAB subroutine *eig*, and we use it to produce the bifurcation diagrams reported in Sections 3.1, 3.2 and 3.3.

Time Evolution

We provide details on the numerical computation of time dependent solutions that complete the information given in the articles. First, we explain and compare different existing approaches through a simple example.

In Section 3.1, semi-implicit numerical methods are presented to compute the time-dependent solutions that appear in Sections 3.2 and 3.3. The correct performance of these methods for convection problems has been proven in several contexts and works, as reported in Section 3.1. In this work, given that it is rather illustrative, we discuss the performance of these methods in a simple, non-linear and stiff problem, the forced Van der Pol oscillator, which is given by

$$\begin{aligned} \frac{\partial x}{\partial t} &= -y, \\ \varepsilon \frac{\partial y}{\partial t} &= x - \left(\frac{y^3}{3} - y \right) = x + y - \frac{y^3}{3}. \end{aligned} \tag{4.33}$$

The limit case $\varepsilon = 0$ corresponds to the unforced Van der Pol problem. This limit is a simple example of a differential algebraic equation (DAE) [52]. DAEs have the general form:

$$M(t, \mathbf{x}) \partial_t \mathbf{x} = f(t, \mathbf{x}), \tag{4.34}$$

where the matrix $M(t, x)$ is singular. For instance, for the Van der Por problem, the matrix M has the form:

$$M = \begin{pmatrix} 1 & 0 \\ 0 & \varepsilon \end{pmatrix}, \tag{4.35}$$

which is singular in the limit $\varepsilon = 0$.

The 2D convection problem with viscosity strongly dependent on temperature and infinite Prandtl number, studied in Sections 3.1, 3.2 and 3.3 is also a DAE, as its governing equations:

$$\nabla \cdot \mathbf{u} = 0, \tag{4.36}$$

$$0 = Ra\theta \vec{e}_3 - \nabla P + \operatorname{div} \left(\frac{\nu(\theta)}{\nu_0} (\nabla \mathbf{u} + (\nabla \mathbf{u})^T) \right), \tag{4.37}$$

$$\partial_t \theta + \mathbf{u} \cdot \nabla \theta = \Delta \theta, \tag{4.38}$$

are related to the expression (4.34), in which the matrix M has the block-form:

$$M = \begin{pmatrix} 0 & 0 & 0 \\ 0 & 0 & 0 \\ 0 & 1 & 0 \end{pmatrix} \quad \text{being } \partial_t \mathbf{x} = \begin{pmatrix} \partial_t \mathbf{u} \\ \partial_t \theta \\ \partial_t P \end{pmatrix}. \tag{4.39}$$

We discuss the performance of several multistep methods which are a good approach for addressing DAE and stiff problems [51, 52]. For computing the solution in a future time $n+1$, these methods make use of the solution at several previous steps $n, n-1$, etc. In particular we use several backward differentiation formulas (BDF). BDF are a family of implicit schemes for which we explore some semi-implicit approaches.

1. **Implicit scheme**. This is used as the reference method for approaching the problem:

$$M(t_{n+1}, \mathbf{x}^{n+1})\partial_t \mathbf{x}^{n+1} = f(t_{n+1}, \mathbf{x}^{n+1}). \tag{4.40}$$

Our scheme uses a third order backward differentiation formula for evaluating the time derivative $\partial_t \mathbf{x}^{n+1}$. This is done by interpolating the field at time $\mathbf{x}^{n+1}$ with a third order Lagrange polynomial, which is then derived. The explicit expression for the derivatives in the fixed time step case is:

$$\partial_t \mathbf{x}^{n+1} = \frac{11\mathbf{x}^{n+1} - 18\mathbf{x}^n + 9\mathbf{x}^{n-1} - 2\mathbf{x}^{n-2}}{6\Delta t}. \tag{4.41}$$

In accordance with this approach, the Van der Por problem is solved with the scheme:

$$\begin{aligned} \frac{11x^{n+1} - 18x^n + 9x^{n-1} - 2x^{n-2}}{6\Delta t} &= -y^{n+1}, \\ \varepsilon\frac{11y^{n+1} - 18y^n + 9y^{n-1} - 2y^{n-2}}{6\Delta t} &= x^{n+1} + y^{n+1} - \frac{(y^{n+1})^3}{3}, \end{aligned} \tag{4.42}$$

and the convection problem is approached as:

$$0 = \nabla \cdot \mathbf{u}^{n+1}, \tag{4.43}$$

$$0 = Ra\theta^{n+1}\vec{e_3} - \nabla P^{n+1} + NL(\theta^{n+1}, \mathbf{u}^{n+1}), \tag{4.44}$$

$$\frac{11\theta^{n+1} - 18\theta^n + 9\theta^{n-1} - 2\theta^{n-2}}{6\Delta t} = -NL(\theta^{n+1}, \mathbf{u}^{n+1}) + \Delta\theta^{n+1}. \tag{4.45}$$

The results reported in Section 3.1 and in Figure 4.4 consider a different version of (4.45), which is suitable for the use of variable time steps. Here, for simplicity, we only annotate the fixed step scheme.

2. **A semi-implicit scheme**. We propose a semi-implicit approach to the fully implicit problem, which assumes that the solution at time $n+1$ is a small perturbation $\tilde{Z}$ of the solution at time n; thus, $\mathbf{z}^{n+1} = \mathbf{z}^n + \tilde{Z}$. Once linear equations for $\tilde{Z}$ are derived, the equations are rewritten by replacing $\tilde{Z} = \mathbf{z}^{n+1} - \mathbf{z}^n$. Under this procedure, the time discretization for the Van der Pol problem is:

$$\begin{aligned} \frac{11x^{n+1} - 18x^n + 9x^{n-1} - 2x^{n-2}}{6\Delta t} &= -y^{n+1}, \\ \varepsilon\frac{11y^{n+1} - 18y^n + 9y^{n-1} - 2y^{n-2}}{6\Delta t} &= x^{n+1} + y^{n+1} - (y^n)^3 - \frac{2(y^n)^2 y^{n+1}}{3}, \end{aligned} \tag{4.46}$$

and the nonlinear algebraic part of our convection problem is reduced to:

$$0 = \nabla \cdot \mathbf{u}^{n+1}, \tag{4.47}$$

$$0 = -\partial_x P^{n+1} + \frac{1}{\nu_0}[L_{11}(\theta^n, u_x^n, u_z^n) + L_{12}(\theta^n)(u_x^{n+1} - u_x^n) + L_{13}(\theta^n)(u_z^{n+1} - u_z^n) + L_{14}(\theta^n, u_x^n, u_z^n)(\theta^{n+1} - \theta^n)], \tag{4.48}$$

$$0 = -P^n + \frac{1}{\nu_0}[L_{21}(\theta^n, u_x^n, u_z^n) + L_{22}(\theta^n)(u_x^{n+1} - u_x^n) + L_{23}(\theta^n)(u_z^{n+1} - u_z^n) + (L_{24}(\theta^n, u_x^n, u_z^n) + Ra)(\theta^{n+1} - \theta^n)], \tag{4.49}$$

$$\frac{11\theta^{n+1} - 18\theta^n + 9\theta^{n-1} - 2\theta^{n-2}}{6\Delta t} = (\mathbf{u}^{n+1} - \mathbf{u}^n) \cdot \nabla\theta^n + \mathbf{u}^n \cdot \nabla(\theta^{n+1} - \theta^n) \tag{4.50}$$

$$+ \mathbf{u}^n \cdot \nabla\theta^n - \Delta\theta^{n+1}, \tag{4.51}$$

where L_{ij} $(i = 1, 2; j = 1, 2, 3, 4)$ are given as in (4.12)-(4.19).

3. **Other semi-implicit schemes.** A semi-implicit scheme was proposed by [58] in the context of Navier-Stokes equation with constant viscosity and classical convection problems. This procedure considers a second order backward differentiation formula and a semi-implicit strategy, as follows:

$$0 = \nabla \cdot \mathbf{u}^{n+1} \tag{4.52}$$

$$0 = Ra\theta^{n+1}\vec{e}_3 - \Delta P^{n+1} + 2NL(\theta^{n+1}, \mathbf{u}^n) - NL(\theta^{n+1}, \mathbf{u}^{n-1}) \tag{4.53}$$

$$\frac{3\theta^{n+1} - 4\theta^n + \theta^{n-1}}{2\Delta t} = -2NL(\theta^n, \mathbf{u}^n) + NL(\theta^{n-1}, \mathbf{u}^{n-1}) + \Delta\theta^{n+1} \tag{4.54}$$

We test this procedure only in the context of the 2D convection problem and do not produce a version for testing it with the Van der Pol equation.

The results reported in Sections 3.1 and in Figure 4.4 consider a different version of (4.54), which is suitable for the use of variable time steps. Here, for simplicity, we only annotate the fixed step scheme.

4. **IMEX-BDF methods (explicit method).** García et al. [41] discuss the performance of IMEX-BDF methods in classical convection problems (constant viscosity) in spherical geometry with finite Prandtl number. Their schemes, which are shown to be efficient in those setups, are tested here in the context of differential algebraic equations (explicit method). In order to obtain an explicit expression for these schemes we rewrite the DAEs $M(t, \mathbf{x})\partial_t \mathbf{x} = f(t, \mathbf{x})$ in the form

$$\mathcal{L}_0 \partial_t \mathbf{x} = \mathcal{L}\mathbf{x} + NL(\mathbf{x}). \tag{4.55}$$

Here $\mathcal{L}_0$ and $\mathcal{L}$ are linear operators that include the boundary conditions and $NL(\mathbf{x})$ are the nonlinear terms. These are treated explicitly in the IMEX-BDF formula, which are related to the backward differentiation formula (BDF) [28, 52]. The unknown variable at time $n+1$, $\mathbf{x}^{n+1}$ is expressed (for constant time step Δt) as:

$$\left(I - \frac{\Delta t}{\gamma_0}\mathcal{L}_0\mathcal{L}^{-1}\right)\mathbf{x}^{n+1} = \sum_{i=0}^{k-1} \frac{\alpha_i}{\gamma_0}\mathbf{x}^{n-i} + \sum_{i=0}^{k-1} \frac{\beta_i \Delta t}{\gamma_0}\mathcal{L}_0 NL(\mathbf{x}^{n-i}), \tag{4.56}$$

Table 4.1. Integration coefficients of BDF-extrapolation formula.

Coefficient	Order					
	1st ($\gamma_0 = 1$)	2st ($\gamma_0 = 3/2$)	3st ($\gamma_0 = 11/6$)	4st ($\gamma_0 = 25/12$)	5st ($\gamma_0 = 137/60$)	6st ($\gamma_0 = 147/60$)
α_0	1	2	3	4	5	6
α_1	0	-1/2	-3/2	-3	-5	-15/2
α_2	0	0	1/3	4/3	10/3	20/3
α_3	0	0	0	-1/4	5/4	-15/4
α_4	0	0	0	0	1/5	6/5
α_5	0	0	0	0	0	-1/6
β_0	1	2	3	4	5	6
β_1	0	-1	-3	-6	-10	-15
β_2	0	0	1	4	10	20
β_3	0	0	0	-1	-5	-15
β_4	0	0	0	0	1	6
β_5	0	0	0	0	0	-1

where I is the identity operator and coefficients α_i, β_j and γ_0, which do not depend on n, are listed in [40] and in Table 4.1. If $k \geq 7$, these methods are unstable and useless for time integration.

These operators for the Van der Pol problem are:

$$\mathcal{L}_0 = \begin{pmatrix} 1 & 0 \\ 0 & \varepsilon \end{pmatrix}, \quad \mathcal{L} = \begin{pmatrix} 0 & -1 \\ 1 & 1 \end{pmatrix} \text{ and } \quad NL(\mathbf{x}) = \begin{pmatrix} 0 \\ -y^3 \end{pmatrix}. \tag{4.57}$$

Performance in the Van der Pol equation

Several tests for the Van der Pol equations are discussed using the fully implicit, the semi-implicit (point 2) and the explicit method described above. The results are summarized in Figure 4.3. First we note that for $\varepsilon = 0$, only the fully implicit method works. The performance of the remaining methods is then ranked in accordance with the smallness of ε at which the method still works. Thus a method that works at small ε is one providing a good performance in a system close to a DAE. Figure 4.3 confirms that the semi-implicit method that we propose is accurate for ε near zero ($\varepsilon = 0.01$), much beyond IMEX-BDF methods that are found to fail for $\varepsilon \leq 0.01$.

2D Convection with variable viscosity.

We now report on the performance of the schemes in the context of a viscosity law that follows

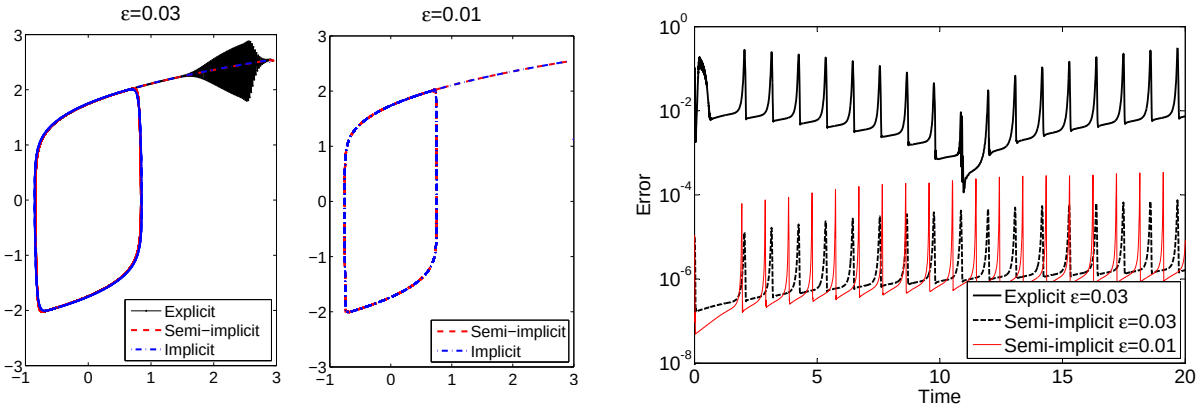

Figure 4.3. Solutions of the Van der Pol problem and the evolutions of error versus time. The relative error is calculated using the two norm and is benchmarked with respect the fully implicit solution.

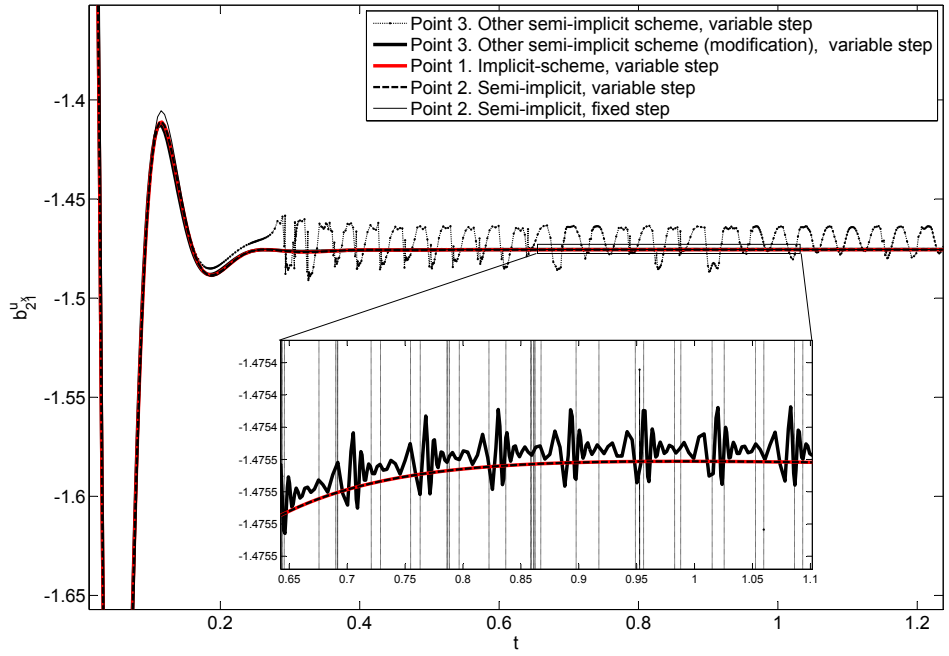

Figure 4.4. Transitory regime of an initial data towards a stationary solution at $\Gamma = 3.4$, $Ra = 1300$, with the "smooth" arctangent viscosity laws with parameter $\beta = 0.9$, $b = 10$ and $a = 0.01$. The modification of the other semi-implicit scheme is the replacement $\partial_z z^2 u_z$ by $-\partial^2_{xz} u_x$.

the "smooth" arctangent laws:

$$\begin{aligned}\frac{\nu(\theta)}{\nu_0} =& C_1 \arctan(\beta(Ra\theta\mu - b)) + C_2,\\ C_1 =& \frac{(1-a)}{\arctan(-\beta b) - \arctan(\beta(2500-b))},\\ C_2 =& 1 - C_1 \arctan(-b\beta),\end{aligned} \tag{4.58}$$

with parameters $\beta = 0.9, b = 10$, $a = 0.01$, $\Gamma = 3.4$ and $Ra = 1300$. Figure 4.4 shows a transitory regime of an initial data towards a stationary solution. These results confirm the good performance of our semi-implicit scheme, as against other semi-implicit approaches such as those discussed in point 3 above. Furthermore, it provides a better CPU performance that the fully implicit methods, as discussed in Section 3.1.

4.1.2. Solutions

Next, we describe in more detail some of the solutions found in Sections 3.2 and 3.3, which are obtained for two laws in which the viscosity changes abruptly with the temperature in a narrow gap. These are the "smooth" and "sharp" arctangent laws.

For the "smooth" arctangent law we explore dependence of the shape and structure of the plumes as a function of the parameters which contribute to it. These paremeters are as follows: a, which measures the inverse of the viscosity contrast; b, which is related to the transition temperature in the viscosity, and Ra, related to the heat transfer across the fluid layer and the bifurcation parameter in our study. A summary of the observed geometries is shown in Figure 4.5:

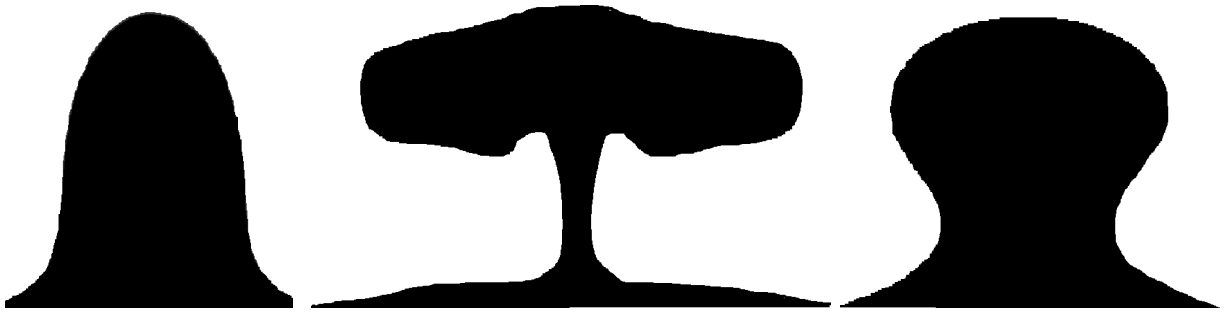

(a) Spout shape (b) Mushroom shape (c) Balloon shape

Figure 4.5. Plume geometries.

- **Spout shape.** This shape can be seen in Figure 4.5(a). Its visualization is achieved by depicting an isotherm at θ_1, which is the temperature at which the viscosity decays by 90% from the maximum ($\nu = 0.1\nu_0$). The temperature values above this threshold are shown in black. This type of pattern is found at small viscosity contrasts ($a = 0.1$) and large b (large transition temperature).

- **Mushroom shape.** This type of plume is represented in Figure 4.5(b). Its visualization depicts the isotherm θ_1, which is the temperature at which the viscosity decays by 90% from the maximum ($\nu = 0.1\nu_0$). The structure of this plume has a thinner tail and a head spread in a mushroom-like shape in the upper part of the fluid. This picture corresponds to small or intermedium b values and high Ra numbers. Moreover, this effect is observed at intermediate values of b and Ra if the viscosity contrast increases by diminishing a.

- **Balloon shape.** This geometry is found both for intermediate values of b with small Ra and high values of b with increasing Ra number and a decreasing to 0.001.

Among the stationary solutions observed along the bifurcation branches obtained either from the "smooth" law (see Section 3.2) or the "sharp" law (see Section 3.3), two of the most interesting are the plumes that break symmetry along their vertical axis and the non-uniformly distributed plumes. These solutions in the "smooth" arctangent law are closer to acquiring a balloon shape, while in the "sharp" arctangent law they approach a mushroom shape. Figure 4.6 illustrates these findings for the smooth arctangent law; it shows two close plumes which are asymmetric with respect to their vertical axis, and a third one which is displaced but maintains its symmetry. For comparison purposes, a solution of uniformly distributed symmetric plumes is displayed in Figure 4.6(b).

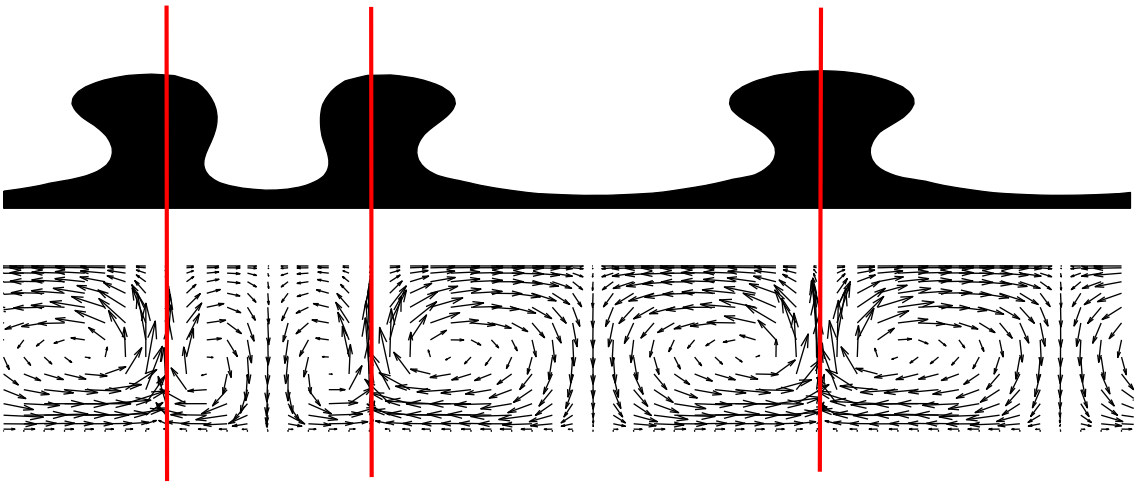

(a) Non-uniformly distributed plumes that break symmetry along their vertical axis. Stable solution.

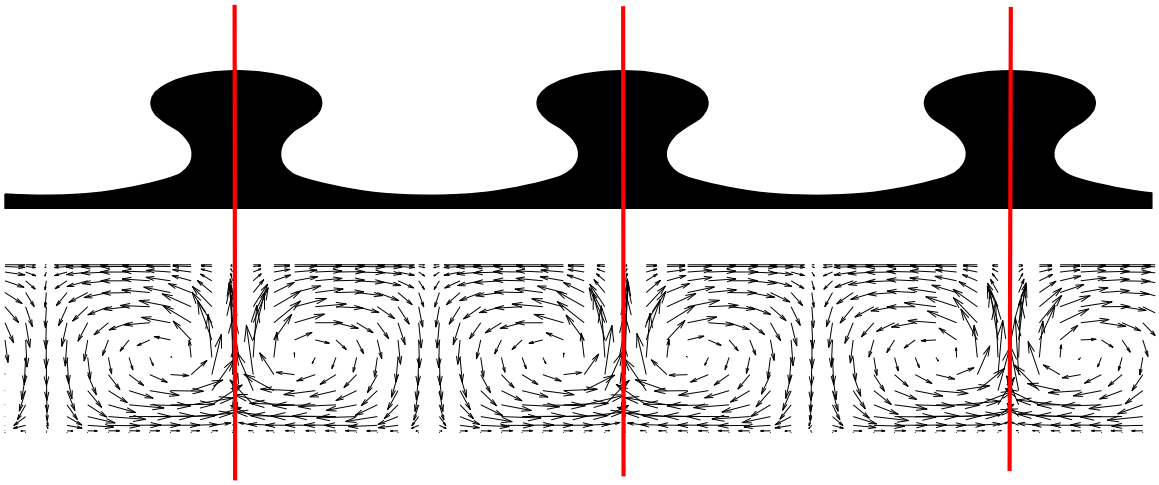

(b) Uniformly distributed plumes with symmetry along their vertical axis. Unstable solution.

Figure 4.6. Shape of temperature plumes and velocity vector field. Solutions of mode $m = 3$ in $\Gamma = 6.9$ and $R = 1500$ obtained using the "smooth" arctangent viscosity law (1.7) with parameter $b = 10$ and $a = 0.001$.

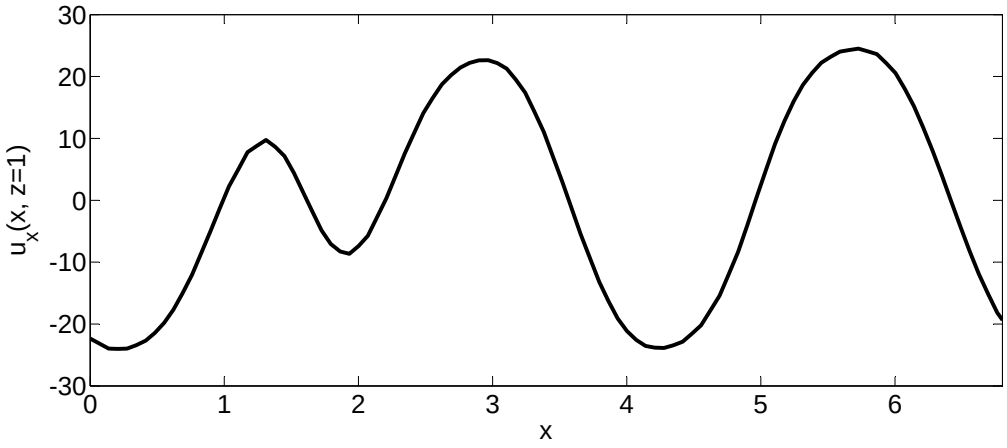

Figure 4.7. Representation of the horizontal velocity, u_x, versus x for the stable stationary solutions with non-uniformly distributed plumes that break symmetry along their vertical axis.

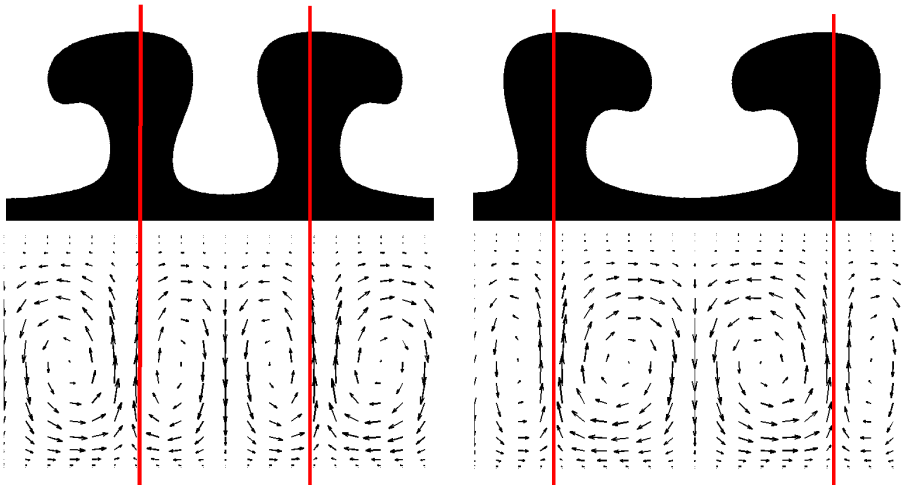

Figure 4.8. Plumes of a stable (right) and an unstable (left) stationary solution at $\Gamma = 2.166$ with $Ra = 155$.

None of the velocity field solutions along the stationary branches of the smooth arctangent law develop a stagnant lid at the surface, even though the upper part corresponds to the region with maximum viscosity. The velocity field in the upper surface sweeps a wide range of values, as displayed in Figure 4.7. This result is dissimilar to that obtained from the "sharp" arctangent law, as explained next, and to those reported in [108]. For the "sharp" arctangent law, the patterns on the stationary branches in the bifurcation diagrams indicate the presence of stagnant lids in the upper surface. Figure 4.8 illustrates solutions for this case which also break their symmetry along their vertical axes. The pattern on the left with the plumes more prominent outwards is unstable, while the pattern on the right with the plumes more prominent inwards is stable.

Coexisting with the stationary solutions of the sharp arctangent law, we find time-dependent

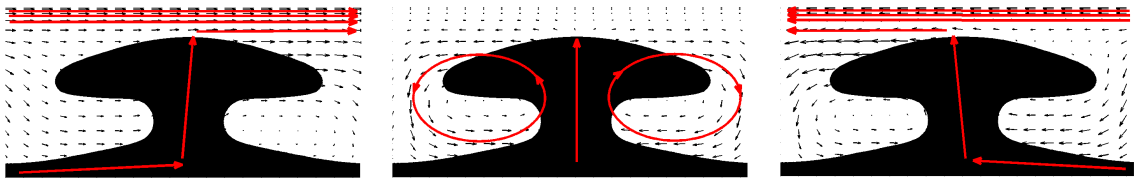

Figure 4.9. Outline of shape of plume and velocity vector field in "plate-like" convective.

regimes that develop plate-like motion within a thin upper layer. Figure 4.9 outlines this evolution for the case of a periodic solution. The central panel shows the time at which a stagnant lid is distinguished. The left and right panels show a time evolution in which the upper surface drifts alternately as a block towards the right and the left, respectively.

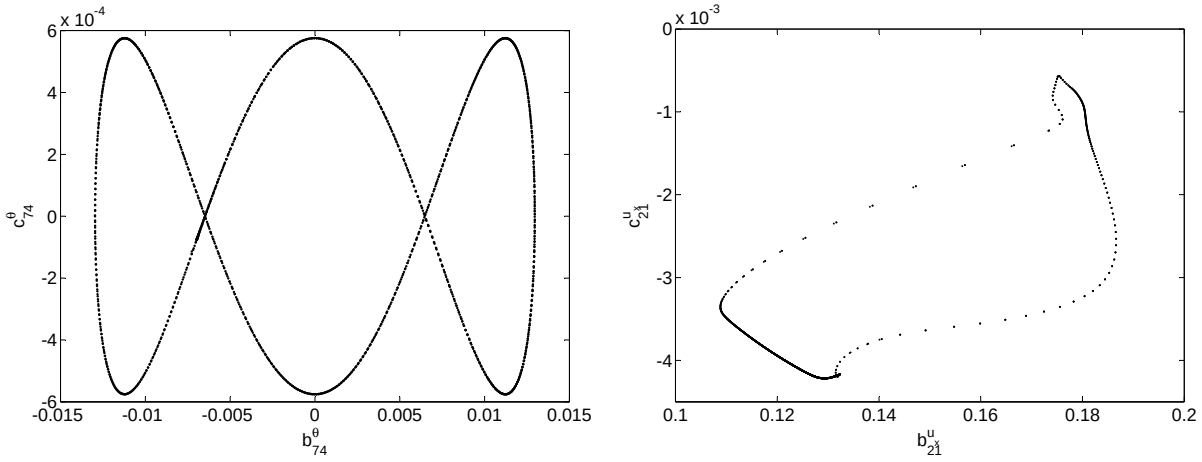

(a) Travelling wave ($Ra = 1300$, $\Gamma = 6.9$, $a = 0.01$).

(b) Cycle limit ($Ra = 2210$, $\Gamma = 7.4$, $a = 0.1$).

Figure 4.10. Time-dependent solution with the "smooth" arctangent laws (1.7) for $b = 10$.

Both the time-dependent solutions found for smooth and sharp arctangent laws show the influence of the symmetry present in the problem, such as travelling waves, limit cycles after a Hopf bifurcation, oscillating solutions in the neighborhood of heteroclinic connections and chaotic regimes. Some examples are reported in Figure 4.10. Figure 4.10(a) shows the projection of the evolution of a travelling wave found after a Hopf bifurcation for $Ra = 2210$, $\Gamma = 7.4$ and $a = 0.1$ with the smooth arctangent law. Figure 4.10(b) shows a projection of a limit cycle, which should be near a heteroclinic connection between two fixed points in which the solution remains for long periods of time. This fact is illustrated by a dot shown at every time step; the accumulation of such dots in the upper right and lower left corner confirm the presence of a fixed point in the neighborhood.

4.2. Confined rotating convection (3D)

4.2.1. Numerical Methods

We outline here the time and the spatial discretizations used in Section 3.4 for studying centrifugal and viscosity effects in a 3D rotating convection problem. A full description is found in [77].

The governing equations for this problem are discretized using the second-order time-splitting method proposed in [58], which constitutes an improvement on the projection scheme proposed in [43] and implemented in [47] in finite element approximations. This method is similar to the one described in point 3 in Section 4.1.1 within the time evolution subsection. The centrifugal force is treated implicitly, and the Coriolis force is treated explicitly. While the scheme does not work for viscosity with a strong dependence on temperature, it does so in the weakly dependent regime on which we focus here. The viscous term is expanded in a part that is independent of the temperature and is treated implicitly, while another part, that explicitly depends on T and is proportional to γ, is treated explicitly in the same way as the Coriolis term.

A complete step in the time evolution consists of a predictor step for pressure and velocity that determine preliminary values, which are then amended in a correction step. First, we obtain a temperature from a Helmholtz-type problem where the nonlinear term in velocity and temperature are treated explicitly:

$$\left(\Delta - \frac{3}{2\Delta t}\right)\theta^{n+1} = -2NL(\theta^n, \mathbf{u}^n) + NL(\theta^{n-1}, \mathbf{u}^{n-1}) + \Delta\theta^{n+1} - \frac{-4\theta^n + \theta^{n-1}}{2\Delta t}. \tag{4.59}$$

The temperature value is inserted into the Navier-Stokes equations, and a preliminary pressure $\overline{p}^{n+1}$ field is obtained from this equation and a continuity equation with a Neumann boundary condition. A predictor velocity $\overline{\mathbf{u}}$ field is calculated from the Navier-Stokes equation by including the predictor pressure with the actual boundary conditions:

$$\left(\Delta - \frac{3}{2\sigma\Delta t}\right)\overline{\mathbf{u}} = \sigma^{-1}\nabla\overline{p}^{n+1} + \sigma^{-1}\left(2NL(\theta^n, \mathbf{u}^n) - NL(\theta^{n-1}, \mathbf{u}^{n-1})\right) + 2F^n - F^{n-1}, \tag{4.60}$$

where F is the gravitational and centrifugal force. In order to decouple the linear diffusion terms in the momentum equations, according to [85] we use the combinations $u_+ = u + iv$ and $u_- = u - iv$. Finally, the corrected pressure and velocity fields are calculated with an explicit evaluation of the final divergence-free velocity field.

The spatial discretization is related with the expansion (4.5) used for our 2D convection problem. We employ cylindrical coordinates (r, θ, z) and use a Chebyshev expansion in the radial and vertical directions. Our polar coordinates on the plane (r, θ) are special in the sense that the radial expansions are considered in $r \in [-R, R]$ (where R is the radio of the cylinder), and the appropriate parity of the origin is forced. This is implemented by Mercader and co-workers in [77] following to Fornberg suggestions [37]. The problem is factorizable in the azimuthal direction and along this coordinate we use a Fourier expansion. The unknowns are the values of the Chebyshev coefficients at each azimuthal wavenumber. With this spatial discretization, several Helmholtz and Poisson equations must be solved for every Fourier mode k, which is done by using a diagonalization technique in the two coordinates r and z. The imposed parity of the Fourier modes guarantees the regularity conditions at the origin needed to solve the Helmholtz equations [78].

This scheme works satisfactorily in the regime of parameters used in Section 3.4, *i.e.* for a weak dependency of viscosity on temperature and the set of Prandtl numbers considered in our study.

4.2.2. Solutions

The effect of viscosity dependent on temperature

We extend the discussion on whether this dependence of viscosity on temperature is important in the nature of and effect on the structure of the solutions for the 3D rotating cylinder. In particular, in this problem we deal with glycerine water mixtures for which the Prandtl number is very large and is fixed to 100. We have performed several tests cited in the appendix to the Section 3.4 and which are summarized in Table 4.2. This table considers the Nusselt number, which is given by

$$< Nu > (z) = -\int_0^{\Gamma}\int_0^{2\pi} \frac{\partial T(r,\theta,z)}{\partial z} r dr d\theta. \tag{4.61}$$

We then compare this function for the solution obtained with constant viscosity $< Nu >_0$ and the solutions with viscosity dependent on temperature $< Nu >_{\varepsilon\Delta T}$. This is done by computing the maximum error (infinite) norm of the difference. We also measure the error in the temperature field T. For high Prandtl, the non-constant viscosity case presents no significant differences with the constant viscosity case. This conclusion is maintained when increasing the Froude numbers. Hence, since the effects of temperature-dependent viscosity are negligible, and yet quite expensive to incorporate computationally, viscosity has been kept constant by setting $\gamma = 0$ in (1.12).

Table 4.2. Effects of viscosity dependent on temperature against the case of constant viscosity ($\sigma = 100$, $\Omega = 625$)

		$Fr = 0$	$Fr = 0.046$	$Fr = 0.2878$	$Fr = 0.901$
$Ra = 9 \times 10^4$	$\| < Nu >_0 - < Nu >_{\varepsilon\Delta T} \|_\infty$	1.6945e-4	2.0822e-4	4.7338e-4	7.0671e-4
	$\|T^0 - T_{\varepsilon\Delta T}\|_\infty$	2.2451e-3	1.9283e-3	7.4668e-3	2.4801e-3
$Ra = 9.8 \times 10^4$	$\| < Nu >_0 - < Nu >_{\varepsilon\Delta T} \|_\infty$	3.8647e-4	3.9859e-4	2.7545e-4	1.8707e-4
	$\|T^0 - T_{\varepsilon\Delta T}\|_\infty$	1.4071e-4	2.1681e-3	1.8372e-3	8.5301e-3

The effect of the Prandtl number variation

The results reported in Section 3.4 correspond to Prandtl numbers obtained for each glycerine-water mixture. At a fixed temperature, an increase in the mass concentration of glycerine in the aqueous solution augments the kinematic viscosity, and thus the Prandtl number increases in such a way that it reaches very large values (see Figure 1.6). In this section we discuss how, in the range of parameters explored, from $\sigma \sim 100$ onwards, the variation of the Prandtl number has not influence on the results, and thus if this number had been fixed to 100 in the simulations, we expect that we would have arrived at the same conclusions.

Ignoring the centrifugal buoyancy ($Fr = 0$) and taking $\Omega = 625$, we examine the effects of increasing the Prandtl number in the initial solution. We test several values of σ beyond the limit

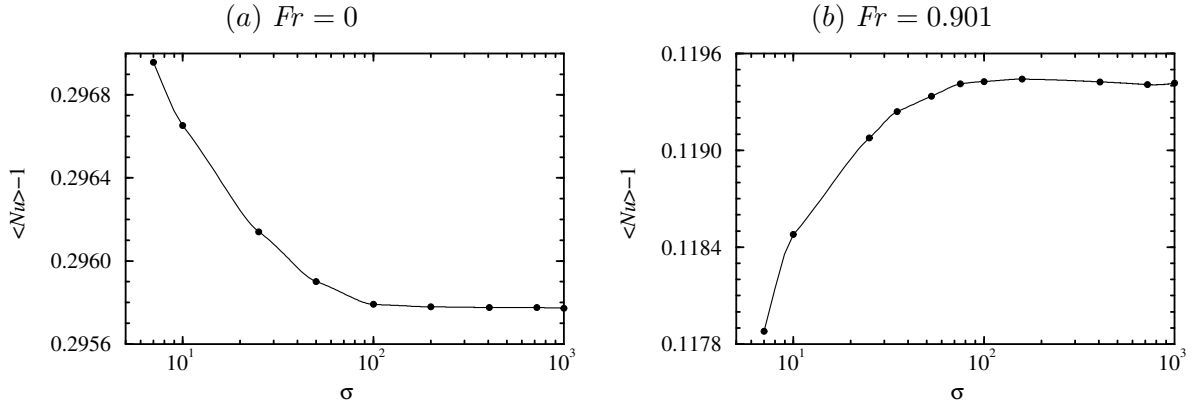

Figure 4.11. Variation of the Nusselt number with Prandtl number for $\Omega = 625$, $Ra = 9 \times 10^4$, $\Gamma = 4$.

$\sigma = 100$ and observe that the wall-modes structure is maintained for different σ, no significant differences being found between the solutions. Figure 4.11(a) shows how in this setup the Nusselt number varies with respect to the Prandtl number. The heat flux associated with the modulated wall modes diminish when increasing σ until $\sigma \sim 100$, and from this point on remains constant. When the centrifugal buoyancy is taken into account, *i.e.* taking $Fr \neq 0$, there is no change the conclusion. Figure 4.11(b) shows how the Nu grows when σ is increased up to $\sigma \sim 100$, and from this point onwards also remains constant.

Our conclusion agrees with those in studies carried out by other authors. The non-rotating experiments of [1], with $Ra \in [3 \times 10^7, 10^{11}]$, suggest that the Nusselt only weakly decreases with increasing Prandtl (they considered $\sigma \in [4, 40]$), and that Nu is independent of σ in the large σ-regime for moderate $Ra \in [10^5 - 10^9]$ (see [48, 97]). The same conclusions are reached in numerical simulations by [111, 113].

Our tests are performed for $Ra = 9 \times 10^4$, well above the critical Rayleigh when $Fr = 0$, $Ra_c \sim 4 \times 10^4$. We choose this Rayleigh number because despite being high, the Nusselt number remains constant for different values of the Froude number and enables simple diagrams to be made in the comparison, such as those in Figure 4.11. This Rayleigh number is the highest for which this situation occurs.

CHAPTER 5

Conclusions

Finally, the conclusions of the contributions of this work are summarized as follows:

First, a spectral semi-implicit method is proposed to solve a convection problem in which the equations are formulated in primitive variables, the viscosity strongly depends on temperature and the Prandtl number is infinity. The proposed scheme evaluates the time derivatives by backwards differentiation formulas (BDFs), which are adapted for performance with a variable time step. The solutions obtained from solving the fully implicit problem are compared with the solutions obtained from the proposed semi-implicit method, and for the problem under study, our semi-implicit method is shown to be accurate and provides a slightly faster performance than the fully implicit scheme. We also show that other semi-implicit schemes, which provide a good performance in classical convection problems with constant viscosity and finite Prandtl number, do not succeed in our setup. Additionally, with the assistance of bifurcation techniques, we gain insight into the stationary solutions displayed by the system and their stability limits, and this analysis is performed for a further validation of the accuracy of the scheme approaching the time evolution problem.

Finite element methods and finite volume methods have been proven to be successful for reaching extremely large viscosity contrasts up to $10^{10} - 10^{20}$. These are the preferred methods in the geophysical community for addressing problems in which viscosity depends on temperature. These limit are not improved with our numerical approach, since viscosity contrasts of 10^4 at most are explored. However our spectral scheme is later applied to viscosity laws in which novel dynamical evolutions derived from the presence of symmetries are found. In these settings, spectral methods may play a more effective role than other discretizations, since these latter approaches may overlook solutions which are fundamentally related to the symmetry.

The proposed techniques are used to explore the solutions obtained with several viscosity laws. The results obtained are as the follows:

- **Exponential law.** The morphology of the plume is described and compared with others obtained in the literature. Stable stationary solutions become unstable through a Hopf bifurcation, and the time-dependent regime is solved by the proposed spectral techniques. The time-dependent solutions found for the exponential viscosity law show no evidence of

influence on the symmetry.

- **"Smooth" arctangent law.** We successfully apply the above scheme to the study of a convection problem in which viscosity depends on temperature in a different way. We assume that it experiences a transition in a temperature gap, which in a first step is not very sharp. This is done by considering a smooth arctangent law. Assisted by bifurcation techniques, we gain insight into the possible stationary solutions satisfied by the basic equations exploring the bifurcations, both for a fixed Ra number as a function of the aspect ratio, and for bifurcations at fixed aspect ratios as a function of the Ra number. Our results report the influence of the values taken by several parameters of the viscosity law on the morphology of the plumes at a low aspect ratio. If the parameter controlling the temperature at which the transition occurs, b, is large, plumes tend to be thicker and show spout-like shapes. Increasing the Ra number induces their evolution towards balloon-shaped plumes, and this effect is more pronounced for high viscosity contrasts (small a). Additionally, if b is small, plumes are thinner, with their heads in the upper part of the fluid tending to spread in a mushroom-like shape.

  Among the stationary solutions obtained along the bifurcation branches, one of the more interesting stable patterns consists of the non-uniformly distributed plumes that break symmetry along their vertical axis. We also find travelling waves, oscillating solutions in the neighbourhood of heteroclinic connections and chaotic regimes characterized by "phase" drifts along the horizontal direction. All these solutions are linked to the presence of the SO(2) symmetry. No stagnant lid regime is observed in any of the physical conditions analyzed.

- **"Sharp" arctangent law.** By means of bifurcation diagrams and time-dependent numerical simulations, we find time-dependent convection regimes which are fundamentally related to the presence of the symmetry. These are limit cycles and time periodic solutions. We observe that during the evolution of the reported limit cycles the energy is abruptly released through "bursts" during which plate-like convection is develops. We find time-periodic solutions that have a similar plate-like dynamic with a smoother time evolution. No plate-like dynamics have hitherto been observed in this type of convection problem.

  These results provide convection examples of moving plates that coexist with subsurface upwards and downwards meandering jets, but without a proper subduction. The findings here suggest that the symmetry may play a role on the origin of the moving plates in the Earth. These examples do not rule out the existence of subduction in the Earth, but can be particularly illustrative for understanding convective styles prior to subduction.

Finally, we explore a rotating convection problem in aqueous glycerine mixtures, the results of which confirm that large Prandtl number convection cannot ignore centrifugal effects considered through the Fr number. The simulations at the largest Ra numbers explored show that the structure and dynamics of the plumes emerging from the top and bottom endwall boundary layers are significantly altered when Fr effects are included. At low Ra numbers, an increase in the glycerine concentration produces the rotating precession frequency gain (in absolute values)

and eventually causes convection to evolve towards target patterns dominated by concentric rings. For large Ra numbers, the wall modes are quenched and if Fr is large enough the wall modes completely disappear. Bulk convection appears in most of the cylinder at large Ra. The effects of glycerine viscosity dependence on temperature are negligible in the parameter range studied, and the influence of the Prandtl number beyond $\sigma = 100$ remains invariable.

5.1. Current and Future Research

Application of the spectral methods in magma conduits/chambers

According to the numerical methods developed to solve the time evolution of convection problems that appear in our previous papers, it should be possible to apply the spectral scheme to realistic data of the upper mantle and thus arrive at novel solutions enabling us to better understand aspects of magma conduits and chambers.

In petrological and volcanological concepts, the magma chamber/conduit is the place where magmas reside, crystallize, mix, differentiate, melt the wall-rock and become contaminated. Since magma chambers/conduits cannot be observed directly, scientific knowledge about them derives from the interpretation of indirect evidence that include observation of erupted rocks and gases, as well as geophysical data. Our attempts to deepen the knowledge of their behaviour will follow the line of physical volcanology by numerical simulation. Our aim is to find results that may have direct implications for models of eruption patterns and may help to predict or evaluate eruption styles.

Effects of the Rayleigh transition number in the structure of the solutions for the "sharp" arctangent law

In Section 3.3 we use the arctangent law given by (1.8) where the transition Rayleigh Ra_t adjusts the temperature at which the transition occurs. The choice of a positive value for Ra_t imposes that there exists a viscosity transition in the interior of a fluid layer even if Ra is very large. In this study, we take $Ra_t = 10$. A natural continuation of this work is to answer the question about how our solutions or their structure change when we increase the value of the Rayleigh transition $Ra_t > 10$, because these choices should lead to thicker stagnant lids near to the instability threshold. Do the plate-like dynamics depends on the size of the stagnant lid? Is the drifting process towards the right or the left maintained when the stagnant lid increases its thickness or does it disappear?

This problem is interesting because determining the impact of the different physical properties on convection styles is an important goal of research into planetary interiors. Our focus has been on examining the instabilities found in a 2D fluid in the presence of the O(2) symmetry, which contemplates a phase transition similar to a melting-solidification processes in which only change in the viscosity are considered. We wish to explore the limits in the parameter space for plate-like motions, the limits for solutions that exhibit energy bursts and the limits for time-dependent solutions that confirm a role for the symmetry.

Numerical scheme for the time evolution of convection with viscosity strongly dependent on temperature in 3D domains

Developing numerical schemes capable of tackling rotating convection problems in which viscosity strongly depends on temperature can provide insights into new dynamics and phenomenology.

On the one hand, we intend to complete the work in Section 3.1 by employing the same methods in a 3D domain, and on the other hand we will study the effect of viscosity strongly dependent on temperature in the presence of rotation, which is the natural continuation of the work in Section 3.4.

Conclusiones

Para terminar se resumen las contribuciones de este trabajo.

Primero, proponemos un método espectral semi-implícito para resolver un problema de convección en el cual las ecuaciones se formulan en variables primitivas, la viscosidad depende fuertemente de la temperatura y el número de Prandtl es infinito. El esquema propuesto evalúa las derivadas temporales mediante las fórmulas de diferenciación hacia atrás (BDFs), las cuales son adaptadas para usarse con pasos de tiempo variable. Comparamos las soluciones obtenidas resolviendo el problema totalmente implícito con las soluciones obtenidas a partir del método semi-implícito que hemos propuesto. Para el problema bajo estudio, nuestro método semi-implícito es preciso y tiene un rendimiento ligeramente más rápido que el esquema totalmente implícito. También mostramos que otros esquemas semi-implícitos, que proporcionan un buen rendimiento en los problemas de convección clásicos con viscosidad constante y número de Prandtl finito, no tienen un buen funcionamiento con nuestra configuración. Además, realizando un análisis de las soluciones mediante técnicas de bifurcación, nos hemos hecho una idea de las posibles soluciones estacionarias y de cuales son sus límites de estabilidad. Hemos utilizado este análisis para una validación adicional de la exactitud del esquema que aborda el problema de evolución temporal.

Los métodos de elementos finitos y los métodos de volúmenes finitos han demostrado tener éxito en los problemas de viscosidad variable alcanzando contrastes de viscosidad extremadamente grandes de hasta $10^{10} - 10^{20}$. Estos métodos son los preferidos en la comunidad geofísica para tratar problemas en los que la viscosidad depende de la temperatura. Con nuestro enfoque numérico no hemos mejorado estos límites, ya que sólo hemos explorado contrastes de viscosidad de 10^4. Sin embargo, nuestro esquema espectral se puede aplicar a otras leyes de viscosidad encontrando evoluciones dinámicas derivadas de la presencia de simetrías. Con esta configuración, los métodos espectrales pueden jugar un mejor papel que otras discretizaciones, las cuales pueden pasar por alto soluciones fundamentalmente relacionadas con la simetría.

Para explorar las soluciones obtenidas con varias leyes de viscosidad usamos las técnicas propuestas. Los resultados obtenidos son los siguientes:

- **Ley Exponencial.** Describimos la morfología de la pluma y la comparamos con otras obtenidas en la literatura. Existen soluciones estacionarias estables que vuelven inestables a través de una bifurcación Hopf. El régimen temporal es resuelto mediante las técnicas espectrales propuestas. Las soluciones dependientes del tiempo que encontramos con la ley exponencial no muestran ninguna evidencia de la influencia de la simetría.

- **Ley arcotangente "suave".** Hemos aplicado con éxito el esquema propuesto en el estudio de un problema de convección en el que la viscosidad depende de la temperatura de un modo diferente al caso anterior. Ahora hemos considerado que la viscosidad experimenta una transición "relativamente brusca" en un intervalo de temperatura pequeño mediante una ley arcotangente suave. Analizando las soluciones mediante técnicas de bifurcación, nos hacemos una idea de las posibles soluciones estacionarias que satisfacen las ecuaciones básicas. Hemos explorado las bifurcaciones tanto para un número Ra fijo en función de la relación de aspecto como para una relación de aspecto fija en función del número de Rayleigh Ra. Nuestros resultados muestran la influencia de los valores tomados por varios parámetros en la ley viscosidad sobre la morfología de las plumas para una relación de aspecto baja. Si el parámetro que controla la temperatura a la que se produce la transición, b, es grande, las plumas tienden a ser más gruesas y muestran forma de protuberancia ("spout"). Aumentar Ra induce su evolución hacia plumas en forma de globo, y este efecto es más pronunciado en los contrastes de viscosidad alta (pequeño a) . Además, si b es pequeño, las plumas son más delgadas y sus cabezas tienden a extenderse, por la parte superior del fluido, adoptando forma de seta.

  Entre las soluciones estacionarias obtenidas sobre las ramas de bifurcación, uno de los patrones estables más interesantes consiste en plumas no uniformemente distribuidas que rompen la simetría a lo largo de su eje vertical. También encontramos ondas viajeras, soluciones oscilatorias en las vecindades de conexiones heteroclínicas y regímenes caóticos caracterizados por "drifts" a lo largo de la dirección horizontal. Todas estas soluciones están vinculadas a la presencia de la simetría SO(2). No observamos ningún régimen de capa estancada para ninguna de las condiciones físicas analizadas.

- **Ley arcotangente "brusca".** Por medio de diagramas de bifurcación y simulaciones numéricas de evolución temporal hemos encontrado regímenes de convección que dependen del tiempo fundamentalmente relacionadas con la presencia de la simetría. Estos son ciclos límite y soluciones temporales periódicas. Observamos que durante la evolución de los ciclos límites encontrados la energía se libera bruscamente a través de "explosiones" durante las cuales se desarrolla convección en forma de placa móvil (hacia la derecha o la izquierda) que alterna en el tiempo con convección que desarrolla un placa superficial estancada. Hemos encontrado soluciones en tiempo periódicas que tienen una forma de placa dinámica similar a las anteriores pero con una evolución temporal más suave. En este tipo de problema no se había observado hasta ahora convección que desarrollara una placa móvil.

  Estos resultados proporcionan ejemplos de convección con placas móviles que coexisten con corrientes sub-superficiales que serpentean ondulantes hacia arriba y hacia abajo, pero sin ser propiamente una subducción. Los resultados sugieren que la simetría puede jugar un papel importante en el origen del movimiento de las placas en la Tierra. Estos ejemplos no descartan la existencia de subducción, pero pueden ser particularmente ilustrativos para entender estilos convectivos antes de la subducción.

Finalmente, en el problema de la convección con rotación, nuestros resultados confirman que para un número de Prandtl elevado no se puede ignorar la influencia del número de Froude en la convección. Hemos observado que incluso para los números de Ra más altos considerados el

número de Fr afecta de manera significativa a la estructura y a la dinámica de las plumas que surgen en la frontera del cilindro. Para bajo Ra aumentando la concentración de glicerina, se produce el aumento de la frecuencia de precesión de rotación (en valores absolutos) y, finalmente, la convección evoluciona hacia modos dominados por anillos concéntricos. Para Ra grandes los modos de pared se debilitan y si el Fr es lo suficientemente grande los modos de pared desaparecen por completo. La convección de la celda completa (*bulk*) aparece para elevado Ra. Los efectos de la dependencia de la viscosidad con la temperatura son insignificantes en el rango de parámetros estudiado y más allá de $\sigma = 100$ la influencia del número de Prandtl no varía.

Trabajo actual y futuro

Aplicaciones de los métodos espectrales en chimeneas volcánicas y cámaras de magma

Siguiendo los métodos numéricos desarrollados para resolver la evolución temporal de los problemas de convección que aparecen en nuestros trabajos anteriores, debería ser capaz de aplicar el esquema espectral a datos realistas del manto superior y encontrar nuevas soluciones que nos permitan entender mejor aspectos de las chimeneas volcánicas y de las cámaras de magma.

En términos petrológicos y vulcanológicos, la cámara/chimenea de magma es el lugar donde el magma reside, se cristaliza, se mezcla, se diferencia y derrite la pared de roca. Como las cámaras/chimeneas de magma no se pueden observar directamente, el conocimiento que tenemos sobre ellos deriva de la interpretación de las evidencias indirectas. Estas evidencias incluyen la observación de las rocas producidas por erupciones volcánicas, los gases, así como de los datos geofísicos. Nuestros intentos de profundizar en el conocimiento de su comportamiento siguen la línea de la vulcanología física mediante la simulación numérica. Nos gustaría encontrar resultados que pueden tener implicaciones directas sobre los modelos de los patrones de erupción y nos ayuden a predecir o evaluar cómo se produce ésta.

Efectos del Rayleigh de transición en la estructura de la solución para la ley arcotangente "brusca"

En la sección 3.3 usamos la ley arcotangente dada por (1.8) donde el Rayleigh de transición Ra_t ajusta la temperatura en la cual la transición ocurre. La elección de un valor positivo para Ra_t impone que exista una transición de la viscosidad en el interior de la capa del fluido aunque Ra sea muy grande. A lo largo de esta memoria de tesis hemos tomamos $Ra_t = 10$. Una continuación natural de este trabajo es preguntarnos sobre cómo nuestras soluciones o su estructura cambian cuando incrementamos el valor del Rayleigh de transición $Ra_t > 10$. Estas alternativas podrían conducir a capas estancadas de mayor espesor cerca al umbral de inestabilidad. ¿Podría la movilidad de la placa verse afectada por su grosor? ¿Se mantienen o desaparecen los deslizamientos hacia la derecha o la izquierda cuando la capa estancada aumenta su espesor?

Este problema es interesante, porque un objetivo importante de la investigación sobre interiores planetarios es buscar el impacto que las diferentes propiedades físicas tienen sobre la convección. Nos hemos centrado en examinar las inestabilidades que se desarrollan en un fluido 2D en presencia de la simetría O(2), contemplando una transición de fase similar a un proceso de fusión-solidificación en la que sólo se consideran cambios en la viscosidad. Queremos explorar el

espacio de parámetros para encontrar los límites que preservan las placas móviles, o las soluciones que liberan energía bruscamente o en definitiva permanezcan las soluciones en las que la simetría juega un papel.

Esquema numérico para la evolución temporal de la convección con viscosidad fuertemente dependiente de la temperatura en dominios 3D

Desarrollar esquemas numéricos que puedan describir la evolución temporal de la convección en la que la viscosidad depende fuertemente de la temperatura puede descubrirnos nuevas dinámicas y fenomenologías.

Por un lado, vamos a completar el trabajo de la sección 3.1 dando una implementación del mismo esquema para un dominio 3D y, por otro lado, como continuación natural del trabajo realizado en la Sección 3.4, se estudiará el efecto de incrementar la dependencia de la viscosidad con la temperatura, en presencia de rotación.

Bibliography

[1] G. Ahlers and X. Xu. Prandtl-number dependence of heat transport in turbulent Rayleigh-Bénard convection. *Phys. Rev. Lett.*, 86:3320–3323, 2001.

[2] D. Armbruster, J. Guckenheimer, and P. Holmes. Heteroclinic cycles and modulated travelling waves in systems with O(2) symmetry. *Physica D*, 29:257–282, 1988.

[3] P. Assemat, A. Bergeon, and E. Knobloch. Nonlinear Marangoni convection in circular and elliptical cylinders. *Physics of Fluids*, 19:104101, 2007.

[4] N. Becker, J. D. Scheel, M. C. Cross, and G. Ahlers. Effect of the centrifugal force on domain chaos in Rayleigh-Bénard convection. *Phys. Rev. E*, 73:066309, 2006.

[5] D. Bercovici. The generation of plate tectonics from mantle convection. *Earth and Planetary Science Letters*, 205:107–121, 2003.

[6] B. Blankenbach, F. H. Busse, U. Christensen, L. Cserepes, D. Gunkel, U. Hansen, H. Harder, G. Jarvis, M. Koch, G. Marquart, D. Moore, P. Olson, H.Schmeling, and M. Schnaubelt. A benchmark comparison for mantle convection codes. *Geophys. J. Int.*, 98:23–38, 1989.

[7] J. R. Booker. Thermal convection with strongly temperature-dependent viscosity. *J. Fluid Mech.*, 76:741–754, 1976.

[8] G. Brandeis and C. Jaupert. On the interaction between convection and crystallization in cooling magma chambers. *Earth Planet. Sci. Lett.*, 77:345–361, 1986.

[9] G. Brandeis and B. D. Marsh. The convective liquidus in a solidifying magma chamber: a fluid dynamic investigation. *Nature*, 339:613–616, 1989.

[10] M. Breden, J.-P. Lessard, and V. M. Global bifurcation diagram of steady states of systems of PDEs via rigorous numerics: a 3-component reaction-diffusion system. *Acta Applicandae Mathematicae*, 128:113, 2013.

[11] H. P. Bunge, M. A. Richards, and J. R. Baumgardner. Effect of depth-dependent viscosity on the planform of mantle convection. *Nature*, 436:436–438, 1996.

[12] F. H. Busse. Pattern of convection in spherical shells. *J. Fluid Mech.*, 72:65–85, 1975.

[13] F. H. Busse and N. Riahi. Pattern of convection in spherical shells II. *J. Fluid Mech.*, 123:283–391, 1982.

[14] O. Cadek and L. Fleitout. Effect of lateral viscosity variations in the top 300 km on the geoid and dynamic topography. *Geophysical Journal International*, 152:566–580, 2003.

[15] C. Canuto, M. Hussaini, A. Quarteroni, and T. A. Zang. *Spectral Methods in Fluid Dynamics*. Springer-Verlag, 1993.

[16] C. F. Chen and S. Thangam. Convective stability of a variable-viscosity fluid in a vertical slot. *J. Fluid Mech.*, 161:161–173, 1985.

[17] N. S. Cheng. Formula for the viscosity of a glycerol-water mixture. *Ind. Eng. Chem. Res.*, 47:3285–3288, 2008.

[18] P. Chossat. Bifurcation and stability of convective flows in a rotating or not rotating spherical shell. *SIAM Journal on Applied Mathematics*, 37:624–647, 1975.

[19] U. Christensen, , and H. Harder. 3-D convection with variable viscosity. *Geophysical Journal International*, 104:213–226, 1991.

[20] P. Constantin, C. Hallstrom, and V. Poutkaradze. Logarithmic bounds for infinite Prandtl number rotating convection. *J. Math. Phys.*, 42:773–783, 2001.

[21] S. M. Copley, A. F. Giamel, S. M. Johnson, and M. F. Hornbecker. The origin of freckles in unidirectionally solidified castings. *Metall. Trans.*, 1:2193–2204, 1970.

[22] M. G. Crandall and P. H. Rabinowitz. Bifurcation from simple eigenvalues. *J. Functional Analysis*, 8:321, 1971.

[23] L. Cserepes. On different numerical solutions of the equations of mantle convection. *Annales Universitatis Scientarum Budapestinensis*, Section of Geophysics and Metorology(ed. Stegena, Eötvös Univesity, Budapest):52–67, 1985.

[24] J. Curbelo, J. Lopez, A. M. Mancho, and F. Marqués. Confined rotating convection with large Prandtl number : Centrifugal effects on wall modes. *Physical Review E*, 89:013019, 2014.

[25] J. Curbelo and A. M. Mancho. Bifurcations and dynamics in convection with temperature-dependent viscosity under the presence of the O(2) symmetry. *Physical Review E*, 88:043005, 2013.

[26] J. Curbelo and A. M. Mancho. Spectral numerical schemes for time-dependent convection with viscosity dependent on temperature. *Communications in Nonlinear Science and Numerical Simulations*, 19(2), 2014.

[27] J. Curbelo and A. M. Mancho. Symmetry and plate-like convection in fluids with temperature-dependent viscosity. *Physics of Fluids*, 26:016602, 2014.

[28] C. Curtiss and J. Hirschfelder. Integration of stiff equations. *Proc. Natl. Acad. Sci.*, 38:235, 1952.

[29] P. Dauby, P. Colinet, and D. Johnson. Theoretical analysis of a dynamic thermoconvective pattern in a circular container. *Phys. Rev. E*, 61:2663, 2000.

[30] G. Davies. *Dynamic Earth. Plates, Plumes and Mantle convection*. Cambridge University Press, 2001.

[31] S. P. Dawson and A. M. Mancho. Collections of heteroclinic cycles in the Kuramoto-Sivashinsky equation. *Physica D: Nonlinear Phenomena*, 100(3-4):231–256, 1997.

[32] S. Day, J.-P. Lessard, and K. Mischaikow. Validated continuation for equilibria of PDEs. *SIAM J. Numer. Anal.*, 45:1398, 2007.

[33] C. R. Doering and P. Constantin. On upper bounds for infinite Prandtl number convection with or without rotation. *J. Math. Phys.*, 42:784 – 795, 2001.

[34] F. Dubuffet, D. A. Yuan, and E. S. G. Rainey. Controlling thermal chaos in the mantle by positive feedback from radiative thermal conductivity. *Nonlinear Proc. Geophys.*, 9:311–323, 2002.

[35] J. D. Dufek and G. W. Bergantz. Transient two-dimensional dynamics in the upper conduit of a rhyolitic eruption: A comparison of the closure models for the granular stress. *J. Volcanol. Geotherm. Res*, 143:113–132, 2005.

[36] J. W. Elder. Convection key to dynamical Geology. *Science Progress*, 56:1–33, 1968.

[37] B. Fornberg. *A Practical Guide to Pseudospectral Methods*. Cambridge University Press, 1998.

[38] D. Forsyth and S. Uyeda. On the relative importance of the driving forces of plate motion. *Geophys. J. R Astr. Soc.*, 43:163–200, 1975.

[39] M. Gameiro and J.-P. Lessard. Analytic estimates and rigorous continuation for equilibria of higher-dimensional PDEs. *J. Differential Equations*, 249:2237, 2010.

[40] F. García, M. Net, B. García-Archilla, and J. Sánchez. Newton-Krylov continuation of periodic orbits for Navier-Stokes flows. *J. Comput. Phys.*, 201:13–33, 2004.

[41] F. García, M. Net, B. García-Archilla, and J. Sánchez. A comparison of high-order time integrators for thermal convection in rotating spherical shells. *J. Comput. Phys.*, 229:7997–8010, 2010.

[42] D. Gartling. *NACHOS– A finite element computer program for incompressible flow problems, Parts I and II*. Sand 77-1333, Sand 77-1334. Sandia National Laboratories, Albuquerque, NM, USA., 1977.

[43] K. Goda. A multistep technique with implicit difference schemes for calculating two- and three- dimensional cavity flows. *J Comput Phys*, 30:76, 1979.

[44] M. Golubitsky and D. Schaeffer. Bifurcation with O(3) symmetry including applications to the Bénard problem. *Communs. Pure. Appl. Math.*, 35:81–11, 1982.

[45] M. Golubitsky, J. W. Swift, and E. Knobloch. Symmetries and pattern selection in Rayleigh-Bénard convection. *Physica D*, 10:249–276, 1984.

[46] S. P. Gregory. Physical properties of glycerine. In E. Jungermann and N. O. V. Sonntag, editors, *Glycerine: A Key Cosmetic Ingredient*, pages 113–156. Marcel Dekker, New York, 1991.

[47] P. Gresho. On the theory of semi-implicit projection methods for viscous incompressible flows and its implementation via a finite element methods that also introduces a nearly consistent mass matrix. Part I. theory. *Int J Number Meth Fluids*, 11:587, 1990.

[48] S. Grossmann and D. Lohse. Thermal convection for large Prandtl numbers. *Phys. Rev. Lett.*, 86:3316–3319, 2001.

[49] J. Guckenheimer and P. Holmes. Structurally stable heteroclinic cycles. *Math. Proc. Cambridge Philos. Soc.*, 103:189–192, 1988.

[50] M. Gunzburger, Y. Saka, and X. Wang. Well-posedness of the infinite Prandtl number model for convection with temperature-dependent viscosity. *Anal. Appl.*, 7:297–308, 2009.

[51] E. Hairer, S. Norsett, and G. Wanner. *Solving Ordinary Differential Equations I. Nonstiff Problems*. Springer, 2009.

[52] E. Hairer and G. Wanner. *Solving Ordinary Differential Equations. II. Stiff and Differential Algebraic Problems*. Springer, 1991.

[53] J. E. Hart. On the influence of centrifugal buoyancy on rotating convection. *J. Fluid Mech.*, 403:133–151, 2000.

[54] H. Herrero and A. M. Mancho. On pressure boundary conditions for thermoconvective problems. *International Journal for Numerical Methods in Fluids*, 39(5):391–402, 2002.

[55] A. M. Hofmeister and D. Yuen. Critical phenomena in thermal conductivity: Implications for lower mantle dynamics. *Journal of Geodynamics*, 44:186–199, 2007.

[56] G. M. Homsy and J. L. Hudson. Centrifugally driven thermal convection in a rotating cylinder. *J. Fluid Mech.*, 35:33–52, 1969.

[57] S. Hoyas, H. Herrero, and A. Mancho. Thermal convection in a cylindrical annulus heated laterally. *Journal of Physics A: Mathematical and General*, 35:4067, 2002.

[58] S. Hugues and A. Randriamampianina. An improved projection scheme applied to pseudospectral methods for the incompressible Navier–Stokes equations. *International Journal for Numerical Methods in Fluids*, 28(3):501–521, 1998.

[59] E. Ihrig and M. Golubitsky. Pattern selection with O(3) symmetry. *Physica D*, 12:1–33, 1984.

[60] A. Ismail-Zadeh and P. Tackley. *Computational Methods for Geodynamics*. Cambridge University Press, 2010.

[61] G. T. Jarvis and D. P. Mckenzie. Convection in a compressible fluid with infinite Prandtl number. *J. Fluid Mech.*, 96(03):515–583, 1980.

[62] R. Katz, R. Ragnarsson, and E. Bodenschatz. Tectonic microplates in a wax model of sea-floor spreading. *New J. Phys.*, 7:37, 2005.

[63] P. Kolodner, D. Bensimon, and C. M. Surko. Traveling-wave convection in an annulus. *Phys. Rev. Lett.*, 60(1):723–726, 1988.

[64] D. Krmpotic, B. Echebarria, and C. Perez-Garcia. Resonant interactions in Bénard-Marangoni convection in cylindrical containers. *Physica D*, 99(4):487–502, 1997.

[65] D. Krmpotic, G. B. Mindlin, and C. Perez-Garcia. Bénard-Marangoni convection in square containers. *Phys. Rev. E*, 54(4):3609–3613, 1996.

[66] R. P. J. Kunnen, B. J. Geurts, and H. J. H. Clercx. Experimental and numerical investigation of turbulent convection in a rotating cylinder. *J. Fluid Mech.*, 642:445–476, 2010.

[67] X. Liu and S. Zhong. Analyses of marginal stability, heat transfer and boundary layer properties for thermal convection in a compressible fluid with infinite Prandtl number. *Geophys. J. Int.*, 194:125–144, 2013.

[68] J. M. Lopez and F. Marques. Centrifugal effects in rotating convection: nonlinear dynamics. *J. Fluid Mech.*, 628:269–297, 2009.

[69] J. M. Lopez, F. Marques, I. Mercader, and O. Batiste. Onset of convection in a moderate aspect-ratio rotating cylinder: Eckhaus-Benjamin-Feir instability. *J. Fluid Mech.*, 590:187–208, 2007.

[70] J. M. Lopez, A. Rubio, and F. Marques. Traveling circular waves in axisymmetric rotating convection. *J. Fluid Mech.*, 569:331–348, 2006.

[71] T. Ma and S. Wang. Dynamic bifurcation and stability in the Rayleigh-Bénard convection. *Commun. Math. Sci.*, 2:159, 2004.

[72] T. Ma and S. Wang. Bifurcation theory and applications. *World Scientific*, 17:199, 2005.

[73] P. Machetel and P. Weber. Intermittent layered convection in a model mantle with an endothermic phase change at 670 km. *Nature*, 350:55–57, 1991.

[74] F. Marques, I. Mercader, O. Batiste, and J. M. Lopez. Centrifugal effects in rotating convection: axisymmetric states and three-dimensional instabilities. *J. Fluid Mech.*, 580:303–318, 2007.

[75] L. G. Mastin. Insights into volcanic conduit flow from an open-source numerical model. *Geochem. Geophys. Geosyst.*, 3:1037, 2002.

[76] D. P. Mckenzie and R. L. Parker. North Pacific: An example of Tectonics on a Sphere. *Nature*, 216:1276–1280, 1967.

[77] I. Mercader, O. Batiste, and A. Alonso. An efficient spectral code for incompressible flows in cylindrical geometries. *Computers & Fluids*, 39(2):215–224, 2010.

[78] I. Mercader, M. Net, and A. Falqués. Spectral methods for high order equations. *Computer Methods in Applied Mechanics and Engineering*, 91(1-3):1245–1251, 1991.

[79] G. B. Mindlin, T. Ondarcuhu, H. L. Mancini, C. Perez-Garcia, and A. Garcimartin. Comparison of data from Bérnard-Marangoni convection in a square container with a model-based on symmetry arguments. *International Journal of Bifurcation and Chaos*, 4(5):1121–1133, 1994.

[80] D. R. Moore, R. R. Peckover, and N. O. Weiss. Difference methods for two-dimensional convection. *Computer Phys. Communs.*, 6:198–220, 1974.

[81] L. N. Moresi and V. S. Solomatov. Numerical investigation of 2D convection with extremely large viscosity variations. *Physics of Fluids*, 7(9):2154–2162, 1995.

[82] M. C. Navarro, H. Herrero, A. M. Mancho, and A. Wathen. Efficient solution of generalized eigenvalue problem arising in a thermoconvective instability. *Communications in Computational Physics*, 3:308–329, 2008.

[83] M. C. Navarro, A. M. Mancho, and H. Herrero. Instabilities in buoyant flows under localized heating. *Chaos: An Interdisciplinary Journal of Nonlinear Science*, 17:023105, 2007.

[84] T. Ondarcuhu, G. B. Mindlin, H. L. Mancini, and C. Perez-Garcia. Dynamic patterns in Bérnard-Marangoni convection in a square container. *Phys. Rev. Lett.*, 70(25):3892–3895, 1993.

[85] S. A. Orszag and A. T. Patera. Secondary instability of wall-bounded shear flows. *J. Fluid Mech.*, 128:347–385, 1983.

[86] E. R. Oxburgh and D. L. Turcotte. Mid-Ocean Ridges and Geotherm Distribution during Mantle Convection. *J. Geophys. Res*, 73(8):2643–2661, 1968.

[87] J. Park. Dynamic bifurcation theory of Rayleigh-Bénard convection with infinite prandtl number. *Disc. Cont. Dynam. Syst. B*, 6:591, 2006.

[88] J. Park. Two-dimensional infinite Prandtl number convection: Structure of bifurcated solutions. *J. Nonlinear Sci.*, 17:199, 2007.

[89] R. Peng and M. Wang. Pattern formation in the Brusselator system. *J. Math. Anal. Appl.*, 309:151, 2005.

[90] F. Pla, A. M. Mancho, and H. Herrero. Bifurcation phenomena in a convection problem with temperature dependent viscosity at low aspect ratio. *Physica D: Nonlinear Phenomena*, 238(5):572–580, 2009.

[91] F. M. Richter, H. C. Nataf, and S. Daly. Heat transfer and horizontally averaged temperature of convection with large viscosity variation. *J. Fluid Mech*, 129:173–192, 1983.

[92] A. Rubio, J. M. Lopez, and F. Marques. Onset of Küppers-Lortz-like dynamics in finite rotating thermal convection. *J. Fluid Mech.*, 644:337–357, 2010.

[93] R. Rubio, J. M. Lopez, and F. Marques. Interacting oscillatory boundary layers and wall modes in modulated rotating convection. *J. Fluid Mech.*, 625:75–96, 2009.

[94] J. M. Sanz-Serna. *Fourier techniques in Numerical methods for Evolutionary problems.* In 3rd granada lectures in Computational Physics. Springer. P: L Garrida and J Marro Eds, 1994.

[95] J. R. Sarazin and A. Hellawell. Channel formation in Pb-Sn, Pb-Sb and Pb-Sn-Sb alloys and comparison with the system NH_4Cl-H_2O. *Metall. Trans.*, 19A:1861–1871, 1988.

[96] J. Schmalzl, M. Breuer, and U. Hansen. On the validity of two-dimensional numerical approaches to time-dependent thermal convection. *Europhysics Letters*, 67(3):390–396, 2004.

[97] G. Silano, K. R. Sreenivasan, and R. Verzicco. Numerical simulations of Rayleigh-Bénard convection for Prandtl numbers between 10^{-1} and 10^4 and Rayleigh numbers between 10^5 and 10^9. *J. Fluid Mech.*, 662:409–446, 2010.

[98] V. S. Solomatov. Initiation of subduction by small-scale convection. *J. Geophys. Res*, 109:B01412, 2004.

[99] V. S. Solomatov and L. N. Moresi. Stagnant lid convection on Venus. *J. Geophys. Res*, 101:4737–4753, 1996.

[100] V. S. Solomatov and L. N. Moresi. Three regimes of mantle convection with non-newtonian viscosity and stagnant lid convection on the terrestrial planets. *Geophysical Research Letters*, 24(15):1907–1910, 1997.

[101] S. C. Solomon, S. E. Smrekar, D. L. Bindschadler, R. E. Grimm, W. M. Kaula, R. J. Phillips, R. S. Saunders, G. Schubert, S. W. Squyres, and E. R. Stofan. Venus tectonics: An overview of Magellan observations. *J. Geophys. Res*, 97(13199-132555), 1992.

[102] E. A. Spiegel. Convection in stars I. Basic Boussinesq convection. *Annu. Rev. Astron. Astrophys.*, 9:323–352, 1971.

[103] R. J. A. M. Stevens, H. J. H. Clercx, and D. Lohse. Heat transport and flow structure in rotating Rayleigh–Bénard convection. *Eur. J. Mech. B-Fluids*, 40:41–49, 2013.

[104] P. J. Tackley. Self-consistent generation of tectonic plates in three dimensional mantle convection. *Earth and Planetary Science Letters*, 157:9–22, 1998.

[105] K. E. Torrance and D. L. Turcotte. Thermal convection with large viscosity variations. *J. Fluid Mech.*, 47(113), 1971.

[106] R. Trompert and U. Hansen. Mantle convection simulations with reologies that generate plate-like behaviour. 395(686-689), 1998.

[107] R. Trompert and U. Hansen. Mantle convection simulations with rheologies that generate plate-like behaviour. *Nature*, 395(6703):686–689, 1998.

[108] M. Ulvrová, S. Labrosse, N. Coltice, P. Raback, and P. Tackley. Numerical modelling of convection interacting with a melting and solidification front: Application to the thermal evolution of the basal magma ocean. *Physics of the Earth and Planetary Interiors*, 206-207:51–66, 2012.

[109] J. B. van den Berg, J.-P. Lessard, and K. Mischaikow. Global smooth solution curves using rigorous branch following. *Math. Comp.*, 79:1565, 2010.

[110] S. A. van Gilsa and J. Mallet-Paret. Hopf bifurcation and symmetry: travelling and standing waves on the circle. *Proceedings of the Royal Society of Edinburgh: Section A*, 104(3-4):279–307, 1986.

[111] R. Verzicco and R. Camussi. Prandtl number effects in convective turbulence. *J. Fluid Mech.*, 383:55–73, 1999.

[112] C. Wang and Z. Zhang. Global well-posedness for the 2-D Boussinesq system with the temperature- dependent viscosity and thermal diffusivity. *Advances in Mathematics*, 228:43–62, 2011.

[113] K. Q. Xia, S. Lam, and S. Q. Zhou. Heat-flux measurement in high-Prandtl-number turbulent Rayleigh-Bénard convection. *Phys. Rev. Lett.*, 88:064501, 2002.

[114] X. Yan. On limits to convective heat transport at infinite Prandtl number with or without rotation. *J. Math. Phys.*, 45:2718, 2004.

[115] T. K. B. Yanagawa, M. Nakada, and D. A. Yuan. The influence of lattice thermal conductivity on thermal convection with strongly temperature-dependent viscosity. *Earth Space Sci.*, 57(15-28), 2005.

[116] J.-Q. Zhong, R. J. A. M. Stevens, H. J. H. Clercx, R. Verzicco, D. Lohse, and G. Ahlers. Prandtl-, Rayleigh-, and Rossby-number dependence of heat transport in turbulent rotating Rayleigh-Bénard convection. *Phys. Rev. Lett.*, 102:044502, 2009.